PROBING THE STANDARD MODEL AND NUCLEON STRUCTURE VIA PARITY-VIOLATING ELECTRON SCATTERING

Thomas Brian Humensky

A DISSERTATION
PRESENTED TO THE FACULTY
OF PRINCETON UNIVERSITY
IN CANDIDACY FOR THE DEGREE
OF DOCTOR OF PHILOSOPHY

RECOMMENDED FOR ACCEPTANCE
BY THE DEPARTMENT OF
PHYSICS

JUNE 2003

Abstract

Parity-violating electron scattering has developed over the last 25 years into a tool to study both the structure of electroweak interactions and the structure of nucleons. Work on two parity-violation experiments is reported in this thesis. They are the Hall A Proton Parity EXperiment (HAPPEX), which ran at Jefferson Laboratory in 1998-1999, and SLAC E-158, which had its first physics running in 2002.

HAPPEX measured the parity-violating asymmetry in elastic e-p scattering at a momentum transfer squared of $Q^2 = 0.477$ GeV^2 and a scattering angle of 12°. This asymmetry is sensitive to the presence of strange sea quarks in the proton. In particular, it is sensitive to the proton's strange elastic form factors. An asymmetry of $A_{LR}^{ep} = -15.05 \pm 0.98 \pm 0.56$ ppm was measured, where the first error is statistical and the second error is systematic. Combining this asymmetry measurement with existing measurements of the electromagnetic form factors of the proton and neutron allowed HAPPEX to set new constraints on the strange elastic form factors of the proton:

$$G_E^s + 0.392 G_M^s = 0.025 \pm 0.020 \pm 0.014, \tag{1}$$

where G_E^s and G_M^s are the strange electric and magnetic form factors of the proton, respectively. The first error is the quadrature sum of the experimental errors and the second error is due to uncertainty in the electromagnetic form factors. This result is consistent with the absence of a contribution from strange quarks. This thesis reports an analysis of the 1999 data set, with a particular focus on the determination of the raw asymmetry and the corrections to the raw asymmetry to account for helicity-correlated asymmetries in properties of the electron beam.

SLAC E-158 is an experiment to measure the right-left cross-section asymmetry in Møller scattering. 45-GeV and 48-GeV longitudinally polarized electron beams are scattered off unpolarized electrons in a liquid hydrogen target at an average momentum transfer squared of $Q^2 = 0.025 \, \text{GeV}^2$.

The parity-violating asymmetry in this process is proportional to $(1/4 - \sin^2\theta_W)$, where $\sin^2\theta_W$ is the weak mixing angle. This measurement tests electroweak theory at the one-loop level and probes for physics beyond the Standard Model, including additional heavy gauge bosons, electron compositeness, and extra spatial dimensions. Within the Standard Model, the raw asymmetry is expected to be approximately 0.1 ppm. E-158 had engineering runs in 2000 and 2001 and had its first two physics runs in the spring and fall of 2002. Data from the physics runs is currently being analyzed.

One class of systematic error to which both of these experiments are sensitive is an asymmetry in the rate of scattered electrons due to helicity-correlated asymmetries in properties of the electron beam. HAPPEX and E-158 are the first two parity-violation experiments to use a "strained" GaAs photocathode as a source of polarized electrons. Strained cathodes give rise to increased asymmetries in beam properties. This thesis describes work done in preparation for each experiment to understand and suppress those asymmetries. Results on beam asymmetries from the 1999 HAPPEX run and the 2000 E-158 engineering run (a beam test called T-437) are presented.

Acknowledgements

I would like to thank my advisor Gordon Cates for his guidance over the last nearly six years. He gave me plenty of space to learn on my own, pushed me when I needed it, and supported me to the end. I would also like to thank Krishna Kumar and Paul Souder for teaching me to think like an experimental physicist during both HAPPEX and E-158. Thanks to Mike Woods for teaching me optics and setting me loose in SLAC's laser lab.

When I joined HAPPEX, I joined an experiment that had already run once successfully, and I learned so much from those who had been working on it for years: Rich Holmes, Bob Michaels, Krishna, Paul, and the other thesis students on the experiment. The students were, from the first run, Wilson Miller, Bill Kahl, Gary Rutledge, and Johan Jardillier, and from the second run, Maud Baylac and Baris Tonguc. The JLab Injector group, and Matt Poelker and John Hansknecht in particular, worked very hard to make HAPPEX happen and it was a pleasure to work with them.

At SLAC, the Polarized Electron Source group was extremely supportive of E-158 and helped me out at every turn. They included Greg Mulhollan, Ray Alley, Tom Galetto, Jim Turner, Axel Brachmann, and Takashi Maruyama. I could not have gotten through without my fellow students, David Relyea, Peter Mastromarino, Mark Jones, and Klejda Bega. So many trips to Denny's and Mr. Chau's and countless bags of chocolate Oreo's. Imran Younus introduced me to the joys of optical-fiber cutting. Outside of the lab, friends added much-needed color to my life. Thank you Brigit, Aron, Craig, Jim, Savio, Mike, Todd, Maria, Dan, and Neal.

By the time I moved "back" from SLAC, Gordon had moved to the University of Virginia,

and I made a new set of friends amongst our group there: Jaideep (who introduced me to fantasy football), Alexandre, Al, Ryan, Scott, and James. Thanks for making another new place feel like home.

My parents, Tom and Suzanne Humensky, my sister, Meredith, and my brother-in-law, Brian, always supported my dream of getting a Ph. D. in physics and while I was in grad school were only a short drive away. They helped me move many times and were always ready with a home-cooked meal and an empty washing machine. Finally, a special thank you to Jennifer, who was first my girlfriend, then my fiancée, and now my wife. Her love, support, patience, sacrifice, and beauty saw me through, and I would not be where I am without her by my side.

Contents

List of Figures

List of Tables

Chapter 1

Introduction

In 1917 Emmy Noether elucidated the deep connection between symmetry principles and conserved quantities [1]: for each symmetry in nature, there exists a corresponding conserved quantity. For example, invariance of the physical laws under translations in spacetime ($p^\mu \to p^\mu + q^\mu$) leads to the conservation of momentum and energy, and invariance under rotations leads to the conservation of angular momentum. Of particular interest to this work, invariance of the strong and electromagnetic interactions under spatial inversion ($x \to -x$) leads to conservation of the parity quantum number of elementary particles. However, following a review of the experimental evidence related to the weak interaction, Lee and Yang argued that spatial inversion symmetry is not obeyed by weak interactions [2]. In 1956, Madame Wu and collaborators verified the parity-violating nature of weak interactions in their classic polarized ^{60}Co beta-decay experiment [3]. This experiment and others demonstrated the vector–axial vector structure of the weak charged-current interaction and showed that it is maximally parity violating. Since then, further studies using parity violation have tested the structure of the Standard Model and, more recently, have probed the structure of the proton. This thesis reports work on two such experiments: SLAC E-158, a precise measurement of the weak mixing angle at $Q^2 = 0.025$ GeV^2; and HAPPEX at Jefferson Lab, a measurement of the strange form factors of the proton.

1.1 Low-Energy Tests of the Standard Model

Weak neutral currents were first observed in 1973, when the scattering of muon neutrinos and antineutrinos off electrons and nuclei was found to yield a cross section comparable in magnitude to other (charged current) weak processes. However, the ν-e and ν-N experiments were unable to determine to what extent, or even whether, the weak neutral current was parity-violating. In 1978, SLAC E-122 measured the parity-violating asymmetry in the cross section for the scattering of longitudinally polarized electrons off a deuteron target. The mixing angle θ_W between the mass and flavor eigenstates of the photon and the Z^0 can be extracted from the asymmetry. The value obtained, $\sin^2 \theta_W = 0.224 \pm 0.020$ [4], indicated an amount of parity violation consistent with the gauge theory of Weinberg and Salam. Various left-right symmetric gauge theories (which predicted zero parity violation) were ruled out with high significance. Other classes of "hybrid" gauge theories in which right-handed electrons are assigned to isospin singlets and right-handed quarks to isospin doublets were not consistent with the combination of the neutrino-nucleon data and the E-122 result. The ability of this experiment to distinguish the Weinberg-Salam model from other classes of gauge theories makes it one of the cornerstone measurements on which the Standard Model is constructed. E-122's measurement of an asymmetry of order $\sim 10^{-4}$ pioneered many of the techniques in use today to measure parity-violating asymmetries up to three orders of magnitude smaller. A decade later, measurements of the asymmetry in parity-violating electron scattering off ^{12}C [5] and ^{9}Be [6] further tested the Standard Model at low energies. Today, SLAC E-158 is part of a new generation of low-energy tests of the Standard Model, with sensitivities to potential new physics rivalling or in certain ways exceeding those of high-energy colliders and providing complementary information.

SLAC E-158 is an experiment to measure the value of $\sin^2 \theta_W$ at low momentum transfer ($Q^2 \approx 0.025$ GeV^2) by looking at the parity-violating asymmetry in the scattering of a longitudinally polarized electron beam off the atomic electrons in a liquid hydrogen target. E-158 plans to measure $\sin^2 \theta_W$ to ~ 0.0008, which would make it the most precise measurement of $\sin^2 \theta_W$

away from the Z^0 resonance and would establish the running* of the weak coupling constant at a significance of $\sim 8\sigma$ within the context of the Standard Model. Such precision provides the potential to detect disagreement with the Standard Model. E-158 has competitive sensitivity to a number of new physics scenarios, including new neutral gauge bosons, electron compositeness, and large extra dimensions. However, the raw asymmetry is expected to be on the order of 10^{-7}, three orders of magnitude smaller than E-122 and one order of magnitude smaller than Bates ^{12}C, which currently holds the record for the smallest asymmetry measured in a parity-violating electron-scattering experiment. E-158 presents a number of interesting experimental challenges, including stringent requirements on the properties of the polarized electron beam, a thick liquid hydrogen target with $< 10^{-4}$ pulse-to-pulse density fluctuations, and the requirement of a high signal-to-background ratio at scattering angles of $\sim 0.4°$.

1.2 Studying the Role of Strange Quarks in Nucleons

The simplest picture of the proton in the quark model is a "bag" containing three valence quarks (two up and one down) confined by the strong forces of QCD. This structure is shown schematically in Figure 1.1a. This naive picture is adequate for understanding some properties of the proton, such as its electric charge, but fails to address such basic properties as its anomalous magnetic moment. It obviously does not allow for the presence of strange quarks. A more accurate view takes into account the presence of copious quantities of gluons and the $q\bar{q}$ pairs (sea quarks) into which the gluons can split, as suggested by Figure 1.1b. The strong coupling between the quarks and gluons gives the proton a very complex, nonperturbative structure. Quantum Chromodynamics (QCD) is believed to be the theory that describes this structure. However, QCD is not calculable at low energies, and so it remains a mystery what role the gluons and sea quarks play in determining the static and dynamic properties of the proton's structure. Strange quarks (and antiquarks) are only present in the sea (unlike up and down quarks), and so measurements that isolate their

---

*The "running" is the change in $\sin^2 \theta_W$ from $Q^2 = M_Z^2$ to $Q^2 = 0.025$ GeV^2, as discussed in section 2.2.2.
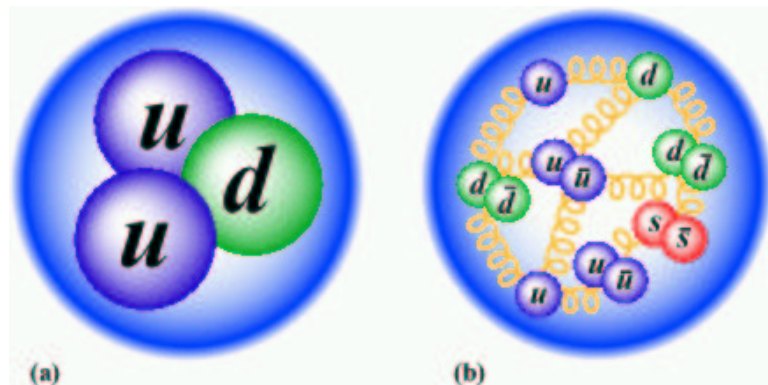
Figure 1.1: Two views of the internal structure of the proton: (a) the proton is built from three valence quarks, (b) the proton includes the valence quarks as well as numerous gluons and sea quarks.

contributions to proton structure provide a unique low-energy probe of the sea.[†]

A number of experiments over the last several decades have pointed to strange sea quarks as significant contributors to the proton's properties. Deep-inelastic neutrino-nucleon scattering [7, 8] indicates that strange quarks carry a sizeable fraction of the momentum carried by the sea. Violations of the Ellis-Jaffe sum rule can be explained by allowing either the strange quark sea or the gluons to be polarized and therefore to contribute significantly to the proton's spin [9, 10, 11]. Measurements of the "sigma term" in pion-nucleon scattering[‡] yield the contribution of the bare quark masses to the proton mass and suggest that strange quarks are responsible for a sizeable fraction of the proton mass, though with 100% theoretical uncertainties [12, 13].

Parity-violating electron scattering contributes to our understanding of the role of strange sea quarks in the nucleon by providing a clean measurement of another observable that is very sensitive to the presence of strange quarks. In elastic polarized electron-proton ($\overrightarrow{e}$-p) scattering, the dominant sensitivity to strange quarks is to the matrix element $\langle p|\overline{s}\gamma_\mu s|p\rangle$, where s is the strange quark spinor. This matrix element is not directly measured by any of the experiments mentioned above. Measuring it yields the strange elastic form factors G_E^s and G_M^s, two unknown quantities

---

[†]However, I should mention that because strange quarks are so much more massive than up and down quarks, it is questionable whether $\overline{s}s$ sea quarks behave the same as $\overline{u}u$ and $\overline{d}d$ sea quarks.

[‡]The sigma term is defined as $\sigma_P = \frac{1}{4M_P}(m_u + m_d)\langle P|(\overline{u}u + \overline{d}d)|P\rangle$.

which describe fundamental features of the proton. At zero momentum transfer, G_E^s and G_M^s can be related to the proton's strangeness radius ρ_s and strange magnetic moment μ_s, respectively, as is discussed below. Several recent reviews have discussed using parity-violating electron scattering to measure strange quark contributions to the proton form factors [14, 15, 16, 17]. One such experiment, the Hall A Proton Parity EXperiment (HAPPEX), was the first in an ongoing series of experiments at Jefferson Laboratory (JLab) in Newport News, VA that use parity violation in the elastic scattering of polarized electrons off unpolarized protons to extract the strange-quark form factors of the proton. HAPPEX measured the combination of strange form factors $G_E^s + 0.39 G_M^s$ at $Q^2 = 0.477$ GeV^2. In addition to this physics result, HAPPEX's successful completion demonstrated that JLab is an excellent facility for measuring small parity-violating asymmetries.

It is difficult to calculate the strange elastic form factors from first principles since $m_s \sim \Lambda_{QCD}$. The energy scale is too low to use perturbative QCD. Instead, theorists use a variety of models, including ones based on chiral perturbation theory, constituent quark approaches, and dispersion relations. However, problems exist with each class of models, and as Figure 1.2 demonstrates, the models yield a wide range of values for ρ_s and μ_s. In this Figure, ρ_s is unitless and μ_s is plotted in units of nuclear magnetons. The corresponding quantities for the proton are $\rho_P \approx 10$ and $\mu_P = 2.79 \mu_N$. One review article [15] discusses the strengths and weaknesses of a number of these approaches. Ultimately, determining the strange elastic form factors is a problem well suited for lattice QCD, and progress is being made on this front. However, since the strange form factors are inherently related to the $\bar{q}q$ sea, unquenched[§] lattice QCD calculations are necessary, and they require more computing power than is currently available in order to be properly done.

The fact that the strange elastic form factors cannot yet be reliably computed adds additional motivation for either measuring or limiting them experimentally. Direct measurements of the

---

[§] In the quenched approximation, "dynamical" quark effects, i.e. $\bar{q}q$ loops, are neglected. Since strange quarks appear in protons only in loops, the quenched approximation must be lifted before lattice QCD can shed light on this problem.
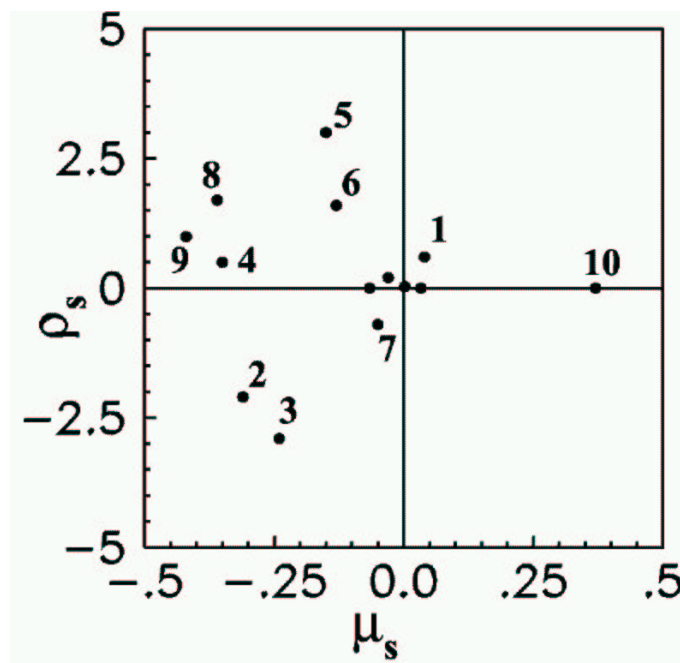
Figure 1.2: Theoretical calculations of the strangeness radius and strange magnetic moment of the proton. The points indicate the predictions of various models: (1) [18], (2) [19], (3) [20], (4) [21], (5) [22], (6) [23], (7) [24], (8) [25], (9) [26], and (10) [27].

strange form factors via parity-violating electron scattering can determine $\bar{s}s$ effects empirically in the elastic regime and can provide a benchmark to validate calculations and guide theory. Therefore, it is important that measurements be sensitive enough to discriminate between models. HAPPEX has made useful first steps in validating the necessary experimental techniques and constraining the available parameter space, as is discussed in Chapter 8.[¶]

In section 2.1, the formalism for interpreting parity-violating $\vec{e}$-p scattering is presented, and in section 8.3 the worldwide experimental program for studying strange quarks via parity violation is summarized.

[¶]An experiment going after similar physics, SAMPLE, has been running at Bates Lab and actually published the first results in this field. It is discussed in section 8.3.

1.3 Controlling Electron Beam Helicity Correlations

This thesis presents my contributions to HAPPEX and E-158. The theme that links my work on these two parity-violating electron-scattering experiments is the requirement of producing a longitudinally polarized electron beam with minimal right-left helicity-correlated differences in its parameters. Helicity-correlated differences in the beam's intensity, energy, position, angle, or spot size (sometimes referred to in this document as $^{\text{beam}}A_{\text{LR}}$'s) can generate false asymmetries in the scattering rate into the detector that can bias the measurement of the physics asymmetry. The 1999 HAPPEX run and E-158 are the first two parity-violating electron scattering experiments to use a strained GaAs photocathode in their polarized electron sources. This type of cathode provides very high electron beam polarizations ($\sim 70 - 80\%$), but at the expense of greatly increased helicity correlations in the electron beam's parameters. I focused on developing an understanding of the causes of beam helicity correlations and implementing means of suppressing these correlations. In this thesis, I also cover a method for systematically evaluating the sensitivity of the detected scattered flux to helicity correlations in the beam parameters, called beam modulation. Beam modulation is discussed and utilized in the analysis of the 1999 HAPPEX data set to calculate the correction to the raw detector asymmetry for $^{\text{beam}}A_{\text{LR}}$'s. I was also responsible for conducting a second independent analysis of the physics and beam asymmetries.

The next chapter is devoted to developing the formalism necessary to interpret the asymmetry measurements made by HAPPEX and E-158. Chapter 3 discusses the general principles behind the design of a parity-violating electron-scattering experiment, and chapters 4 and 5 discuss the implementation of those principles for HAPPEX and E-158, respectively. Chapter 6 reprints most of a NIM paper I wrote that discusses the polarized electron source optics system for E-158 and the control of electron beam helicity correlations for that experiment; this work was central to my thesis. Chapter 7 discusses the analysis of the 1999 HAPPEX run. Finally, I conclude in chapter 8 by interpreting the combined 1998 and 1999 HAPPEX results in terms of strange form factors and

by summarizing the planned experimental program in parity-violating electron scattering. In this

thesis, I generally adopt the convention $\hbar = c = 1$, except where otherwise noted.

Chapter 2

Parity-Violating Electron Scattering as a Tool

In this chapter, I present the formalism that is required for interpreting HAPPEX and E-158. The first half of the chapter is devoted to a discussion of electron-proton (e-p) scattering and the second half to electron-electron (Møller) scattering.

2.1 Electron-Proton Scattering

Electrons can scatter off of protons by exchanging either a virtual γ or a virtual Z^0, as shown in Figure 2.1. Until 1977, electrons had been used solely as an electromagnetic probe of the nucleon because of the smallness of the amplitude for weak neutral-current scattering at low energy. A number of facilities (JLab, SLAC, Bates, Mainz) now provide a high enough luminosity to make feasible studies of the nucleon via its weak neutral-current coupling. The weak neutral current can be accessed by measuring a parity-violating asymmetry that is proportional to the interference term between weak and electromagnetic scattering amplitudes. We present a formalism for understanding this process. We begin with a discussion of purely electromagnetic scattering, and show that while it can teach us much about the structure of the nucleon, electromagnetic scattering alone is insufficient to reveal the full detail of that structure. Then we introduce the weak neutral current and show how it provides access to the remaining structure. Finally, we show how parity violation can be used to gain access to the neutral current interaction.

(a) One-photon exchange. (b) Z^0 exchange.
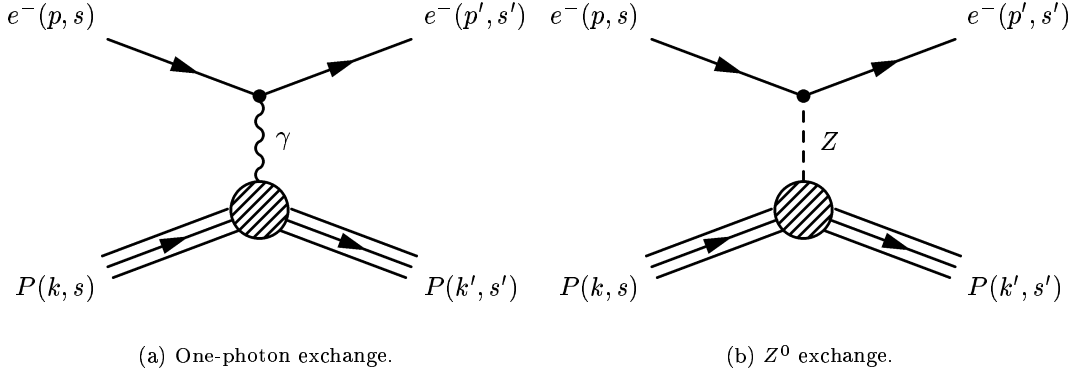
Figure 2.1: Tree-level Feynman diagrams for *e-p* scattering.

2.1.1 Electromagnetic Scattering

We begin by considering electromagnetic elastic scattering of electrons off protons (Figure 2.1a). The scattering amplitude for this process is a product of currents for the electron and the proton, sandwiched around the photon propagator:

$$\mathcal{M}_\gamma = j_\mu \left(\frac{1}{q^2} \right) J^\mu, \tag{2.1}$$

where q^2 is the square of the four-momentum transfer and the electron current j_μ is given by

$$j_\mu = -e\overline{u}_e(p', s')\gamma_\mu u_e(p, s). \tag{2.2}$$

The hadronic current could be similarly expressed if the proton were a point-like particle. Since this is not the case, we describe the current by the most general Lorentz invariant quantity we can construct that satisfies parity and time-reversal invariance and current conservation, all of which are obeyed by the electromagnetic interaction:

$$J^\mu = e\overline{u}_p(k', s') \left(F_1(q^2)\gamma^\mu + \frac{i}{2M_p}F_2(q^2)\sigma^{\mu\nu}q_\nu \right) u_p(k, s), \tag{2.3}$$

where the "form factors" F_1 and F_2 depend only on q^2, M_p is the proton mass, and u_p is the proton spinor. These form factors are experimentally measured quantities. They describe the deviation from point-particle scattering and parameterize the structure of the proton. This structure is determined primarily by strong-force interactions between the constituents of the proton. At present, the theory of strong interactions, QCD, is not fully calculable at low energies and calculations of the form factors rely on various models. We discuss recent measurements of the electromagnetic form factors in section 2.1.4.

We typically use a particular linear combination of F_1 and F_2 called the Sachs form factors G_E and G_M because they lead to a particularly convenient expression for the differential cross section:

$$G_E^{p,n} \equiv F_1^{p,n} - \tau\kappa F_2^{p,n}, \qquad G_M^{p,n} \equiv F_1^{p,n} + \kappa F_2^{p,n}, \tag{2.4}$$

where $\tau = Q^2/4M_p^2$, $Q^2 \equiv -q^2 > 0$ is the four-momentum transfer, and κ is the nucleon's anomalous magnetic moment. As $Q^2 \to 0$, the Sachs form factors approximate Fourier transforms of the distribution of charge and magnetic moment within the nucleons:

$$\lim_{q^2 \to 0} G_E = \frac{\mathcal{Q}}{e}, \qquad \lim_{q^2 \to 0} G_M = \frac{\mu_N}{e/2M_p}, \tag{2.5}$$

where $\mathcal{Q}$ is the nucleon electric charge and $\mu_N = e/2M_p$ is the nucleon magnetic moment. At $Q^2 = 0$ the Sachs form factors for the proton and neutron take the values

$$G_E^p = 1, \qquad G_M^p = \mu_p = 2.79\mu_N, \tag{2.6}$$

$$G_E^n = 0, \qquad G_M^n = \mu_n = -1.91\mu_N. \tag{2.7}$$

We can also define the mean square charge and magnetic radii, $\langle r^2 \rangle_{E,M}$, of the proton, as the slope of $G_{E,M}^p$ at $q^2 = 0$. This can be seen as follows. At sufficiently low momentum transfer, the proton's recoil can be neglected and the Sachs form factors can be interpreted as the Fourier

transform of its charge (or current) density $\rho_{E,M}$ according to

$$G^p_{E,M} = \int_V \rho_{E,M}(\overrightarrow{r})e^{i\overrightarrow{q}\cdot\overrightarrow{r}}r^2\sin\theta dr d\theta d\phi, \qquad (2.8)$$

where $\overrightarrow{r}$ and $\overrightarrow{q}$ are three vectors. Assuming the charge distribution is radially symmetric and integrating over θ and ϕ yields

$$G^p_{E,M} = \frac{4\pi}{q}\int r\rho_{E,M}(r)\sin qr dr. \qquad (2.9)$$

If we expand $\sin qr$ in a Taylor series about $qr = 0$, we find

$$G^p_{E,M} = \frac{4\pi}{q}\int r\rho_{E,M}(r)\{qr - \frac{1}{6}(qr)^3 + \ldots\}dr \approx 1 - \frac{q^2}{6}\langle r^2\rangle_{E,M}, \qquad (2.10)$$

where the charge (or current) normalization has been set equal to one and $\langle r^2\rangle_{E,M}$ is the mean square charge (magnetic moment) radius of the proton. At low momentum transfer, these radii can be extracted by looking at the slope of $G^p_{E,M}$:

$$\langle r^2\rangle_{E,M} = 6\left(\frac{dG^p_{E,M}(q^2)}{dq^2}\right)_{q^2=0}. \qquad (2.11)$$

These radii are a useful way of characterizing the size of the proton and are both ~ 0.86 fm. This size corresponds to an energy scale of about 200 MeV, meaning the charge and magnetic radii of the proton are comparable to its mass. This fact explains why the Sachs form factors do not actually convey the Fourier transform of the electric charge and magnetic moment distributions of the proton at $Q^2 > 0$. Experiments at large enough Q^2 to probe the distribution of electric charge and magnetic current within the proton impart to the proton a sizeable recoil energy. This recoil energy causes the electric and magnetic form factors to mix in a way that depends upon unknown details of the proton's internal dynamics.

Expressed in terms of the Sachs form factors, the unpolarized $\vec{e}$-p cross section is [28]

$$\frac{d\sigma}{d\Omega}\bigg|_{\text{lab}} = \left(\frac{\alpha^2}{4E^2 \sin^4 \theta/2}\right) \frac{E'}{E} \left\{ \frac{(G_E^{p\gamma})^2 + \tau(G_M^{p\gamma})^2}{1+\tau} \cos^2 \frac{\theta}{2} + 2\tau(G_M^{p\gamma})^2 \sin^2 \frac{\theta}{2} \right\}, \qquad (2.12)$$

where α is the fine structure constant, E is the energy of the incident electron, E' is the energy of the scattered electron, and θ is the scattering angle in the lab frame. This expression reflects the utility of the Sachs form factors in that no cross terms ($G_E^{p\gamma} G_M^{p\gamma}$) appear. One other feature to note is the $\sin^{-4} \theta/2$ angular dependence of the cross section. For small angles, this leads to a significant variation of the scattering rate into a particular solid angle with variation of the incident beam's position and angle on the target. Much of the work in this thesis is motivated by the presence of this strong angular dependence. It is also useful to note that changing the superscript p to n yields the corresponding neutron cross section.

Alternatively, we can think of the proton as containing a distribution of point-like quarks. We define a set of flavor form factors $G_{E,M}^i(q^2)$ to describe the charge and magnetism distribution in space of each quark species i ($i = u, d, s, ...$). Up and down quarks contribute as both valence and sea quarks, whereas strange and heavier quarks contribute only as sea quarks. For the rest of this analysis we can neglect the contributions of quarks heavier than the strange quark. Their contributions to proton structure are negligible because they have $m_q \gg \Lambda_{QCD} \sim 200$ MeV. The proton current can be expressed in terms of the quark flavor currents,

$$J^\mu = \langle p | [\frac{2}{3}\overline{u}\gamma^\mu u - \frac{1}{3}\overline{d}\gamma^\mu d - \frac{1}{3}\overline{s}\gamma^\mu s] | p \rangle, \qquad (2.13)$$

$$= \overline{u}_P \left[\sum_{i=u,d,s} q_i (F_1^i \gamma^\mu + \frac{i}{2M_P} F_2^i \sigma_{\mu\nu} q^\nu) \right] u_P, \qquad (2.14)$$

where the individual quark currents carry coefficients equal to their electric charges q^i. Again, it is more convenient to express the quark form factors in the "Sachs" form (equation 2.4). We can

then relate the Sachs form factors G_E and G_M to the quark form factors G^u, G^d, and G^s:

$$G_{E,M}^{p\gamma} = \frac{2}{3}G_{E,M}^u - \frac{1}{3}(G_{E,M}^d + G_{E,M}^s). \qquad (2.15)$$

If we define the quark form factors as their contributions to the structure of the proton, then we can use charge symmetry [29], a restricted form of the $SU(2)$ isospin symmetry between the up and down quarks,* to gain a second relationship between the quark form factors and the Sachs form factors. Charge symmetry asserts invariance under the set of interchanges $p \leftrightarrow n$, $u \leftrightarrow d$, $s \leftrightarrow s$ and gives the relation

$$G_{E,M}^{n\gamma} = \frac{2}{3}G_{E,M}^d - \frac{1}{3}(G_{E,M}^u + G_{E,M}^s), \qquad (2.16)$$

Violations of charge symmetry are expected to be small and to alter the values of the electromagnetic form factors by less than 1% [29]. However, to separate the contributions of the u, d, and s quarks, we need a third linearly independent relationship between the quark form factors. The weak neutral current provides that relationship and is discussed next.

2.1.2 Weak Neutral Currents

Electron-proton scattering also proceeds via Z^0 exchange (as in Figure 2.1b), leading to a second amplitude $\mathcal{M}_Z$. At low energies, this amplitude can be approximated as

$$\mathcal{M}_Z = j_\mu \left(\frac{1}{M_Z^2} \right) J^\mu, \qquad (2.17)$$

---

*Charge symmetry refers to the invariance of the QCD Lagrangian under interchange of the up and down quarks that is obtained by neglecting the difference in their masses and electromagnetic effects. Charge symmetry is a specific rotation in isospin space and is therefore more restrictive than $SU(2)$ isospin symmetry, which holds for any rotation in isospin space.

The weak neutral current of the electron can be written as

$$j_{Z,\mu} = (-\frac{1}{4} + \sin^2\theta_W)\overline{e}\gamma_\mu e + \frac{1}{4}\overline{e}\gamma_\mu\gamma_5 e. \tag{2.18}$$

Note that because $\sin^2\theta_W \approx 0.23$, the weak vector coupling of the electron to the Z^0 is a factor of 10 smaller than the electron's axial-vector coupling. As in the electromagnetic case, the proton's weak neutral current can be expressed in terms of either the phenomenological form factors or a sum of individual quark currents:

$$J_Z^\mu = \langle p(k',s')|j_\mu^Z|p(k,s)\rangle$$

$$= \overline{u}_p(k',s')[F_1^Z(Q^2)\gamma_\mu + \frac{i}{2M}F_2^Z(Q^2)\sigma_{\mu\nu}q^\nu + G_A^Z(Q^2)\gamma_\mu\gamma^5 + G_P^Z(Q^2)\gamma^5 q_\mu]u_p(k,s) \tag{2.19}$$

$$= \langle p(k',s')|\left[(\frac{1}{4} - \frac{2}{3}\sin^2\theta_W)\overline{u}\gamma_\mu u - (\frac{1}{4} - \frac{1}{3}\sin^2\theta_W)(\overline{d}\gamma_\mu d + \overline{s}\gamma_\mu s)\right]|p(k,s)\rangle \tag{2.20}$$

$$- \langle p(k',s')|\left[\frac{1}{4}\overline{u}\gamma_\mu\gamma_5 u + \frac{1}{4}\overline{d}\gamma_\mu\gamma_5 d + \frac{1}{4}\overline{s}\gamma_\mu\gamma_5 s\right]|p(k,s)\rangle.$$

Because the weak interaction is parity-violating, two new form factors are needed. The axial form factor G_A^Z characterizes the axial structure of the proton but contributes little in HAPPEX's kinematics; it is most important at backward angles. The pseudoscalar form factor G_P^Z is strongly suppressed due to kinematics in elastic $\overrightarrow{e}$-p scattering [14], and we neglect it. As before, we reexpress F_1^Z and F_2^Z in terms of Sachs form factors $G_{E,M}^{pZ}$ for the weak neutral current. Relating $G_{E,M}^{pZ}$ to their quark flavor form factors yields

$$G_{E,M}^{pZ} = (\frac{1}{4} - \frac{2}{3}\sin^2\theta_W)G_{E,M}^u - (\frac{1}{4} - \frac{1}{3}\sin^2\theta_W)(G_{E,M}^d + G_{E,M}^s). \tag{2.21}$$

We can express $G_{E,M}^u$, $G_{E,M}^d$, and $G_{E,M}^s$ in terms of $G_{E,M}^{p,n\gamma}$ and $G_{E,M}^{p,nZ}$, and we now have enough

observables to separate the three quark-flavor form factors:

$$G^u_{E,M} = (3 - 4\sin^2\theta_W)G^{p\gamma}_{E,M} - G^{pZ}_{E,M},$$

$$G^d_{E,M} = (2 - 4\sin^2\theta_W)G^{p\gamma}_{E,M} + G^{n\gamma}_{E,M} - G^{pZ}_{E,M}, \qquad (2.22)$$

$$G^s_{E,M} = (1 - 4\sin^2\theta_W)G^{p\gamma}_{E,M} - G^{n\gamma}_{E,M} - G^{pZ}_{E,M}.$$

Any set of three independent electric (and magnetic) form factors can be used to calculate cross sections and asymmetries. A convenient choice in our case is to use the previously measured form factors $G^{p\gamma}_{E,M}$ and $G^{n\gamma}_{E,M}$ and the unknown form factors $G^s_{E,M}$.

We summarize the charges for the electromagnetic and weak neutral currents in Table 2.1. q^{EM} is the electromagnetic charge of a particle, while g^A, g^V, g^R, and g^L, respectively, are the weak axial, vector, right-helicity, and left-helicity charges (with $g^R = g^V + g^A$ and $g^L = g^V - g^A$). The electromagnetic and weak charges are comparable in size. However, comparing the propagators of the EM and weak neutral interactions, we see that the weak interaction is suppressed at each vertex by a factor of $\sim Q^2/M_Z^2$. This leads to a suppression factor of $\sim 10^9$ at $Q^2 = 0.48$ GeV^2 in the cross section.

Table 2.1: Electromagnetic and weak neutral current charges.

Particle	q^{EM}	g^A	g^V	g^R	g^L
e^-	-1	$\frac{1}{4}$	$-\frac{1}{4} + \sin^2\theta_W$ ~ -0.02	$\sin^2\theta_W$ ~ 0.23	$-\frac{1}{2} + \sin^2\theta_W$ ~ -0.27
u	$\frac{2}{3}$	$-\frac{1}{4}$	$\frac{1}{4} - \frac{2}{3}\sin^2\theta_W$ ~ 0.09	$-\frac{2}{3}\sin^2\theta_W$ ~ -0.16	$\frac{1}{2} - \frac{2}{3}\sin^2\theta_W$ ~ 0.34
d,s	$-\frac{1}{3}$	$\frac{1}{4}$	$-\frac{1}{4} + \frac{1}{3}\sin^2\theta_W$ ~ -0.17	$\frac{1}{3}\sin^2\theta_W$ ~ 0.08	$-\frac{1}{2} + \frac{1}{3}\sin^2\theta_W$ ~ -0.42

2.1.3 Parity Violation

The amplitude for Z^0 exchange is tiny compared to the electromagnetic amplitude at low Q^2 and the contribution to the cross section from Z^0 exchange can not be measured directly. Instead,

we use parity violation and measure an asymmetry A_{LR}^{ep} to take advantage of interference terms that are a product of EM and weak amplitudes. Considering again Figure 2.1, we can express the total scattering amplitude as a sum of weak and electromagnetic amplitudes. We can denote the electromagnetic amplitude by $\mathcal{M}_\gamma$. Because the electromagnetic interaction is parity conserving, we do not need separate right- and left-handed amplitudes. For the weak amplitude, we can write $\mathcal{M}_Z^r$ and $\mathcal{M}_Z^l$ for the amplitudes for incident right- and left-handed electrons, respectively. The cross sections for scattering right- and left-handed electrons off an unpolarized electron target are proportional to the square of the total amplitudes,

$$\sigma^r \propto (\mathcal{M}_\gamma + \mathcal{M}_Z^r)^2, \qquad \sigma^l \propto (\mathcal{M}_\gamma + \mathcal{M}_Z^l)^2, \tag{2.23}$$

and so we can express the parity-violating asymmetry as

$$A_{LR}^{ep} \propto \frac{(\mathcal{M}_\gamma + \mathcal{M}_Z^r)^2 - (\mathcal{M}_\gamma + \mathcal{M}_Z^l)^2}{(\mathcal{M}_\gamma + \mathcal{M}_Z^r)^2 + (\mathcal{M}_\gamma + \mathcal{M}_Z^l)^2} \approx \frac{\mathcal{M}_Z^r - \mathcal{M}_Z^l}{\mathcal{M}_\gamma}. \tag{2.24}$$

Measuring the parity-violating asymmetry allows us to access the weak neutral current in a ratio of amplitudes rather than a ratio of the squares of amplitudes, greatly enhancing its relative contribution. We can make an order-of-magnitude estimate of the asymmetry from the ratio of the propagators:

$$A_{LR}^{ep} \approx \frac{Q^2}{M_Z^2} \approx 30 \text{ ppm at } Q^2 = 0.477 \text{ GeV}^2. \tag{2.25}$$

A complete analysis finds the full result at tree level to be [14]

$$A_{LR}^{ep} = \left[\frac{-G_F M_p^2 \tau}{\pi \alpha \sqrt{2}}\right] \left\{ (1 - 4\sin^2\theta_W) - \frac{\varepsilon G_E^{p\gamma}(G_E^{n\gamma} + G_E^s) + \tau G_M^{p\gamma}(G_M^{n\gamma} + G_M^s)}{\varepsilon(G_E^{p\gamma})^2 + \tau(G_M^{p\gamma})^2} \right.$$
$$\left. - \frac{(1 - 4\sin^2\theta_W)\varepsilon' G_M^{p\gamma}(-G_A^{(1)} + \frac{1}{2}G_A^s)}{\varepsilon(G_E^{p\gamma})^2 + \tau(G_M^{p\gamma})^2} \right\}, \tag{2.26}$$

where $\varepsilon = [1 + 2(1 + \tau)\tan^2(\theta/2)]^{-1}$ is the degree of longitudinal polarization of the exchanged virtual photon and $\varepsilon' = \sqrt{\tau(1 + \tau)(1 - \varepsilon^2)}$. The asymmetry depends on both strange and non-strange form factors. For a scattering angle of 12.3° and a Q^2 of 0.477 GeV^2 (corresponding to the kinematics of HAPPEX), equation 2.26 predicts $A_{LR}^{ep} = -16.3$ ppm in the absence of strange quarks and assuming the axial term contributes an asymmetry $A_A = 0.56 \pm 0.23$ ppm [30, 31]. We also use for the electromagnetic form factors the values listed in Table 8.1.

Another convenient form factor to use is $G_{E,M}^0$, defined as

$$G_{E,M}^0 = \frac{1}{3}(G_{E,M}^u + G_{E,M}^d + G_{E,M}^s) = G_{E,M}^{p\gamma} + G_{E,M}^{n\gamma} + G_{E,M}^s. \tag{2.27}$$

Expressed in terms of $G_{E,M}^0$, $G_{E,M}^{p\gamma}$, and $G_{E,M}^{n\gamma}$, A_{LR}^{ep} becomes

$$A_{LR}^{ep} = \left[\frac{-G_F M_p^2 \tau}{\pi\alpha\sqrt{2}}\right]\left\{(2 - 4\sin^2\theta_W) - \frac{\varepsilon\eta_p}{\varepsilon\eta_p^2 + \tau\mu_p^2}\frac{G_E^0 + \beta G_M^0}{(G_M^{p\gamma}/\mu_p)}\right\} - A_A, \tag{2.28}$$

where $\eta_p = G_E^{p\gamma}/(G_M^{p\gamma}/\mu_p)$ and $\beta = \frac{\tau\mu_p}{\varepsilon\eta_p}$, and A_A is the asymmetry from the third term of equation 2.26.

Figure 2.2 shows an estimate of the contribution to A_{LR}^{ep} from each of the strange form factors as a function of scattering angle. To generate this estimate, we take typical values for $\rho_s \equiv \frac{dG_E^s}{d\tau}|_{\tau=0}$ and $\mu_s \equiv G_M^s(Q^2 = 0)$ from models, assume a Q^2 dependence following the Galster parameterization (see section 2.1.4), and evaluate the form factors at $Q^2 = 0.25$ GeV^2. We see that G_M^s contributes significantly at all angles but is the largest contributor at backward angles. G_E^s dominates at forward angles and the uncertainty in axial radiative corrections δR_A (assumed here to be 0.42) is significant at backward angles. Measurements of A_{LR}^{ep} at forward (HAPPEX) [32, 33] and backward (SAMPLE) [34, 35, 36] angles have been made, and additional measurements are planned. A natural thought is that an additional measurement at intermediate angles would allow the separation of all three form factors. Unfortunately, a measurement at intermediate angles works out to be very nearly a linear combination of the forward- and backward-angle measurements

and would provide little new information [14]. The SAMPLE and HAPPEX collaborations are pursuing two alternate strategies. The SAMPLE collaboration is measuring A_{LR} in quasielastic electron-deuteron scattering, for which G_A^s alone dominates at backward angles. Combining their backward-angle hydrogen and deuterium results allows separation of G_M^s and G_A^s. The HAPPEX collaboration is planning a forward-angle measurement on ^{4}He, for which only G_E^s contributes to A_{LR}^{ep}. These and other experimental efforts are summarized in section 8.3. Equation 2.26 also indicates that A_{LR}^{ep} is very sensitive to the electromagnetic form factors of the proton and neutron. We briefly discuss the current state of knowledge of the electromagnetic form factors in the next section and discuss their impact on the extraction of the strange form factors in section 8.1.
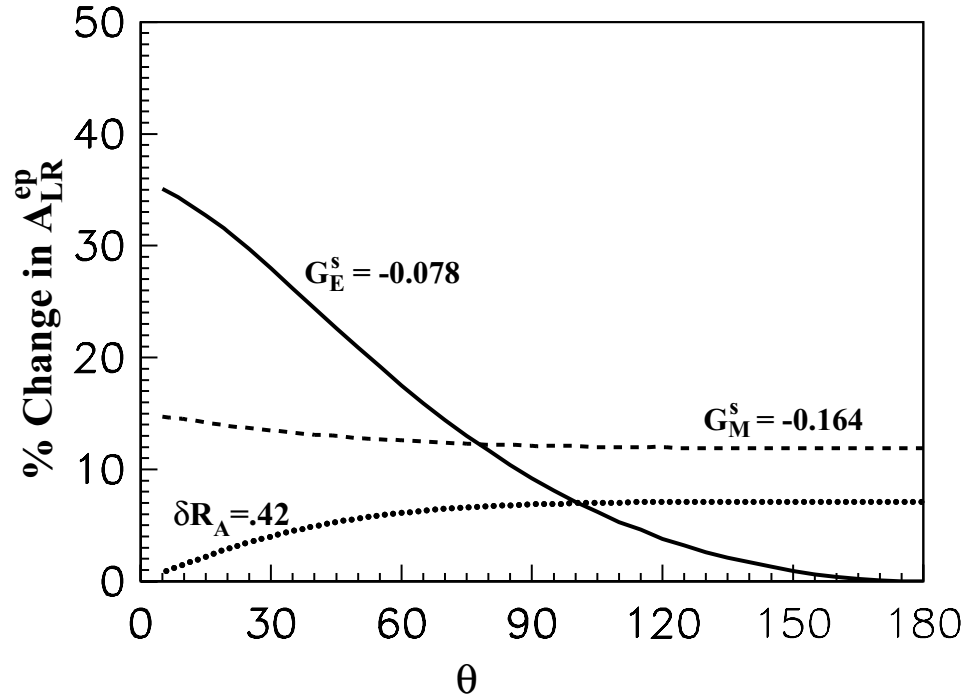
Figure 2.2: Fractional change in A_{LR}^{ep} due to nonzero strange form factors as a function of lab-frame scattering angle evaluated at $Q^2 = 0.25$ GeV^2. The solid curve shows the effect of $G_E^s = -0.078$, the dashed curve shows the effect of $G_M^s = -0.164$, and the dotted curve shows the effect of the axial radiative correction, assuming $\delta R_A = 0.42$.

2.1.4   Electromagnetic Form Factors

Equation 2.26 indicates that extracting the strange form factors from a measurement of A_{LR}^{ep} requires as input all four electromagnetic form factors of the proton and neutron. Measuring these form factors as a function of Q^2 has been an active area of research for the last 50 years [37]. The traditional method is to measure the angular dependence of the *e-p* or *e-n* cross section at a particular value of Q^2 and perform a "Rosenbluth separation" [28] using equation 2.12. This procedure works best when $G_E^2 \sim \tau G_M^2$, which implies $Q^2 \sim 0.5$ GeV^2. In the last decade, however, new techniques for measuring the form factors that take advantage of spin observables have enabled more precise measurements in kinematic regimes where the Rosenbluth separation method becomes difficult, such as at $Q^2 > 1$ GeV^2, as well as a new technique for comparison at lower momentum transfer. Studies of strange form factors are focusing on the region $Q^2 < 1$ GeV^2, and I briefly discuss the state of knowledge of the electromagnetic form factors in this region.

The proton form factors have been measured to the few-percent level for $Q^2 < 0.8$ GeV^2. Over this range in momentum transfer (and over a much broader range for G_M^p), the proton form factors can be fit well to a dipole form,

$$G_E^p = G_D \equiv \frac{1}{(1 + \lambda_D \tau)^2}, \quad G_M^p = \mu_p G_D, \tag{2.29}$$

where $\lambda_D = 4.97$. Recent results on G_E^p/G_M^p and G_M^p are shown in Figures 2.3a and 2.3b, respectively. In Figure 2.3a, we see that the data from a global analysis [38] of experiments performed using the Rosenbluth separation and the data from a recent experiment using spin observables [39] agree for $Q^2 < 0.8$ GeV^2 (which covers the range of interest to HAPPEX) but disagree at higher Q^2, where control of systematic errors becomes a more serious issue when using the Rosenbluth separation method.

There is no free neutron target, and the neutron form factors have traditionally been measured using a deuterium target and the Rosenbluth separation method. Uncertainties in the nuclear
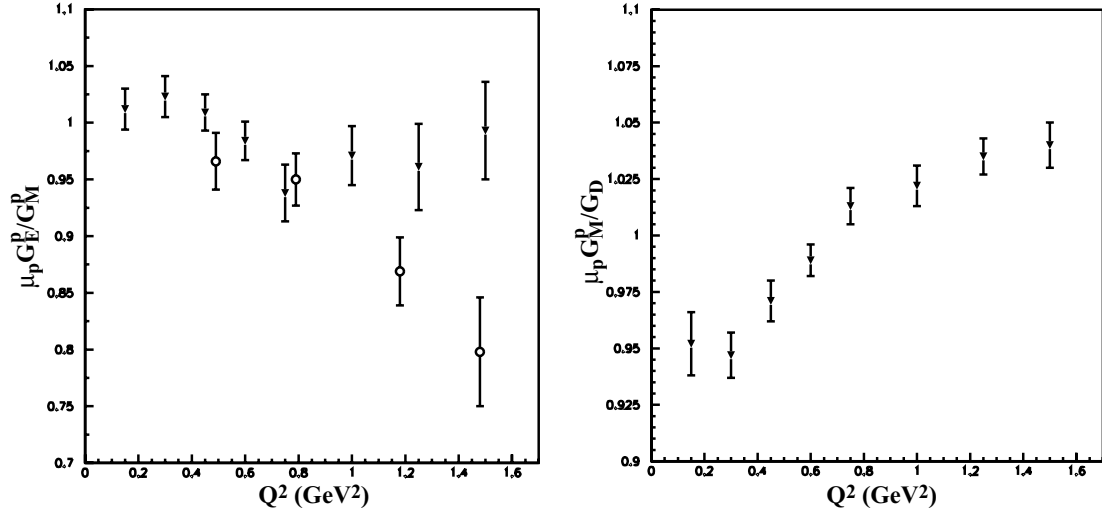
(a) $\mu_P G_E^p / G_M^p$ from a global analysis (filled triangles) [38] and a recent experiment using spin observables (empty circles) [39].

(b) $\mu_P G_M^p / G_D$ from a global analysis [38].

Figure 2.3: Recent measurements of the proton electromagnetic form factors.

structure have limited the accuracy of these measurements. Experiments taking advantage of spin observables (and using both deuterium and ^{3}He targets) have begun improving the precision with which G_E^n and G_M^n are known, and recent measurements of G_E^n and G_M^n are shown in Figures 2.4a and 2.4b, respectively. While G_M^n also appears to follow a dipole form, G_E^n is constrained to be zero at $Q^2 = 0$, and is usually taken to follow the Galster parameterization [40]:

$$G_E^n = -\frac{\mu_n \tau}{(1 + \lambda_n \tau)} G_D, \quad G_M^n = -\mu_n G_D, \tag{2.30}$$

where $\lambda_n = 5.6$.

The data on the proton form factors are sufficiently precise that the errors do not contribute significantly when we extract a result for the strange form factors from A_{LR}^{ep}. This is not the case with the neutron form factors, but experiments are in progress and in preparation that will reduce the uncertainty in the neutron form factors over the range of interest to HAPPEX. Our choices of electromagnetic form factors and the impact of uncertainty in the neutron form factors
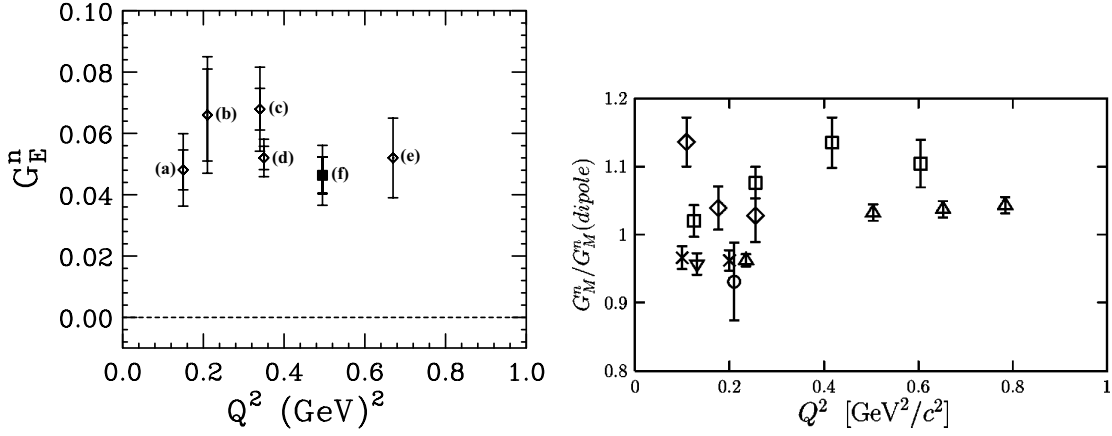
(a) Comparison of recent measurements of G_E^n from (a) [41], (b) [42], (c) [43], (d) [44], (e) [45], and (f) [46]. Adapted from [46].

(b) Values of G_M^n taken from several measurements on the deuteron ([47] ($\diamond$), [48] ($\triangledown$), [49] ($\square$), [50] ($\triangle$)) and on ^{3}He ([51, 52] ($\bigcirc$), [53] ($\times$)). The Q^2 points of [48, 51, 52] are slightly shifted for clarity. Reprinted from [54].

Figure 2.4: Recent measurements of the neutron electromagnetic form factors.

are discussed in section 8.1.

2.1.5 Radiative Corrections

One of the critical aspects of the Standard Model is that it is renormalizable, and in most cases higher-order corrections to electroweak processes are small and can be computed reliably. This is because the coupling constant, $\alpha/4\pi \sim 0.001$, is small. Higher-order contributions are generally suppressed by one or more powers of $\alpha/4\pi$. This is true for the radiative corrections involved in measuring the vector strange form factors–they are small ($\sim 1\%$) compared to the projected experimental errors and are well known.

However, higher-order corrections are not necessarily suppressed for measurements of the axial strange form factor. When the Z^0 has a vector coupling to the electron and an axial vector coupling to the proton, the corrections can be both large relative to the tree-level diagrams and difficult to calculate. They can be large due to the electron's small vector coupling ($-\frac{1}{4} + \sin^2\theta_W \sim 0.02$) at tree level and to enhancement factors like $\ln(\frac{M_Z^2}{M_p^2}) \sim 9$. Rather than scaling as $\alpha/4\pi$, radiative

corrections to the axial-vector coupling of the proton can contribute as [14]

$$\frac{1}{1 - 4\sin^2\theta_W} \frac{\alpha}{4\pi} \ln\left(\frac{M_Z^2}{M_p^2}\right) \sim 0.1. \tag{2.31}$$

In addition, because these corrections involve coupling to the proton, they have hadronic contributions which cannot be calculated reliably.

Since the radiative corrections are primarily a problem for the axial vector coupling of the proton, they are most important for measurements of G_A^s. HAPPEX is measuring the asymmetry at forward angle, and G_A^s contributes only a few percent to the asymmetry in these kinematics. The vector form factors G_E^s and G_M^s have small, well understood radiative corrections, and so uncertainty due to radiative corrections contributes little to the HAPPEX's systematic error. Theoretical work is continuing on the axial radiative corrections, and the SAMPLE collaboration is studying them experimentally as well (see section 8.3). Further discussion of radiative corrections can be found in, e.g., [14, 15, 16, 55, 56, 57].

2.1.6   Spinless Isoscalar Targets

The HAPPEX collaboration is planning two additional experiments at a lower Q^2 of ~ 0.1 GeV^2, using hydrogen [58] and ^{4}He [59]. Certain models predict that G_E^s will be significantly larger in this Q^2 range (see, e.g., [22]) than at $Q^2 \sim 0.5$ GeV^2 as in the earlier experiment. The asymmetry A_{LR}^{00} for elastic scattering from a spinless isoscalar target, such as ^{4}He or ^{12}C, can be derived in terms of $G_{E,M}^{p\gamma}$, $G_{E,M}^{n\gamma}$, and $G_{E,M}^s$ as above for $\vec{e}$-p scattering. The only additional assumption required is that the nucleus can be described by a product of nucleon form factors and a form factor describing the shape of the nucleus. The result is [14]

$$A_{LR}^{00} = \frac{G_F Q^2}{\pi\alpha\sqrt{2}}\left[\sin^2\theta_W + \frac{G_E^s}{2(G_E^p + G_E^n)}\right] = 8.3 \text{ ppm}, \tag{2.32}$$

assuming $Q^2 = 0.1$ GeV^2 and $G_E^s = 0$. The asymmetry is independent of G_M^s as one would expect for a spinless isoscalar target. It is also independent of G_A^s. ^{4}He is favored over ^{12}C for making this measurement because the corrections for its nuclear structure are better understood. Thus, parity-violating electron scattering off both hydrogen and ^{4}He at the same Q^2 should provide a particularly clean method for measuring and separating G_E^s and G_M^s.

Since the net strangeness of protons is zero, $G_E^s \to 0$ as $Q^2 \to 0$. In this case, a measurement of A_{LR} can be used to extract $\sin^2 \theta_W$. In fact, the Bates carbon parity violation experiment [5] made this measurement at a momentum transfer of 150 MeV on the ^{12}C nucleus.

2.2 Electron-Electron Scattering

The parity-violating asymmetry in electron-electron scattering, or Møller scattering, also contains interesting physics. The asymmetry provides a sensitive measurement of the weak mixing angle, $\sin^2 \theta_W$. The tree-level diagrams for Møller scattering are shown in Figure 2.5. Because the two electrons are identical, there are a total of four diagrams which contribute to the scattering amplitude: photon or Z^0 exchange for both direct and crossed diagrams.

(a) Direct   (b) Crossed
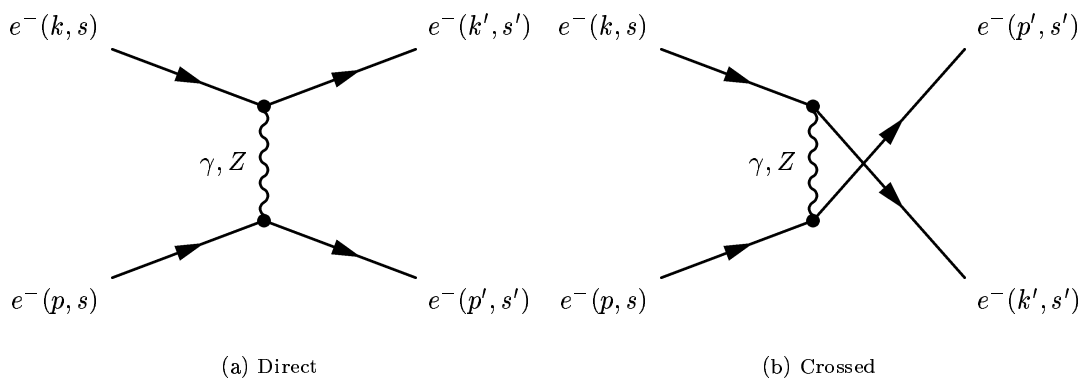
Figure 2.5: Tree-level Feynman diagrams for Møller scattering.

The unpolarized Møller scattering cross section, derived in Appendix B, is given by

$$\frac{d\sigma}{d\Omega} = \frac{\alpha^2}{2m_e E_b} \frac{(3 + \cos^2 \theta_{cm})^2}{\sin^4 \theta_{cm}},$$ (2.33)

where α is the fine structure constant, E_b is the energy of the incident electron beam, m_e is the electron mass, and θ_{cm} is the scattering angle in the center-of-momentum frame.

2.2.1   Parity Violation in Møller Scattering

The parity-violating asymmetry A_{LR}^{ee} is [60]

$$A_{LR}^{ee} = m_e E_b \frac{G_F}{\sqrt{2}\pi\alpha} \frac{16 \sin^2 \theta_{cm}}{(3 + \cos^2 \theta_{cm})^2} g_{ee},$$ (2.34)

where G_F is the Fermi coupling constant and g_{ee} is the pseudoscalar weak neutral-current coupling for Møller scattering (see [61] for a derivation of A_{LR}^{ee}.). Within the context of the Standard Model, at tree level g_{ee} is the product of a vector electron-photon vertex and an axial-vector electron-photon vertex and takes the value (from Table 2.1)

$$g_{ee} \equiv \rho \cdot g_{Ve} \cdot g_{Ae} = \frac{1}{4} - \sin^2 \theta_W,$$ (2.35)

where ρ (= 1 within the Standard Model) is the relative strength of the weak neutral and charged current interactions:

$$\rho \equiv \frac{M_W^2}{M_Z^2 \cos^2 \theta_W}.$$ (2.36)

Note that g_{ee} is close to zero since $\sin^2 \theta_W \sim 0.023$. Thus, a small (relative) change in $\sin^2 \theta_W$ introduces a much larger relative change in g_{ee} and hence A_{LR}^{ee}. Turning that statement around, E-158's sensitivity to $\sin^2 \theta_W$ is greatly improved by its closeness to 0.25, and an 8% measurement of A_{LR}^{ee} yields a 0.3% measurement of $\sin^2 \theta_W$.

For E-158's kinematics, $E = 50$ GeV and $\theta_{cm} \approx 90°$, and assuming 100% beam polariza-

tion, equation 2.34 yields $A^{ee}_{LR} = 2.97 \cdot 10^{-7}$. The running of $\sin^2\theta_W$ from the Z^0 resonance

to $Q^2 = 0.025 \text{ GeV}^2$ (due to the radiative corrections discussed below) reduces this prediction to

180 ppb [62]. Including kinematic factors and the beam's $\sim 85\%$ polarization lowers the raw asym-

metry expected within the context of the Standard Model to 140 ppb. E-158 plans to make an 8%

measurement of A^{ee}_{LR}, which will give $\delta(\sin^2\theta_W) = 0.0008$. The predicted running of $\sin^2\theta_W(Q^2)$

(within the context of the Standard Model) from the value obtained at $Q^2 = M^2_Z$ in measurements

by SLC and LEP [63, 64] is shown in Figure 2.6. Also shown are existing lower-energy measure-

ments from NuTeV [65] and atomic parity violation [66, 67]. It is this running that E-158 seeks

to establish with high precision. The projected E-158 error bar is shown for the first physics run

(April/May 2002) and the proposal goal. The data for Run I is currently being analyzed.
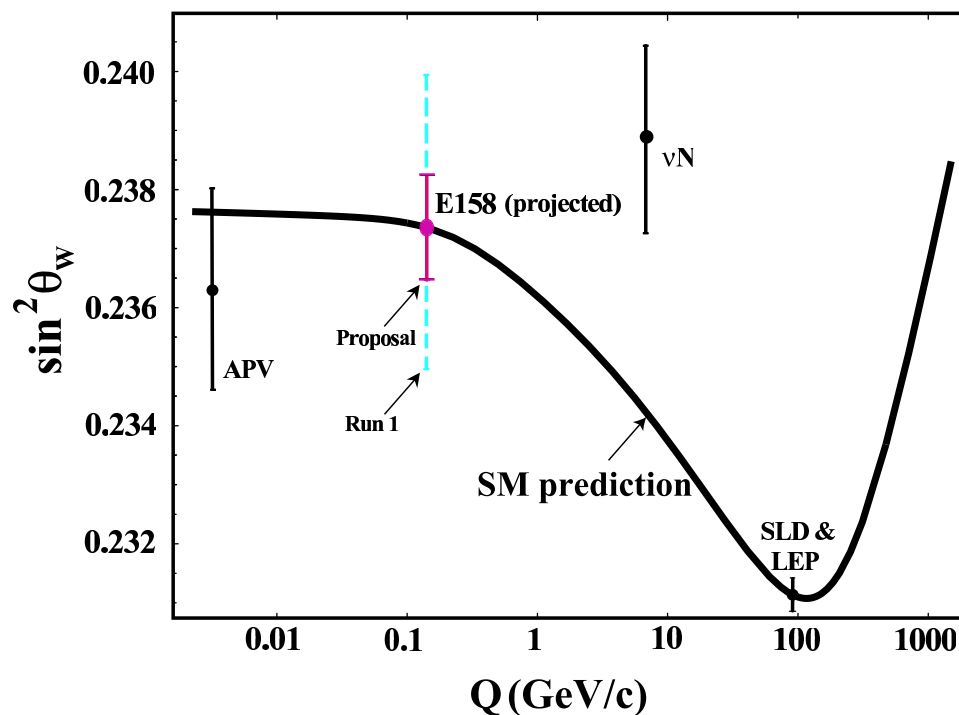
Figure 2.6: Running of $\sin^2\theta_W$ from the precision measurement at the Z^0 resonance as predicted by the Standard Model (Adapted from [68].). The NuTeV result is from [65] and the atomic PV result is from [66, 67]. The E-158 results are projected results for Run I (completed April-May, 2002) and for the proposal goal.

Returning for a moment to Figure 2.6, note that the neutrino-nucleon scattering experiment

is three sigma above the Standard Model prediction and the atomic parity violation result is two sigma below the Standard Model. There are many possible new-physics scenarios that can account for these results. A few to which E-158 is sensitive are discussed in section 2.2.3. It is important to recognize that because the experiments involve different sets of physics processes, their responses to a particular new-physics scenario can differ and the comparison of multiple low-energy experiments can provide additional constraints on new physics. It is also worth mentioning that, as discussed in [69, 67], there has been a significant amount of theoretical activity on the extraction of the weak charge of cesium and the central value of the atomic parity-violation data point has been wandering between $1 - 3\ \sigma$ from the Standard-Model prediction since the publication of [66].

2.2.2   Radiative Corrections and the Running of $\sin^2 \theta_W$

The Feynman diagram formalism is a perturbative expansion. The tree-level diagrams of Figure 2.5 represent the first-order, or one-boson-exchange, processes that contribute to the expansion. The coupling constants and parameters like $\sin^2 \theta_W$ are initially defined in terms of the quantities that appear in the tree-level diagrams. However, what E-158 measures is a sum over all orders of the perturbative expansion, and for E-158, a number of one-loop and box diagrams (second-order processes in the expansion) also contribute at an important level. Figures 2.7 and 2.8 show some of these processes. The inclusion of higher-order terms tends to lead to divergences when the coupling constants defined at tree level are used. The way out, a procedure called renormalization, is to redefine the coupling constants in terms of the experimentally measured values that inherently include the contributions from higher-order processes. The relative importance of each of these higher-order diagrams then depends on the energy scale of the experiment.[†] The energy scale is set by the momentum transfer, and is ~ 0.16 GeV for E-158. As the contributions from higher-order diagrams evolve with momentum transfer, they change the effective value of the coupling

---

[†]This is because of the "screening" of the electron's charge by the virtual particle cloud surrounding it. The energy scale is inversely proportional to the distance scale probed by the experiment. A higher energy scale implies a shorter distance scale, and hence a deeper penetration of the virtual-particle cloud. Deeper penetration reduces the amount of screening and changes the effective value of the electron's charge.

constants. This is referred to as the "running" of the coupling constants. In the case of E-158, it is the running of $\sin^2\theta_W$ from its value at $Q^2 = M_Z^2$ to $Q^2 = 0.025$ GeV^2 that is of interest.

The electroweak radiative corrections to polarized Møller scattering were calculated by Czarnecki and Marciano [62]. They use the modified minimal subtraction ($\overline{MS}$) scheme and define the renormalized weak mixing angle at an energy scale of M_Z. At that energy scale, the weak mixing angle has been measured to be $\sin^2\theta_W(m_Z)_{\overline{MS}} = 0.2314$ [63, 64]. The dominant contributions to the radiative corrections arise from $\gamma - Z^0$ mixing and certain anapole moment[‡] contributions; the relevant Feynman diagrams are shown in Figure 2.7. These contributions increase the value of $\sin^2\theta_W$ by 3% from its value at the Z^0 resonance, and can be interpreted as a running of the value of $\sin^2\theta_W$ from $Q^2 = M_Z^2$ to $Q^2 = 0.025$ GeV^2. The running results in a $\sim 40\%$ reduction in A_{LR}^{ee} because the asymmetry is proportional to $\frac{1}{4} - \sin^2\theta_W$. WW and ZZ box diagrams (Figure 2.8) also contribute a sizeable, though much smaller, correction to $\sin^2\theta_W$. Including a number of smaller contributions (due to the choice of renormalization scheme, photonic corrections to the external legs and vertices of Figure 2.5, and two-photon exchange diagrams), Czarnecki and Marciano conclude that

$$\frac{1}{4} - \sin^2\theta_W(m_Z)_{\overline{MS}} = 0.0744 \xrightarrow[Q^2 \to 0.025 \text{ GeV}^2]{} 0.0450 \pm 0.0023 \pm 0.0010, \tag{2.37}$$

where the errors represent theoretical uncertainties. The first error arises from hadronic loops in $\gamma - Z^0$ mixing diagrams and the second from uncertainty in the photonic corrections to the external legs and vertices of Figure 2.5 and two-photon exchange diagrams. The theoretical uncertainty is already at the level of the projected statistical error of the experiment ($\sim 10^{-8}$) and could readily be improved by a factor of two with a more detailed analysis.

In summary, because Møller scattering is a fully leptonic process, its one-loop radiative corrections can be calculated to high precision. E-158 provides a similarly precise measurement of

---

[‡]The "anapole moment" is a parity-violating electron-photon coupling that arises from higher-order contributions involving weak vector bosons, such as Figure 2.7d.
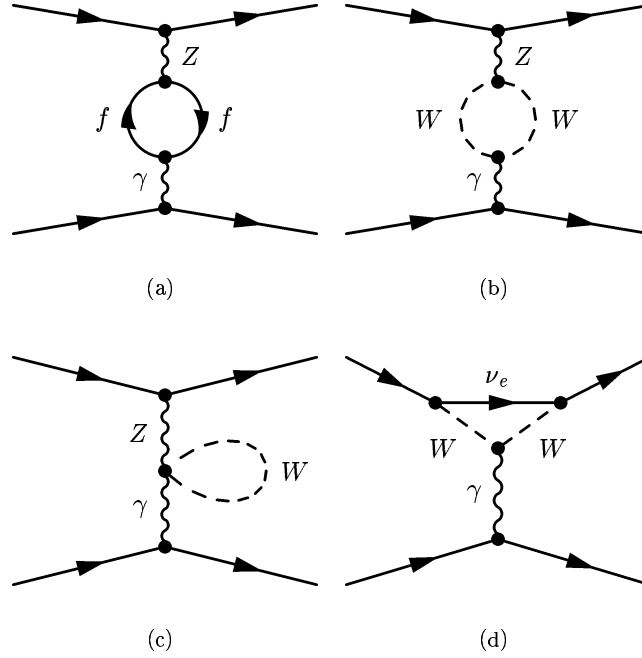
Figure 2.7: $\gamma - Z$ mixing diagrams (a-c) and the W-loop contribution to the anapole moment (d). Inverted and crossed diagrams contribute as well.

those radiative corrections, allowing it to test the electroweak sector of the Standard Model at the one-loop level.

2.2.3   Sensitivity to New Physics

The ability of E-158 to test the predictions of one-loop electroweak radiative corrections to high precision simultaneously implies its ability to probe for physics beyond the Standard Model. E-158 is sensitive to a number of new-physics scenarios, including additional Z' bosons (arising from GUT's or large extra spatial dimensions), other new contact (short-range) interactions (such as electron compositeness or doubly charged scalar exchange), and oblique corrections. We discuss each of these cases briefly below. Of course, E-158 is measuring a single number and is unable to distinguish between the various possibilities. However, taken in conjunction with existing precision measurements on the Z-pole and upcoming results from Tevatron Run II and other experiments,
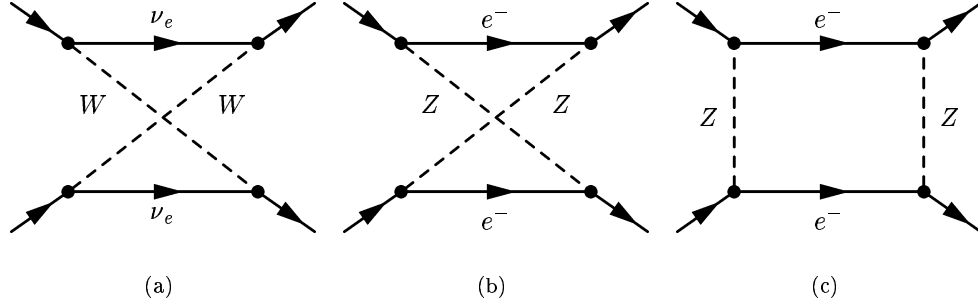
Figure 2.8: Box diagram contributions involving two heavy bosons. Crossed diagrams contribute as well.

E-158 can contribute significantly to constraining the parameter space of possible new-physics scenarios.

Many extensions to the Standard Model predict the presence of additional gauge bosons at the TeV mass scale [70, 71]. If one or more such Z' bosons exists and has a small mixing angle with the Z^0, then it could have escaped detection in existing experiments. The response of A_{LR}^{ee} to an additional boson exchanged at tree level is strongly model dependent. We can define the sensitivity of E-158's measurement as the mass required for a Z' boson such that it leads to a difference between the experimental measurement and the Standard Model prediction of two standard deviations. Under this definition, E-158 will be sensitive to new Z' bosons of masses up to $600 - 900$ GeV depending on the model, comparable to the expected sensitivity of the Tevatron's Run II. Many Grand Unified Theories (GUT's) predict additional Z' bosons that could fall in this mass range. Certain string-theory models allow for one or more large extra dimensions. These models predict the presence of Z' bosons which are Kaluza-Klein excitations§ of the Standard Model photon and Z^0, in some cases with masses at the 1-TeV scale. The direction of the change in A_{LR}^{ee} from the Standard Model prediction indicates whether right- or left-handed electrons couple more strongly to the Z'. This feature makes E-158's measurement an excellent complement to the

---

§These "large" extra dimensions are of finite extent with a length scale $R \sim$ TeV^{-1}. Particles propagating in them would have quantized momenta $\sim n/R, n = 1, 2, ..., \infty$. These particles would manifest themselves as Kaluza-Klein excitations with masses equal to their quantized momentum spectrum.

study of a Z' at a high-energy collider.

E-158 is also sensitive to other types of new contact interactions. Electron compositeness can be parameterized as a contact interaction with a Lagrangian of the form [72]

$$\mathcal{L} = \frac{4\pi}{2\Lambda_{ee}^2} \left[\eta_{LL}(\overline{\psi}_L \gamma_\mu \psi_L)^2 + \eta_{RR}(\overline{\psi}_R \gamma_\mu \psi_R)^2 + 2\eta_{LR}(\overline{\psi}_R \gamma_\mu \psi_R)(\overline{\psi}_L \gamma_\mu \psi_L) \right], \qquad (2.38)$$

where Λ_{ee} is the energy scale at which the internal dynamics of the electron become important and $|\eta_{if}| \leq 1$. If the contact interaction possesses parity-violating terms then E-158 can have a large sensitivity to it:

$$g_{ee}(\text{meas.}) - g_{ee}(\text{SM}) = \pm \frac{\pi}{G_F \sqrt{2}} \frac{\eta_{RR} - \eta_{LL}}{\Lambda_{ee}^2}. \qquad (2.39)$$

For η_{RR} or η_{LL} equal to ± 1, E-158 is sensitive to electron compositeness at energy scales up to 14 TeV, a significant improvement on current collider constraints at the $1 - 4$ TeV level. Lepton-flavor-violating processes, such as exchange of a doubly-charged Higgs boson Δ^{++}, can also be probed by E-158 with a level of sensitivity an order of magnitude greater than current indirect constraints.

Very massive particles that do not couple to the electron at tree level can manifest themselves by modifying the low-energy coupling constants through contributions in higher-order loop diagrams. These changes to the low-energy coupling constants are referred to as "oblique corrections" [73, 74]. For new physics at mass scales much greater than M_Z, only three parameters are needed to describe oblique corrections [75], and they are called S, T, and U. Only S and T affect Z^0 pole observables [76, 75], and they are now tightly constrained by LEP and SLC measurements. For new physics at mass scales down to M_Z, an additional three parameters called V, W, and X are needed [77, 78]. The parameter X can be interpreted as a measure of the running of $\sin^2 \theta_W$ due to physics beyond the Standard Model. It can be approximated as

$$\sin^2 \hat{\theta}_W(M_Z^2) - \sin^2 \hat{\theta}_W(0) \simeq \alpha X, \qquad (2.40)$$

where α is the fine structure constant. The current world average is $X = 0.38 \pm 0.51$ [79]. E-158 would be sensitive to X at the level of 0.15. If X is nonzero it would indicate that the mass scale for new physics is not much higher than M_Z and that the new physics does not couple strongly to the Z^0.

Returning for a moment to equation 2.26, we see that at sufficiently forward angles and low Q^2, the contribution of strange quarks to the asymmetry becomes negligible and the asymmetry becomes a measurement of $\sin^2 \theta_W$ instead. This measurement is complementary to E-158 because it measures the weak charge of the proton and is therefore sensitive to hadronic couplings of the Z^0 rather than leptonic couplings. An experiment called Q_{weak} is being planned for JLab to make this measurement. It is anticipated to run in Hall C in $\sim$ 2006. The Q_{weak} result will complement E-158's result nicely because the two are projected to have similar precision and will have markedly different responses to the various new physics scenarios.

In summary, E-158 is sensitive to a number of plausible new-physics scenarios and is running at a time when the Tevatron Run II is just getting underway and LHC is years away. It has a unique window to provide a tantalizing glimpse of new physics beyond the Standard Model and will nicely complement the information acquired in upcoming experiments at the energy frontier.

Chapter 3

General Design Principles

In this chapter, I discuss the general principles involved in conducting any measurement of a small parity-violating asymmetry via electron scattering. Chapters 4 and 5 discuss the implementation of these principles for HAPPEX and E-158.

3.1 Overview of the Experimental Technique

The basic idea in a parity-violating electron-scattering experiment is to measure the asymmetry in the cross section for scattering of longitudinally polarized electrons (*i.e.* electrons whose spin points either parallel or antiparallel to their momenta) off an unpolarized target. This asymmetry is defined as

$$A_{LR} = \frac{\sigma_R - \sigma_L}{\sigma_R + \sigma_L},\tag{3.1}$$

where σ_R (σ_L) is the cross section for incident right- (left-) helicity polarized electrons. It suffices to measure a quantity that is proportional to the cross section. When one calculates the helicity-correlated asymmetry in the quantity, common factors (including many classes of systematic errors) cancel out.

Figure 3.1 gives a schematic illustration of the experimental setup for HAPPEX and provides a useful overview of the methodology used in both experiments. Unlike most electron-scattering experiments, parity-violation experiments require that the experimenters have some measure of control over the entire facility. In this sense, parity-violation experiments resemble table-top exper-
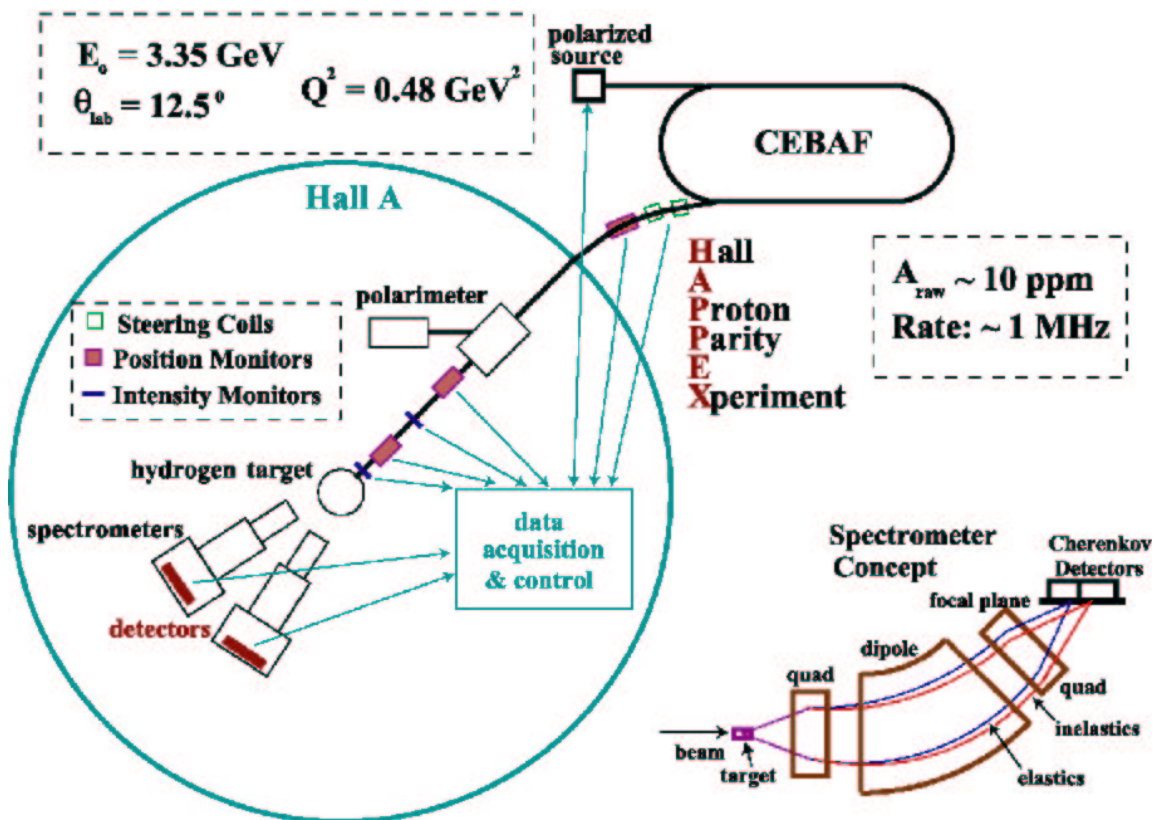
Figure 3.1: An overview of the HAPPEX experimental setup.

iments, albeit on a much larger scale. Polarized electrons are generated at the source, accelerated, and extracted into the experimental Hall's beam line. A number of steering coils may be placed along the beam line in such a way that they can be used to systematically perturb the beam's properties on target. A series of precision beam monitors allows measurements of the beam's properties (intensity, energy, position, and angle) as it approaches the target. One or more polarimeters provide either a periodic (invasive) or continuous (noninvasive) monitoring of the beam polarization. Both HAPPEX and E-158 use a liquid hydrogen target. Magnetic spectrometers use kinematics and collimation to separate the signal from various backgrounds. Calorimetric detectors integrate the scattered flux. Finally, a central data acqusition and control system (DAQ) reads out and controls properties of the polarized source, the magnetic coils, the beam monitors, and the detectors.

3.2 Measuring an Asymmetry

The most robust method for measuring an asymmetry is to flip the helicity of the beam very rapidly, on a pulse-by-pulse basis, and form asymmetries between pairs of pulses with opposite beam helicities that are near one another in time. The cross section σ is proportional to the "normalized flux," the ratio of the detected scattered flux D and the beam intensity I: $\sigma \propto D/I$. Thus, measuring an asymmetry in the cross section is equivalent to measuring an asymmetry in the normalized flux:

$$A_{LR} = \frac{\sigma_R - \sigma_L}{\sigma_R + \sigma_L} = \frac{D_R/I_R - D_L/I_L}{D_R/I_R + D_L/I_L}, \tag{3.2}$$

where the subscripts R and L refer to incident right- and left-helicity electrons. The constant of proportionality between the cross section and the ratio D/I cancels in the asymmetry. To avoid a multiplication of notation, from here on I define $\sigma \equiv D/I$.

Absolute cross-section measurements are very difficult, and it is unrealistic to consider making measurements with part-per-million precision. However, asymmetry measurements bear several advantages over absolute measurements, as we now discuss. Let us describe the systematic errors in the cross section measurements with three parameters: a scale factor S, a common-mode offset $\Delta\sigma_{CM}$, and a helicity-correlated offset $\Delta\sigma_{HC}$, where $\Delta\sigma_{CM}, \Delta\sigma_{HC} \ll \sigma_{R(L)}$. Then we can express the asymmetry as

$$A_{LR}^{meas} = \frac{S(\sigma_R + \Delta\sigma_{CM} + \Delta\sigma_{HC}) - S(\sigma_L + \Delta\sigma_{CM} - \Delta\sigma_{HC})}{S(\sigma_R + \Delta\sigma_{CM} + \Delta\sigma_{HC}) + S(\sigma_L + \Delta\sigma_{CM} - \Delta\sigma_{HC})}. \tag{3.3}$$

The scale factor S cancels out in the ratio, and with a little algebra the expression can be simplified to

$$A_{LR}^{meas} = A_{LR}\left(1 - \frac{\Delta\sigma_{CM}}{\sigma}\right) + \frac{\Delta\sigma_{HC}}{\sigma}, \tag{3.4}$$

where A_{LR} is the true physics asymmetry (in the absence of systematic errors), $\sigma = (\sigma_R + \sigma_L)/2$ is the average normalized flux, and I have kept only first-order terms in $\Delta\sigma_{CM}$ and $\Delta\sigma_{HC}$. We

see that the fractional error due to a common-mode offset introduces a fractional error of equal magnitude in the true asymmetry. For example, a 1% error in the normalized flux yields a 1% error in the asymmetry. Thus, an asymmetry measurement is fairly insensitive to common-mode offset errors and very insensitive to scale errors in measuring the normalized flux. Such is not the case, however, for helicity-correlated errors. Such errors introduce an error in the measurement of the asymmetry that is independent of the size of the asymmetry, and can thus be very dangerous. In order to have confidence in the measurement, these errors must be reduced to a fractional size much less than the proposed statistical error.

The statistical error on the asymmetry calculated from a single pair of events is, in principle, due to the counting statistics of the experiment. If N_R and N_L are the number of detected electrons for right- and left-helicity pulses, respectively, then the statistical error ε for a single pair is

$$\varepsilon = \frac{1}{\sqrt{N_R + N_L}}. \tag{3.5}$$

Given a distribution of pairs, the width of the distribution is equal to the statistical error on a single pair. In practice, the counting statistics of the rate of detected electrons gives the minimum width that distribution can have. Other sources of noise broaden the distribution of pairwise asymmetries. These sources can include finite resolution of the detector and beam monitor electronics, fluctuations in properties of the electron beam and the density of the target, and slow drifts in other parameters of the experiment. These sources of noise are generally random and therefore derive from a normal distribution. Thus, they add in quadrature with counting statistics to determine the statistical error.* To minimize the running time required to make a given measurement, asymmetry experiments are designed such that contributions to the statistical error from sources other than counting statistics are held well below the level of counting statistics. For example, E-158 expects a counting-statistics error of ~ 200 ppm per pair and so requires that pulse-by-pulse

---

*Generally speaking, physicists tend to equate "statistics" with "counting statistics." In parity-violation experiments, the concept of "statistics" is used slightly differently and refers to the width of a particular distribution. "Counting statistics" is then the minimum value that width can take.
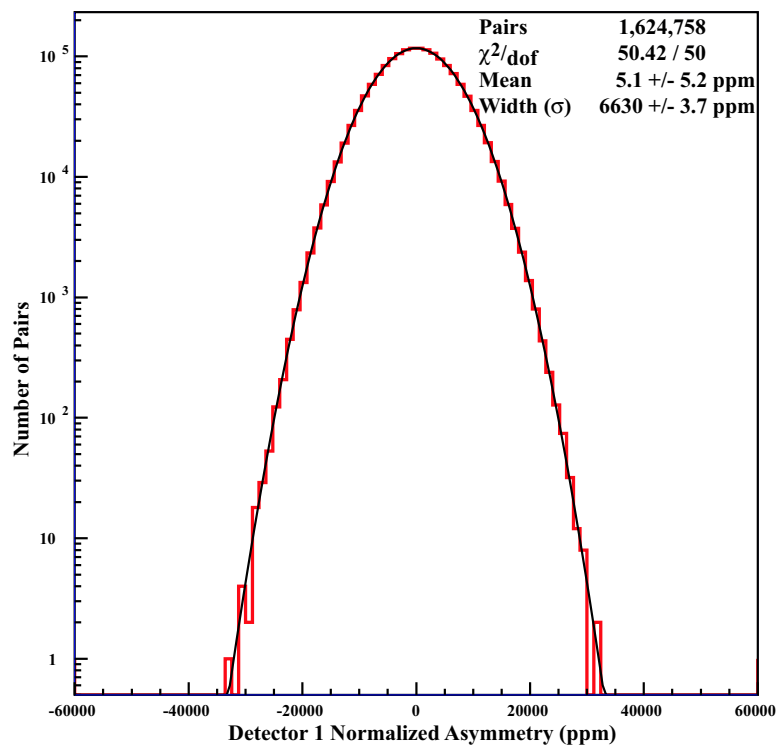
Figure 3.2: A histogram (red) of the normalized detector asymmetry (equation 3.2) for one detector for a portion of the 1999 HAPPEX run. The black curve is a gaussian fit to the histogram. The histogram is plotted on a log scale to emphasize the absence of nongaussian tails.

density fluctuations in the target be held below 100 ppm. Because random noise sources add in quadrature, this ensures that target density fluctuations add little to the statistical error.

A histogram of the asymmetry in the normalized flux for one detector from a portion of the 1999 HAPPEX run is shown in Figure 3.2 and illustrates some of the important features of the statistics. The 1.6 million pairs that make up the histogram represent approximately two days of running. The mean of the distribution is the average asymmetry and the width of the distribution gives a measure of the statistical error per pulse pair. The black curve is a gaussian fit to the histogram. The distribution is gaussian over five decades, indicating that the statistics of the experiment are dominated by counting statistics.

While any fluctuations in properties of the experiment increase the statistical error, helicity-correlated fluctuations also induce systematic errors. The experimental design is thus optimized to suppress fluctuations and in particular helicity-correlated fluctuations. Several experimental

design features are key to this effort and worth discussing in this chapter, before showing how they are implemented for HAPPEX and E-158. These features include integrating the detected flux, rapidly reversing the beam helicity, incorporating multiple methods of slow helicity reversal, developing a procedure for removing the effects of fluctuations in beam properties from the scattering rate, learning to suppress and correct for helicity correlations in beam properties ($^{\mathrm{beam}}A_{\mathrm{LR}}$'s), and suppressing electronic cross talk between the source (where the beam helicity is known) and the DAQ. The use of integration raises certain issues with regards to detector linearity and the suppression of backgrounds. Finally, the beam polarization also needs to be monitored during the experiment. I discuss each of these topics in the remainder of this chapter.

3.3   Integration

Scattering rates in a parity-violation experiment are often in excess of 1-10 MHz. These high rates present the experimenters with two options: 1. Develop a detector and DAQ of incredible segmentation capable of identifying and counting individual scatters, or 2. Integrate the detected flux. Two experiments, A4 and G0, are using the former technique [80, 81] and are discussed in section 8.3. Both HAPPEX and E-158 choose to integrate the detected flux. Integration allows one to use a relatively simple detector and DAQ package and eliminates deadtime and hence potentially dangerous corrections for helicity-correlated deadtime. One challenge of the integration technique is that it provides no opportunity to identify and reject background events during production running. Correcting for backgrounds is discussed below in section 3.12. In addition, integration places stringent requirements on the linearity and resolution of the detector's readout electronics. These issues are discussed later in this chapter.

3.4   Slow Drifts, Fast Reversal

Slow drifts in properties of the experimental apparatus can potentially increase the statistical error and generate systematic errors. By flipping the helicity rapidly and calculating asymmetries on pairs of pulses that are close together in time, we remove noise induced by temporal changes. The experiment becomes insensitive to noise or drifts with characteristic frequencies much lower than the flipping rate. Essentially, what we are doing is keeping track of the asymmetry in the cross section rather than the separate right- and left-helicity cross sections. In order to break any potential correlations between either slow drifts or fast noise and helicity, we flip the helicity according to a pseudorandom algorithm.

3.5   Slow Reversals

While the fast helicity flipping minimizes sensitivity to slow drifts, it introduces its own set of systematic effects. The fast flipping is achieved using a Pockels cell, a type of voltage-controlled retardation plate. By applying $\sim \pm 2.5$ kV across the Pockels cell, it can be made to act like a quarter-wave plate of either sign. However, this means generating a helicity-correlated high-voltage pulse at the polarized electron source; this pulse can be picked up by components of the DAQ and can cause false asymmetries. In addition, imperfections associated with this method of helicity flipping (discussed in Chapter 6) can lead to $^{\text{beam}}A_{\text{LR}}$'s.

Two classes of slow reversal can help to characterize and mitigate these systematic effects. One class of slow reversal flips the helicity of the electron beam in a passive way. This can be done, for example, by inserting a half-wave plate into the laser beam at the source after the beam has been circularly polarized. The half-wave plate flips the helicity of the laser beam and hence of the electron beam. Because the DAQ is not informed of the passive flip, the sign of the physics asymmetry flips while its magnitude remains the same. If the magnitude changes, it could signal the presence of a false asymmetry contribution. Running for equal amounts of time in each state

should result in cancellation of certain classes of false asymmetries.

The second class of slow reversal is designed to flip certain classes of false asymmetry while leaving the physics asymmetry untouched. For instance, one might seek specifically to cancel position asymmetries arising from the helicity-flipping Pockels cell by following it with a set of telescopes which can invert the laser beam's spatial profile. Again, running for equal amounts of time in each configuration can provide some cancellation of the false asymmetry that would arise from the position asymmetries.

3.6 Fluctuations in Beam Properties

Fluctuations in the properties of the electron beam (intensity, position, angle, energy, and spot size) as it is incident on the target cause fluctuations in the scattering rate into the detector. This is because the unpolarized cross sections for Mott and Møller scattering are strongly dependent on scattering angle and energy. Likewise, spot-size fluctuations can change the scattering rate by inducing fluctuations in the target density as discussed in the next section. In addition, the sensitivity of the detected flux to beam fluctuations depends strongly on the choices of target and kinematics. Heavier targets recoil less, increasing the angular dependence of the scattered electrons from $\sim \sin^{-2} \theta$ for an electron target to $\sim \sin^{-4} \theta$ for a nuclear target.

Two related methods exist to extract the experimental sensitivities of the scattering rate on beam parameters: using the natural jitter in the beam parameters to study the correlations between detector rate and beam parameters (correlation analysis), and deliberately modulating the beam parameters in a controlled way (beam modulation analysis).[†] Both the beam modulation and the correlation analyses assume that, for small fluctuations in the beam parameters, the detector's

---

[†] "Beam modulation" has actually gone by several names. It was first used for the Bates ^{12}C and referred to as "coil pulsing" because it only involved modulating the beam position and angle on target using coils along the beam line; energy dependence was checked using a correlation analysis. HAPPEX uses an energy vernier at the end of the accelerator, and since the energy vernier is not a "coil," HAPPEX adopted the term "beam modulation" to describe the same procedure. Finally, E-158 uses the term "dithering" to match the existing terminology in use at SLAC. I use "beam modulation" throughout this thesis in order to be consistent with the HAPPEX usage.

response to fluctuations is linear and can be parameterized as

$$A_{LR} = \frac{\Delta D}{2D} - \frac{\Delta I}{2I} + \alpha_E \frac{\Delta E}{2E} + \sum_i \alpha_i \Delta X_i, \qquad (3.6)$$

where D is the average detected scattered flux for right- and left-helicity pulses, I is the beam intensity, E is the beam energy, the X_i run over position and angle in x and y, and α_E and the α_i are correlation coefficients between energy, position, and angle and the detector signal. These coefficients are measured simultaneously with data-taking. Δ refers to the right-left difference in each of the above parameters. In the correlation analysis, the asymmetry in the detector rate is regressed against the asymmetry in each beam parameter. This regression is done by fitting a scatter plot of detector asymmetry A_D versus asymmetry in one beam parameter $^{\text{beam}}A^i_{\text{LR}}$ to a line and then removing the dependence on the beam asymmetry from the detector asymmetry according to

$$A_D^{reg} = A_D - m_i *^{\text{beam}} A^i_{\text{LR}}, \qquad (3.7)$$

where m_i is the slope of the line. The procedure is then repeated for each of the other beam parameters. In the beam-modulation analysis (described in detail in section 7.2), the correlations between the detector rate and each beam parameter are found by deliberately perturbing each beam parameter individually and measuring the detector's response to that perturbation. Magnetic coils and energy verniers allow the experimenter to ensure that each beam property is perturbed at the target over the full range of interest, which is generally taken to be an amount comparable to the natural beam jitter.

A correlation analysis bears two weaknesses that can be overcome by using beam modulation. First, correlations between beam parameters make it difficult to extract the contributions to the scattering rate that are due to each individual parameter. This does not mean that the analysis is incorrect. The detector rate is appropriately corrected for fluctuations in beam properties and the raw asymmetry is determined properly. However, it is difficult to say how much effect each beam

parameter had on the detector asymmetry. Beam modulation provides additional information by *deliberately* modulating each beam parameter individually in a controlled way. By looking at the correlation between scattering rate and a particular beam parameter only while specifically modulating that parameter we can extract the contribution to the noise in the rate that is due solely to that parameter.

Second, and potentially more serious, it is conceivable that the natural beam jitter does not sample a region of phase space that is sampled by helicity correlations in the beam. In this case, the correction for dependence on beam helicity correlations would be wrong, leading to an unidentified systematic error in the measurement. Beam modulation is designed to span the full phase space of beam fluctuations in order to prevent this scenario from happening.

The HAPPEX analysis relies solely on a beam modulation analysis. The corrections due to beam fluctuations and helicity correlations are expected to be much smaller than the statistical error, so one analysis is deemed sufficient. The E-158 collaboration plans to use both a correlation analysis and a beam modulation analysis and to compare the results as a cross check because the corrections for individual $^{\text{beam}}A_{\text{LR}}$'s are likely to be comparable in size to the statistical error. The formalism for the beam modulation-analysis is presented in Chapter 7.

3.7 Fluctuations in Target Density

Just as fluctuations in beam parameters can introduce additional noise into the detector measurement, so can fluctuations in the target density. Both HAPPEX and E-158 use liquid-hydrogen targets cooled to 18-19 K. With several hundred watts of power being dumped into this cold fluid, it is easy to imagine that local heating can result in significant fluctuations in the target thickness from pulse to pulse. Note that what these experiments care about is *fluctuations* in the total target density along the beam's path; a reduction in the target density (and hence luminosity) due to heating is not a significant problem so long as it is stable from pulse to pulse. In addition, if the density fluctuations are helicity correlated, they can also induce a false asymmetry

that can be potentially difficult to characterize and correct. For these reasons, one design requirement for liquid-hydrogen targets used in parity-violation experiments is that they suppress density fluctuations significantly below the level of the experiment's counting statistics.

3.8   Electronic Cross Talk

Another potential source of false asymmetries is electronic cross talk between the source and the DAQ. Several helicity-correlated signals are produced at the source. These include multiple copies of signals indicating the polarization state of each pulse and the signals used to drive the polarization Pockels cells and asymmetry feedback devices. A number of standard techniques have been developed to suppress helicity-correlated cross talk.

1. The helicity-flipping Pockels cell is pulsed at $\sim$ 2.5 kV and acts as an antenna, loudly broadcasting information about the beam helicity in time with each pulse. To suppress pickup of this signal by the DAQ, both the source electronics and the DAQ are designed carefully to minimize ground loops.

2. On a pulsed machine, the Pockels cell's high voltage can be given long rise and fall times, on the order of 1 ms, which reduces its tendency to capacitively couple to other signals.

3. The DAQ must record the beam helicity information for each pulse, but it does not necessarily need to do so in time with each pulse. To break the correlation between the helicity information present in the DAQ and the actual beam helicity, we delay the transmission of helicity information from the source by a fixed number of pulses. This delay is then compensated for in the data-analysis software.

4. On a pulsed machine, the helicity information is also sent out of time with the electron pulse.

3.9 Helicity-Correlated Intensity Asymmetry

A helicity-correlated intensity asymmetry[‡] (A_I) generates a false asymmetry in the detected flux that is equal in size to the intensity asymmetry, as shown by equation 3.6. To first order, we correct for A_I by normalizing the detector signal to the beam current, as in equation 3.2. However, a nonzero A_I leads to other effects as well. One effect is an additional false-asymmetry contribution to A_{LR} proportional to the nonlinearity of the detector. A second effect arises from cross talk between properties of the electron beam: a nonzero A_I can generate other $^{\text{beam}}A_{\text{LR}}$'s as well.

3.9.1 Detector Linearity

An integrating detector is designed to output a signal that is linearly proportional to the detected flux, but in practice it is unlikely to do so perfectly. We can model the detector's behavior as $D = F + \epsilon F^2$, where D is the measured detector signal, F is the actual detector flux, and ϵ parameterizes the degree of nonlinearity. The flux is proportional to the product of the cross section and the beam intensity: $F = C\sigma I$, where C is a constant that includes other factors such as the solid-angle acceptance of the spectrometer and the target thickness. Thus, we have for each helicity

$$D_{R(L)} = C\sigma_{R(L)}I_{R(L)} + \epsilon C^2 \sigma_{R(L)}^2 I_{R(L)}^2. \tag{3.8}$$

Substituting equation 3.8 into equation 3.2, we can write the measured asymmetry A_{LR}^{meas} as

$$A_{LR}^{meas} = \frac{(C\sigma_R I_R + \epsilon C^2 \sigma_R^2 I_R^2)/I_R - (C\sigma_L I_L + \epsilon C^2 \sigma_L^2 I_L^2)/I_L}{(C\sigma_R I_R + \epsilon C^2 \sigma_R^2 I_R^2)/I_R + (C\sigma_L I_L + \epsilon C^2 \sigma_L^2 I_L^2)/I_L}. \tag{3.9}$$

[‡]When the intensity asymmetry is on the electron beam (as opposed to the laser beam) I sometimes use the term "charge asymmetry" as well.

A lot of algebra reveals that to first order in the asymmetries (and assuming $\epsilon F \ll 1$), the measured asymmetry can be expressed as

$$A_{LR}^{meas} = A_{LR} + x(A_{LR} + A_I), \tag{3.10}$$

where $x = \epsilon C \sigma I \equiv$ nonlinearity (where σ and I are the average cross section and beam intensity, respectively, and x is unitless) and

$$A_{LR} = \frac{\sigma_R - \sigma_L}{\sigma_R + \sigma_L} \quad \text{and} \quad A_I = \frac{I_R - I_L}{I_R + I_L}. \tag{3.11}$$

This result shows that the systematic error due to detector nonlinearity scales in proportion to the sum of the physics asymmetry and the intensity asymmetry. We can draw two conclusions. First, it is a sufficient goal to require that the intensity asymmetry be equal to or less than the raw physics asymmetry in magnitude. Second, detector linearity is an important concern for asymmetry measurements because the resulting fractional systematic error in the asymmetry is equal to the nonlinearity x.

3.9.2 Beam Loading

The acceleration process causes correlations to develop between beam properties, allowing an intensity asymmetry to generate other $^{beam}A_{LR}$'s. The most significant effect is a coupling between intensity and energy via "beam loading." Beam loading induces a correlation between intensity and energy because the accelerator is slightly resistive. Thus, beam loading causes an intensity asymmetry to generate an energy asymmetry. This effect is the dominant source of energy asymmetries and is discussed in more detail in the context of the SLAC accelerator in section 6.4.3. Wakefield effects and imperfections in the accelerator's magnetic optics can then couple both intensity and energy asymmetries into position and angle.

3.10 Helicity Correlations in Position, Angle, Spot Size, and Energy: $^{\mathrm{beam}}\mathrm{A_{LR}}$'s

As was discussed in section 3.6, the unpolarized scattering rate depends on the beam's position, angle, spot size, and energy at the target. If the asymmetries in any of these parameters, averaged over the entire experiment, are nonzero, they are capable of introducing a false asymmetry component into the measured asymmetry. The beam modulation analysis characterizes the detector's sensitivity to $^{\mathrm{beam}}\mathrm{A_{LR}}$'s and allows us to correct the measured asymmetry for helicity-correlated asymmetries in position, angle, and energy according to the same algorithm as is used to remove noise in the scattering rate due to beam property fluctuations (equation 3.6). For E-158, we are also concerned about the possibility of helicity correlations in higher-order properties of the electron beam (such as spot size) coupling to the scattering rate, and so we place a wire array in the beam just upstream of the target. The wire array allows us to measure higher-order moments of each pulse's charge distribution and study correlations between these moments and the detected flux.

3.11 Polarimetry

The beam polarization needs to be monitored during the experiment. The measured asymmetry is the physics asymmetry scaled by the beam polarization. This can be seen by considering the cross section to have two components: a parity-conserving electromagnetic piece σ_{EM} that is equal for both helicity states, and a parity-violating piece σ_{PV} that arises from the interference of weak and electromagnetic amplitudes and has opposite signs for the two beam helicities. The contribution of σ_{PV} scales with the beam polarization P_B. Thus, $\sigma_R = \sigma_{EM} + P_B\sigma_{PV}$ and $\sigma_L = \sigma_{EM} - P_B\sigma_{PV}$ and the measured asymmetry is (assuming $\sigma_{PV} \ll \sigma_{EM}$)

$$A_{LR}^{meas} = \frac{(\sigma_{EM} + P_B\sigma_{PV}) - (\sigma_{EM} - P_B\sigma_{PV})}{(\sigma_{EM} + P_B\sigma_{PV}) + (\sigma_{EM} - P_B\sigma_{PV})} \approx P_B\frac{\sigma_{PV}}{\sigma_{EM}} = P_B A_{LR}, \qquad (3.12)$$

where A_{LR}^{meas} is the measured asymmetry and A_{LR} is the physics asymmetry. Because the beam polarization enters as a scale factor, the systematic error in the physics asymmetry due to beam polarization is equal to the fractional error in the beam polarization. For the current generation of parity-violation experiments, the systematic error in beam polarization typically enters at the $\sim$ 3-4% level, and is generally one of the dominant systematic errors.

3.12 Backgrounds

One weakness of the integration technique is that it does not allow for event-by-event background rejection. To suppress backgrounds, both HAPPEX and E-158 use a magnetic spectrometer to separate the scattered particles of interest from backgrounds and collimation to define the kinematic acceptance and provide further background rejection. In order to evaluate the remaining background flux in the detector, both experiments conduct auxiliary studies periodically. Contributions of the background flux to the measured asymmetry can then be corrected according to (modifying equation 3.12)

$$A_{LR} = \frac{1}{P_B} \frac{A_{LR}^{meas} - f_{bkg} A_{bkg}}{1 - f_{bkg}} \tag{3.13}$$

where A_{LR} is the physics asymmetry determined from the experiment, f_{bkg} is the fraction of the detected flux which comes from background processes, and A_{bkg} is the flux-weighted asymmetry in those background processes. The asymmetries in the background processes can in some cases be calculated with sufficient precision to make a correction (if necessary) and to quantify the resulting systematic error. In other cases, such as for the pion and *e-p* backgrounds for E-158, the background fluxes and asymmetries are sufficiently uncertain that they need to be measured by auxiliary detectors during the experiment in order to apply a correction with sufficient precision.

Chapter 4

HAPPEX Experimental Design

HAPPEX ran at the Thomas Jefferson National Accelerator Facility (TJNAF, more commonly referred to as JLab) in 1998 and 1999. HAPPEX used a polarized electron beam provided by JLab's accelerator, the Continuous Electron Beam Accelerator Facility (CEBAF, shown schematically in Figure 4.1). CEBAF provided beams for three experimental halls, and HAPPEX utilized Hall A. The experimental configuration was very similar for the 1998 and 1999 runs, with the most prominent differences being associated with the polarized electron source. The experimental configuration for the 1999 run is discussed in this chapter.

4.1 Overview

CEBAF consists of an Injector, two linear accelerators connected by two sets of recirculation arcs, and an Extractor. The Injector region includes the polarized electron source and the hardware required to prepare the electron beam for acceleration. The polarized electron source is designed to provide three interleaved beams, one for use in each experimental hall. The recirculation arcs allow each beam to make up to five passes through each linear accelerator. After an appropriate number of passes (determined by the energy required by a given Hall), each beam can be separately extracted and sent to its experimental hall. By extracting different beams after differing numbers
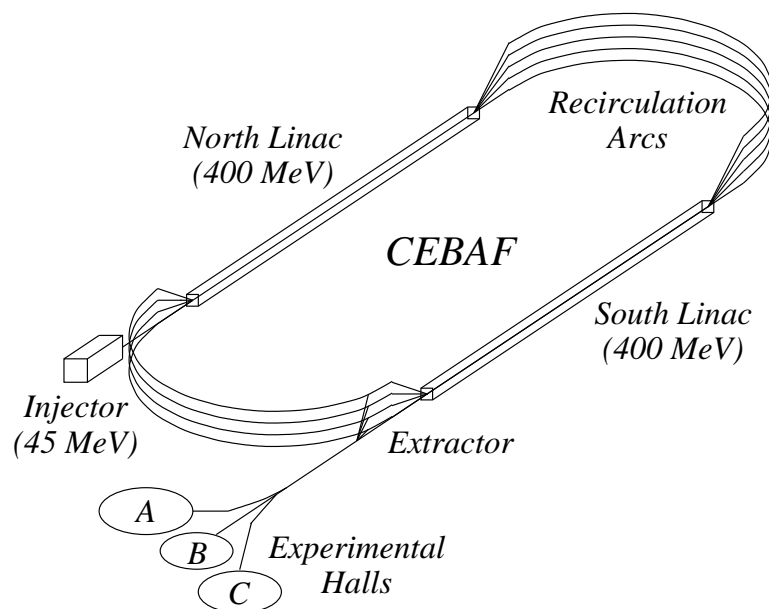
Figure 4.1: Overview of CEBAF.

of passes through the accelerator, it is possible to run experiments simultaneously in the three Halls at different energies. Each linear accelerator is designed to provide 400 MeV per pass,* and a total of five passes thus allows a beam energy up to 4 GeV. Continued development work on the accelerating cavities has allowed them to exceed these design specs, and at the time of this writing the maximum available energy is ~ 6 GeV.

For HAPPEX, the Hall A beam was accelerated to an energy of 3.355 GeV before being extracted into the Hall A beam line. The experimental setup in Hall A was shown schematically in Figure 3.1. The Hall A beam line contained a number of elements that were important to the experiment: magnetic coils used for beam modulation (energy modulation was performed using one of the accelerator's energy verniers); monitors of the beam's intensity, position, angle, and energy; and two polarimeters. A 15-cm-long liquid hydrogen cell, one of the standard Hall A cryotargets, provided a proton target. Following the target, two high-resolution spectrometers were set symmetrically at a scattering angle of 12.3°. In the focal plane of each spectrometer, we

---

*Each linear accelerator has 160 superconducting RF accelerating cavities. The cavities were designed to have a nominal gradient of 5 MV/m and are 0.5 m long, hence 160×5 MV/m $\times 0.5$ m $= 400$ MeV per accelerator.

installed a specialized detector built for this experiment.

The remainder of this chapter discusses the important elements of the experimental setup. First, however, we take a detour to estimate the rate of electrons scattered into the detector in order to gain a perspective on the counting rates and statistics in the experiment.

4.2   Estimate of Rate

We can estimate the scattering rate with the help of equation 2.12. At a beam energy of 3.355 GeV, a momentum transfer of 0.477 GeV^2, and an average scattering angle of 12.3°, the differential cross section is

$$\frac{d\sigma}{d\Omega} = 0.74 \text{ microbarns/steradian } (\mu\text{barn/sr}). \tag{4.1}$$

The number of electrons per second N_s scattered into each spectrometer's acceptance can be expressed as

$$N_s = \frac{d\sigma}{d\Omega} \cdot I \cdot \rho \cdot L \cdot \Delta\Omega \cdot f_b, \tag{4.2}$$

where I is the beam current, ρ is the target density, L is the target length, $\Delta\Omega$ is the solid angle acceptance of each spectrometer, and f_b is a correction factor to account for particles lost due to Bremsstrahlung in the target. Using the values

$$\frac{d\sigma}{d\Omega} = 0.74 \ \mu\text{barn/sr} = 7.4 \cdot 10^{-31} \text{ cm}^2/\text{sr},$$
$$I = 40 \ \mu\text{A} = 2.5 \cdot 10^{14} \text{ electrons/s},$$
$$\rho = 0.072 \text{ g/cm}^3 = 4.3 \cdot 10^{22} \text{ protons/cm}^3,$$
$$L = 15 \text{ cm},$$
$$\Delta\Omega = 5.5 \text{ msr},$$
$$\text{and } f_b = 0.8,$$

we find that the rate in each detector should be 525 kHz.[†]

The detector signal was integrated for 32 ms during each window and so an average of 16,800

[†]I have assumed a beam current of 40 μA in this calculation. During the experiment, the beam current varied between 25-50 μA.

electrons were counted per detector per window, or 33,600 per window pair. Counting statistics determined the minimum width of the statistical distribution of pair asymmetries, and therefore we expected a width greater than or equal to

$$\sigma_{min}(A_{pair}) = \frac{1}{\sqrt{33,600}} \approx 5500 \text{ ppm}. \tag{4.3}$$

In order to take full advantage of the available statistics, we required that all other sources of noise in the detector signal be much less than 5500 ppm. We typically observed an RMS width on the distribution of asymmetries of ~ 5800 ppm when running at a beam current of 40 μA.

4.3   Polarized Electron Source

JLab's polarized electron source is based on photoemission from GaAs. In the photoemission process, an electron within the crystal absorbs a photon and is excited from the valence band into the conduction band. The electron migrates to the surface of the crystal, and escapes into vacuum. The electron is able to escape because the crystal's surface is specially prepared to have a negative electron affinity. The GaAs crystal acts as the cathode of the polarized electron gun and is held at a bias voltage of -100 kV in order to draw the electrons away from the cathode and into the accelerator.

The reason the electrons can be emitted in a polarized state is related to their initial excitation into the conduction band. GaAs is a direct band-gap crystal. The band structure is illustrated in Figure 4.2. The conduction band behaves like an $S_{1/2}$ band. The valence band is split into two bands by a spin-orbit interaction: $P_{1/2}$ and $P_{3/2}$. For our purposes, we can neglect the $P_{1/2}$ band. In a "bulk" GaAs crystal (Figure 4.2a), the $P_{3/2}$ valence band is fourfold degenerate. When the crystal is illuminated with circularly polarized light, the relative transition probabilities from the valence band to the conduction band (indicated in Figure 4.2) are such that the maximum theoretically achievable polarization is 50%. However, inducing a strain in the crystalline lattice

(a) Bulk or unstrained GaAs.   **(b) Strained GaAs.**
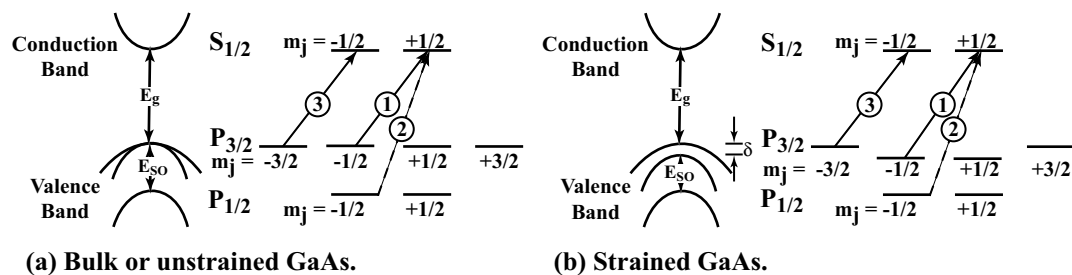
Figure 4.2: Band Structure of GaAs. The relative transition probabilities for incident right-helicity light are indicated by the numbers in circles. E_g is the band gap energy, typically ~ 1.6 eV. E_{SO} is the splitting of the valence-band $P_{1/2}$ and $P_{3/2}$ levels due to a spin-orbit interaction. In (b), δ is the splitting of the $P_{3/2}$ states due to the strain applied by the lattice mismatch and is ~ 50 meV.

breaks the degeneracy between the $J = \frac{1}{2}$ and $J = \frac{3}{2}$ energy levels (Figure 4.2b); proper tuning of the wavelength of the laser used to illuminate the cathode can then allow a theoretical polarization of 100%. Such a "strained" cathode is made by growing a thin layer (~ 100 nm) of GaAs on a substrate of GaAsP; the mismatch in the lattice constants of the two layers induces the required strain in the GaAs. HAPPEX used a bulk cathode during its 1998 run and measured an average beam polarization 38%. For the 1999 run, HAPPEX used a strained cathode and measured an average polarization of 71%.

In a strained GaAs crystal, the quantum efficiency (QE) for incident linearly polarized light depends strongly on the orientation of the light's polarization axis with respect to the "strain axis" of the crystal. We refer to this effect as a "QE anisotropy." The QE anisotropy has been observed to depend on the details of each cathode's structure [82]. The magnitude of the QE anisotropy is defined as $\frac{\Delta QE}{2\langle QE \rangle}$, where ΔQE is the difference between the maximum and minimum QE's and $\langle QE \rangle$ is their average. The QE anisotropy is typically observed to be ~ 5-15%.

The QE anisotropy can generate a helicity-correlated intensity asymmetry on the electron beam if the laser light illuminating the GaAs crystal is not perfectly circularly polarized. In practice, perfect circular polarization can not be attained, and some residual linear polarization remains. The axis for this linear polarization component is, in general, different for the two helicities of the laser light. Because the linear polarization axes are different, the QE seen by the linear polarization also differs, and an asymmetry in the number of photoemitted electrons is generated. This coupling

between the QE anisotropy and residual linear polarization is in fact one of the dominant sources of $^{beam}A_{LR}$'s. It is discussed in detail in Chapter 6 and more briefly in the context of HAPPEX in section 4.11.

CEBAF's beam was, for all practical purposes, continuous-wave(cw) rather than pulsed. It could be considered cw because polarized electrons were extracted from the GaAs crystal in "bunches" of ~ 100 ps at 499 MHz for each experimental Hall. With all three experimental halls running, electrons were extracted from the crystal at a maximum rate of 3×499 MHz = 1497 MHz. The accelerating cavities were continuously fed RF power at this frequency. For HAPPEX, the source flipped helicity at 30 Hz. Hence, in place of "pulses" or "events," we spoke of "windows" of 33.3-ms duration during which the beam had a definite helicity.

There was a one-month shutdown in the middle of the 1999 run[‡] (June) during which the source configuration changed significantly. In April and May, there was a single polarized electron gun at the Injector. It was called the "vertical gun" due to the fact that the laser beam was directed vertically into it in order to illuminate the cathode. During the shutdown, the vertical gun was removed and replaced with a pair of "horizontal guns," for which the laser beam remains in the horizontal plane. Each horizontal gun was located at a small angle to the Injector beam line. The idea was to provide a spare gun ready for use in case one gun failed catastrophically. Changing from the vertical gun to the two horizontal guns necessitated some alterations to the layout of the optics system, as described in the following section.

4.3.1 Laser and Optics Systems

Each Hall has a dedicated laser system. The configurations of the laser and optics systems for the vertical gun and the horizontal guns are shown in Figures 4.3 and 4.4, respectively. The lasers were master/slave systems where the master (labeled "seed" in the figures) was a gain-switched diode laser that output pulses at a repetition rate of 499 MHz. The slave (labeled "amplifier") was a

---

[‡]The 1999 run had two segments, April 6-May 27 and July 8-27.

semiconductor optical amplifier; its output pulses were 60-80 ps in length. Following the amplifier for each laser was a slit that acted as a spatial filter to ensure that the laser profile was gaussian. The lens and cylindrical lens following the amplifier ensured that the beam was roughly round through the remainder of the optics system. Separate attenuators for each laser system provided independent control of the electron beam current for each Hall. Beam-combining optics aligned the three beams on top of one another before they reached the Pockels cell. The laser wavelength was chosen to be 840 nm in order to match the band gap of the GaAs cathode.

Figure 4.3 gives a schematic of the laser and optics systems as they were configured for use with the vertical gun during April and May, 1999. Following the beam-splitting cube was an insertable half-wave plate that was oriented to rotate the linearly polarized light by 90°. It was used to provide a means of slow helicity reversal. The last mirror redirected the beam vertically and was followed by the helicity-flipping Pockels cell, the rotateable half-wave plate (not shown), a lens (not shown), and the vacuum window at the entrance to the electron gun. The rotateable half-wave plate was used to control the relative orientation between the Pockels cell's fast axis and the strain axis of the cathode and was useful for suppressing helicity-correlated beam asymmetries, as described in section 4.11.2. The lens was used to properly size the beam on the cathode and also provided a means of steering the beam in order to illuminate a region of the cathode that possessed both high polarization and high QE.

During the June 1999 shutdown, the change from the vertical gun to the two horizontal guns necessitated a reconfiguration of the optics system. The laser system remained the same. Figure 4.4 shows the optics layout in the new configuration. For the July running period, Gun #1 was used. An insertable periscope could be used to redirect the combined laser beams to the optics line for Gun #2. As before, an insertable half-wave plate was available for slow helicity reversal. Following the last mirror were the helicity-flipping Pockels cell, a rotateable half-wave plate, and a lens.

In April and May, the laser spot size on the cathode was ~ 300 μm FWHM, and in July it was ~ 600 μm FWHM. Both sizes are small compared to the ~ 5-mm diameter active area of the
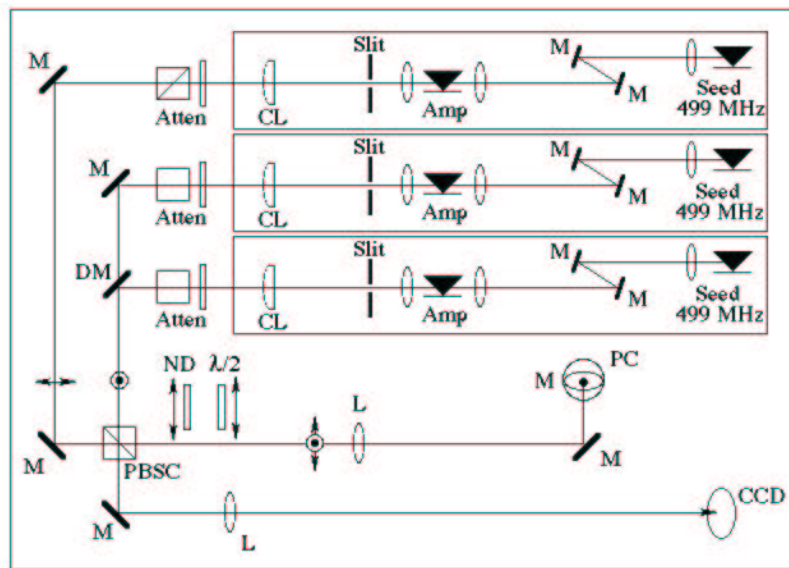
Figure 4.3: JLab's polarized source laser system as it was configured for the April/May 1999 running of HAPPEX. (M, DM) Mirror, (L) Lens, (CL) Cylindrical Lens, (ND) Neutral Density Filter, ($\lambda/2$) Half-Wave Plate, (PBSC) Polarizing Beam-Splitting Cube, (PC) Pockels Cell, (CCD) Camera, and (Atten) Attenuators.
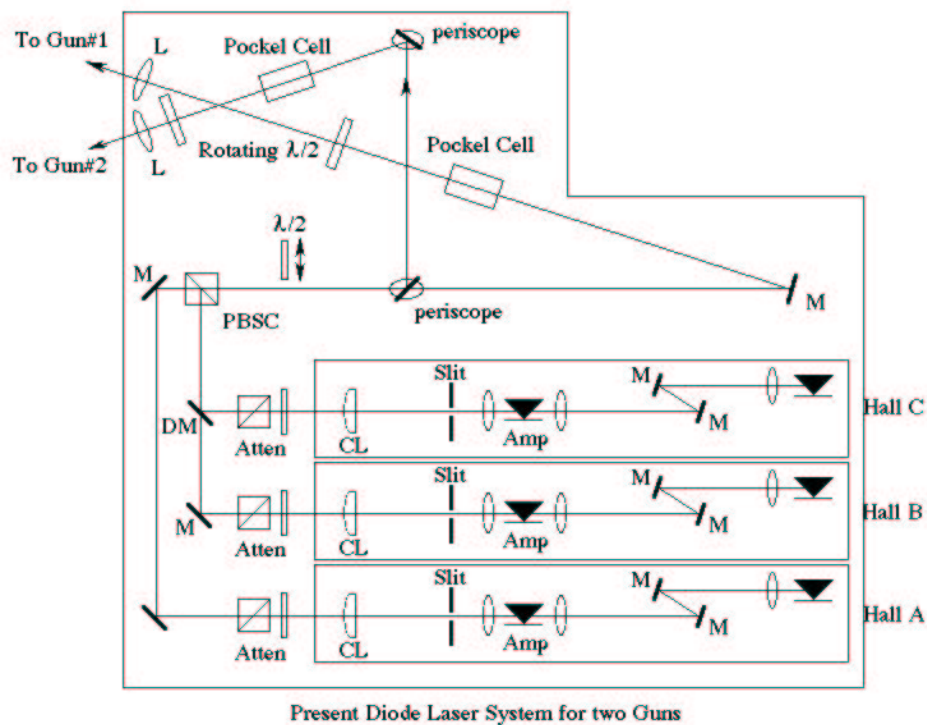
Figure 4.4: JLab's polarized source laser system as it was configured for the July 1999 running of HAPPEX. HAPPEX used Gun #1.

cathode.

4.3.2 Helicity Sequence and Timing Signal Generation and Distribution

We required that the 30-Hz helicity windows be chosen pseudorandomly and be locked to the 60-Hz power line frequency. The pseudorandom sequence we used involves choosing one window's helicity randomly and forcing the following window to have the complementary helicity. The next window's helicity was again chosen randomly, and so on. An example sequence would be, "RL RL LR RL LR." We generated the pseudorandom sequence according to the algorithm described in [83]. The helicity windows were locked to the power line to eliminate sensitivity to noise at 60 Hz (the dominant frequency in the accelerator's noise spectrum) and its harmonics. At 30 Hz, each helicity window integrated over an integral number of 60-Hz periods.

The helicity sequence and associated timing signals were generated by an electronics box at the

polarized electron source that was designed by graduate student Wilson Miller; the details of its design can be found in his thesis [84]. The helicity and timing signals were transported from the source to the HAPPEX DAQ in Hall A's control room (or "Counting House") via fiber optics to avoid coupling the source and Hall electrical grounds. Before transmission, the helicity sequence was delayed by eight windows in order to break the correlation between the beam's helicity and the DAQ's knowledge of it. A total of three signals were sent to Hall A. They were

1. Helicity – The helicity of the beam during the window eight windows previous to the current window.

2. Master Trigger – A timing signal that marked the beginning of a new helicity window at the source. It was used to generate timing signals to control the ADC boards.

3. Realtime – A signal that indicated whether the current window was the first or second window of a pair.

4.4   Injector

The Injector region prepared the beam to enter the main accelerator. It accelerated the beam to 45 MeV, sufficiently relativistic to be able to stay in phase with the accelerator's RF. A Wein Filter located shortly after the polarized electron gun was used to rotate the beam polarization and compensated for $g - 2$ spin precession in the accelerator's recirculation arcs and the bends in each Hall's beam line. The Wien Filter ensured that longitudinally polarized electrons reach the Halls.

4.5   Beam Diagnostics and Beam Modulation

A number of devices along the Hall A beam line were used to monitor the beam's properties and to introduce a slow, deliberate modulation of those properties. They included

- Two Beam Current Monitors (BCM), referred to as "BCM 1" and "BCM 2," located ~ 24.5 m upstream of the target. These two precision monitors were RF resonance cavities. When tuned to the accelerator's frequency of 1497 MHz, they output a signal proportional to the beam intensity and provided a resolution of $\sim$ 50-60 ppm per window pair. The BCM's were linear to better than 0.5% for beam currents between 8 and 52 μA [85].

- One Unser Monitor [86, 87, 88], another type of current monitor, located between the two cavity BCM's. The Unser Monitor was much noisier than the cavity monitors but had the advantage of being linear down to zero current, whereas the cavity BCM's required a minimum current of several μA in order to read out properly. The Unser Monitor was useful in evaluating the linearity of both the cavity BCM's and the detectors [85].

- One additional BCM located in Hall C. This BCM was used to monitor the intensity asymmetry in the Hall C beam and to provide the error signal for the feedback used to suppress that asymmetry, as described in section 4.11.5.

- Two stripline Beam Position Monitors (BPM's) [89, 90] located 1.286 m (BPM 3b) and 7.524 m (BPM 3a) upstream of the target. These BPM's were downstream of all the magnetic optics in the beamline. Together, these two position monitors tracked the position (x and y) and angle (x' and y') of the beam on target.

- Three additional stripline BPM's located in the Hall A beam-line bend. One of these, BPM 12, was at a point of high dispersion and its horizontal position measurement was sensitive to the energy of the beam.

- Seven dithering coils, four to modulate the beam horizontally and three to modulate the beam vertically, spaced along the Hall A beam line upstream of the BPM's. Each 20-cm-long coil could be driven with a current as large as $\pm$300 mA, yielding a field of up to 20 gauss. The coils were able to introduce a maximum angular deflection of $\sim$ 35 μrad. The position offset induced at a particular BPM by a particular coil depended on the magnetic optics between

them and was typically on the order of 100 μm.

- One energy vernier at the end of the accelerator that was used to modulate the energy of the beam. Note that the energy vernier was part of the accelerator, which meant that it affected the beams for all three experimental halls. Care had to be taken with the amplitude and frequency of the energy modulation to avoid a negative impact on the beam quality in Halls B and C. We restricted the energy modulation to a maximum of ± 500 keV, or $\sim 10^{-4}$ of the beam energy, comparable to the natural energy jitter in the accelerator. Thus, the energy modulation had negligible impact on the other experimental halls.

The beam modulation analysis requires knowledge of the dependence of the scattering rate on the position, angle, and energy of the beam at the target, $d\sigma(x, y, x', y', E)$. We cannot measure those parameters at the target per se, but we can measure them at the BPM's upstream of the target. A linear transformation connects the five on-target variables to the quantities measured at the BPM's. Strictly speaking, it is not important for us to know the transformation between the two sets of variables. It is enough to verify that the five measurements are linearly independent, and thus span the five-dimensional parameter space of the scattering rate. Clearly, there are correlations between the measurements at each BPM. These correlations are accounted for in the formalism presented in section 7.2.

4.6   Electron Beam Polarimetry

During the 1999 HAPPEX run, three polarimeters were used to monitor the beam polarization, one in the Injector and two in Hall A. At the 5-MeV region in the Injector, a polarimeter based on Mott scattering from a gold foil (the "Mott Polarimeter" [91]) was used by the Injector group to characterize the polarization as a function of position across the cathode and select a position on the cathode that provided high polarization.

Two polarimeters were located in Hall A. The "Møller Polarimeter" [92] was based on Møller

scattering of the beam from electrons in a polarized iron foil. Such a measurement of the beam polarization was inherently invasive, and therefore required auxiliary runs. We made Møller Polarimeter measurements before and after a change in the state of the insertable half-wave plate or whenever the source configuration changed significantly. The second polarimeter, the "Compton Polarimeter" [93], was based on Compton scattering of circularly polarized light off the beam. The cross section for Compton scattering is low enough that the Compton Polarimeter is essentially noninvasive and can be used to continually monitor the beam polarization during the experiment. The Compton Polarimeter was commissioned during the 1999 HAPPEX run. It provided continuous monitoring of the relative beam polarization during the later parts of the run and was useful in confirming that the beam polarization was indeed stable between Møller Polarimeter measurements, but it was not used in determining the average beam polarization. The results of the polarimetry studies are discussed in section 7.4.

4.7   Liquid Hydrogen Target and Raster

Part of the standard Hall A equipment package is a cryogenic target system [92]. This system provides access to liquid hydrogen and deuterium targets, a gaseous helium target, and a number of solid targets. HAPPEX used a 15-cm liquid hydrogen target. This target operated at a pressure of 0.17 MPa and a temperature of 19 K, and had a density of 0.0723 g/cm^3. Cooling was provided by 15-K He and was able to remove up to 1000 W of heat, including 700 W from the beam (at 130 μA) and 300 W from the circulating fans and a heater used to keep the temperature stable when the beam trips off. The beam size at the target was typically small–less than 100 μm–and therefore deposited heat in such a small region as to risk damaging the target. A "raster" system scanned the beam position over a several-millimeter range in x and y across the face of the target at rates of 17-24 kHz in order to spread the heat deposition over a safe volume.

One of the target features that was of greatest concern to HAPPEX was fluctuations in the target density, as was discussed in section 3.7. HAPPEX studied target density fluctuations in an

auxiliary run prior to the 1998 physics run. For this auxiliary run, HAPPEX ran at an energy of 925 MeV in order to increase the scattering rate to 50 MHz per detector at a beam current of 100 μA. With a higher rate, the contribution to the width of the detector asymmetry distribution that was due to counting statistics decreased from the 5500 ppm we estimated earlier (equation 4.3) to approximately 560 ppm. Since the contributions to the width from counting statistics and target density fluctuations add in quadrature, reducing the width due to counting statistics made it easier to identify a contribution from target density fluctuations. Figure 4.5 shows the results of a study in which the width of the detector asymmetry distribution was measured as a function of beam current I and raster size. The results are normalized to the width one would expect for a beam current of 100 μA (*i.e.*, $normalized\,width = measured\,width \times \sqrt{I/100}$). In the absence of target density fluctuations, the results should be independent of beam current and raster size. To aid in comparing the results, the mean value and one-sigma uncertainty of the data point at a beam current of 11.6 μA and a raster size of 2.0 mm are drawn across the plot as horizontal lines. The width was observed to rise with beam current for a fixed raster size and to decrease as the raster size was expanded at constant beam current. Note, however, that even at the smallest raster size and highest beam current the noise from density fluctuations was well below 10^{-3} and hence had a small effect when added in quadrature with the ~ 5500-ppm width from counting statistics obtained during the physics run. During physics running, we monitored density fluctuations by looking at the correlation between the scattering rates into the detectors in each spectrometer; density fluctuations typically added at most a few percent to the detector asymmetry distribution widths and hence are negligible.

4.8 Magnetic Spectrometers

Hall A was equipped with two nearly identical High-Resolution Spectrometers (HRS) [92]. They were designed for use in coincidence experiments; HAPPEX used both simply to double the solid-angle acceptance of the experiment. On top of each spectrometer was a shielded detector hut,
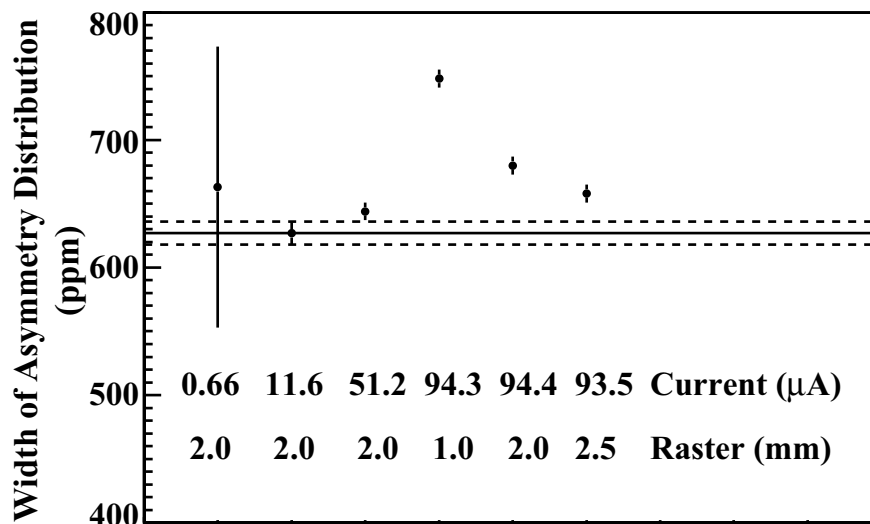
Figure 4.5: Width of the detector asymmetry distribution as a function of beam current and raster size, normalized to the widths expected for a beam current of 100 μA as described in the text.

housing both the standard Hall A detector package and the HAPPEX detector. Each spectrometer had a 5.5-msr acceptance. The spectrometers had a resolution of $\delta p/p \sim 10^{-4}$ over a momentum range of $0.8 - 4.0$ GeV for the scattered particles. For HAPPEX, this high resolution achieved the separation we required between the elastically scattered electrons which made up our physics signal and the inelastically scattered electrons, pions, and other scattered particles which were potential backgrounds. Figure 4.6 shows a scatter plot of electrons accepted by the spectrometer as a function of position in the spectrometer's focal plane. The rectangle indicates the location of the HAPPEX detector. The dark stripe contained within the rectangle was produced by elastically scattered electrons. The separate stripe below and to the right of the rectangle was produced by inelastically scattered electrons and was clearly well separated from the detector's acceptance.

4.9 Detectors

Two sets of detectors were installed in each spectrometer for use during HAPPEX: the "standard Hall A" detector package and a dedicated "HAPPEX detector." The standard Hall A detector packages contain elements for particle ID, tracking, and calorimetry. Those detector packages
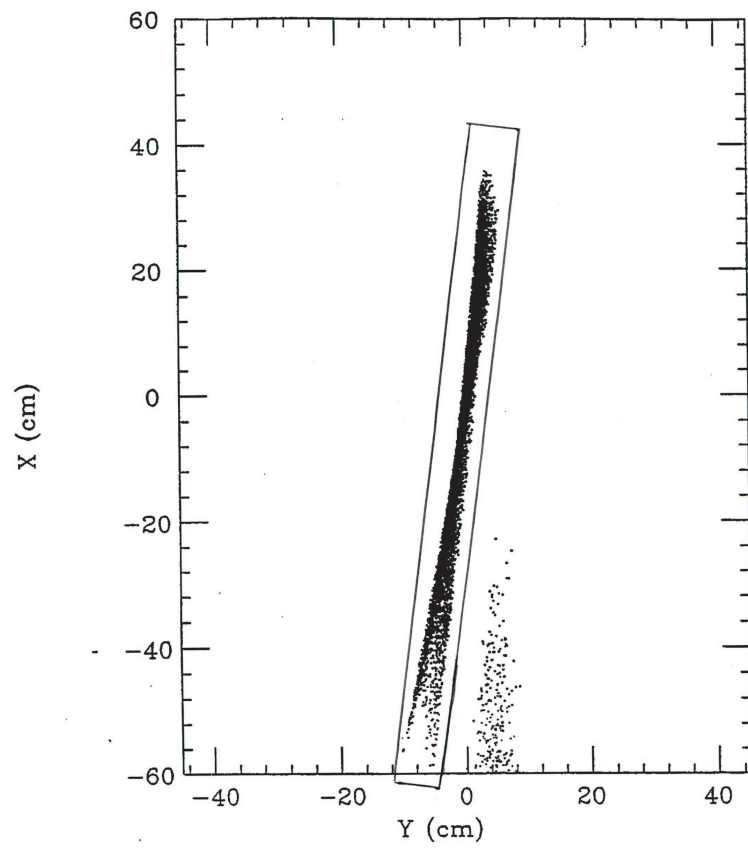
Figure 4.6: Scatter plot of particle positions in the focal plane of one spectrometer.
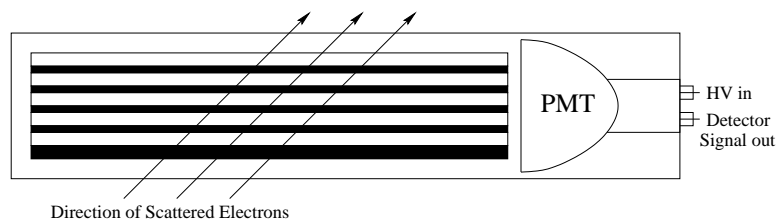
Figure 4.7: Schematic of the HAPPEX integrating detector. The detector consisted of alternating layers of lead (bottom layer 0.5-inch thick, remaining layers 0.25-inch thick) and lucite (0.5-inch thick).

measured properties of individual electrons and were useful for counting rates up to ~ 2 kHz. During HAPPEX, they were used with a low beam current for auxiliary studies such as evaluating background contributions and determining the average momentum transfer of the detected flux. However, these detectors packages could not handle the high rates (~ 500 kHz) present during physics running and were turned off at those times.

The two HAPPEX detectors, one located in the focal plane of each spectrometer, were designed to meet several criteria: radiation hardness, good linearity (nonlinearity of order 1%), and reasonable energy resolution. Radiation hardness drove the selection of materials; alternating sheets of lead and lucite were chosen and arranged as in Figure 4.7. The detectors contained five layers each of lead and lucite. The lead caused the electrons to shower, generating copious electrons and positrons which then emitted Cherenkov radiation as they traversed the lucite. The detector was oriented at 45° to the incoming electrons, so a portion of the Cherenkov cone was emitted parallel to the lucite sheets and transmitted with high efficiency to a single 5-inch photomultiplier tube (PMT) at the end of the detector. The PMT was a Burle 8854. The output current of the PMT was proportional to the flux of electrons incident on the detector. The output current signal was sent to the HAPPEX DAQ where it was integrated, as described in the next section. The detectors were linear to better than 0.3% for beam currents of 10-50 μA [85].

The energy resolution of the detectors was required to be good enough that it would not degrade

the statistical power of the measurement:

$$\sigma = \frac{1}{\sqrt{N_R + N_L}}\sqrt{1 + \left(\frac{\Delta E}{\langle E \rangle}\right)^2}, \qquad (4.4)$$

where σ was the width of the pairwise asymmetry distribution for one detector, $(N_R + N_L)$ was the number of electrons detected in a pair of windows, E was the scattered electron energy, and ΔE was the energy resolution. GEANT simulations indicated that this design would provide a fractional energy resolution of 15% [94], implying an increase in the width over counting statistics of about 2%. A 2% increase was deemed acceptable.

4.10   Data Acquisition

HAPPEX used a custom-built DAQ for physics running and the standard Hall A DAQ for certain auxiliary studies. The standard Hall A DAQ is described elsewhere (see, *e.g.*, [92]). The HAPPEX DAQ hardware is described in detail in Wilson Miller's thesis [84].

As discussed in section 3.3, HAPPEX measured the detected electron flux by integrating the detector signal rather than (as in most nuclear-physics experiments) by counting individual electrons. The basic idea of integration is to feed the output current signal from each detector's PMT into an integrating analog-to-digital converter (ADC). The PMT signal is integrated by allowing it to charge a capacitor. The change in the voltage across the capacitor from the beginning to the end of a helicity window provides a measure of the electron flux during that window. This voltage is then digitized and recorded, and the capacitor is then discharged in preparation for the next window.

The HAPPEX DAQ (shown in schematic form in Figure 4.8) was located in the Hall A Counting House. Signals from the detector PMT's, BCM's, BPM's, and several batteries (used to monitor electronic cross talk) were transported from Hall A up to the Counting House. These signals were processed by custom-built 16-bit integrating analog-to-digital converters (ADC's). The ADC's
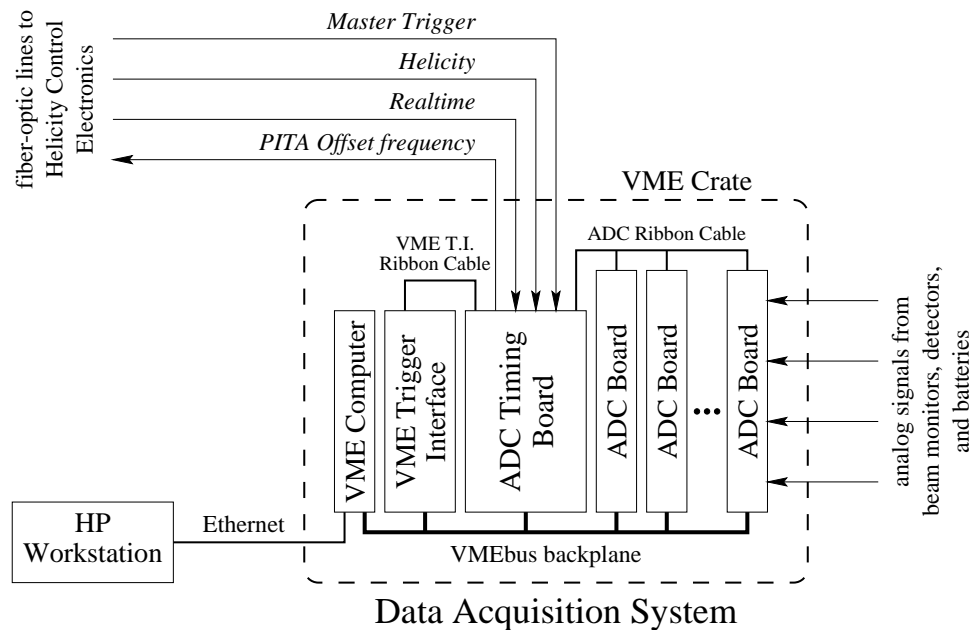
Figure 4.8: Schematic of the HAPPEX Hall A DAQ.

were housed in a VME crate, along with several other boards: the VME Computer, the VME Trigger Interface, and the ADC Timing Board.

The ADC Timing board received the Helicity, Master Trigger, and Realtime signals via fiber optics from the Injector. In addition, the ADC Timing Board also sends one signal back to the Injector over fiber optics. That signal, the "PITA Offset Frequency," is discussed below in section 4.11.1.

The 16-bit ADC boards were the heart of the DAQ. The boards were designed by John Oliver at the Harvard University High Energy Physics Laboratory. Each board had four independent channels. Each channel could be configured to integrate either a voltage or a current signal via minor on-board modifications. The boards were optimized to measure nearly DC signals with high resolution and low nonlinearity. The boards had a pedestal noise of ~ 1.5 bins out of $2^{16} (= 65,536)$, or 30 ppm for a signal height of 50,000 ADC bins. The integral nonlinearity (defined as the maximum deviation from a straight line connecting the endpoints of the ADC transfer function) was below 10 bins, and the differential nonlinearity was much less than 1 bin.

The "integration gate," the period of time during which each signal was integrated, was chosen to be 32.6 ms, slightly shorter than each 33.3-ms helicity window. The integration gate began 400 μs after the receipt of a Master Trigger. The delay at the beginning allowed the Pockels cell retardation and the electron beam polarization time to settle. The integration gate ended approximately 300 μs before the next Master Trigger. This time was used to read data out of the ADC's and prepare for the next window. It was also possible to set the timing so that there were multiple integration gates within each window. This "oversampling" mode allowed us to study the time structure of beam fluctuations and asymmetries within each window and was used for certain special studies.

At an appropriate time after receiving a Master Trigger, the ADC Timing Board sent a signal to the VME Trigger Interface, causing the ADC's to be read out. The VME Computer collected data from the VME Trigger Interface and the ADC's and communicated it to a Hewlett-Packard workstation for storage and analysis.

Prior to the 1999 run, a second nearly identical DAQ was assembled at the Injector. It was used to read out a BCM and two BPM's located at the 5-MeV point in the Injector.

4.11   Suppression of Beam Asymmetries

In this final section, I focus on how we used the above hardware to suppress beam asymmetries for the 1999 run. The primary techniques, described in more detail in the following sections, were to

1. Suppress the intensity asymmetry via an active feedback, the "PITA feedback" that is described below.

2. Suppress position differences at the source by rotating the rotateable half-wave plate to an orientation where position differences appeared to be intrinsically small.

3. Gain additional suppression of position differences by properly tuning the accelerator to take advantage of "adiabatic damping."

4. Suppress the intensity asymmetry of the Hall C beam by use of a second intensity asymmetry feedback system.

5. Gain some additional cancellation of beam asymmetries by using the insertable half-wave plate as a means of slow helicity reversal. The cancellation achieved is discussed in section 7.1.6.

4.11.1 The PITA Effect and PITA Feedback

One of the dominant sources of helicity-correlated beam asymmetries is the Polarization-Induced Transport Asymmetry (PITA) effect [95]. The PITA effect is discussed in detail in section 6.2.4, but it is necessary to describe it briefly here in order to understand how we controlled beam asymmetries for HAPPEX. The Pockels cell that is used to circularly polarize the laser beam acts as a quarter-wave plate. Depending on the sign of the voltage applied to it, it can produce light of either helicity. The Pockels cell is an imperfect quarter-wave plate, however, and we can parameterize the phase shift it induces on the laser beam according to

$$\delta_R = -(\frac{\pi}{2} + \alpha) - \Delta, \qquad \delta_L = +(\frac{\pi}{2} + \alpha) - \Delta, \qquad (4.5)$$

where δ_R (δ_L) is the phase shift induced by the Pockels cell to produce right- (left) helicity light. The imperfections in the phase shift are given by α ("symmetric" offset) and Δ ("antisymmetric" offset), and perfect circular polarization is given by the condition $\alpha = \Delta = 0$. This parameterization is extended to a system involving two Pockels cells and four phase shifts in section 6.2.4. When an imperfectly circularly polarized laser beam illuminates a GaAs crystal that has a QE anisotropy, an intensity asymmetry results that depends on the antisymmetric phase, Δ. To first order, this intensity asymmetry can be expressed as

$$A = -\frac{\epsilon}{T} \cos 2\theta \cdot (\Delta - \Delta^0), \qquad (4.6)$$

where the ratio $\frac{\epsilon}{T}$ is the "analyzing power" of the cathode and is equal to the QE anisotropy, θ is the angle between the Pockels cell's fast axis and the strain axis of the cathode, and Δ^0 is an offset phase shift introduced by residual birefringence in the Pockels cell and the optics downstream of it. The intensity asymmetry is proportional to Δ, and the constant of proportionality $\frac{\epsilon}{T}\cos 2\theta$ is referred to as the "PITA slope," m.

By controlling the phase Δ, we can control the size of the intensity asymmetry. Δ can be adjusted by changing the voltage applied to the Pockels cell according to $V_\Delta = \Delta \cdot \frac{V_{\lambda/2}}{\pi}$, where V_Δ is the change in Pockels cell voltage required to induce a phase shift Δ and $V_{\lambda/2}$ is the voltage required for the Pockels cell to provide a half wave of retardation (~ 5.5 kV).

For HAPPEX, we established a feedback loop between the intensity asymmetry measured by a BCM located near the target and the phase Δ. This feedback loop was called the "PITA Feedback." The algorithm worked as follows. The default Pockels cell voltages for right- and left-helicity (V_R^0 and V_L^0, respectively, with $V_R^0 \approx -V_L^0$) were determined while aligning the Pockels cell. During physics running, the DAQ monitored the intensity asymmetry in real time and, every 2500 window pairs (approximately every three minutes), adjusted the Pockels cell voltages to null the intensity asymmetry measured on the preceding 2500 pairs. We referred to each set of 2500 pairs as a "minirun." The feedback is initialized with the offset voltage set to zero and the voltages for right and left helicity set to their default values:

$$V_\Delta^1 = 0,$$
$$V_R^1 = V_R^0, \qquad (4.7)$$
$$V_L^1 = V_L^0.$$

We apply a correction for the nth minirun according to For minirun n, the Pockels cell voltages

were

$$V_\Delta^n = V_\Delta^{n-1} - \frac{A_I^{n-1}}{m},$$

$$V_R^n = V_R^0 + V_\Delta^n, \tag{4.8}$$

$$V_L^n = V_L^0 + V_\Delta^n.$$

The HAPPEX DAQ in the Hall A Counting House was responsible for calculating the intensity asymmetry and the required correction to the Pockels cell voltages for each minirun. The correction voltage V_Δ^n was encoded as a frequency and transmitted back to the Injector over a fiber-optic line. This signal was referred to as the "PITA Offset Frequency." In the Injector, it was translated back into a voltage and used to apply the offset to the voltages applied to the Pockels cells. This algorithm worked effectively; as discussed in more detail in section 7.1.6, the intensity asymmetry averaged over the entire 1999 run was -1.15 ± 0.09 ppm, an order of magnitude smaller than the physics asymmetry and therefore satisfying the requirements of section 3.9.

4.11.2 The Rotateable Half-Wave Plate

The rotateable half-wave plate gives us control over the orientation of the laser beam's polarization ellipse with respect to the cathode's strain axes. To describe its utility, we can extend equation 4.6 to include effects due to the half-wave plate and the vacuum window at the entrance to the polarized gun. We assume that the half-wave plate is imperfect and induces a retardation of $\pi + \gamma$, where $\gamma \ll 1$. In addition, we assume that the vacuum window possesses a small amount of birefringence $\beta \ll 1$. A more detailed analysis is given in section 6.3.4; here we simply quote the result:

$$A_I = -\frac{\epsilon}{T}[(\Delta - \Delta^0)\cos(2\theta - 4\psi) - \gamma\sin(2\theta - 2\psi) - \beta\sin(2\theta - 2\rho)], \tag{4.9}$$

where ψ and ρ are orientation angles for the half-wave plate and the vacuum window fast axes, respectively, as measured from the horizontal axis. In equation 4.6, the contributions from the

half-wave plate and the vacuum window were included in the term Δ^0. This new expression has three terms:

1. The first term, proportional to Δ, is now modulated by the orientation of the half-wave plate with a 90° period.

2. The second term, proportional to γ, arises from using an imperfect half-wave plate and also depends on the half-wave plate's orientation but with a 180° period.

3. The third term, proportional to β, arises from the vacuum window and is independent of the half-wave plate's orientation because the vacuum window is downstream of the half-wave plate. This term generates a constant offset to the intensity asymmetry.

Figure 4.9 shows a measurement of intensity asymmetry as a function of half-wave plate orientation angle from the 1999 run. The function fit to the data allowed us to extract the relative contributions of the half-wave plate error, the vacuum window, and the Pockels cell. The three terms contributed at roughly the same magnitude, though the offset was large enough that the curve did not pass through zero intensity asymmetry. In addition, we found, as discussed more below, that the PITA slope was generally maximized at the extrema of this curve. These facts motivated us to choose to operate at an extremum (in this case, at 1425°) in order to minimize the voltage offset required to null the intensity asymmetry.

The strained cathode's large analyzing power greatly enhanced a time-history effect associated with the Pockels cell. When the high voltage applied to the Pockels cell flipped sign (a change of ~ 5 kV), the retardation provided by the Pockels cell appeared to have a time constant associated with it that was something on the order of 1 ms. This time constant caused the intensity asymmetry to have a small time dependence within each window pair and to depend on the helicity of the window immediately preceding each pair, as explained below.

If we consider a pair of helicity windows and the helicity of the window immediately preceding them, we find that there are four possible combinations. Those four combinations are R RL,
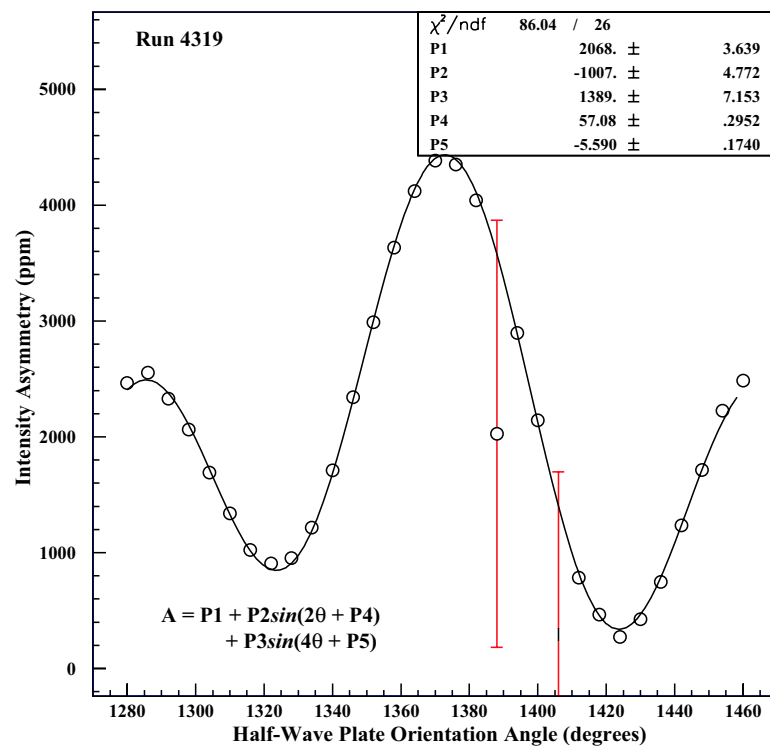
Figure 4.9: Intensity asymmetry as a function of rotateable half-wave plate orientation.

L RL, R LR, and L LR. Consider the first two combinations. The pair ordered RL is in one case preceded by a right-helicity window and in the other by a left-helicity window. Since the pair starts with a right-helicity window, the L RL combination begins with the Pockels cell high voltage making a transition, whereas the R RL combination does not. Thus, the Pockels cell retardation early in the first window of the pair differs slightly between the R RL and L RL combinations, and if one selects pairs based on the helicity ordering, one finds that they measure systematically different intensity asymmetries. The same goes for the R LR and L LR combinations. This effect is dramatically illustrated in Figure 4.10, a histogram of intensity asymmetry for a run with a fairly large PITA slope. The histogram, normally gaussian, is split into three peaks, with the central peak twice as large as the side peaks and the side peaks equally separated from the central peak. The central peak corresponds to asymmetries from pairs for which both members of the pair are preceded by a high-voltage transition: the L RL and R LR combinations. The side peaks are due to the combinations R RL and L LR. The first member of each pair is not preceded by
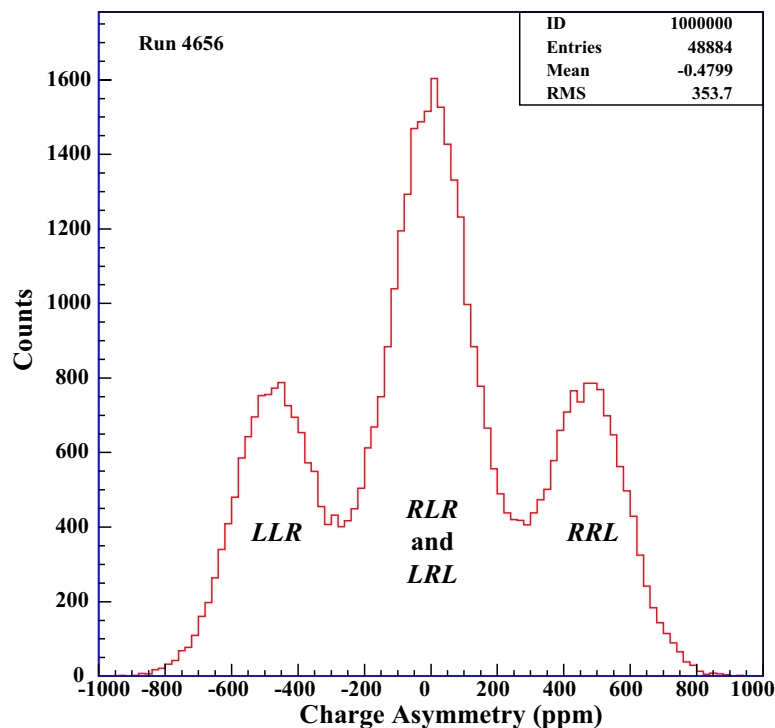
Figure 4.10: A histogram of the intensity asymmetry of the electron beam. The distribution acquired side lobes due to a time-history effect that arose from the polarization sequence.

a high-voltage transition, and so the average intensity asymmetries given by these combinations are offset by equal amounts in opposite directions. We found that the amplitude of the separation between the two side peaks is proportional to the PITA slope, and is thus a very useful diagnostic. Figure 4.11 shows this "splitting" as a function of rotateable half-wave plate orientation for the same data as Figure 4.9. The curve has a nearly pure 4ψ dependence, lending support to the idea that the effect arises from the Pockels cell. As we saw in equation 4.9, the first term, corresponding to the Pockels cell, possesses a 4ψ dependence.

It is natural to ask whether such a nongaussian distribution in the intensity asymmetry can induce a systematic error in the measurement of the normalized detector asymmetry (equation 3.2). Two facts suggest that the answer is no:

1. The side lobes are symmetric about the central peak.

2. While this splitting distorts the gaussian distribution of intensity asymmetries, it does not
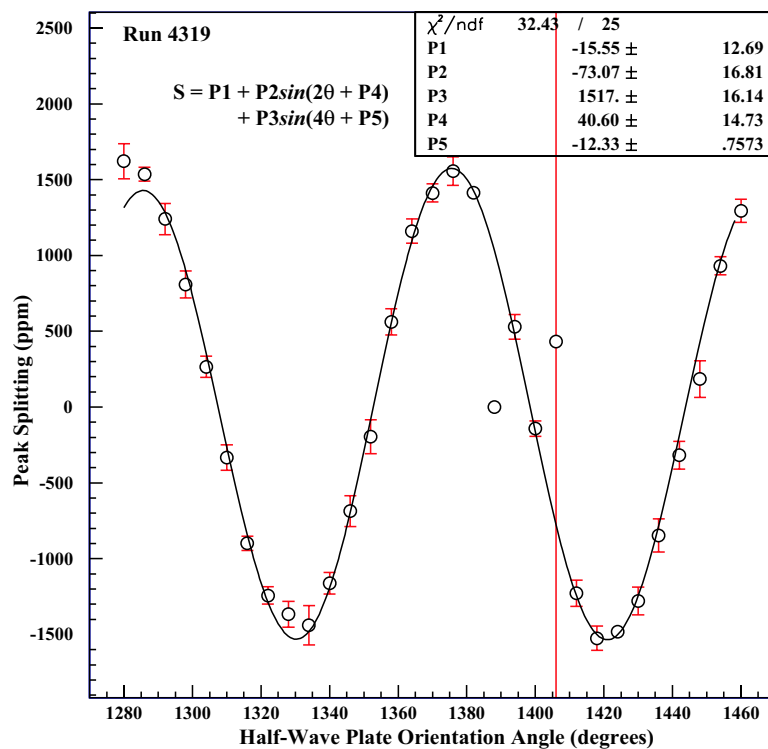
Figure 4.11: The splitting of the intensity asymmetry as a function of rotateable half-wave plate orientation.

distort the gaussian distribution of normalized detector asymmetries because the separation of the peaks is much less than the width of the normalized detector asymmetry distribution.

Figure 4.12 shows the results of a separate study conducted prior to the start of the 1999 run in which the position differences were also measured using BPM's located at the 5-MeV point in the Injector. We observed a fairly strong correlation between the intensity asymmetry and the position differences. It was not clear what the underlying cause of this correlation was, but it was certainly clear that by minimizing the intensity asymmetry we simultaneously suppressed position differences. For this reason, during the 1999 run our strategy was to measure the intensity asymmetry as a function of half-wave plate orientation using a Hall A BCM and to choose an orientation angle which minimized the intensity asymmetry; by implication, this should have also minimized the position differences. It would have been preferable to measure the position difference in the Injector and choose a half-wave plate orientation that minimized them directly, but such a
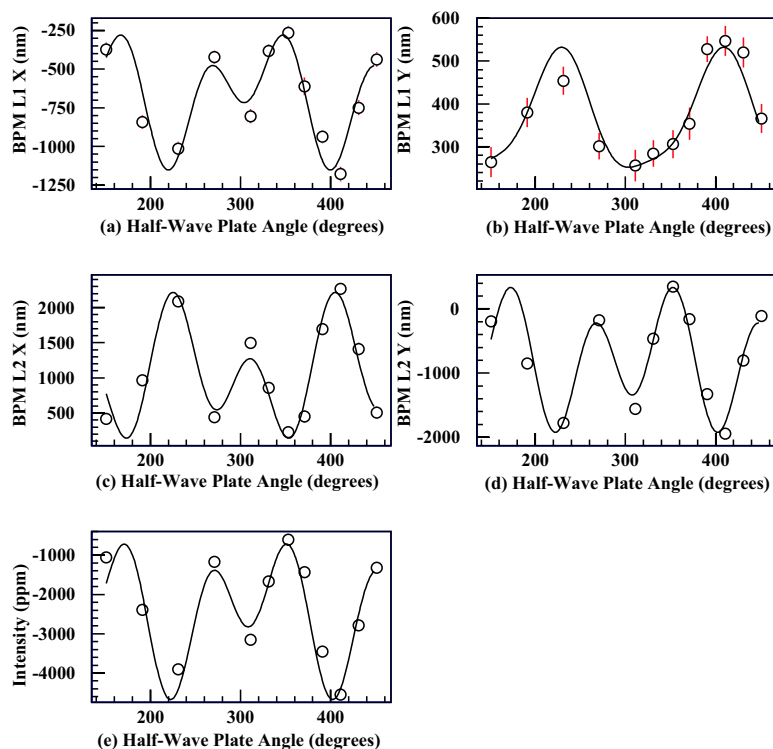
Figure 4.12: Dependence of position differences measured by two BPM's at the 5-MeV point in the Injector (a-d) on the orientation of the rotateable half-wave plate. The position differences show a strong correlation with the intensity asymmetry (e).

study would have required turning off beam to Hall C for several hours to conduct the study, and that level of interference with an experiment running in another Hall was unacceptable.

4.11.3   5-MeV Position Differences

Helicity-correlated position differences tended to be much larger in the Injector than in Hall A for reasons discussed in the next section, and so we found it to be very useful to measure them in the Injector. A second DAQ, the Injector DAQ, recorded beam charge and position information from a BCM and two BPM's located at the 5-MeV point in the Injector during the 1999 run. Unfortunately, these monitors recorded beam properties that were an average (weighted by beam current) over all of the beams were running at a given time. During most of the HAPPEX run, Hall C ran at a beam current comparable to Hall A's and the Injector DAQ data could not be used to measure the position differences on the Hall A beam (Hall B used a beam current

~ 3 orders of magnitude lower than Hall A, and the effect of their beam on the others could be neglected.). However, there were times when the Hall C beam was off and we were able to measure the position differences on the Hall A beam at 5 MeV. Figure 4.13 shows those measurements. The vertical bands separate data points by slug. The position differences were typically several hundred nanometers in the Injector.

(a) X Position Differences   (b) Y Position Differences
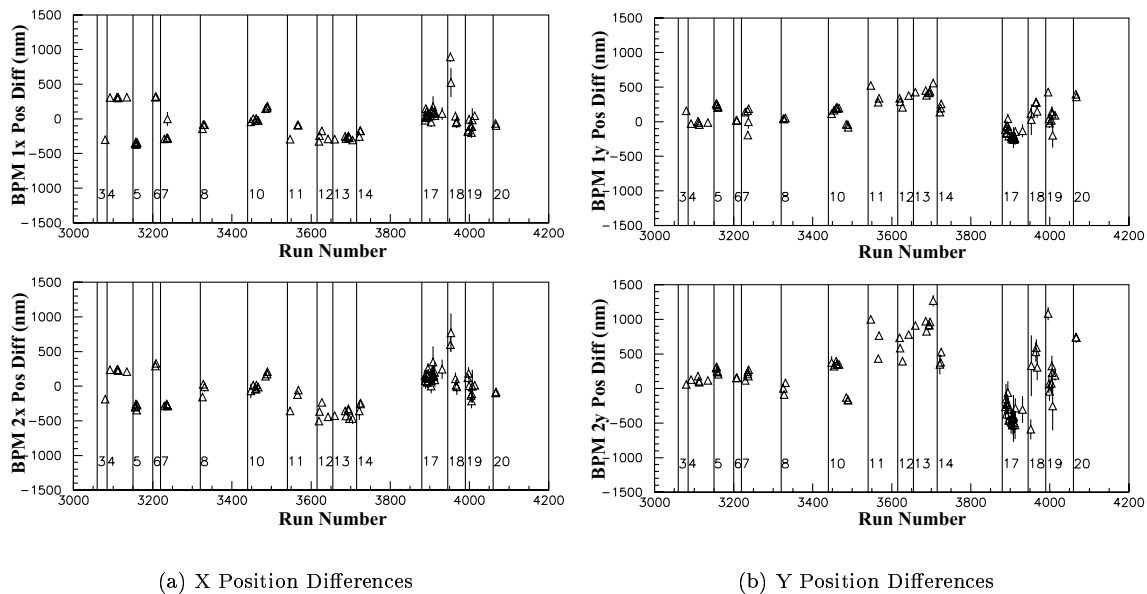
Figure 4.13: Position differences at the 5-MeV point in the Injector. Results shown are only for runs during which the Hall C beam was absent. The vertical bands separate results from the 20 slugs.

4.11.4   Adiabatic Damping

Position differences scale with the size of the electron beam. One way to suppress position differences, therefore, is to reduce the size of the beam. The accelerator tends to reduce the beam size naturally via "adiabatic damping." Accelerating the beam reduces the transverse phase space available to the beam, and hence tends to reduce both its size and divergence angle. The phase space is reduced by the ratio of the beam energies, and, assuming this reduction is split equally between position and angle, for HAPPEX one might expect position differences to be reduced by a factor of $\sqrt{(3.3 \text{ GeV})/(5 \text{ MeV})} \sim 25$ between the 5-MeV region and the target. Achieving this

reduction also depends on properly matching the beam emittance between various regions of the machine; a mismatch in the magnetic focusing lattice can cause the beam size to increase.

4.11.5 Suppressing the Hall C Intensity Asymmetry

During most of the 1999 run, experiments were running in Hall C that required a beam current comparable to Hall A's. While the PITA feedback suppressed the intensity asymmetry in Hall A, it was quite possible for a large intensity asymmetry to develop on the Hall C beam. Large asymmetries in the properties of the Hall C beam were capable of inducing asymmetries in properties of the Hall A beam. Prior to the start of the 1999 run, we studied the cross talk between the beams by running with 50 μA of beam to Hall A and 10 μA of beam to Hall C. We took a series of short (15 minute) runs in which we either introduced a 3% intensity asymmetry onto the Hall C beam or kept the Hall C intensity asymmetry below 0.3% intensity asymmetry. Figure 4.14 shows the results of these studies, where the black data points are from runs with a Hall C intensity asymmetry < 0.3% and the red data points are from runs with a 3% intensity asymmetry. We found a clear correlation between the Hall C intensity asymetry and both the Y position differences and energy differences (measured by BPM x12). We also saw 250-300 ppm of intensity asymmetry induced in the Hall A beam when the Hall C beam had a large asymmetry. The energy difference was likely due to beam loading. The intensity asymmetry was believed to be due to saturation effects in the cathode: the electrons most readily available for photoemission were more strongly depleted by one helicity of the Hall C beam than the other and the cathode did not have time to recover before electrons for Hall A were emitted. It was not clear what mechanism produced the Y position asymmetry.

To control the Hall C intensity asymmetry (and to induce it for these tests) we had the ability to introduce a helicity-correlated offset in the current driving the Hall C seed laser. This ability allowed us to modulate the intensity of Hall C's laser beam and suppress the intensity asymmetry on Hall C's electron beam. We found that by manually adjusting the offset once an hour to null
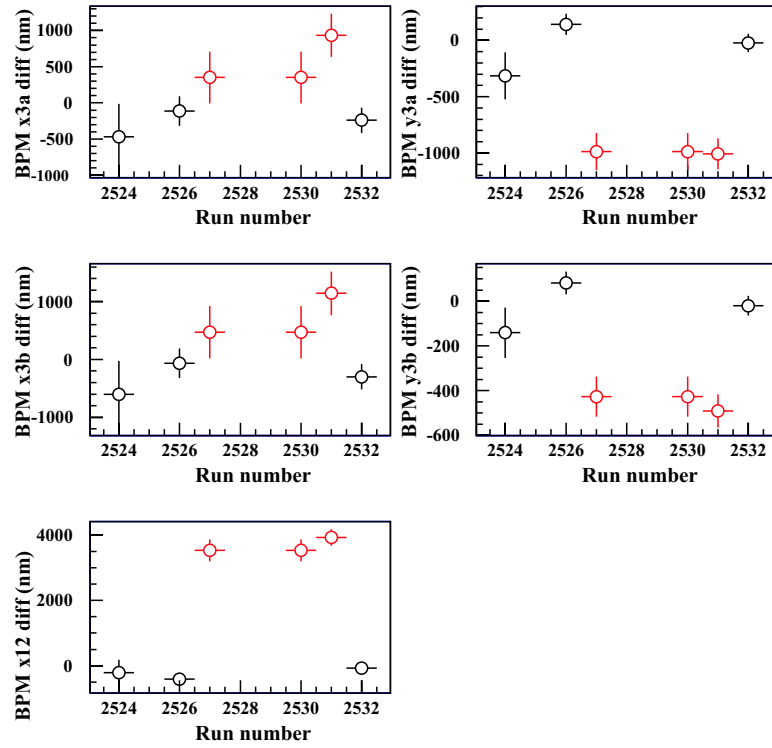
Figure 4.14: Demonstration of beam loading effects on the Hall A beam caused by a large intensity asymmetry on Hall C's electron beam. Black points: Hall C $A_I < 0.3\%$. Red points: Hall C $A_I \approx 3.0\%$.

the Hall C intensity asymmetry, we were able to keep the asymmetry around the 10-ppm level, which was small enough to make its effects on the Hall A beam negligible.

4.11.6   Measurement of Electronic Crosstalk

During the run, we tracked asymmetries in a number of quantities which gave us confidence that electronic cross talk produced negligible systematic errors in our measurements. These quantities included two batteries in each detector hut and batteries located near the BPM electronics in the Hall. The cabling for these batteries ran parallel to the signal cables for the detectors and BPM's. In addition, one spare ADC channel in the DAQ was used to measure cross talk solely within the DAQ. Table 4.1 summarizes the results of these measurements, all of which we found to be consistent with zero at a level much less than the statistical error of the detector asymmetry. We concluded that false asymmetries due to electronic cross talk were negligible.

Table 4.1: Summary of the asymmetries measured on various signals used to monitor the presence of false asymmetries due to electronic cross talk.

Asymmetry Measurements (ppm)	
Det Batt 1	-0.008 ± 0.008
Det Batt 2	-0.008 ± 0.008
Det Batt 3	-0.007 ± 0.013
Det Batt 4	-0.002 ± 0.013
BPM Batt 1	-0.008 ± 0.004
BPM Batt 2	0.010 ± 0.009
BPM Batt 3	0.003 ± 0.004
Difference Measurements (millichannels)	
Spare Chan 1	0.037 ± 0.487

Chapter 5

E-158 Experimental Design

E-158 is running at the Stanford Linear Accelerator Center (SLAC) in End Station A (ESA). E-158 had engineering runs in 2000 and 2001. Its first two physics runs were conducted in the spring and fall of 2002, and a final physics run is planned for the fall of 2003. The experimental configuration for E-158's 2002 physics runs is described in this chapter. The optics system for the polarized electron source and the control of beam asymmetries, which were central pieces of my thesis work, are discussed separately in Chapter 6.

5.1 Overview

E-158's experimental configuration was very similar to HAPPEX in its basic design: polarized electrons struck a liquid hydrogen target, and a magnetic spectrometer and collimator system selected the scattered electrons of interest. These electrons were detected by a Cherenkov calorimeter, and the resulting PMT signal was integrated. Additional detectors were used to determine the average Q^2 and the background flux and asymmetries. However, there were several significant differences between the two experiments:

  1. The SLAC beam, rather than being cw, was pulsed at 120 Hz. Each pulse was ~ 270 ns

long. Pulsed beams tend to be less stable, and indeed pulse-to-pulse fluctuations in beam properties were much larger for the SLAC beam than at JLab (for example, position jitter was typically $\sim 50\ \mu$m at SLAC and $\sim 10\ \mu$m at JLab). However, one advantage provided by a pulsed beam was the ability to transmit all beam helicity information out of time with the beam pulse. In addition, the time-history effects associated with helicity flipping (described in section 4.11.2) were not an issue with a pulsed beam.

2. The scattering rate, which we estimate below, was 2-$4 \cdot 10^7$ electrons per pulse, giving an asymmetry distribution width of ~ 150 ppm from counting statistics alone (compared with ~ 5500 ppm for HAPPEX). Making full use of such high statistics required that we maintain noise contributions from other sources (beam monitor resolution, target density fluctuations, detector resolution, etc.) at levels below 100 ppm.

3. The scattering angle in the lab frame was 0.27-0.41°, making it a challenge to design a spectrometer capable of separating the signal from the background while simultaneously suppressing soft photon backgrounds.

4. The raw asymmetry was expected to be ~ 0.1 ppm, two orders of magnitude smaller than the HAPPEX raw asymmetry. Thus, control of individual systematic errors at the part-per-billion (ppb) level was required.

5.2 Estimate of Rate

The scattering cross section can be estimated by integrating equation 2.33 over the scattering-angle acceptance of the spectrometer ($65.9° < \theta_{CM} < 89.4°$ and assuming 2π acceptance in azimuth) and assuming a beam energy of 48.3 GeV. We find $\sigma \approx 11.2\ \mu$barn.* The number of detected

---

*The corresponding figures for a 45.0-GeV beam are $67.7° < \theta_{CM} < 91.4°$ and $\sigma \approx 11.7\ \mu$barn.

scattered electrons per pulse N_s can then be estimated as

$$N_s = \sigma \cdot I \cdot \rho \cdot L \cdot f_S, \tag{5.1}$$

where I is the beam current, ρ is the target density, L is the target length, and f_S is a correction factor to account for losses due to collimators that block synchrotron radiation in the horizontal plane.[†] Using the values

$$\sigma = 11.2 \ \mu\text{barn}, \tag{5.2}$$

$$I = 3.5 \cdot 10^{11} \ \text{electrons/pulse},$$

$$\rho = 0.072 \ \text{g/cm}^3 = 4.3 \cdot 10^{22} \ \text{electrons/cm}^3,$$

$$L = 150 \ \text{cm}$$

$$f_S = 0.89,$$

we find that the rate into the detector should be 22.5 million electrons per pulse, or 2.7 GHz at 120 Hz. Thus, we expect the pairwise asymmetry distribution to have a width of $\sim 1/\sqrt{45 \cdot 10^6} = 150$ ppm. During the 2002 physics runs, we typically observed widths of $\sim$ 190-200 ppm, indicating a residual noise of $\sim$ 120 ppm from other sources. This noise arose from several sources, including finite toroid and BPM resolution, detector pedestal fluctuations, and detector amplifier noise.

5.3   Polarized Electron Source

The SLAC polarized electron source was based on photoemission from strained GaAs or GaAsP cathodes and was described in detail in [96]. It was very similar to the JLab polarized electron source (section 4.3) in its basic operating principles. A flashlamp-pumped Ti:Sapphire laser (the

---

[†]The large solid-angle acceptance of the spectrometer, $\sim$ 2.5 sr in the center-of-momentum frame, means that losses due to Bremsstrahlung are small and can be neglected for this estimate.

"Flash:Ti") induced photoemission of the $\sim$ 270-ns electron pulses used for E-158. A second laser system, an Nd:YLF-pumped Ti:Sapphire laser, was used to generate short (2 ns) pulses for use in the PEP-II rings by the BaBar experiment. Both the Flash:Ti laser system and the associated optics system saw significant upgrades in preparation for E-158; this work is described in the NIM paper included as Chapter 6 (optics system) and Appendix A (laser system) of this thesis.

5.4 Accelerator

SLAC's accelerator is made up of roughly 300 RF cavities distributed over a two-mile-long accelerating structure. It is capable of a peak repetition rate of 120 pulses per second, and its timing system provides sufficient flexibility to divide these 120 pulses between multiple beams. An overview of SLAC is shown in Figure 5.1. The beam can be provided by either a polarized electron gun or a thermionic (unpolarized) gun. The Injector[‡] possesses diagnostics that were useful for commissioning E-158's beam and monitoring beam asymmetries at the electron source. The Injector also contained elements that prepared each beam pulse for acceleration by appropriately bunching it to match the accelerator's 2856-MHz RF power structure.

The Accelerator Structure SETup (ASSET) region, at which the beam energy is 1 GeV, is a several-meter-long region of the accelerator in which test setups can be placed. It is often used to test advanced RF accelerator-cavity designs. E-158 used ASSET as a low-energy diagnostic point for beam properties and beam asymmetries, as described more in the next section.

At the end of the accelerator, the Beam Switch Yard (BSY) kicked individual pulses into one of several beam lines: positron and electron beam lines for either the SLD interaction point or Babar and electron beam lines for End Station A (ESA) and End Station B (ESB). In addition, the "Final Focus Test Beam" was used as a test bed for magnetic optics for the Next Linear Collider and for experiments testing novel means of electron acceleration. E-158 occupied ESA. Following the BSY, a series of 12 dipole magnets bent the beam by 24° in order to bring it into ESA. Between the

---

[‡]SLAC's injector region was generally referred to as CID, "Collider Injector Development."
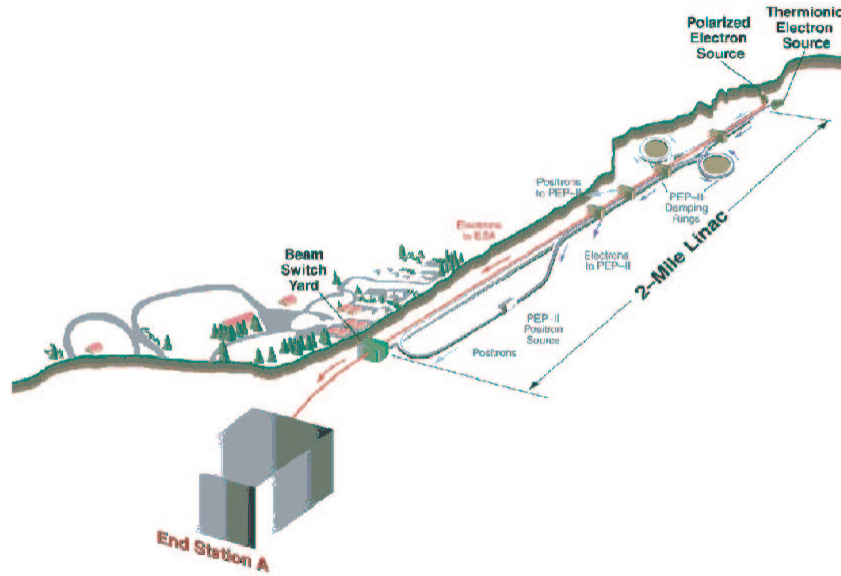
Figure 5.1: Overview of the Stanford Linear Accelerator Center.

6th and 7th dipoles were a set of momentum-defining slits; for E-158, they were set to collimate electrons to have an energy within 1% of the nominal beam energy. E-158 used beams of 45.0 GeV and 48.3 GeV, the highest two energies available at SLAC at which the electron polarization was longitudinal in ESA.

5.5   Beam Monitoring and Dithering

E-158 made use of beam monitors located in the Injector, at ASSET, and in the A-Line. In addition, several A-Line magnets and the phase of a klystron near the end of the accelerator were used to implement a beam modulation system (beam "dithering" at SLAC) similar to what was used for HAPPEX.

5.5.1   Injector Diagnostics

Several beam diagnostics were available at the Injector to aid in studying the beam's properties and commissioning control of beam asymmetries. They included three stripline beam position monitors (BPM's) immediately following the cathode and two beam charge monitors (BCM's) located after the first accelerating section. These diagnostics were under the control of the SLC Control Program (SCP), the system used to control the accelerator. E-158 used them to commission the optics hardware that controlled the helicity-correlated feedbacks on intensity and position asymmetries (described in sections 6.2.4 and 6.4.4). We also used them to attempt to diagnose sources of beam asymmetries and to optimize the optics setup to minimize beam asymmetries.

The Injector diagnostics were also used by the accelerator in feedback loops to control the absolute (not helicity-correlated) electron beam intensity and position at the cathode. The feedback loops corrected for slow drifts in the Flash:Ti cavity's output power and in the steering of the laser beam through the optics system. The intensity of the electron beam at the Injector BCM's was held constant by controlling the amplitude of laser light transmitted by the SLICE Pockels cell (see Appendix A). The position of the electron beam at a BPM located ~ 1 foot downstream of the cathode was held constant by the Cathode Diagnostics Bench telescope (section 6.2.3). One lens of this telescope was mounted on an x-y-z translation stage. The position of the laser beam on the cathode (and hence of the electron beam at the nearby BPM) was controlled by translating this lens in x or y.

5.5.2   E-158 Beam Diagnostics

E-158 had high-resolution beam diagnostics at relatively low energy (1 GeV at ASSET) and high energy ($\sim$ 48 GeV at the A-Line), as indicated in Figure 5.2. The ASSET beam diagnostics included two BCM's and three BPM's. The BPM's were spaced at 1-m intervals, with the BCM's between them. These monitors were used to control the helicity-correlated intensity and position asymmetry feedbacks during production running.
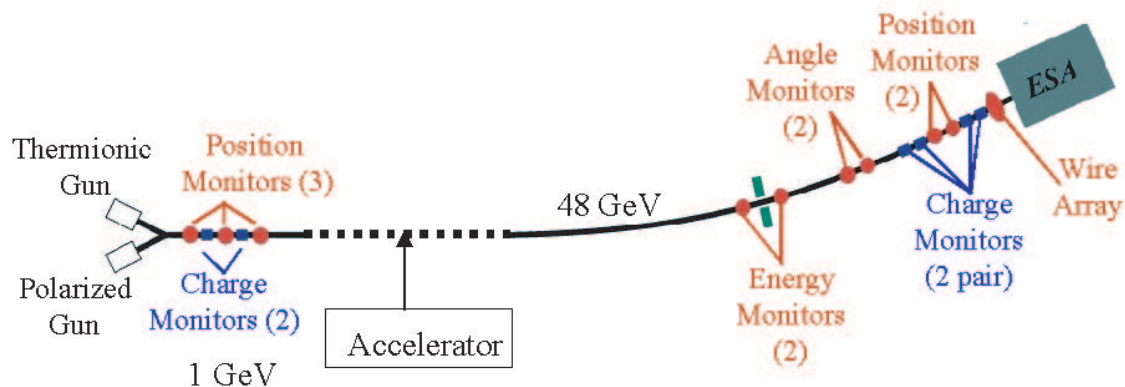
Figure 5.2: Beam diagnostics for E-158.

The SLAC BCM's were toroids made of copper wire wound around an iron core. When the electron beam passed through a toroid, it induced a pulse in the windings. The toroid acted as the inductive element of an RLC circuit that caused the induced pulse to ring. This ringing signal was amplified and then transmitted $\sim$ 100 feet from the beam line to the readout electronics. The signal was then rectified by an absolute value circuit and fed into a custom 16-bit ADC (described below in section 5.7). The toroids had a resolution of 60 ppm, which, when added in quadrature with counting statistics, increased the detector asymmetry distribution width by $\sim 8\%$.

The SLAC BPM's were resonant cavity monitors tuned to the accelerator's frequency of 2856 MHz. Each BPM had three cavities. Each cavity was tuned to resonate in a particular mode (TEM00, TEM10, or TEM01). When an electron pulse passed through a cavity, it excited the resonant mode with an amplitude proportional to the beam property to which that mode was sensitive. A TEM00 cavity was sensitive to the total beam current, a TEM10 cavity was sensitive to the beam's horizontal displacement from center, and a TEM01 cavity was sensitive to the beam's vertical displacement from center. An antenna inside the cavity picked up the induced signal, and the signal was transmitted $\sim$ 100 feet from the beam line to the processing electronics. The processing electronics mixed the signal with a reference 2856-MHz oscillator locked to the accelerator's RF. The mixer outputs could be considered to be the "real" and "imaginary" parts of the BPM signal. During production running, the mixer's phase was offset for each BPM to

maximize the real part of the signal and minimize the imaginary part. The real and imaginary parts were then fed into 16-bit ADC's. The BPM resolution was $\sim 1 - 3$ μm per pulse pair.

The A-Line was instrumented with the beam diagnostics that were used to correct the detector rate for fluctuations in beam properties and for beam asymmetries. These diagnostics included

1. Two pairs of toroids located a few meters upstream of the target. The toroids measured the beam's total charge and helicity-correlated intensity asymmetry and were used to normalize the detected scattered flux in calculating the asymmetry according to equation 3.2.

2. Two pairs of BPM's. One pair was located ~ 2 m upstream of the target and measured beam position at the target. The second pair was ~ 40 m upstream of the target and provided information on the beam's angle at the target. These BPM's were used to remove from the detector signal correlations with beam position and angle.

3. A third pair of BPM's located at the middle of the A-Line bend, one before and one after the momentum-defining slits. The beam position in the bend was very sensitive to variations in the beam energy from its nominal setpoint, so these two BPM's were monitors of the beam energy. These BPM's were used to remove from the detector signal correlations with beam energy.

4. A synchrotron light monitor (SLM), also located at the A-Line bend, measured the intensity of the synchrotron radiation emitted by the beam. As the intensity of the synchrotron radiation was directly proportional to the beam energy, the SLM provided another measure of the beam energy.

5. A wire array located ~ 1 m upstream of the target. The wire array consisted of two planes of 48 wires (one running horizontally and the other vertically). The wire array provided a measure of the electron beam's intensity profile in two dimensions and was used to measure the beam spot size and other higher-order moments.

Note that every beam diagnostic (except the wire array) was part of a pair or triplet. This redundancy was very important. It permitted us to compare measurements made by neighboring diagnostics that see essentially the same beam, allowing measurements of diagnostic resolution and rapid identification of hardware problems. In addition, if a single diagnostic broke during the run, its partner could be used alone until a convenient opportunity arose to make repairs.

5.5.3 Beam Modulation Hardware

"Dithering" coils at the beginning of the A-Line were used to modulate the beam's position and angle on target. There were a total of eight coils: four each for modulation in the horizontal and vertical planes. The coils were set at varying distances from the BPM's and allowed us to determine empirically which set of coils best spanned the space of position and angle fluctuations. Modulation of the phase of a klystron near the end of the accelerator provided modulation of the beam's energy.

5.6 End Station A

Figure 5.3 shows a schematic of the End Station A layout. ESA housed a polarimeter for measuring the electron beam polarization (not shown), the liquid hydrogen target, the spectrometer, the Møller detector, and a number of auxiliary detectors needed for the experiment. Each of these components are discussed in the following subsections.

5.6.1 Electron Beam Polarimetry

The electron beam polarization was measured periodically throughout the run using a Møller polarimeter. The Møller polarimeter made use of magnetized iron foils of $20 - 100$ μm thickness that could be inserted into the beam just upstream of the target. A set of Helmholtz coils polarized the foils. They had a maximum field of 92 gauss, significantly less than the ~ 200 gauss needed to saturate the foils. The LH_2 target was removed for these measurements. The E-158 spectrometer
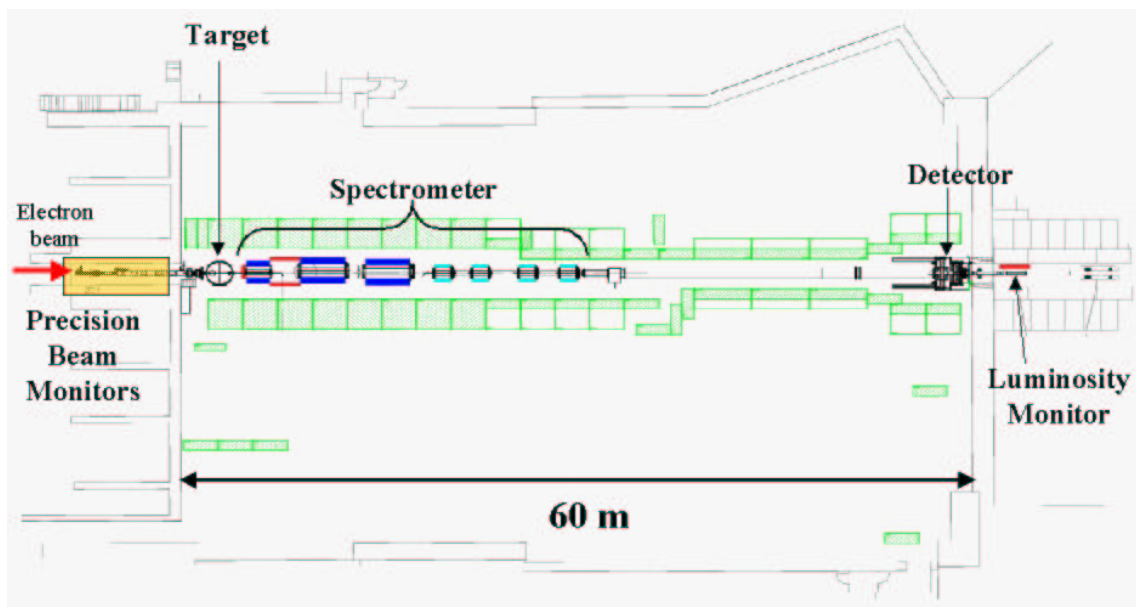
Figure 5.3: Overview of the experimental setup in End Station A.

focused scattered electrons onto an auxiliary detector (discussed below) that could be inserted remotely just in front of the Møller detector. The polarization was measured both before and after toggling the state of the insertable half-wave plate at the polarized electron source (used for slow helicity reversal). The polarimetry measurement was projected to have a relative uncertainty of 4%. The uncertainty was dominated by systematic errors, including the background subtraction (e-p radiative tail, $\sim 10\%$ of the detected rate), the Levchuk effect (a smearing of the Møller-scattering peak due to transverse momentum of the inner-shell atomic electrons [97]), and uncertainty in the iron foil's magnetization.

5.6.2 Liquid Hydrogen Target

E-158's target was a 1.5 m-long liquid hydrogen target built by Caltech [98]. Liquid hydrogen was chosen for its high ratio of electrons to nucleons. This target contained the largest volume of liquid hydrogen ever used for a fixed-target experiment. Figure 5.4 is a schematic of the target design. The liquid hydrogen flowed in a loop consisting of the fan, the target cell, a heater, and a heat exchanger. The heat exchanger contained a copper coil through which helium (at 4 K) flows. The
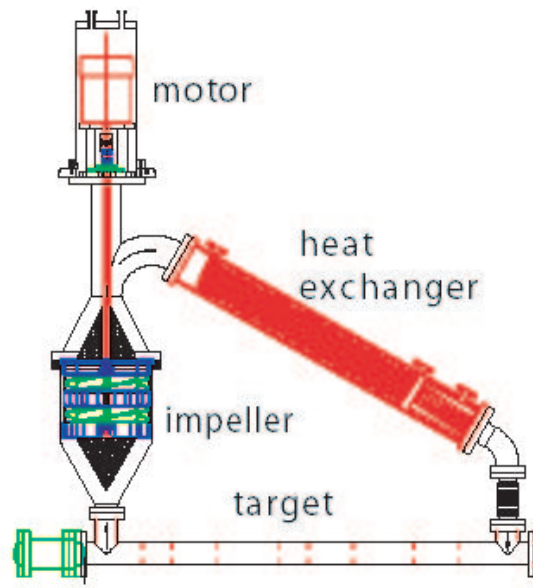
Figure 5.4: A schematic of the liquid hydrogen target loop. The liquid hydrogen moved left to right through the target cell.

heat exchanger was designed to remove up to 1000 W of heat from the target. The heater was

used to maintain the heat load on the target at a constant level when the beam current changed.

Table 5.1 summarizes the target's operating parameters.

Table 5.1: Liquid hydrogen target parameters.

Max. Heat Load:	
Beam	500 W
Heat Leaks	200 W
Pumping	100 W
Length	1.5 m
Thickness	0.17 rad. len.
Volume of LH_2	55 L
Temperature	18 K
Flow Rate	10 m/s
Reynolds Number	10^6
Density Fluctuations	$\leq$ 100 ppm/pulse

The target absorbed 500 W of power from the beam and yet it was required to have density

fluctuations below the 10^{-4} level so as not to significantly degrade the statistical power of the

measurement. The key design feature for suppressing density fluctuations was a series of eight
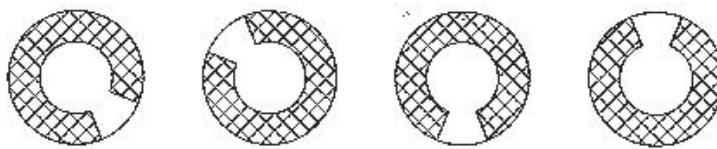
Figure 5.5: Examples of the wire mesh disks spaced along the length of the liquid hydrogen target.

wire-mesh disks spaced along the target cell's length in order to introduce a transverse velocity component and generate turbulent flow at a size scale comparable to the beam diameter. Four of the wire-mesh disks are pictured in Figure 5.5. Density fluctuations due to the induced turbulence were conservatively estimated to be below the 10^{-5} level [99]. Density fluctuations due to the electron beam were studied by looking at the residual correlation between the Møller detector and luminosity monitor rates after removing all correlations with beam properties. An upper limit on density fluctuations during normal physics-running conditions (120 Hz repetition rate, $6 \cdot 10^{11}$ electrons/pulse at 45 GeV, and 1 mm *rms* beam radius) [98] of 65 ppm was set.

An aluminum scattering chamber held at vacuum (to prevent warming due to conduction) housed the target loop. The target loop was mounted so that it could be lifted out of the beam path by remote control. The scattering chamber also contained a table holding several carbon targets that were used for spectrometer and detector studies. When the liquid hydrogen target was lifted clear of the beam, the table could slide horizontally to bring any one of the carbon targets into position. Interlocks ensured that only one of the targets–either the liquid hydrogen or one of the carbon targets–could be in the beam at one time.

A Labview-based DAQ monitored and controlled properties of the target. The DAQ displayed a number of temperature and pressure measurements taken at several points around the loop and cooling lines and controlled the power setting of the heater in order to keep the target temperature stable at the 0.1-K level.
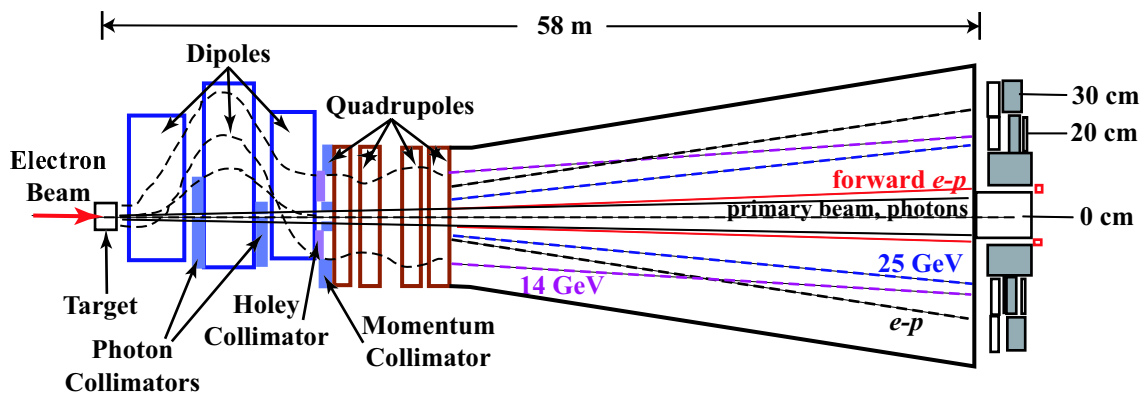
Figure 5.6: A top-view schematic of the layout of the E-158 spectrometer.

5.6.3   Spectrometer and Collimators

E-158 used a spectrometer that was designed specifically for this experiment. It was optimized for the detection of very forward-angle (0.27°-0.41°) Møller scattering with suppression of photon and e-p elastic and inelastic backgrounds. A schematic of the spectrometer is shown in Figure 5.6. The spectrometer ran the entire length of ESA and included

1. No iron that might be struck by either the scattered or the primary beam. Electrons scattering off polarized iron within the spectrometer would do so with a very large electromagnetic asymmetry.

2. A dipole chicane for suppression of soft (low-momentum) backgrounds. This chicane, which used three dipole magnets (called D1, D2, and D3), redirected the primary electron beam and allowed collimation of the high-power photon beam generated by the target along the beam axis. The chicane also eliminated low-energy electrons and positrons. The chicane was designed to avoid collimating the Møller flux and was tuned to preserve the azimuthal symmetry of the scattered flux. The azimuthal symmetry was imperfect leaving the chicane, but was corrected by the last quadrupole magnet, discussed below. The chicane generated a swath of synchrotron radiation in the horizontal plane that needed to be collimated.

3. Photon collimators that blocked line of sight between the target and the Møller detector
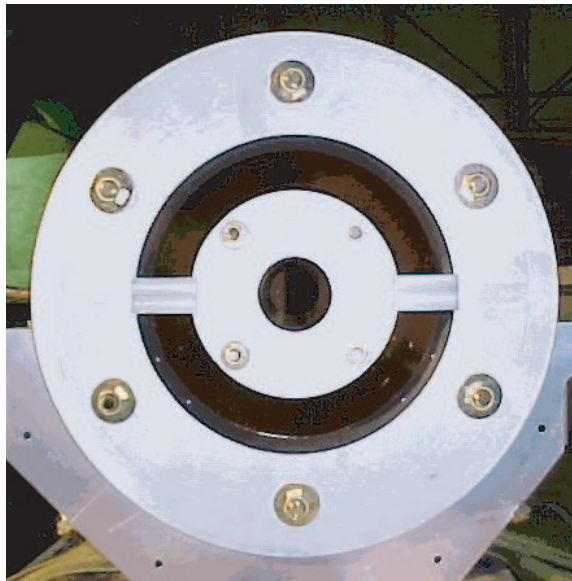
Figure 5.7: Photograph of the momentum collimator. The momentum collimator passes electrons are radii between 7 and 12.5 cm from the beam axis.

and the luminosity monitor. There were two photon collimators, each a 40-radiation-length tungsten cylinder centered on the beam axis. One was located between D1 and D2 and the other at the downstream end of D2.

4. The momentum collimator, QC1B. This collimator defined the momentum acceptance of the spectrometer. It was made of two concentric cylinders, connected by spokes in the horizontal plane as shown in Figure 5.7. QC1B was 40 radiation lengths thick, split roughly equally between copper (front half) and tungsten (back half). It passed Møller electrons with momenta in the range $13 - 25$ GeV and $e\text{-}p$ electrons with momenta of ~ 40 GeV. Figure 5.8 shows a simulated profile of the Møller and $e\text{-}p$ fluxes as a function of distance from the beam axis. Quadrupole magnets downstream of QC1B then separated the Møller and $e\text{-}p$ fluxes.

5. Synchrotron collimators to block the broad swath of synchrotron radiation in the horizontal plane. If the electron beam had a transverse polarization component, it could couple to misalignment of the dipole magnets and induce a helicity-correlated asymmetry in the intensity of the synchrotron radiation. The synchrotron collimators were designed to suppress the

synchrotron radiation background at the detector by a factor of 100. The spokes supporting the inner ring of QC1B blocked much of the synchrotron radiation, but some light passed through QC1B's central hole. Additional spokes both following the last quadrupole magnet and mounted to the front face of the detector blocked the remaining radiation. These downstream spokes were located in the shadow of QC1B so that it remained the momentum-defining collimator. Eleven percent of the Møller flux was lost due to the synchrotron collimators.

6. The "Holey" collimator, QC1A, a single ring that was remotely insertable and filled the gap between the inner and outer rings of the momentum collimator. QC1A was used to study the *e-p* inelastic flux and measure the electron beam polarization. To study the *e-p* inelastic flux, it had four holes (1 cm^2) located 90° apart and at different radii. Each hole allowed only a small momentum bite to reach the detector plane, resulting in excellent separation of the Møller and *e-p* elastic peaks. The remaining flux between the peaks was due to inelastic *e-p* scattering. These measurements of the inelastic *e-p* flux as a function of radius were necessary to apply an accurate background correction. There were also two one-inch-wide holes located in the vertical plane that were used similarly to separate the Møller and *e-p* fluxes for measuring the electron beam polarization.

7. Four quadrupole magnets that were used to separate the Møller and *e-p* fluxes. The quadrupole magnets were located immediately downstream of QC1B in order to maximize the drift distance to the detector. The magnet positions and field strengths were optimized to simultaneously maximize the separation between the Møller and *e-p* fluxes and maintain the azimuthal symmetry of the fluxes. The quadrupoles' focusing was proportional to the energy of the particles passing through them, and so the lower-energy Møller flux was much more strongly focused than the *e-p* flux. Figure 5.9 shows measurements of the radial profile of the flux at the detector plane for the quadrupole magnets off (a) and on (b). With the quadrupole magnets off, a single peak that includes both Møller and *e-p* electrons is visible centered on a
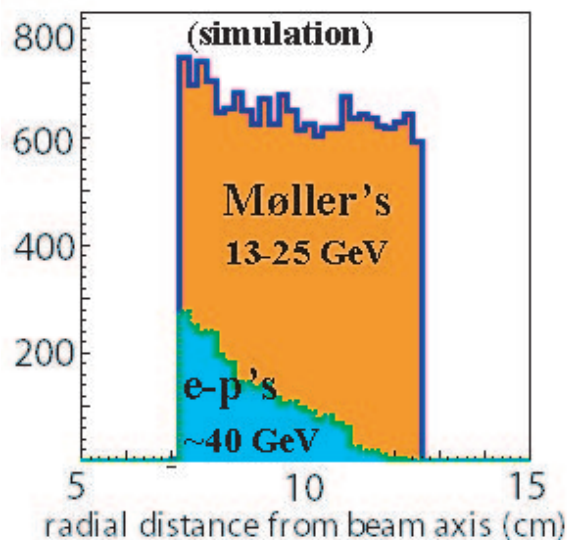
Figure 5.8: Møller- and *e-p*-scattered electron profiles at the acceptance-defining collimator.

radius of ~ 30 cm. This profile looks qualitatively like the sum of the Møller and *e-p* profiles in Figure 5.8, allowed to drift to the detector plane. Figure 5.9b shows the profile with the quadrupoles on: two peaks are now visible, with the inner peak being predominantly the Møller-scattered electrons and the outer peak the *e-p* electrons. The blue and green bands indicate the radial acceptance of the detectors for the Møller and *e-p* electrons, respectively.

8. A drift region from the quadrupole magnets to the the detector. The drift region was enclosed in a beam pipe held under vacuum in order to prevent the beam quality from degrading.

5.6.4   Detectors

E-158 used a number of detectors to make both the primary physics measurement as well as several necessary auxiliary measurements. These detectors were the Møller detector, the *e-p* detector, the pion detector, the profile detectors, the polarimetry detector, and the luminosity monitor. They are shown schematically in Figure 5.10 and described in the following sections.
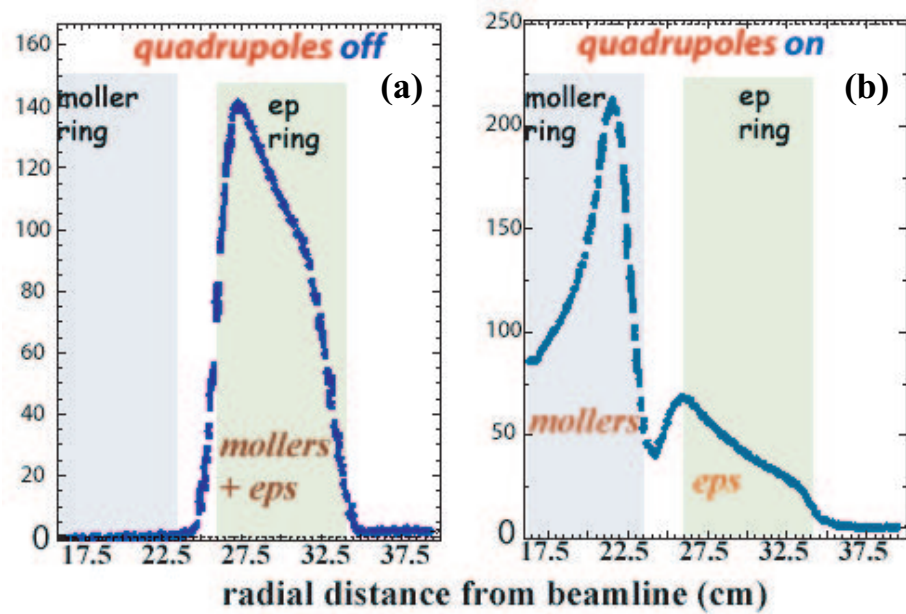
Figure 5.9: Measured electron profile at the detector plane. (a) Quadrupole magnets off. (b) Quadrupole magnets on. The blue and green bands indicate the radial acceptance of the detectors for Møller and *e-p* electrons, respectively.
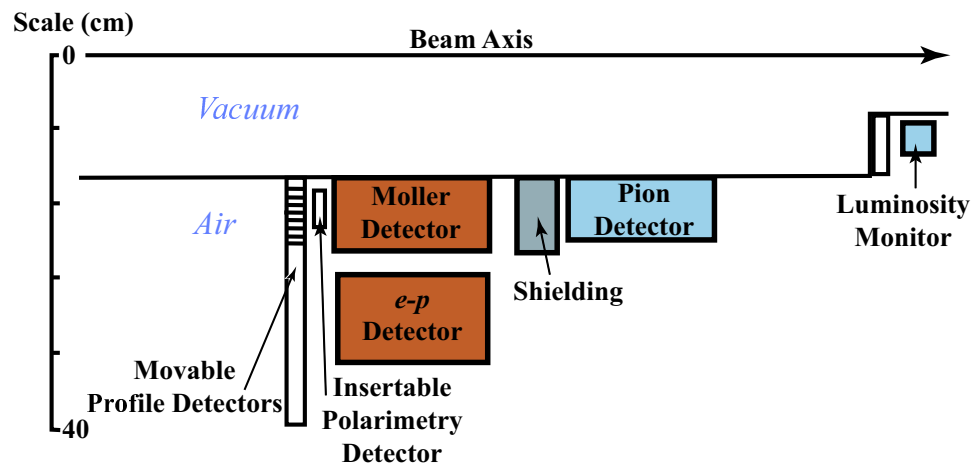
Figure 5.10: Layout of the E-158 detector package. The detector package is azimuthally symmetric about the beam axis and a radial slice is shown schematically here.

Møller and *e-p* Detectors

The main detector was a Cherenkov calorimeter, pictured partially assembled in Figure 5.11. It consisted of two cylinders concentric about the beam pipe. The inner cylinder detected Møller electrons and the outer cylinder detected *e-p* electrons. A schematic cross section is shown in Figure 5.12. Each cylinder consisted of a sandwich of layers of copper plates and quartz optical fibers (15 radiation lengths thick), oriented at 45° to the incident electrons. The copper acted as a radiator, and the resulting electromagnetic shower produces many electrons and positrons which emitted Cherenkov radiation as they passed through the quartz fibers. Because the fibers are at 45° to the incident electrons, a portion of the Cherenkov radiation cone was emitted parallel to the fibers and was tranmitted efficiently down their length to air light guides. The light guides transported the Cherenkov radiation to Hamamatsu R2154 PMT's buried in lead shielding. Groups of fibers were bundled and directed their light to particular PMT's. The Møller detector's fibers were split into 50 bundles, providing radial and azimuthal segmentation of the detector. There were three radial bins, with the inner bin read out by 10 PMT's and the middle and outer bins each read out by 20 PMT's. The *e-p* detector was segmented only in the azimuthal direction and was read out by 10 PMT's. The Møller detector provided the primary physics measurement for the experiment. The *e-p* detector provided a measurement of the *e-p* flux and *e-p* asymmetry and was used to correct for the residual *e-p* background under the Møller flux.

The Møller detector itself provided no background rejection, so additional detectors were necessary to characterize background fluxes and asymmetries. These detectors included the *e-p* detector, the pion detector, and the profile detectors.

The Møller detector readout electronics were designed to have sufficient resolution that the detector measurement would be dominated by counting statistics. The goals were to achieve a resolution of 200 ppm per channel and 40 ppm averaged over the entire Møller detector. However, during the 2002 physics runs the detector resolution was approximately 110 ppm. The detector resolution was the primary reason the detector asymmetry distribution width was $\sim$ 200 ppm,
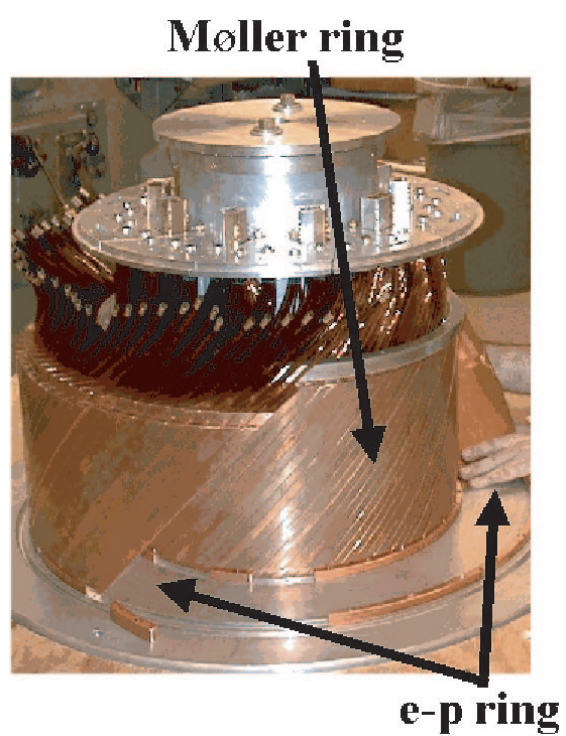
Figure 5.11: Photograph of the Møller detector. The inner ring detected Møller electrons, and the outer ring detected *e-p* electrons.
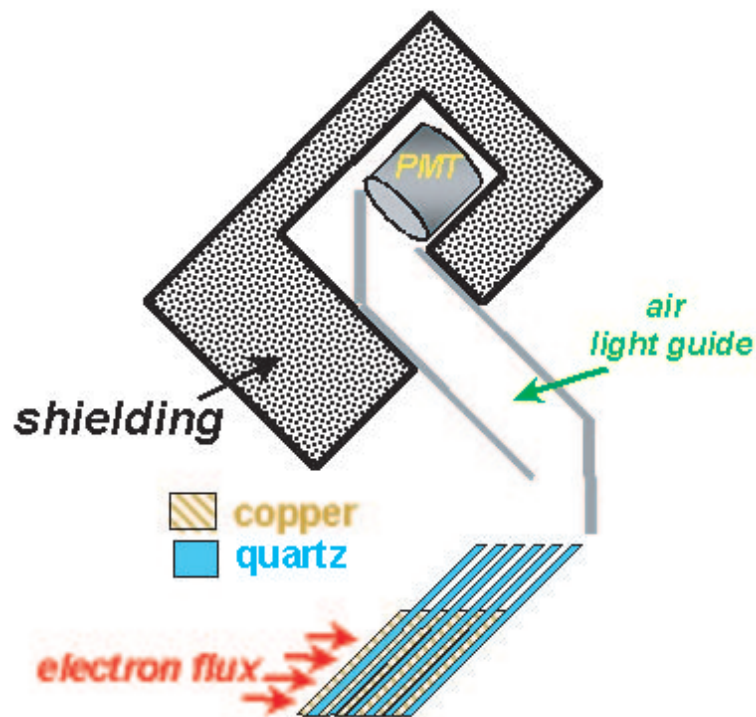
Figure 5.12: Schematic cross-section of the Møller detector.

significantly larger than the ~ 150 ppm width expected from counting statistics alone. The Møller electronics were designed to generate a ringing signal that could be processed much like the toroid signal. In the PMT, the high-voltage and signal grounds were the same, so an isolation transformer was placed on the signal output to break potentially large ground loops. This transformer could be considered equivalent to the toroids used to measure beam current, and we adapted the toroid electronics for the detector readout. Adding a resistor and a capacitor yielded an RLC circuit that produced a ringing signal. The signal was amplified in ESA and then run 200 feet to an electronics hut located just outside ESA. The signal passed through a rectifier circuit similar to the one used for the toroids and was finally digitized by 16-bit ADC's (discussed below). It appears at the time of this writing that pedestal noise in the detector contributes ~ 40 ppm of noise and that the rest is due to noise in the amplifiers.

Pion Detector

The pion detector was used to measure the pion flux and asymmetry. It was located immediately behind the Møller and *e-p* detectors and was shielded by them from the Møller and *e-p* signals and photon backgrounds. However, high-energy pions were able to punch through the Møller detector to reach it. The pion detector was made of ten quartz blocks oriented at 45° to the beam pipe; PMT's attached to the quartz blocks detect Cherenkov radiation emitted by incident pions.

Profile Detectors

The profile detectors were used to map the radial and azimuthal flux distribution incident on the Møller and *e-p* detectors. They consisted of four quartz bars spaced by 90° in azimuth. The quartz bars were mounted on translation stages to cover the full radial range of interest; the translation stages were in turn mounted on a wheel capable of rotating up to 180° in order to cover the full range in azimuth. Vacuum light guides carried the Cherenkov light from the quartz bars to PMT's. Figure 5.9 was generated using these profile detectors. The profile detector wheel was located just upstream of the Møller detector. When the profile detectors were not in use, they were retracted to a radius well outside the outer edge of the *e-p* detector.

Polarimetry Detector

When measurements of the beam polarization were made using collimator QC1A, only a small bin in radius and azimuth was allowed to reach the detector plane. An additional small Cherenkov calorimeter, made of alternating sheets of tungsten and quartz, was inserted remotely for these measurements. The detector (not shown in Figure 5.10) was mounted between the profile detectors and the Møller detector.

Luminosity Monitor

The luminosity monitor, located 7 m downstream of the Møller detector, detected extremely forward-angle ($\sim 0.1°$) Møller and *e-p* electrons. It was made of an aluminum preradiator fol-

lowed by two rings of eight individual gas chamber proportional counters. It was useful for two reasons:

1. The expected physics asymmetry in the luminosity monitor was < 10 ppb, comparable to the expected statistical error on its measurement, so it tested our ability to measure a null asymmetry and provided a means of verifying our understanding of systematic errors.

2. Once fluctuations in beam parameters have been removed from the luminosity monitor and Møller detector signals, there should be no correlation between the signals. Any residual correlation could indicate the presence of target density fluctuations; as mentioned above this analysis yielded an upper limit of 65 ppm on target density fluctuations.

5.7   Data Acquisition System

The DAQ was designed with two goals in mind:

1. It had to be low in noise so that measurements would remain dominated by counting statistics.

2. It had to have a very low level of cross talk between signals and a minimum of ground loops in order to avoid picking up spurious electronic asymmetries that could bias the measurement.

In addition, the DAQ was responsible for acquiring data from several locations:

1. The detector readout electronics in an electronics hut outside of ESA.

2. The A-Line beam diagnostics readout electronics in the Counting House.

3. The ASSET beam diagnostics readout electronics in the accelerator gallery directly above the ASSET region.

4. Readout electronics for certain polarized source laser diagnostics at CID.and

The DAQ also controlled the beam asymmetry feedback hardware at CID.

The detector and beam diagnostics that required high-resolution readout electronics were fed into custom integrating ADC boards designed at SLAC specifically to meet E-158's requirements. The boards were similar in design to those used for HAPPEX (section 4.10). They integrated the input signals by charging a capacitor, measured an analog difference between the voltages across the capacitor before and after integrating the signal pulse, and digitized that difference with 16-bit resolution. The timing of the integration gate and the gain of the integrator circuit were remotely programmable. The same ADC boards were used for the Møller and e-p detectors, the luminosity monitor, the pion detector, the BPM's and the toroids. The values of the integration capacitors and the resistors which set each channel's gain were optimized for each type of measurement.

Data for all of the detectors and beam monitors were read out at 120 Hz and stored to disk. The data were also processed for online monitoring and feedback for suppression of beam asymmetries. Additional "slow monitoring" data was fed into the data stream every few seconds. These data included items such as properties of the target (temperature, pressure, etc.), detector high voltage, and source and accelerator parameters. Completed "runs" of $\sim$ one hour in length were backed up to tape.

The feedbacks on beam asymmetries were controlled by a program called fbanal. Fbanal analyzed 100% of the data in realtime and tagged each event as to whether or not it was used in the feedback analysis. Fbanal controlled the IA, Phase, and POS loops described in sections refsec:af and 6.4.4. The IA and Phase loops were used to suppress the electron beam's intensity asymmetry and the POS loop was used to suppress its position and angle asymmetries.

Chapter 6

SLAC's Polarized Electron Source Laser and Optics Systems and Minimization of Helicity Correlations for the E-158 Parity Violation Experiment

In this chapter I describe the SLAC polarized electron source optics system and efforts to understand and control $^{\text{beam}}A_{\text{LR}}$'s for E-158. This chapter is based on an article I wrote that has been provisionally accepted by Nuclear Instruments and Methods A [100]. One section of that paper, describing the laser system and pulse-shaping optics, was written primarily by Axel Brachmann and is included in this thesis as Appendix A. The remainder of the paper is reproduced here, edited to avoid redundancy and for consistency with the rest of this thesis in notation and vocabulary.

6.1 Introduction

SLAC's polarized electron source is based on photoemission from a strained GaAs cathode pumped by an intense, circularly polarized laser beam [96, 101]. Two laser systems exist to pump the cathode: a Nd:YLF-pumped Ti:Sapphire laser (the "YLF:Ti") that generates short (2-ns) pulses of electrons for SLAC's Positron Electron Project (PEP) rings, and a flashlamp-pumped Ti:Sapphire laser (the "Flash:Ti") used to generate 270-ns pulses for use in fixed-target experiments in ESA

such as E-158.

As discussed in Chapter 1.3, E-158 is measuring the asymmetry in the cross section for elastic scattering of longitudinally polarized electrons with an energy of 45 GeV off an unpolarized electron target:

$$A_{LR}^{ee} = \frac{\sigma_R - \sigma_L}{\sigma_R + \sigma_L}, \tag{6.1}$$

where σ_R (σ_L) is the cross section for incident right- (left-) helicity electrons [60, 102]. The asymmetry will be measured to an accuracy of better than 10^{-8}, with the expected Standard Model asymmetry being approximately 10^{-7}.

One critical challenge for E-158 is the suppression of helicity-correlated asymmetries in the properties of the electron beam when it is incident on the liquid hydrogen target. Helicity-correlated asymmetries in the electron beam must be held to very small levels to prevent them from contributing false asymmetries to the measurement at a significant level. For instance, because typical fixed-target scattering cross sections are proportional to $\sin^{-4}\theta$ and the detector accepts electrons with scattering angles of 0.27-0.41˚, the scattered flux reaching the detector is strongly dependent on the position and angle of the beam at the target. If, for example, over the length of the experiment the average beam position on target for right- and left-helicity pulses is different, a false asymmetry is measured that is proportional to the magnitude of that difference. The Møller physics asymmetry in equation 6.1 can be expressed in terms of measured detector and beam quantities, as was more briefly discussed in section 3.6. Consider first a single pair of pulses corresponding to right- and left-helicity beam incident on the E-158 target. For the case of small right-left differences (and neglecting background contributions), the asymmetry for a single pair A_{LR}^P can be written as

$$A_{LR}^P = P_B \cdot A_{LR}^{ee} = \frac{\Delta D}{2D} - \frac{\Delta I}{2I} + \alpha_E \frac{\Delta E}{2E} + \sum_i \alpha_i \Delta X_i \tag{6.2}$$

$$= \frac{\Delta D}{2D} - {}^{beam}\widetilde{A}_{LR},$$

where P_B is the beam polarization, $D \propto \sigma$ is the average detected scattered flux for right- and left-helicity pulses, I is the beam intensity, E is the beam energy, the X_i run over position and angle in x and y, and α_E and the α_i are correlation coefficients between energy, position, and angle and the detector signal. These coefficients are measured simultaneously with data-taking. Δ refers to the right-left difference in each of the above properties. We use the symbol $^{beam}\widetilde{A}_{LR}$ to refer to the contribution to the measured detector asymmetry arising from helicity-correlated beam asymmetries. We frequently use the acronym " $^{beam}A_{LR}$" to refer to a helicity-correlated asymmetry (or difference) in the intensity, energy, position, angle, or other properties of the electron beam. On occasion we use the terms "helicity correlation" or "helicity-correlated asymmetry" to also refer to these beam asymmetries. E-158 will accumulate many right-left pairs ($\sim 3 \cdot 10^8$) over the length of the physics run. Taking into account the detector's nonlinearity (projected to be 0.5%) and estimates of the sensitivity of the scattering cross section to energy, position, and angle (determined by measuring α_E and the α_i), we estimate that the intensity asymmetry A_I, the energy asymmetry A_E, and the position and angle differences $D_{X(Y)}$ and $D_{X'(Y')}$ must be held below the following limits:

$$A_I = \langle \frac{I_R - I_L}{I_R + I_L} \rangle < 2 \cdot 10^{-7}, \qquad A_E = \langle \frac{E_R - E_L}{E_R + E_L} \rangle < 2 \cdot 10^{-8}, \qquad (6.3)$$

$$D_X = \langle x_R - x_L \rangle < 10 \text{ nm}, \qquad D_{X'} = \langle x'_R - x'_L \rangle < 0.4 \text{ nrad},$$

where the angled brackets denote averaging over all pairs. Achieving these limits will keep contributions to the systematic error on A_{LR}^{ee} at the level of 1 ppb or less from each $^{beam}A_{LR}$ and keep the cumulative systematic error contribution from all $^{beam}A_{LR}$'s at the level of 3 ppb, a level comfortably below the projected statistical error of 8 ppb. The derivation of these limits is discussed in more detail in [60, 103]. A major focus of the work presented in this chapter is the implementation of a number of methods for controlling $^{beam}A_{LR}$'s at a level that will allow achieving the requirements of equations 6.3.

The Flash:Ti system was originally designed and commissioned in 1993 [96, 104] and has seen extensive upgrades in preparation for E-158. Table 6.1 summarizes the parameters of the Flash:Ti laser beam for E-158. Likewise, the polarization and transport optics have also seen significant upgrades. The focus of these upgrades has been to improve the suppression and control of $^{\text{beam}}A_{\text{LR}}$'s. An overview of the polarized source laser and optics systems as they are configured for E-158 is illustrated in Figure 6.1. The laser and optics systems are housed in an environmentally controlled room outside of the accelerator tunnel. The "Flash:Ti Bench" holds the laser cavity and pulse-shaping optics. The "Diagnostics Bench" has photodiodes for monitoring the laser's intensity and temporal profile and a monochromator for measuring its wavelength. The "Helicity Control Bench" houses the optics for controlling the polarization state of the beam and for suppressing $^{\text{beam}}A_{\text{LR}}$'s. A 20-m Transport Pipe transports the beam into the accelerator tunnel, where it crosses the "Cathode Diagnostics Bench" and is directed onto the cathode of the polarized gun. The "Cathode Diagnostics Bench" holds optics for setting the position of the beam spot on the cathode and an auxiliary diagnostic line. The photoelectrons emitted by the cathode are bent through 38° and enter the accelerator.

Table 6.1: Parameters of the Flash:Ti laser beam as it ran for E-158 2002 Physics Run I. The position jitter at the photocathode is measured on the electron beam but is dominated by laser jitter. The other entries are measured directly on the laser beam.

Wavelength	805 nm*
Bandwidth	0.7 nm FWHM
Repetition rate	120 Hz
Pulse length	270 ns†
Pulse energy	60 μJ‡
Circular polarization	99.8%
Energy jitter	0.5% rms
Position jitter at photocathode	< 70 μm rms§

The heart of the polarized electron source is its photocathode. A new gradient-doped strained

*Tunable over $750 - 850$ nm.
†Tunable over $50 - 370$ ns.
‡Typical operating energy. The maximum available energy is 600 μJ in a 370-ns pulse.
§For 1 cm $1/e^2$ diameter.
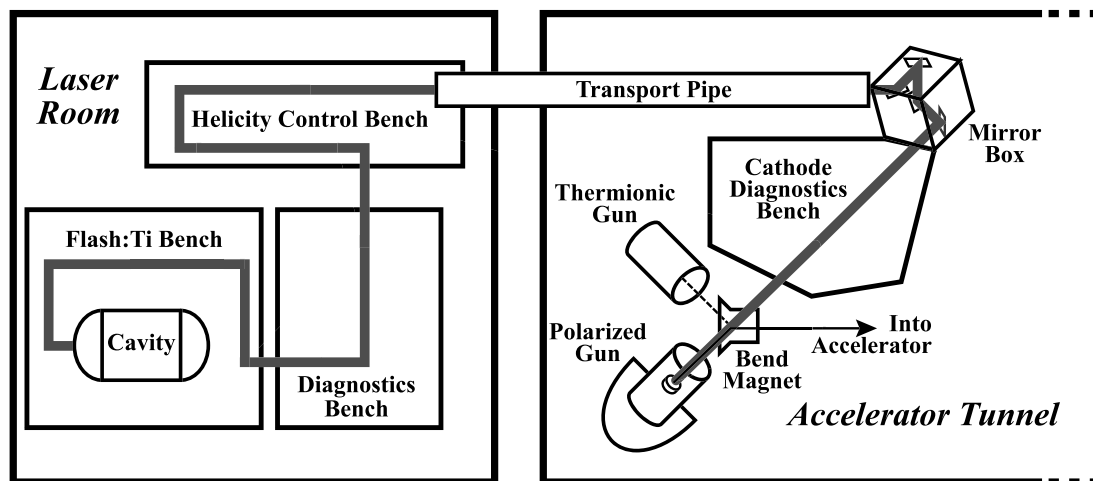
Figure 6.1: An overview of the Polarized Electron Source as it is configured for E-158.

GaAsP cathode was installed prior to E-158's 2002 physics running. This cathode, which is more fully described in [105], was developed in a R&D project for the Next Linear Collider (NLC) project [106]. NLC requires roughly 2.5 times more charge than E-158 in a 270-ns pulse and $> \sim 80\%$ electron polarization [101]. With the available laser power, this cathode can yield a charge of $2 \cdot 10^{12}$ electrons in 100 ns. This is significantly more charge than is required by E-158 (and significantly more than yielded by the previous cathode), providing additional flexibility in optimizing the optics system. In order to provide an electron beam polarization as high as $\sim 80\%$, a strain is applied to the active layer of the cathode to break the degeneracy of the $P_{3/2}$ energy levels as illustrated in Figure 6.2. However, the amount of strain varies in direction with respect to the crystalline lattice. This variation induces a "QE anisotropy" in the cathode, whereby the quantum efficiency (QE) of the cathode becomes dependent on the orientation of the linear polarization of incident laser light, with a typical analyzing power of $5 - 15\%$ [82]. The QE anisotropy is a dominant ingredient contributing to $^{\mathrm{beam}}A_{\mathrm{LR}}$'s and its effects are discussed in section 4.

The relationship between the helicity of the laser beam and the helicity of the resulting polarized electron beam can be determined by considering the bandgap diagram for GaAsP, shown in Figure 6.2. The laser light pumps electrons from the $P_{3/2}$ valence band into the $S_{1/2}$ conduction band. Right-helicity laser light excites electrons into the $m_J = -1/2$ state in the conduction band.
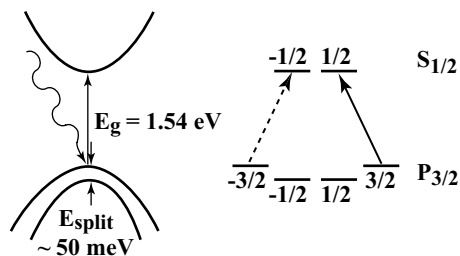
Figure 6.2: A diagram of the bandgap and energy levels for strained GaAsP. The arrows indicate the allowed transitions for right- and left-helicity photons of $\lambda = 805$ nm. Adapted from [109].

a) right helicity

b) left helicity

c) right helicity
(left-circular)

d) left helicity
(right-circular)
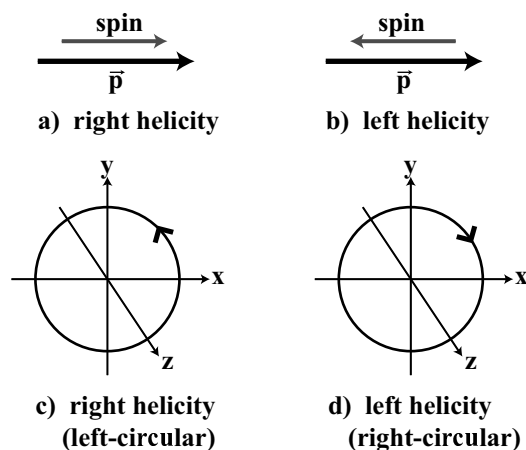
Figure 6.3: Conventions used for electron beam helicity and laser beam polarization. a) and b) define right- (left-) helicity photon and electron beams as having the particle spin aligned (antialigned) with the particle momentum. c) and d) show the commonly used optics convention. The arrows on the polarization ellipses indicate increasing time.

Because we operate the cathode in reflection mode (the emitted electrons move in the direction opposite of the incoming laser light), the extracted electrons are also right-helicity. Similarly, left-helicity laser light excites electrons into the $m_J = +1/2$ state, and in reflection yields left-helicity electrons. In this chapter we define the handedness of the photon and electron beams according to their helicity [107] as shown in Figure 6.3.¶

The operating wavelength and required bandwidth of the Flash:Ti are determined by the photoemission properties of the cathode. Figure 6.4 shows, as a function of wavelength, the cathode QE and the polarization of the photoemitted electrons for the cathode used during E-158 Physics

---

¶This convention results in right- (left-) helicity photons corresponding to left- (right-) circular polarization photons in the commonly used optics convention given in [108].
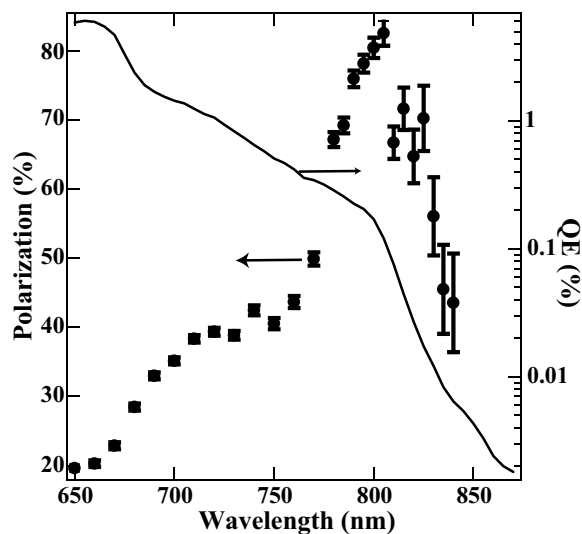
Figure 6.4: Electron polarization and cathode QE as a function of wavelength. This data is from a different sample of the same GaAsP wafer as the cathode installed prior to E-158 physics running. Reprinted from [105].

Run I. As shown in Table 6.1, we have chosen an operating wavelength of 805 nm in order to sit at the polarization peak, and the Flash:Ti's 0.7 nm FWHM bandwidth is narrow enough to ensure that all of the laser power is used to generate electrons at the peak polarization.

A particular focus of this chapter is on the parts of the optical system that are responsible for producing a circularly polarized laser beam and for suppressing and controlling $^{\text{beam}}A_{\text{LR}}$'s. As is discussed in section 6.2.4, a high degree of circular polarization is critical for minimizing $^{\text{beam}}A_{\text{LR}}$'s. We use a linear polarizer and a pair of Pockels cells on the Helicity Control Bench to gain control over the laser beam polarization and to switch between helicity states on a pulse-by-pulse basis. To achieve further suppression of $^{\text{beam}}A_{\text{LR}}$'s, a number of features are built into the optical system. These features include

   i) optimization of the beam spot size and waist location at the polarization Pockels cells;

   ii) imaging of the polarization Pockels cells onto the photocathode;

   iii) active feedbacks to null A_I, $D_{X(Y)}$, and $D_{X'(Y')}$;

   iv) an insertable half-wave plate to reverse the laser helicity; and

v) the ability to toggle between two beam expanders which provide a magnification of equal magnitude and opposite sign to reverse certain contributions to $D_{X(Y)}$ and $D_{X'(Y')}$.

This chapter includes performance results for the laser and optics system from three runs: T-437, a test-beam run in November 2000 which commissioned the polarized source for E-158; an E-158 engineering run in January-May 2001; and E-158 Physics Run I in April-May 2002. Table 6.2 summarizes changes in key parameters of the laser beam between runs. The wavelength was changed prior to Physics Run I to accomodate the new cathode. In addition, a few results are presented from the Gun Test Laboratory, a test facility which reproduces the first few meters of the beam line.

Table 6.2: Summary of changes in key operating parameters of the Flash:Ti laser between E-158-related runs.

Run	Laser Rate	Wavelength	Energy Jitter
T-437	60 Hz	852 nm	1.0%
2001 Engineering Run	60 Hz	852 nm	1.5%
Physics Run I	120 Hz	805 nm	0.5%

As mentioned earlier, Appendix A discusses the design and implementation of the Flash:Ti laser system and the associated pulse-shaping optics. Section 6.2 of this chapter presents the optics used to circularly polarize the laser beam, to transport the beam to the photocathode, and to control $^{\text{beam}}A_{\text{LR}}$'s. Section 6.2.4 discusses how $^{\text{beam}}A_{\text{LR}}$'s can arise from interactions between imperfections in the laser circular polarization and the cathode's QE anisotropy. Section 6.4 discusses how the laser polarization and transport optical systems are configured and optimized to suppress $^{\text{beam}}A_{\text{LR}}$'s and presents results from T-437. Finally, section 6.5 summarizes many effects which can generate $^{\text{beam}}A_{\text{LR}}$'s and notes their relevance to the SLAC source and E-158.
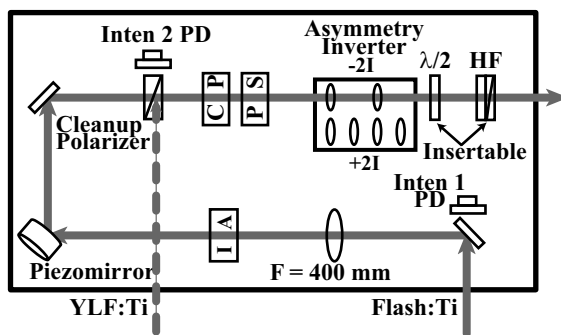
Figure 6.5: The Helicity Control Bench contains the optics for control of the laser beam's polarization and $^{beam}A_{LR}$'s.

6.2 Helicity Control Bench and Transport Optics to Cathode

In this section we describe the optics that follow the laser and pulse-shaping systems. These optics circularly polarize the laser beam in a manner that permits selecting the helicity in a pseudorandom sequence on a pulse-by-pulse basis. The circularly polarized light is then transported to the cathode and care is taken to minimize distortions in the laser polarization. As mentioned below (and discussed in detail in section 6.2.4), small distortions generate significant amounts of linear polarization and ultimately contribute to helicity-correlated asymmetries. The optics are configured to passively minimize and actively null $^{beam}A_{LR}$'s.

6.2.1 Circular Polarization

The polarization optics, shown in Figure 6.5, are designed to generate highly circularly polarized light of either helicity while minimizing $^{beam}A_{LR}$'s. The "Cleanup Polarizer" and the "Circular Polarization" (CP) and "Phase Shift" (PS) Pockels cells collectively determine the polarization of the beam.* The Cleanup Polarizer also functions to combine the YLF:Ti beam used to generate electrons for the PEP rings† with the Flash:Ti beam so that they share a common path through the remaining transport optics. The CP cell acts as a quarter-wave plate with its fast axis at 45° from

---

*All three Pockels cells on the Helicity Control Bench (CP, PS, and IA) are 20-mm-aperture Cleveland Crystals model QX2035, specified to be windowless, to be parallel to better than 0.5 arcminute, and to be broadband AR-coated centered at 800 nm. Cleveland Crystals, Inc., 676 Alpha Dr., Highland Hts., OH 44143, USA.

†For E-158's Physics Run I, it shared accelerator pulses with the BaBar experiment that utilized the PEP storage rings [110]. The BaBar experiment does not utilize the beam polarization.

the horizontal. The sign of its retardation can be chosen on a pulse-by-pulse basis, generating circularly polarized light of either helicity. Its quarter-wave voltage is approximately 2.7 kV. Adjusting its voltage from the quarter-wave setting allows the CP cell to compensate for linear polarization along the horizontal and vertical axes that arises from either residual birefringence in the Pockels cell or phase shifts in the optics between the Pockels cells and the photocathode. The PS cell, with a vertical fast axis, is pulsed at low voltages ($\lesssim 150$ V) and is used to compensate for residual linear polarization along the axes at $\pm 45°$. The phase shift $\delta_{CP(PS)}$ induced by the CP (PS) cell is given by the relation

$$\delta_{CP(PS)} = \frac{\pi}{V_{\lambda/2}} \cdot V_{CP(PS)}, \tag{6.4}$$

where $V_{\lambda/2}$ is the voltage required for half-wave retardation (typically ~ 5.4 kV) and $V_{CP(PS)}$ is the voltage across the CP (PS) cell.

In the following subsections we discuss the polarization control given by the CP and PS cells, our procedures for aligning them, the insertable half-wave plates that are used to generate a slow helicity reversal, and the data acquisition and control systems used to determine the polarization sequence and set the Pockels cell voltages.

Polarization Analysis

To understand the function of the CP and PS cells, it is useful to develop expressions for the polarization of the laser beam in terms of the phase shifts induced by the CP and PS cells. The electric field of a 100% polarized laser beam can be written as

$$\vec{E} = E_0 (\cos\theta \cdot \hat{x} + e^{i\phi}\sin\theta \cdot \hat{y}) \cdot e^{i(kz-\omega t)} = \begin{bmatrix} \cos\theta \\ e^{i\phi}\sin\theta \end{bmatrix}, \tag{6.5}$$

where the vector expression is the Jones matrix notation [111]. A useful method for characterizing the polarization of the beam utilizes the Stokes parameters. If we assume that the beam is totally

polarized and normalize the Stokes parameters to the intensity we then have

$$
\begin{aligned}
S_1 &= \cos 2\theta = (X - Y)/(X + Y), \\
S_2 &= -\sin 2\theta \cos \phi = (U - V)/(U + V), \\
S_3^H &= -\sin 2\theta \sin \phi = (R^H - L^H)/(R^H + L^H), \\
(S_1^2 + S_2^2) + (S_3^H)^2 &= L^2 + C^2 = 1,
\end{aligned}
\tag{6.6}
$$

where S_1 is a measure of linear polarization along the horizontal and vertical axes, S_2 is a measure of linear polarization along the axes at $\pm 45°$ to the vertical, S_3^H is a measure of the degree of circular polarization, X and Y represent intensities projected along the horizontal and vertical axes, U and V represent intensities projected along the axes at $\pm 45°$ to the vertical, and R^H and L^H represent intensities projected onto a decomposition into right- and left-helicity circularly polarized light. The superscript "H" is to indicate that we refer to the circular polarization in terms of its helicity for consistency with the particle physics definition, and S_3^H is defined such that it is $+1$ for right-helicity circular polarization. Two parameters, S_1 and S_2, are required to completely describe the linear polarization state of the beam. We see from the last line of equations 6.6 that the linear and circular polarization components are constrained to add in quadrature to a value of one. One implication is that for a reasonably well circularly polarized beam, a small phase shift may have a negligible effect on the magnitude of the circular polarization while simultaneously inducing a large linear polarization. For instance, a perfectly circularly polarized beam at 805 nm which acquires a 2-nm phase shift passing through a thin low-stress window will have a circular polarization of 99.988% and a linear polarization of 1.6%.

The SLAC polarized source optical system includes elements such as the CP and PS Pockels cells, a half-wave plate, and additional optical elements that may each possess a small amount of birefringence. These components can be well approximated as different cases of a unitary Jones

matrix for a rotated retardation plate [111]:

$$J_{RET} = \begin{bmatrix} \cos^2\gamma + e^{i\delta}\sin^2\gamma & (1 - e^{i\delta})\sin\gamma\cos\gamma \\ (1 - e^{i\delta})\sin\gamma\cos\gamma & \sin^2\gamma + e^{i\delta}\cos^2\gamma \end{bmatrix}. \tag{6.7}$$

Here, γ is the angle between the retarder's fast axis and the horizontal axis and δ is the retardation induced between the fast and slow axes.

The Cleanup Polarizer is oriented to transmit horizontally linearly polarized light; thus the initial electric vector can be represented as

$$\vec{E_i} = \begin{bmatrix} 1 \\ 0 \end{bmatrix}. \tag{6.8}$$

The CP cell has its fast axis at 45° from the horizontal ($\gamma = \pi/4$), induces a retardation δ_{CP}, and can be represented by the matrix

$$J_{CP} = \frac{1}{2}\begin{bmatrix} 1 + e^{i\delta_{CP}} & 1 - e^{i\delta_{CP}} \\ 1 - e^{i\delta_{CP}} & 1 + e^{i\delta_{CP}} \end{bmatrix}. \tag{6.9}$$

The PS cell has its fast axis vertical ($\gamma = \pi/2$), induces a retardation δ_{PS}, and can be represented by the matrix

$$J_{PS} = \begin{bmatrix} e^{i\delta_{PS}} & 0 \\ 0 & 1 \end{bmatrix}. \tag{6.10}$$

Calculating the state of the polarization vector immediately following the PS cell and multiplying both components by an additional phase shift in order to write the vector in a convenient form yields

$$\vec{E_f} = J_{PS} \cdot J_{CP} \cdot \vec{E_i} = \begin{bmatrix} \cos\delta_{CP}/2 \\ e^{-i(\frac{\pi}{2}+\delta_{PS})}\sin\delta_{CP}/2 \end{bmatrix}. \tag{6.11}$$

This optical configuration allows the generation of arbitrary elliptically polarized light. Comparing

equations 6.5 and 6.11, we see that δ_{CP} determines the relative amplitude of the x and y components of the electric field, and δ_{PS} determines their relative phase. Writing down the Stokes parameters for the light leaving the PS cell, we have

$$S_1 = \cos \delta_{CP},$$
$$S_2 = -\sin \delta_{CP} \sin \delta_{PS}, \tag{6.12}$$
$$S_3^H = -\sin \delta_{CP} \cos \delta_{PS}.$$

As we indicated earlier, δ_{CP} is set to values close to $\pm \pi/2$ and δ_{PS} is set to values close to 0. For these values, the Stokes parameter S_1 is sensitive to small changes in δ_{CP}, while S_2 is sensitive to small changes in δ_{PS}. Utilizing the Cleanup Polarizer and CP and PS cells in this configuration allows us to generate a laser beam of arbitrary elliptical polarization. A convenient feature of this configuration is that any residual linear polarization can be decomposed into components that are separately adjustable by the CP cell (S_1) and the PS cell (S_2).

Pockels Cell Alignment

It is important to be able to properly align the Pockels cells with respect to the laser beam and to choose the portion of the crystal through which the beam passes. To this end, we choose mounts for the Pockels cells that are adjustable in pitch, yaw, and roll and allow translation along both axes perpendicular to the beam. The Pockels cells are initially aligned for pitch and yaw between crossed polarizers (the Cleanup Polarizer and an auxiliary analyzer), first adding the CP cell and recovering extinction, and then adding the PS cell. Care is taken to be sure that the Pockels cell orientations are not at secondary minima.[‡] The orientation of the Pockels cell fast and slow axes can be determined by then pulsing them one at a time at a high voltage (~ 2 kV) and adjusting the roll angle until extinction is recovered. In this configuration, either the fast or slow axis is now

---

[‡]As either the pitch and yaw angles are adjusted, the transmitted light goes through a series of minima. The minimum of least amplitude provides the best alignment, but often the neighboring minima are not much larger in amplitude. However, the neighboring minima do not result in quite as good an extinction and often the Pockels cell can be seen to be misaligned by eye when at those minima.

parallel to the upstream polarizer. The CP cell is then rotated by 45°; its orientation is verified and set more precisely later. The PS cell is left in this orientation.

At this point, the analyzer is removed and the Helicity Filter[§] (HF) is used to check the alignment and set the initial Pockels cell voltages. The HF consists of a linear polarizer and a quarter-wave plate fixed in orientation so that it transmits right-helicity light and extinguishes left-helicity light. The nominal quarter-wave voltages for each helicity are set by sweeping the CP cell through the range $\pm(1500 - 3900 \text{ V})$ in 11 steps, measuring the transmitted light intensity, and fitting a parabola to the results. Similarly, the nominal PS voltages are determined by setting the CP quarter-wave voltage for each state and sweeping the PS cell from -1500 V to $+1500 \text{ V}$ in 11 steps, measuring the transmitted light intensity, and again fitting a parabola to the results. To be satisfied with the alignment, we require that the extinction ratio between transmitted and extinguished states be greater than 1000:1, that the sum of the CP right- and left-helicity voltages be below 100 V, and that the difference of the PS right- and left-helicity voltages be below 100 V. The difference between the PS voltages is very sensitive to the alignment of the CP cell roll angle and provides the best means of verifying that it is properly oriented. If the PS cell voltages are greater than 100 V apart, the CP and PS cells are set to their left-helicity voltages so that they are extinguished by the HF, and the roll angle of the CP cell is adjusted to minimize transmission. Then the voltage scans are repeated. Requiring an extinction ratio of $\geq$ 1000:1 implies a circular polarization of $\geq$ 99.8% and an unpolarized component of $\leq$ 0.2%. An additional check of the voltages for right-helicity light, which are measured above in transmission, can be made by using the insertable half-wave plate mounted just upstream of the HF. This allows us to measure the voltages for right-helicity light in extinction. Finally, we check the quality of the laser beam polarization on the photocathode. We do this by letting the beam strike the cathode and measuring the intensity asymmetry as the Pockels cell voltages are varied from their nominal values. This procedure is described in more detail in section 6.4.1 and allows us to adjust the CP and PS cell voltages to

---

[§]Meadowlark Optics, Frederick, Colorado, USA.

compensate for residual birefringence in the optics between them and the photocathode. A final cross check on the laser beam polarization is a scan of the Pockels cell voltages while measuring the electron beam polarization. The only available electron beam polarimeter is the Møller polarimeter in End Station A, so this check can only be conducted while E-158 is running. Typical operating voltages for the CP and PS cells are given in Table 6.3, section 6.4.1.

Insertable Half-Wave Plates

We have two insertable zeroth-order half-wave plates in the optics system following the polarization optics that can be used to introduce a slow reversal of the laser helicity. This flips the definition of helicity relative to what the data acquisition system (DAQ) is expecting, thus reversing the sign of the physics asymmetry. Such a reversal is very useful for suppressing certain classes of systematic errors, and is discussed in section 6.4.5. One half-wave plate is located on the Helicity Control Bench (Figure 6.5), where it is also useful for setting the initial Pockels cell voltages with the HF. The second half-wave plate is located on the Cathode Diagnostics Bench (Figure 6.7) and is the last optical element before the vacuum window at the entrance to the polarized electron gun. Either half-wave plate can be used to effect the slow reversal, but we choose to use the one on the Cathode Diagnostics Bench for reasons discussed in section 6.3.4.

6.2.2 Helicity Control and Data Acquisition

The beam helicity is controlled by the "Polarization MONitor" (PMON) system. PMON's interaction with the optics hardware and the DAQs is shown in schematic form in Figure 6.6. PMON is a set of SLAC-built custom electronics that generates a pseudorandom sequence of polarization states ("polbits") using a 33-bit shift register algorithm as described in [83]. At 120 Hz, this sequence repeats approximately once every two years. Because the dominant noise in the electronic environment surrounding the accelerator is at 60 Hz, we choose to treat the 120-Hz triggering as two separate 60-Hz time slots. We do this by imposing a quadruplet structure on the helicity

sequence in which two consecutive pulses have randomly chosen helicities and the subsequent two pulses are chosen to be their complements. For example, a possible sequence could be "LRRL LLRR." In the data analysis, asymmetries are calculated for each pair of events, where pairs are formed between the first and third members of the quadruplet, and between the second and fourth members. In this way we calculate pairwise asymmetries between pulses that are at the same phase with respect to the 60-Hz noise. The pseudorandom sequence also provides a means of error checking in the offline analysis. Observing the helicity state of 33 consecutive pairs allows one to predict the state of future pairs. Comparing the predicted state with the actual state transmitted to the DAQ can be used to look for data acquisition errors. PMON determines the pulse sequence, sets the appropriate voltages for all helicity-correlated devices (the CP, PS, and IA Pockels cells and the piezomirror), and distributes the helicity information and pulse identification number to the DAQs.

PMON interacts with two DAQs in order to control the helicity-correlated devices. For testing and commissioning the source optics, we use PMON with the SLC Control Program (SCP). For test beams and physics running, PMON works with the E-158 DAQ to control the optics. Switching between the two DAQ systems is done by swapping a pair of cables at the PMON Interface Module that are used for the setting and readback of voltages for the helicity-correlated devices. SCP is also used to control which algorithm the PMON Controller uses to generate the helicity sequence. Five sequences are available: the pseudorandom sequence described above, an alternating left/right sequence, all left-helicity pulses, all right-helicity pulses, and all no-helicity pulses (for which none of the helicity-correlated devices are operated). The "Insertable Optics Controller" is a SLAC-built module which receives control signals from SCP and sends the appropriate voltage levels to the insertable optical elements. It also sends status information to the E-158 I/O Register.

Three techniques are implemented in PMON to prevent the transmission of helicity information to the DAQs from introducing false asymmetries via electronic cross talk. First, PMON delays the transmission of helicity information by one pulse. This delay destroys the correlation between the
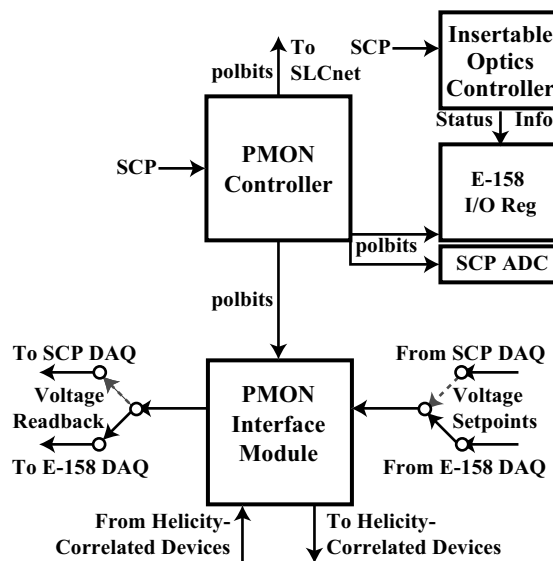
Figure 6.6: A schematic of the Polarization MONitor (PMON) electronics. Control of the helicity-correlated devices can be switched between the SCP and E-158 DAQs by swapping the "Voltage Setpoints" and "Voltage Readback" cables at the PMON Interface Module. Additional copies of the polarization states (polbits) are available to an ADC read out by the SCP DAQ and to an E-158 I/O Register during commissioning but are eliminated during physics running.

actual beam helicity and the helicity information received by the DAQ. Second, PMON converts the helicity information from a digital signal to an RF signal before transmitting it to the experiment over "SLCnet," a dedicated copper transmission line. A PMON Receiver module in the E-158 DAQ decodes the RF signal. Third, additional copies of the polarization information that are available as analog voltage levels during commissioning of the SCP and E-158 DAQs are eliminated for physics running.

6.2.3 Laser Transport Optics and Cathode Diagnostics Bench

We describe next the optical system between the polarization optics and the cathode. These optics image the CP cell onto the cathode while preserving the circular polarization of the beam. An "Asymmetry Inverter" consisting of two beam expanders with magnifications of equal magnitude and opposite sign (see Figure 6.5) can be toggled between two positions to provide some cancellation for helicity correlations in the laser beam position and angle. We used the software packages PARAXIA and ZEMAX to model gaussian beam propagation through the transport optics and to

design the transport optics.

Imaging

We image the CP cell onto the cathode in order to minimize the contribution of any helicity-correlated steering arising from the CP cell. The imaging optics consist of the 5-m lens in the Transport Pipe and the telescope on the Cathode Diagnostics Bench (both shown in Figure 6.7). The location of the image point is most sensitive to the setting of the telescope on the Cathode Diagnostics Bench. The downstream lens of that telescope is adjustable in x, y, and z, allowing us to set the beam size and position on the cathode and thereby dictating the location of the object point on the Helicity Control Bench. We replaced the previous $3' \times 1'$ Helicity Control Bench with a $6' \times 16''$ bench to allow some freedom of movement to locate the CP cell at the object point. The new cathode described in the introduction gives us additional flexibility to choose the laser spot size on the cathode. Full illumination of the 20-mm-diameter cathode is no longer needed to achieve the required electron beam current. By reducing the spot size to ~ 1 cm for the $1/e^2$ diameter, we place the object point within a few centimeters of the CP cell and also improve the electron beam properties and transmission. The imaging optics are designed to bring the laser beam through a waist between the telescope and the cathode to avoid clipping in the 14-mm-diameter pipe that leads from the Cathode Diagnostics Bench to the cathode. Because the laser beam gets as large as 1 inch in diameter while being transported from the Laser Room to the cathode, we use 2-inch lenses and mirrors for the imaging optics and the Mirror Box to avoid clipping.

The remotely insertable 50% mirror at the exit of the Cathode Laser Diagnostics Bench redirects the beam into a diagnostic line that has the same length as the distance between the mirror and the cathode. The Cathode Target provides an image of the beam as it appears on the cathode and is an extremely useful diagnostic, in particular for understanding the imaging of the beam and for measuring the position dependence of the cathode's QE. We determine the location of the object point by placing a wire-mesh screen in the beam near the CP cell and moving it along the
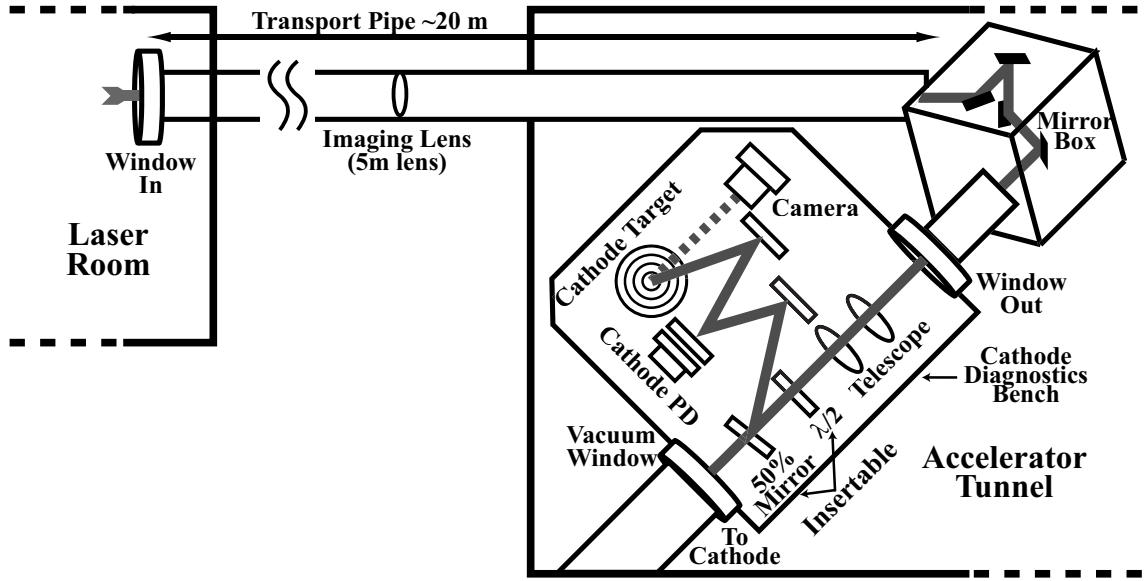
Figure 6.7: The optical transport system and the Cathode Diagnostics Bench.

beam axis while studying the quality of the image on the Cathode Target. We observe that the object point is within a few centimeters of the CP cell. This provides a significant reduction of the effective lever arm from the ~ 25 m actual distance between the CP cell and the cathode. The object point is observed to be the same for both states of the Asymmetry Inverter.

Asymmetry Inverter

The "Asymmetry Inverter" (AI) consists of two beam expanders on a translation stage as shown in Figure 6.5. The effect of the AI on an optics ray can be described by $|\tilde{x}\rangle = M |x\rangle$, or equivalently

$$
\begin{bmatrix} \tilde{x} \\ \tilde{x}' \end{bmatrix} = \begin{bmatrix} M_{11} & M_{12} \\ M_{21} & M_{22} \end{bmatrix} \begin{bmatrix} x \\ x' \end{bmatrix},
\tag{6.13}
$$

where x (x') is the position (angle $= dx/dz$) of the optics ray entering the AI, $\tilde{x}$ $(\tilde{x}')$ is the position (angle) of the optics ray exiting the AI, and M is the transport matrix characterizing the AI. We

designed the "+" and "−" optics to yield

$$M^{\pm} = \begin{bmatrix} \pm 2.25 & 0 \\ 0 & \pm 0.44 \end{bmatrix} . \tag{6.14}$$

Thus, the rays leaving the AI satisfy

$$|\tilde{x}\rangle^{-} = -|\tilde{x}\rangle^{+} . \tag{6.15}$$

The magnification of 2.25 is needed to assist in the beam transport to the cathode. Taking equal amounts of physics data in the two AI configurations allows for cancellation of certain contributions to the $^{\mathrm{beam}}A_{\mathrm{LR}}$'s and is discussed in section 6.4.5.

Preserving Circular Polarization

The transported laser beam must retain a high degree of circular polarization. We employ several strategies to achieve this. First, we minimize the number of optical elements in the transport system by placing the laser beam diagnostics in the auxiliary diagnostic line accessed by the insertable 50% mirror. Second, the four mirrors in the Mirror Box are arranged in two helicity-compensating pairs, for which the bounces within each pair interchange 's' and 'p' polarizations. Thus, the difference in phase shifts and losses between the 's' and 'p' polarizations for a given mirror are cancelled between the members of each pair. Care was taken to make certain that the four mirrors all came from the same coating run.¶ Finally, the Transport Pipe, which has historically been held under vacuum as part of a Class-IV laser containment system, is being used at atmospheric pressure for E-158 in order to minimize stress-induced birefringence in its end windows. Alternate arrangements have been made to ensure the integrity of the Transport Pipe for laser safety purposes.

¶The mirrors are CVI TLM2-825-45-2037, specified to be from the same spindle and same coating run. CVI Laser Corporation, Albuquerque, NM, USA.

6.2.4 Helicity-Correlated Feedbacks

Three active feedback loops are used to further suppress $^{\text{beam}}A_{LR}$'s. One feedback loop (the "IA loop") balances A_I between the two helicity states. This is accomplished by using the "Intensity Asymmetry" (IA) Pockels cell, located upstream of the Cleanup Polarizer (see Figure 6.5). When pulsed differently on right- and left-helicity pulses by a few tens of volts, the IA cell introduces a helicity-correlated phase shift into the beam. The Cleanup Polarizer transforms this phase shift difference into an intensity asymmetry on the laser beam which compensates for the measured intensity asymmetry on the electron beam.

A second feedback loop (the "POS loop") compensates for $D_{X(Y)}$ and $D_{X'(Y')}$. This is accomplished by the "piezomirror," a standard 1-inch diameter mirror attached to a Physik Instrumente model S-311.10$^\|$ piezoelectric mount (see Figure 6.5). This unit has three piezoelectric stacks that can be pulsed individually up to 100 V. The independent operation of the three stacks gives the freedom to translate the face of the mount up to 6 μm, or to tilt in an arbitrary direction by up to 600 μrad. The piezomirror changes the angle of the laser beam through the remainder of the optical system and can produce helicity-correlated displacements on the cathode of $20 - 50$ μm (depending on the effective lever arm between the piezomirror and the cathode), comparable in magnitude to the beam position jitter.

The third feedback loop (the "Phase Feedback") provides a mechanism for keeping the corrections induced by the IA loop small. It looks at the correction induced by the IA loop averaged over a specified length of time and adjusts the CP and PS cell voltages in such a way as to drive the IA loop correction to zero. Essentially, the Phase Feedback compensates for drifts in the polarization state of the laser beam that can give rise to an intensity asymmetry as described in section 6.2.4.

The IA and POS loops utilize measurements from low-energy (1-GeV) electron beam diagnostics and act on the laser beam. Additional independent diagnostics at both low and high (45 GeV) energy are used to monitor the performance of the feedback loops and to measure $^{\text{beam}}A_{LR}$'s at

---

$^\|$Physik Instrumente GmbH and Co, Auf der Roemerstrasse D-76228 Karlsruhe/Palmbach, Germany.

the E-158 target. We choose to generate the measurements for the feedback loops from beam diagnostics at low energy in order to minimize coupling between the various $^{beam}A_{LR}$'s as a result of beam loading, residual dispersion, and wakefield effects in the accelerator. The IA, POS, and Phase Feedback loops are discussed in more detail in section 6.4.4.

6.3 Primary Sources of Helicity-Correlated Electron Beam Asymmetries

The primary mechanism for generating a helicity-correlated asymmetry in the intensity of the polarized electron beam, A_I, is a coupling between helicity-correlated changes in the orientation of residual linear polarization in the laser beam and the cathode's QE anisotropy. The linear polarization components are a consequence of residual birefringence in the CP and PS cells and in the optics between them and the cathode. This residual birefringence is significant: a typical low-birefringence window produces a phase shift per unit thickness of 5 nm/cm. The strained GaAs cathode's QE anisotropy provides a large analyzing power for incident linear polarization, typically on the order of $5 - 15\%$ [82]. Uncorrected, a 5-nm phase shift can produce a helicity-correlated variation in electron beam intensity at the level of 0.4%, four orders of magnitude larger than the experimental requirement. Similar polarization-related effects have sometimes been referred to [95] as PITA (Polarization-Induced Transport Asymmetry) effects and are often a dominant source of $^{beam}A_{LR}$'s. We derive an expression for A_I for the case of the SLAC polarized electron source optics, identify the relevant phases, and examine the implications for controlling $^{beam}A_{LR}$'s. We also find that if the residual linear polarization of the laser beam varies spatially, it can give rise to helicity-correlated position and spot size differences. We note that while in the analysis below the only analyzing power is a transport element in the optics system, the QE anisotropy of the cathode behaves formally in the same way.

6.3.1 Derivation of the Polarization-Induced Transport Asymmetry

We can understand the origin of A_I by considering a system (as described in section 6.2.1) comprised of horizontally polarized light incident in turn on the CP cell, the PS cell, and an asymmetric

transport element. The final electric vector can be computed by multiplying the initial electric vector by the appropriate matrices:

$$\vec{E_f} = J_{AT} \cdot J_{PS} \cdot J_{CP} \cdot \vec{E_i}, \tag{6.16}$$

where J_{CP} and J_{PS} are given by equations 6.9 and 6.10 and J_{AT} is an asymmetric transport element which provides an analyzing power that is sensitive to the orientation of linear polarization and does not introduce any depolarization. Assuming the asymmetric transport element has transmission coefficients $T_{x'}$ and $T_{y'}$ along some axes x' and y', we have

$$J_{AT} = \begin{bmatrix} T + \frac{\epsilon}{2}\cos 2\theta & \frac{\epsilon}{2}\sin 2\theta \\ \frac{\epsilon}{2}\sin 2\theta & T - \frac{\epsilon}{2}\cos 2\theta \end{bmatrix}, \tag{6.17}$$

where $T = (T_{x'} + T_{y'})/2$, $\epsilon = T_{x'} - T_{y'}$, and θ is the angle between x' and the horizontal axis. The difference in transport efficiency along x' and y' is taken to be small ($\epsilon << T$). Forming the intensity,

$$I = \vec{E_f^*} \cdot \vec{E_f}$$
$$= T^2 + \frac{\epsilon^2}{4} + \epsilon T \cos \delta_{CP} \cos 2\theta - \epsilon T \sin \delta_{CP} \sin \delta_{PS} \sin 2\theta, \tag{6.18}$$

we see that the final intensity of the beam is modulated by the phase shifts induced by the CP and PS cells and the orientation of the asymmetric transport element. We allow the CP and PS cells to induce retardations that provide a fully general description of elliptically polarized light. We choose a particular way to write them, however, so that the asymmetry has a simple form:

$$\delta_{CP}^R = -(\frac{\pi}{2} + \alpha_1) - \Delta_1, \qquad\qquad \delta_{CP}^L = +(\frac{\pi}{2} + \alpha_1) - \Delta_1, \tag{6.19}$$

$$\delta_{PS}^R = -\alpha_2 - \Delta_2, \qquad\qquad \delta_{PS}^L = +\alpha_2 - \Delta_2,$$

where the superscripts R, L indicate right- and left-helicity light and the imperfect phase shifts have been parameterized in terms of "symmetric" (α) and "antisymmetric" (Δ) pieces such that $\alpha_1 =$

$\Delta_1 = \alpha_2 = \Delta_2 = 0$ corresponds to perfectly circularly polarized light. We give the phases from the CP cell a subscript "1" because Stokes parameter S_1 is particularly sensitive to δ_{CP}. Similarly, the phases induced by the PS cell carry a subscript "2" to emphasize that Stokes parameter S_2 is particularly sensitive to δ_{PS}. These sensitivities are evident from the Stokes vector for the light following the PS cell in this parameterization (where the small-angle approximation is made):

$$
\begin{aligned}
S_1^R &= -\alpha_1 - \Delta_1, & S_1^L &= -\alpha_1 + \Delta_1, \\
S_2^R &= -\alpha_2 - \Delta_2, & S_2^L &= -\alpha_2 + \Delta_2, & (6.20)\\
S_3^{H,R} &= +1, & S_3^{H,L} &= -1.
\end{aligned}
$$

The reason for the names "symmetric" and "antisymmetric" is apparent from Figure 6.8. A nonzero α phase shift (Figures 6.8a and 6.8b) turns circular polarization into elliptical polarization for which both helicities have the same major and minor axes, i.e., the phase shift affects the two polarization ellipses symmetrically. A nonzero Δ phase (Figures 6.8c and 6.8d), however, results in elliptical polarization for which the two polarization ellipses have their major and minor axes interchanged, an antisymmetric behavior.

The parameterization given in equations 6.19 gives a completely general description of the elliptical polarization reaching the cathode, where additional phase shifts from components downstream of the CP and PS cells (providing they impose unitary transformations on the polarization vector) can be included as additional contributions to the α's and Δ's. Two special cases, the addition of a slightly birefringent optic and the addition of an imperfect half-wave plate, are discussed below in section 6.3.4; in those cases we separate out from the α's and Δ's the contributions made by those optics in order to make explicit the helicity-correlated effects they induce.

Before calculating A_I, we can argue that to first order, only the antisymmetric phase shifts Δ_1 and Δ_2 contribute to it. From equations 6.20, we see that $S_1^R - S_1^L = -2\Delta_1$ and $S_2^R - S_2^L = -2\Delta_2$. The helicity-correlated difference in the amount of linear polarization depends solely on the
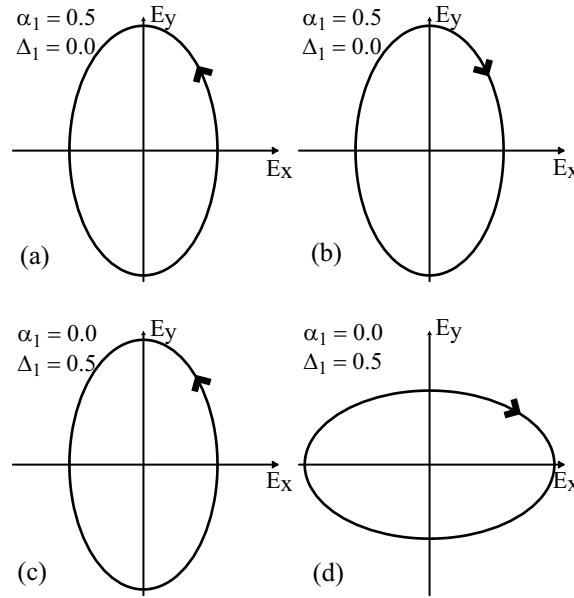
Figure 6.8: a) and b) Polarization ellipses generated for right- and left-helicity light, respectively, allowing α_1 to be nonzero. c) and d) Polarization ellipses generated for right- and left-helicity light, respectively, allowing Δ_1 to be nonzero. In each case, the other phases in equations 6.19 are set to zero. The arrows indicate the direction of increasing time.

antisymmetric phases. That this can give rise to A_I can be seen by considering again the ellipses in Figure 6.8. If one imagines that the polarization ellipses are propagated through an asymmetric transport element with greater transmission along the vertical axis than the horizontal, it is clear that the ellipses with symmetric phase shifts are transmitted with equal intensity while the ellipses with antisymmetric phase shifts are not.

Finally, we insert equations 6.19 into equation 6.18 and calculate A_I. We use the small-angle approximation and only keep terms that are first order in phase shifts and first order in ϵ:

$$A_I = \frac{I(\delta_{CP}^R, \delta_{PS}^R) - I(\delta_{CP}^L, \delta_{PS}^L)}{I(\delta_{CP}^R, \delta_{PS}^R) + I(\delta_{CP}^L, \delta_{PS}^L)} = -\frac{\epsilon}{T}[(\Delta_1 - \Delta_1^0)\cos 2\theta + (\Delta_2 - \Delta_2^0)\sin 2\theta]. \qquad (6.21)$$

We allow that residual birefringence in the Pockels cells or the optics downstream of them may introduce offsets by including the terms Δ_1^0 and Δ_2^0. Note that birefringence in downstream optics can only contribute antisymmetric (Δ-type) phase shifts. The formalism above assumes that the asymmetric transport element is a component of the optical system. Examples would include any

optical element that is not exactly normal to the beam. However, equation 6.21 remains valid if the optical analyzing power is replaced by a cathode with a QE anisotropy. The strained GaAs cathodes in use at SLAC provide the dominant analyzing power in the system.

6.3.2 PITA Slopes

Note that A_I depends linearly on the two antisymmetric phase shifts, Δ_1 and Δ_2. This allows us to define two "PITA slopes" m_1 and m_2 that are easily measurable and characterize the sensitivity to residual linear polarization of a given optical system and analyzer. The PITA slopes play a central role in our techniques for minimizing $^{\text{beam}}A_{\text{LR}}$'s. In practice, it is convenient to express the asymmetry formula in terms of these observables:

$$m_1 = -\frac{\epsilon}{T}\cos 2\theta$$
$$m_2 = -\frac{\epsilon}{T}\sin 2\theta \tag{6.22}$$
$$A_I = m_1 \cdot (\Delta_1 - \Delta_1^0) + m_2 \cdot (\Delta_2 - \Delta_2^0.)$$

The phases Δ_1 and Δ_2 can be converted to voltages using equation 6.4. By adjusting the voltages on the CP and PS cells in an antisymmetric fashion, one can adjust the size of either the Stokes 1 or the Stokes 2 components, and thus the size of A_I. For instance, suppose one optimizes the laser circular polarization after the PS cell (using the HF to maximize or minimize the transmitted light) and finds that the CP cell voltages should initially be set to $V_1^R = +2700$ V and $V_1^L = -2700$ V. To measure the CP cell's PITA slope, one applies offset voltages Δ_1 and measures the resulting A_I as shown in Figure 6.9. For $\Delta_1 = +200$ V, we have $V_1^R = +2900$ V and $V_1^L = -2500$ V in this example. Once the PITA slopes are measured and A_I is measured for $\Delta_1 = \Delta_2 = 0$, offset voltages for Δ_1 and Δ_2 can be applied to null A_I. This procedure is further described in section 6.4.
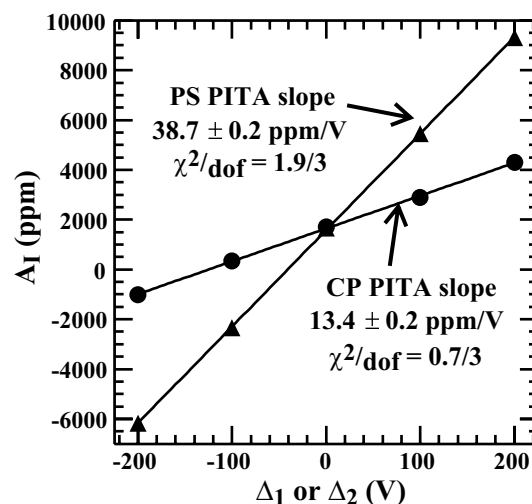
Figure 6.9: PITA slopes for both the CP and PS cells from T-437. Slopes are plotted in terms of ppm of intensity asymmetry per volt of antisymmetric offset voltage applied to the Pockels cells and are typical values for strained GaAs cathodes. Reprinted from [103].

6.3.3 Spatial Variation of Birefringence

We have seen that A_I is directly proportional to $\Delta_1 - \Delta_1^0$ and $\Delta_2 - \Delta_2^0$. We have assumed, however, that if an optical element introduced a phase shift Δ, the phase shift is the same regardless of the point on the face of the element through which the light passed. What if the phase shift varied across the face of the optical element? If we allow that the residual birefringences Δ_1^0 and Δ_2^0 may have a spatial dependence to them, then it follows that A_I also has a spatial dependence. A spatially varying A_I opens the possibility of higher-order helicity correlations. For instance, a laser beam with a Δ_1^0 varying linearly in x as in Figure 6.10a produces an electron beam with a linearly varying A_I. This variation has the effect of shifting the centroids of the right- and left-helicity electron beams in opposite directions as illustrated in Figure 6.10b and yields an electron beam with a helicity-correlated horizontal position difference. Such effects are certainly present in the Pockels cells and are likely present at some level in the downstream optics as well.

A spatially varying Δ retardation is one of the dominant sources of higher-order (position, spot size, and spot shape) helicity correlations in the spatial profile of the electron beam. A convenient way to characterize the spatially varying phase shift is via "moments" similar to the moments of a
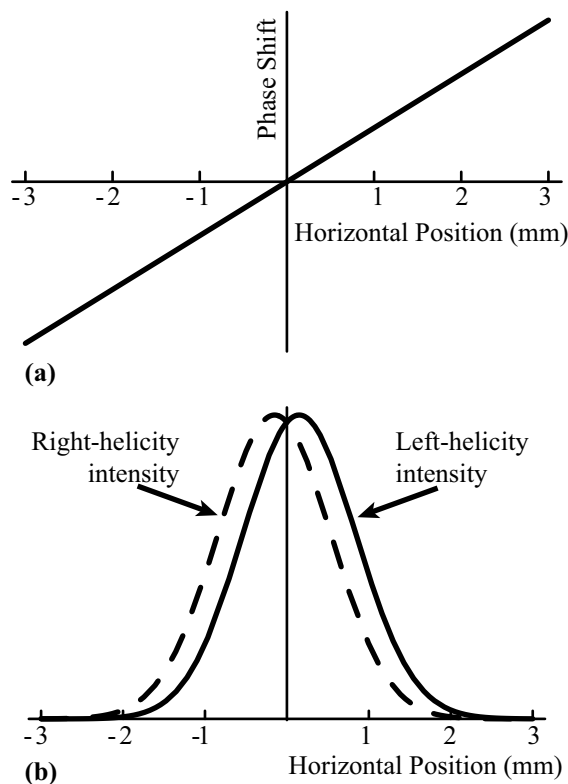
Figure 6.10: Demonstration of the effect of a linear gradient in the phase across the face of the laser beam on the resulting spatial intensity profile of the electron beam. a) The linear gradient in phase, exaggerated to demonstrate the effect. b) The resulting intensity profiles for right- and left-helicity electron beams, assuming the incident laser beam had a gaussian profile. The gradient shifts the centroids of the right- and left-helicity beams in opposite directions, generating a helicity-correlated position difference.

statistical distribution. Each moment can then be connected to a particular $^{\text{beam}}A_{\text{LR}}$. The zeroth moment (the average phase shift across the beam) gives rise to A_I. The first moment is related to the gradient in phase shift across the beam and gives rise to $D_{X(Y)}$. The second moment is related to the curvature of the phase shift across the beam and gives rise to spot size differences. Similarly, higher-order moments can be related to higher-order helicity correlations in the beam profile. Note from equation 6.22 that the sensitivity of the electron beam to spatial variations in Δ_1^0 and Δ_2^0 scales with m_1 and m_2, respectively. We discuss characterizing and minimizing such effects further in section 6.4.1.

6.3.4 Vacuum Window Birefringence and Half-Wave Plate Cancellation

As we consider how to suppress $^{\text{beam}}A_{\text{LR}}$'s arising from residual linear polarization, it is useful to separate out of the offset terms Δ_1^0 and Δ_2^0 the contributions that arise from the insertable half-wave plate used for slow helicity reversal and the vacuum window at the entrance to the polarized electron gun. The vacuum window possesses a significant stress-induced birefringence and is unavoidably downstream of the half-wave plate and the Asymmetry Inverter, making it difficult to arrange cancellations of helicity-correlated asymmetries that arise from it. For the remainder of the chapter, we redefine Δ_1^0 and Δ_2^0 to exclude the residual birefringence associated with the vacuum window and the insertable half-wave plate, each of which we consider separately. We model the vacuum window as a retardation plate with a small retardation β and an arbitrary orientation angle ρ measured from the horizontal axis. The vacuum window can then be represented as

$$J_{VW} = \begin{bmatrix} \cos^2\rho + e^{i\beta}\sin^2\rho & (1 - e^{i\beta})\sin\rho\cos\rho \\ (1 - e^{i\beta})\sin\rho\cos\rho & \sin^2\rho + e^{i\beta}\cos^2\rho \end{bmatrix}. \tag{6.23}$$

The final electric field vector including the vacuum window is

$$\overrightarrow{E_f} = J_{AT} \cdot J_{VW} \cdot J_{PS} \cdot J_{CP} \cdot \overrightarrow{E_i}. \tag{6.24}$$

The vacuum window contribution, having been separated out of Δ_1^0 and Δ_2^0, manifests itself as a third term in the asymmetry equation:

$$A_I = -\frac{\epsilon}{T}[(\Delta_1 - \Delta_1^0)\cos 2\theta + (\Delta_2 - \Delta_2^0)\sin 2\theta + \beta\sin(2\theta - 2\rho)]. \tag{6.25}$$

Next we consider the insertion of the half-wave plate used for slow helicity reversal, as discussed in sections 6.2.1 and 6.4.5. Here we focus on how the half-wave plate manipulates residual linear polarization. We want to understand to what degree a cancellation of position and spot size differences can be achieved if they arise from spatial variations in the residual birefringence of

particular optical elements.

We assume that downstream of the PS cell we have an imperfect half-wave plate followed by the vacuum window. The half-wave plate is allowed an arbitrary orientation ψ and a deviation γ from perfect half-wave retardation and can be represented as

$$
J_{HW} = \begin{bmatrix}
\cos^2 \psi + e^{i(\pi+\gamma)} \sin^2 \psi & (1 - e^{i(\pi+\gamma)}) \sin \psi \cos \psi \\
(1 - e^{i(\pi+\gamma)}) \sin \psi \cos \psi & e^{i(\pi+\gamma)} \cos^2 \psi + \sin^2 \psi
\end{bmatrix}.
\tag{6.26}
$$

The final electric vector is calculated as

$$
\overrightarrow{E_f} = J_{AT} \cdot J_{VW} \cdot J_{HW} \cdot J_{PS} \cdot J_{CP} \cdot \overrightarrow{E_i},
\tag{6.27}
$$

and the resulting intensity asymmetry is

$$
A_I = -\frac{\epsilon}{T}[(\Delta_1 - \Delta_1^0) \cos(2\theta - 4\psi) - (\Delta_2 - \Delta_2^0) \sin(2\theta - 4\psi)
$$
$$
- \beta \sin(2\theta - 2\rho) - \gamma \sin(2\theta - 2\psi)].
\tag{6.28}
$$

We compare this result to equation 6.25, bearing in mind that the coefficients multiplying each term (Δ_1^0, Δ_2^0, β, and γ) may have a spatial dependence that could give rise to helicity-correlated position or spot size differences. Comparing the first two terms of each equation, which include the contributions of all optics upstream of the half-wave plate, we see that they have acquired both a relative minus sign and a dependence on the orientation of the half-wave plate. We gain some freedom to choose the PITA slopes by appropriately orienting the half-wave plate, but their values cannot be chosen independently. The optimal cancellation of position and spot size differences would be gained by inserting the half-wave plate in an orientation such that the PITA slopes are unchanged, but the relative minus sign prevents that. However, if one can arrange for one PITA slope to be much larger in magnitude than the other, then one can orient the half-wave plate to preserve the large PITA slope and perhaps still achieve a reasonable cancellation of effects arising

from the upstream optics. Unfortunately, this procedure requires control over the orientation of the cathode's analyzing power and such control is impractical.

Comparing the third terms of equations 6.25 and 6.28, we see that the vacuum window contribution flips sign with insertion of the half-wave plate. The sign flip prevents any cancellation of $^{\text{beam}}A_{\text{LR}}$'s arising from optics downstream of the half-wave plate, motivating us to place the half-wave plate as far downstream as possible.

The half-wave plate itself introduces a fourth term that is proportional to the deviation of its retardation from π. To the extent that this term is significant, it poses an obvious problem for arranging a cancellation.

In summary, higher-order effects are not preserved but change in a complex way with insertion of the half-wave plate, resulting in a decrease in the amount of cancellation. One further strategy that can be pursued is to measure $^{\text{beam}}A_{\text{LR}}$'s for a number of half-wave plate orientations and empirically determine which provides the best cancellation, but again this is not feasible because the half-wave plate is not readily accessible. None of these complications pose a problem for minimizing A_I, however: one simply measures the new PITA slopes and adjusts Δ_1 and Δ_2 accordingly as is discussed more later.

A second option for using a half-wave plate insertion to generate a slow helicity reversal is to insert the half-wave plate between the Clean-up Polarizer and the CP cell (as was done at JLab for HAPPEX). By inserting the half-wave plate with its fast axis at 45° to the horizontal, the initial linear polarization is rotated from horizontal to vertical and the sense of the circular polarization generated by the CP cell is reversed. The half-wave plate matrix for this case is given by equation 6.26 with $\psi = 45°$. The final electric vector is calculated as

$$\overrightarrow{E_f} = J_{AT} \cdot J_{VW} \cdot J_{PS} \cdot J_{CP} \cdot J_{HW} \cdot \overrightarrow{E_i}, \tag{6.29}$$

and A_I becomes

$$A_I = -\frac{\epsilon}{T}[-(\Delta_1 - \Delta_1^0)\cos 2\theta - (\Delta_2 - \Delta_2^0)\sin 2\theta$$
$$-\beta\sin(2\theta - 2\rho) + \gamma\cos 2\theta]. \tag{6.30}$$

The upstream half-wave plate inverts the sign of each of the first three terms relative to eqn. 6.25. Using the half-wave plate in this configuration is guaranteed to flip the sign of any $^{\text{beam}}A_{\text{LR}}$'s arising from spatial variation in birefringence; no cancellation is gained. For E-158, we choose to use a half-wave plate placed as far downstream as possible, immediately before the vacuum window on the polarized gun, to gain the best cancellation possible, accepting that the cancellation is imperfect.

6.4 Techniques for Minimizing $^{\text{beam}}A_{\text{LR}}{}'$s

We have adopted a number of strategies for designing the polarized source optics system that are specifically aimed at minimizing $^{\text{beam}}A_{\text{LR}}$'s. Passive strategies include careful selection and setup of the CP and PS Pockels cells, imaging of the CP cell onto the cathode, and shaping of the laser pulse's temporal profile to compensate for beam loading effects. Active strategies include feedbacks on A_I and $D_{X(Y)}$. Finally, introducing slow reversals of helicity correlations with respect to the physics asymmetry generates cancellations and provides a tool for studying systematic errors. Each of these strategies is described in detail in the following subsections. We finish this section by presenting results on the control of helicity-correlated asymmetries from T-437.

We are motivated to minimize $^{\text{beam}}A_{\text{LR}}$'s via passive means as well as possible before using active feedbacks for two reasons. First, an active feedback on a particular $^{\text{beam}}A_{\text{LR}}$ can generate helicity correlations in other $^{\text{beam}}A_{\text{LR}}$'s as a side effect. Second, minimizing the $^{\text{beam}}A_{\text{LR}}$'s we can control also likely suppresses higher-order $^{\text{beam}}A_{\text{LR}}$'s that we cannot directly control and for which we have no active feedbacks. Similarly, this concern motivates the use of "Phase Feedback" on the intensity asymmetry. Another strategy is to monitor the higher-order moments of the electron beam's spatial intensity profile. We are able to measure the beam's spatial intensity profile with a

wire array located just upstream of the E-158 target. These measurements allow us to determine whether higher-order $^{\mathrm{beam}}A_{\mathrm{LR}}$'s are present in the electron beam at a significant level.

6.4.1   Optimizing the CP and PS cells and the Laser Beam Polarization

We optimize the CP and PS cells by selecting them for uniformity of retardation, orienting them relative to the beam carefully, setting their voltages to maximize the circular polarization after the PS cell, and then adjusting their voltages to minimize A_I on the electron beam. The basic setup of the polarization optics is discussed in section 6.2.1. Here we discuss those aspects of the setup that are specifically related to suppressing $^{\mathrm{beam}}A_{\mathrm{LR}}$'s.

Measuring the PITA Slopes and Correcting the Intensity Asymmetry

As was discussed in section 6.3.2, the PITA slopes characterize the sensitivity of a particular optical system and cathode to the presence of small linear polarization components and provide a key tool for minimizing A_I. We determine the PITA slope for the CP cell by first measuring A_I on the electron beam as we vary Δ_1 in five steps over the range ± 200 V (or $\sim \pm 7°$, see equation 6.4) and then fitting a line to the resulting data. Similarly varying Δ_2 yields the PS cell PITA slope. The PITA slopes for T-437 are shown in Figure 6.9. We can then define a "voltage space" representing a two-dimensional plane whose x- and y-axes correspond to Δ_1 and Δ_2. Considering again equation 6.22, we see that if we set the left-hand-side equal to zero, we define a line in this voltage space along which the intensity asymmetry is zero, the "$A_I = 0$ line." As was discussed in section 6.2, the voltages determined for the CP and PS cells using the Helicity Filter need to be adjusted to compensate for phase shifts in the optics downstream of them. This adjustment is equivalent to moving onto the $A_I = 0$ line. The $A_I = 0$ line can be clearly seen in Figure 6.11. These data were taken in the Gun Test Laboratory (on a different cathode than those used for the E-158 runs), which reproduces the first several meters of the accelerator. The point of large A_I at the origin is the intensity asymmetry measured using the nominal voltages
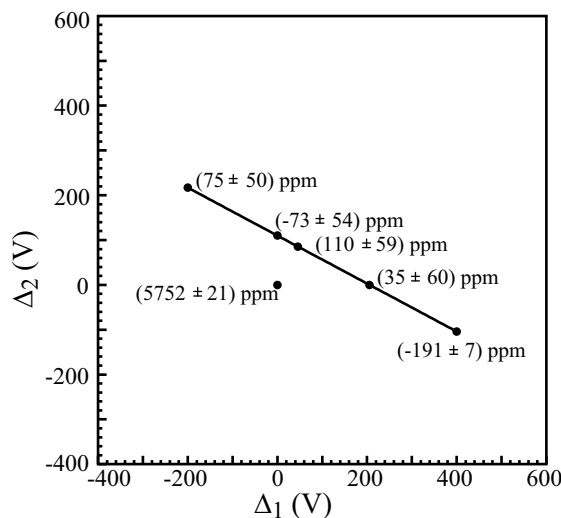
Figure 6.11: Electron beam intensity asymmetry measured along the $A_I = 0$ line and at $\Delta_1 = \Delta_2 = 0$.

determined via the Helicity Filter. We have to choose a particular point on the line as optimal, and our strategy is to move toward the $A_I = 0$ line in a perpendicular fashion in order to change the laser beam polarization by the minimum amount necessary to zero A_I. The required Δ_1 and Δ_2 are then determined by

$$\Delta_1 = -\frac{A_I \cdot m_1}{m_1^2 + m_2^2}, \qquad \Delta_2 = -\frac{A_I \cdot m_2}{m_1^2 + m_2^2} \qquad (6.31)$$

where A_I is the measured intensity asymmetry that needs to be corrected.

We verify that this is a good choice of voltages by performing a similar scan of Δ_1 and Δ_2 and showing that the voltages which maximize the electron beam's polarization agree with those found by using equations 6.31. This check requires that the electron beam can be brought into End Station A in order to use the Møller polarimeter located there. Figure 6.12 shows an example of such a study. In Figure 6.12, the electron beam polarization is measured as a function of Δ_2, with $\Delta_1 = 0$. The peak polarization is found to be at an offset voltage of $\Delta_2 = (-15 \pm 32)$ V, which is consistent with the values found by using equation 6.31 to move onto the $A_I = 0$ line. Table 6.3 summarizes typical operating voltages for the CP and PS cells as measured with the HF
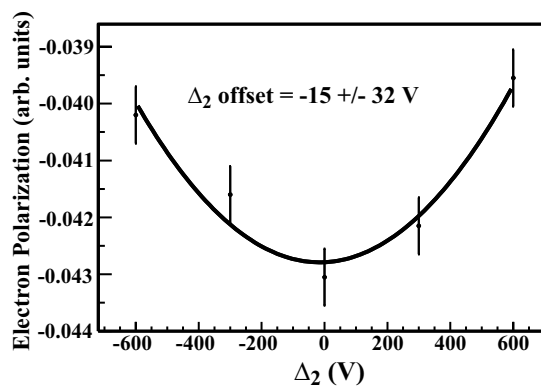
Figure 6.12: Electron beam polarization as a function of PS cell offset Δ_2. The CP cell offset $\Delta_1 = 0$ V. A parabola is fit to the data to approximate the $\cos(\frac{\pi \cdot \Delta_2}{V_{\lambda/2}})$ dependence for $\Delta_2 \ll V_{\lambda/2}$.

scans and after either using the PITA slopes to null A_I or using the Møller polarimeter to measure the peak electron beam polarization.

Table 6.3: Typical operating voltages for the CP and PS cells for production of right- and left-helicity light for E-158 2002 Physics Run I.

	CP Right	CP Left	PS Right	PS Left
HF Scan	2607 V	-2732 V	-5 V	-9 V
$\lambda/2$ OUT Null IA	2574	-2765	-5	-9
$\lambda/2$ OUT Polarimeter	2582 ± 40	-2757 ± 40	-20 ± 32	-24 ± 32
$\lambda/2$ IN Null IA	2736	-2603	-105	-109
$\lambda/2$ IN Polarimeter	2667 ± 39	-2672 ± 39	-159 ± 35	-163 ± 35

It is also interesting to note that the position differences are typically sensitive to the choice of location along the $A_I = 0$ line, as demonstrated in Figure 6.13. These data were taken in the Gun Test Laboratory concurrent with the data shown in Figure 6.11. Here, D_X and D_Y are plotted as a function of Δ_1, with Δ_2 correspondingly set to null A_I. The physical mechanism underlying this behavior is not understood, although the sensitivity of position differences to the choice of Δ_1 and Δ_2 has been observed to depend on the ratio of m_1 to m_2 and on the choice of cathode. One possibility is that this observation is caused by variations in the magnitude or orientation of the analyzing power across the face of the cathode. In most cases, the dependence of $D_{X(Y)}$ on the choice of Δ_1 and Δ_2 was observed to be too small to provide a useful tool for minimizing $D_{X(Y)}$.
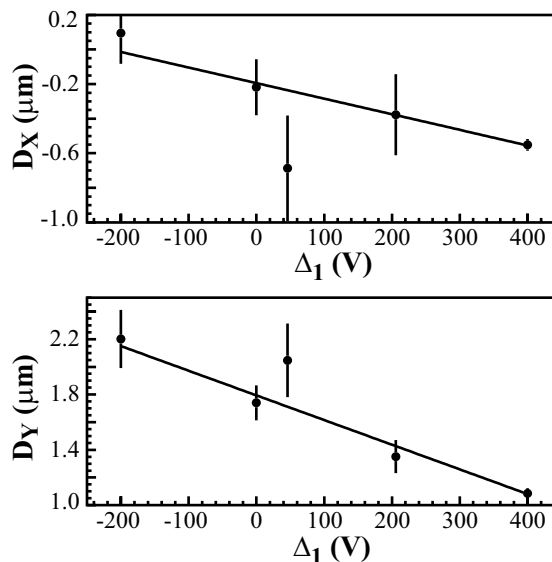
Figure 6.13: Electron beam position differences as a function of Δ_1 as Δ_1 and Δ_2 are simultaneously adjusted to slide along the $A_I = 0$ line.

This fact also suggests that the mechanism which gives rise to this dependence is not one of the dominant mechanisms for generating $^{\text{beam}}A_{\text{LR}}$'s in the SLAC system.

Selection and Setup of Pockels Cells

The presence of spatially varying residual birefringence in the Pockels cells makes the selection of the Pockels cells and the setup of the beam through them important for suppressing helicity-correlated position and spot size differences. We studied the residual birefringence in six QX2035 and one QX1020 Pockels cells and found that the peak-to-peak change in the residual birefringence across them varied between $\sim 1.5-7$ nm, depending on the Pockels cell. A typical study of a Pockels cell, made in the Gun Test Laboratory, is shown in Figure 6.14. The measurements are made by placing a linear polarizer immediately after the Pockels cell in order to maximize the analyzing power.* By orienting the polarizer at 45˚ to the Pockels cell's fast axis, we gain maximum sensitivity to variations in its residual birefringence. The beam is detected by a linear array photodiode.†

---

*In the case of a polarizer, the asymmetry expression must be modified because the polarizer does not satisfy the assumption $\epsilon \ll T$. The asymmetry becomes $A_I = -\frac{4\epsilon T}{\epsilon^2+4T^2}[(\Delta_1 - \Delta_1^0)\cos 2\theta + (\Delta_2 - \Delta_2^0)\sin 2\theta]$.

†Model A2V-76, UDT Sensors Inc., Hawthorne, CA, USA.

Twelve elements in the central portion of the array are instrumented, alternating instrumented and uninstrumented elements, providing a total detection area of 6.45 mm $\times$ 6.44 mm with 50% coverage. The resulting signals are analyzed to determine the helicity-correlated intensity asymmetry and, along a single axis, the helicity-correlated position and spot size differences. The position difference is obtained by computing the weighted mean of the position for each helicity according to $\overline{x}^{R(L)} = \sum_i (I_i^{R(L)} x_i^{R(L)}) / \sum_i I_i^{R(L)}$, where x_i is the position of the ith element and $I_i^{R(L)}$ is the intensity measured by the ith element for right- (left-) helicity pulses. The spot size difference is similarly calculated as the difference between the *rms*'s for right- and left-helicity pulses. The detector can be rotated by 90° to measure position and spot size differences along the other axis. The detector is placed immediately after the polarizer in order to minimize the lever arm over which helicity-correlated lensing or steering differences can operate.

For the particular study shown in Figure 6.14, the polarizer was oriented to transmit vertically polarized light (yielding a PITA slope $m_1 = 550$ ppm/V), the PS cell was removed, and the laser beam had a sigma of 1 mm. The laser beam remained fixed in position while the CP cell was translated horizontally. The three plots in Figure 6.14, from top to bottom, show the intensity asymmetry, horizontal position difference, and horizontal size difference on the laser beam as a function of the horizontal position of the CP cell. Based on the analysis given in section 6.2.4, we interpret the variation in the intensity asymmetry as a spatial variation in the magnitude of the CP cell's residual birefringence. The peak-to-peak variation in the intensity asymmetry of 1.1% corresponds to a peak-to-peak variation in the phase shift of 1.5 nm, consistent with the expected level of residual birefringence variation for this model of Pockels cell. There is a clear though imperfect correlation between the slope of the intensity asymmetry curve and the size of the position difference: at a horizontal setting of 10, for instance, the intensity asymmetry reaches its maximal positive slope and the position difference also reaches an extremum. Likewise, the position differences cross through zero at two points, 12.5 and 16.7, where the slope of the intensity asymmetry curve is near zero. A similar imperfect correlation can be identified between
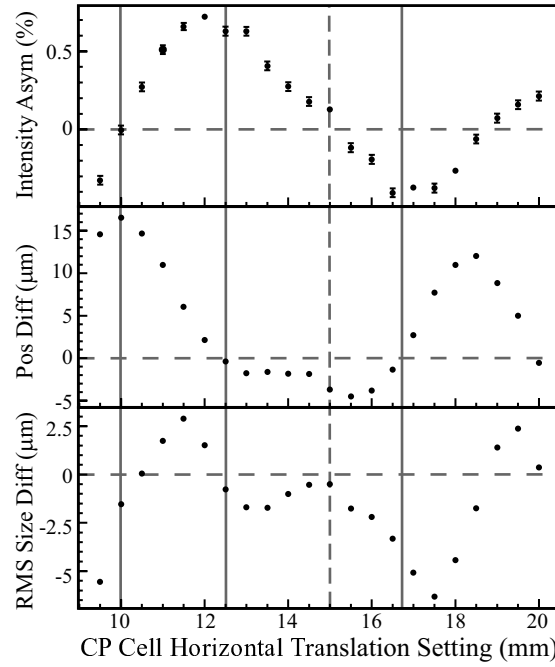
Figure 6.14: a) The helicity-correlated intensity asymmetry measured on the laser beam as a function of the Pockels cell's position as the Pockels cell is translated horizontally and the laser beam remains stationary. b) Laser spot horizontal position difference vs. Pockels cell position. c) Laser spot horizontal size difference vs. Pockels cell position. The dashed vertical line indicates the position at which the laser beam is centered on the Pockels cell. The solid vertical lines mark positions discussed in the text.

the curvature of the intensity asymmetry curve and the size of the spot size difference. For example, the spot size difference reaches extrema of opposite signs at horizontal settings of 11.5 and 17.5, points where the intensity asymmetry exhibits relatively large degrees of curvature of opposite signs.

The $^{\text{beam}}A_{\text{LR}}$'s generated by birefringence gradients scale with the magnitude of the PITA slope; considering typical $18 - 50$ ppm/V PITA slopes arising from the analyzing power of the cathode and taking into account a factor of 2.5 magnification in spot size from the CP cell to the cathode, this Pockels cell would yield position differences as large as $1.3 - 3.8$ μm and spot size differences as large as $0.5 - 1.5$ μm on the electron beam.

We chose the two QX2035 Pockels cells with the smallest gradients in birefringence and least curvature to use as the CP and PS cells. We placed them on two-axis translation stages in order to be able to optimize in situ the points on the crystals through which the laser beam passes. Because the gradients across these two Pockels cells are significantly smaller than those observed on other cells and the cathode used during 2002 Physics Run I has an analyzing power that is a factor of two smaller than the previous cathode, the sensitivity of $^{\text{beam}}A_{\text{LR}}$'s to their translation is significantly reduced. In addition, the contributions to $^{\text{beam}}A_{\text{LR}}$'s from these two Pockels cells are relatively small when they are centered on the beam (similar to the Pockels cell scan shown in Figure 6.14). We decided to run with them centered on the beam for Physics Run I.

We also observed that by minimizing the diameter of the laser beam at the Pockels cells we could further reduce our sensitivity to gradients in the residual birefringence. However, because the Pockels cells are naturally birefringent,[‡] it is important to keep the beam well collimated passing through them for two reasons: to ensure that all rays receive an equal retardation and to minimize the correlation between position and angle within the beam. We designed the upstream optical transport system (consisting of the three lenses on the Flash:Ti, Diagnostics, and Helicity Control benches, see Figures A.1 and 6.5) to bring the beam through a gentle focus at the CP and PS

[‡]The optic axis has $n_e = 1.4638$ and the transverse plane has $n_o = 1.5021$ at $\lambda = 694$ nm.

cells. Balancing the conflicting requirements that the beam be both small and well collimated, we found the optimum beam sigma to be approximately 1 mm at the CP and PS cells.

6.4.2 Imaging and Transport Optics

As was discussed earlier in section 6.2.3, we image the CP cell onto the cathode to minimize helicity-correlated lensing or steering differences that may arise from its high-voltage operation. Studies of helicity correlations arising from the helicity-flipping Pockels cell were made in preparation for the Bates ^{12}C experiment [112]. They clearly demonstrated that the Pockels cell produced helicity-correlated lensing or steering differences and that imaging could be used to suppress these differences. While exhaustive studies of helicity-correlated lensing and steering differences have not yet been carried out on the SLAC system, we use a similar model of Pockels cell and have seen significant evidence for the presence of such effects in a variety of measurements. Uncontrolled, we suspect that they have the potential to contribute to $^{beam}A_{LR}$'s at a level comparable to or even greater than birefringence gradients. We estimate that by imaging the CP cell to the cathode we have reduced the effective lever arm from ~ 25 m to a few centimeters, thereby strongly suppressing any helicity-correlated lensing or steering differences that may be present. We also optimized the transport optics to preserve a high degree of circular polarization as described in section 6.2.3.

6.4.3 Beam Loading Compensation

The primary mechanism for introducing a helicity-correlated energy asymmetry, A_E, into the electron beam is through "beam loading." The electrons early in a pulse absorb power from an accelerating cavity as it accelerates them. Electrons later in the pulse therefore find less power available to accelerate them. If the electron pulse's temporal profile were flat, the later electrons would be accelerated less, creating an energy spread along the length of the pulse. In addition, a further time dependence to the power available for acceleration is imposed by the time structure of the RF voltage applied to the cavities. We compensate for this beam loading effect and the

curvature of the applied RF voltage by shaping the laser pulse's intensity profile with TOPS as described in section A.2 and Figure A.9. The optimal temporal profile is sloped, with its intensity decreasing with time. The average beam loading (over the length of the pulse) is 5%, and the energy spread is reduced to 0.1% by the pulse shaping and other accelerator tuning techniques [110]. Beam loading introduces an anticorrelation between the intensity and the energy of the beam: we would expect that the 0.5% intensity jitter during Physics Run I should drive an energy jitter of 0.025%. The energy jitter was typically measured to be 0.03% during the run. To the extent that the jitter in the beam energy is in fact driven by jitter in the beam intensity, A_E tracks A_I and benefits from the performance of the IA feedback loop described below. If we achieve our goal of $A_I < 2 \cdot 10^{-7}$ then we should also achieve our goal of $A_E < 2 \cdot 10^{-8}$, providing other mechanisms do not contribute significantly.

6.4.4 Active Feedbacks on $^{\text{beam}}A_{\text{LR}}$'s

Active feedbacks on A_I and $D_{X(Y)}$ provide additional suppression of these helicity-correlated asymmetries beyond what is achieved by the polarization optimization procedures and imaging. The implementations of the IA, POS, and Phase Feedback loops are described in the following subsections. The hardware for the feedback loops is described above in section 6.2.4. First, we outline the general algorithm and discuss how the active nature of the feedback can suppress the mean value of the quantity being fed back on faster than one would expect from counting statistics. Performance results for the feedback loops from T-437 are discussed in section 6.4.6.

Feedback Algorithm and 1/N Scaling

The feedback loops each require three ingredients: a control device capable of being driven in a helicity-correlated fashion, the optical system and cathode which generate $^{\text{beam}}A_{\text{LR}}$'s, and a set of diagnostic devices on the electron beam to measure $^{\text{beam}}A_{\text{LR}}$'s. The measured beam asymmetry (or difference, in the case of position) can be represented as a sum of the contributions from each

part of the loop,

$$A_{beam} = A_{ctrl} + A_{opt} + A_{stat},\qquad(6.32)$$

where A_{ctrl} is the asymmetry induced by the control device, A_{opt} is the helicity-correlated asymmetry caused by the optics and cathode, and A_{stat} is the contribution from statistical jitter in the measured electron beam parameter. The asymmetry is averaged over a "minirun" of M pulse pairs (where each pair consists of one pulse of each helicity) and then a correction is applied on the following minirun according to the general algorithm

$$A^1_{ctrl} = 0,$$
$$A^n_{ctrl} = A^{n-1}_{ctrl} - gA^{n-1}_{beam},\qquad(6.33)$$

where "g" is the gain of the loop and "n" is the number of the minirun.

An active feedback loop can cause the central value to converge to zero faster than one would naively expect based on a knowledge of the jitter in the measurement and the available statistics. Consider an ideal feedback loop, in which the control device has perfect resolution, a unity gain is chosen, A_{opt} is constant, and the statistical jitter in the beam parameter contributes a noise asymmetry A_{stat} for each minirun. The noise asymmetry contribution has a width σ_{stat}. Then allowing the feedback to run for N miniruns, the algorithm outlined above generates the following behavior:

$$
\begin{aligned}
A^1_{ctrl} &= 0, & A^1_{beam} &= A^1_{ctrl} + A_{opt} + A^1_{stat} \qquad (6.34)\\
A^2_{ctrl} &= A^1_{ctrl} - A^1_{beam}, & A^2_{beam} &= A^2_{ctrl} + A_{opt} + A^2_{stat},\\
&= -A_{opt} - A^1_{stat}, & &= -A^1_{stat} + A^2_{stat},\\
&\;\;\vdots & &\;\;\vdots \\
A^N_{ctrl} &= A^{N-1}_{ctrl} - A^{N-1}_{beam}, & A^N_{beam} &= A^N_{ctrl} + A_{opt} + A^N_{stat},\\
&= -A_{opt} - A^{N-1}_{stat}, & &= -A^{N-1}_{stat} + A^N_{stat}.
\end{aligned}
$$

Averaging the N miniruns then yields

$$\overline{A} = \frac{1}{N} \sum_{n=1}^{N} A_{beam}^n \tag{6.35}$$

$$= \frac{1}{N} \left(A_{opt} + A_{stat}^1 - A_{stat}^1 + A_{stat}^2 - \cdots - A_{stat}^{N-1} + A_{stat}^N \right)$$

$$= \frac{1}{N} \left(A_{opt} + A_{stat}^N \right)$$

The active nature of the feedback arranges a cancellation of the contributions to the asymmetry arising from statistical jitter for all miniruns except the last. We see that the mean measured asymmetry scales as $(A_{opt} + A_{stat}^N)/N$. We refer to this as "1/N scaling," in contrast with the normal statistical behavior in the absence of feedback for which the mean measured asymmetry scales as $A_{opt} + \sigma_{stat}/\sqrt{N}$.

Intensity Asymmetry Feedback

The IA loop is responsible for ensuring that A_I converges to zero and that it does so rapidly enough to meet the requirements of equations 6.3 within the available statistics. Because the intensity jitter is $\sim 0.3 - 1.0\%$, there are not necessarily enough statistics ($\sim 3 \cdot 10^8$ pairs) in the experiment to ensure that the final asymmetry meets E-158's requirement of $A_I < 2 \cdot 10^{-7}$, so we require that the IA loop provide sufficient 1/N scaling to achieve this requirement.

The IA Pockels cell controls the loop by introducing into the laser beam a helicity-correlated phase shift which the Cleanup Polarizer transforms into the desired intensity asymmetry correction. The transmission through the Cleanup Polarizer is given by

$$T = \cos^2 \left(\frac{V - V_0^{IA}}{V_{\lambda/2}^{IA}} \cdot \frac{\pi}{2} \right), \tag{6.36}$$

where T is the transmission, V_0^{IA} is an offset voltage which arises from residual birefringence or misalignment, and $V_{\lambda/2}^{IA}$ is the half-wave voltage of the IA cell. We reduce our sensitivity to drifts in V_0^{IA} by running both states nominally at 99% transmission. Doing so also has the effect of

reducing the amplitude of helicity-correlated voltage changes. The feedback is initialized with both left and right states at the bias voltage V_B that yields a bias transmission $T_B = 99\%$,

$$A_{IA}^1 = 0,$$
$$V_R^1 = V_B, \tag{6.37}$$
$$V_L^1 = V_B.$$

We apply a correction by increasing the attenuation on the appropriate state according to

$$A_{IA}^n = A_{IA}^{n-1} - A_I^{n-1} \tag{6.38}$$

$$\text{IF } A_{IA}^n \leq 0 \text{ THEN } \quad V_L^n = V_{\lambda/2} \cdot \frac{2}{\pi} \sin^{-1} \left[\left(1 - T_B \cdot \frac{1 - A_{IA}^n}{1 + A_{IA}^n} \right)^{1/2} \right] + V_0,$$

$$V_R^n = V_B,$$

$$\text{ELSE } \quad V_L^n = V_B,$$

$$V_R^n = V_{\lambda/2} \cdot \frac{2}{\pi} \sin^{-1} \left[\left(1 - T_B \cdot \frac{1 + A_{IA}^n}{1 - A_{IA}^n} \right)^{1/2} \right] + V_0.$$

The gain has been set equal to one. The IA cell has a half-wave voltage of ~ 5800 V and can be driven to 750 V, yielding a range of asymmetry correction on the order of $\pm 3\%$, much larger than the typical induced correction of $(1 - 5) \cdot 10^{-4}$.

A number of factors limit the 1/N scaling we can achieve with the IA loop. The ultimate limiting factor is the finite resolution of the beam current monitors, which in our case is typically 50 ppm/pair, negligible compared to the $\sim 0.5\%$ intensity jitter. The more severe limitation on 1/N scaling for our system comes from the fact that while we are running the feedback at 1 GeV, the important measurement of A_I for the experiment is the one made in front of the E-158 target, two miles downstream. Beam losses in the accelerator can add a new source of intensity jitter at a potentially significant level. We are currently evaluating whether this source of jitter is small enough to allow adequate scaling of A_I and are considering using a current monitor at 45 GeV for

the feedback. In addition, matching the data set used in the offline analysis to that used by the feedback to generate 1/N scaling in the online analysis is a solvable but nontrivial challenge. We should also note that to achieve full 1/N scaling one must run with a unity gain.

Phase Feedback

As is discussed in section 6.2.4, the dominant source of A_I is the interaction between phase shifts in the optics and the cathode's analyzing power. Phase Feedback refers to a second layer of feedback on A_I which averages over the IA loop correction for a number of miniruns (typically 30) and then adjusts the CP and PS cell voltages to null the IA loop correction. This procedure provides compensation for drifts in the residual birefringence of the Pockels cells and the optics downstream of them that can cause the IA loop correction to wander at the 100-ppm level. We adjust the CP and PS voltages by an amount proportional to the average asymmetry induced by the IA cell over the last N miniruns, A_{ind}, according to the prescription of equations 6.31 with A_I replaced by $-A_{ind}$. In principle, the Phase Feedback can be used alone to null A_I, but using two layers of feedback provides flexibility. The IA loop can be run on a short time scale to take advantage of 1/N scaling, while the Phase Feedback can be run on a longer time scale that is appropriate for keeping the IA loop correction small. The IA loop alone typically applies a correction at the 100-ppm level, which is three orders of magnitude larger than the physics asymmetry. The Phase Feedback is capable of reducing the IA loop correction to the few ppm level when averaged over several days.

Position Difference Feedback

E-158 requires that the helicity-correlated position differences $D_{X(Y)}$ be below 10 nm averaged over several months of data taking. The position differences are typically several microns at the cathode when no effort is made to control them; with various optimizations (choice of Pockels cells, translation of Pockels cells, choice of operating voltages, and imaging) we achieve $D_{X(Y)}$ as small as $0.5 - 1.0$ μm. We also observe approximately an order of magnitude reduction in $D_{X(Y)}$

between the cathode and the E-158 target. This is due in part to a drop in spot size from a 2.5-mm sigma at the cathode to 1 mm at the target. The remainder comes from emittance growth due to synchrotron radiation emission. The emittance growth causes the spot size to increase, and the additional magnetic focusing required further suppresses the phase space available for $D_{X(Y)}$. The goal is to achieve 1-2 orders of magnitude of suppression of $D_{X(Y)}$ from an active feedback system. The position jitter at the E-158 target is typically $\lesssim 50$ μm per pair so it should be possible to achieve a statistical error on $D_{X(Y)}$ of a few nm averaged over the entire run. The statistical error bar will be small enough that additional suppression from 1/N scaling is not necessary. We use the POS loop to suppress both $D_{X(Y)}$ and $D_{X'(Y')}$ simultaneously. We can use one feedback on the laser beam to suppress two effects on the electron beam because they are not linearly independent. There should only be position differences at the cathode; angle differences at the E-158 target arise because the cathode is not imaged onto it by the electron beam optics.

The piezomirror, described in section 6.2.4, is the control device for the POS loop. A schematic of its operation is shown in Figure 6.15. The points A, B, and C represent the three piezo stacks. The angles α and β represent tilt about the x- and y-axes, respectively. Pure tilts about the x- and y-axes can be achieved by applying voltages to A, B, and C according to

$$
\begin{aligned}
\alpha &= \frac{A - \frac{1}{2}(B + C)}{a}, \\
\beta &= \frac{B - C}{b}, \\
A + B + C &= 0,
\end{aligned}
\tag{6.39}
$$

where A, B, and C are given in millimeters of expansion. The constraint that A, B, and C sum to zero implies that the piezomirror undergoes a pure tilt, with no translation. When the feedback is

initialized, it produces zero correction for the first minirun, and the voltages are set to

$$D^1_{Xpz} = 0 \text{ nm}, \qquad D^1_{Ypz} = 0 \text{ nm},$$

$$A^1_L = 0 \text{ V}, \qquad B^1_L = 0 \text{ V}, \qquad C^1_L = 0 \text{ V}, \qquad (6.40)$$

$$A^1_R = 0 \text{ V}, \qquad B^1_R = 0 \text{ V}, \qquad C^1_R = 0 \text{ V},$$

where D^1_{Xpz} and D^1_{Ypz} are the position differences being induced by the POS loop on the first minirun and now $A^1_{R(L)}$, $B^1_{R(L)}$, and $C^1_{R(L)}$ are given in volts. For subsequent miniruns, the induced position differences and piezomirror voltages evolve according to

$$D^n_{Xpz} = D^{n-1}_{Xpz} - D^{n-1}_X, \quad D^n_{Ypz} = D^{n-1}_{Ypz} - D^{n-1}_Y,$$

$$A^n_L = -A^n_R = \frac{a}{3l} \cdot D^n_{Ypz} \cdot 1.67 \cdot 10^4 (\text{V/mm}), \qquad (6.41)$$

$$B^n_L = -B^n_R = \frac{1}{4l} \cdot (bD^n_{Xpz} - \frac{2}{3}aD^n_{Ypz}) \cdot 1.67 \cdot 10^4 (\text{V/mm}),$$

$$C^n_L = -C^n_R = \frac{1}{4l} \cdot (-bD^n_{Xpz} - \frac{2}{3}aD^n_{Ypz}) \cdot 1.67 \cdot 10^4 (\text{V/mm}),$$

where D^{n-1}_X and D^{n-1}_Y are the position differences measured on the $(n-1)^{th}$ minirun, l is the effective lever arm from the piezomirror to the cathode, and the numerical factor is a conversion factor between voltage applied to a piezo stack and the resulting expansion.

The piezomirror provided a range at the cathode of ± 50 μm helicity-correlated displacement (measured on the electron beam), and a range of ± 4 (± 25) μm in x (y) at the 1-GeV beam diagnostics during T-437. The range has dropped to ± 20 μm at the cathode and $\sim \pm(1-2)$ μm at 1 GeV for the engineering and physics runs because of adjustment of the imaging optics and changes to the accelerator focusing lattice due to requirements for compatibility with other accelerator programs. In fact, the constraints imposed on the electron optics by compatibility of multiple beams are severe enough that it was a challenge to make the POS loop work during Physics Run I. The primary issue was that the phase advances of the electron beam in x and y from the cathode
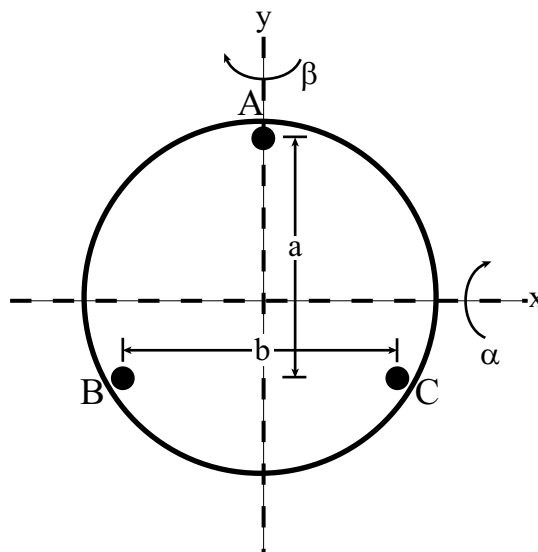
Figure 6.15: A schematic of the piezomirror. The points labelled A, B, and C are the three piezo stacks. The geometric factors a ($= 10.4$ mm) and b ($= 12.0$ mm) are relevant for determining the rotation angles α and β about the x- and y-axes, respectively.

to the 1-GeV diagnostics differed by $\sim 90°$. This made it difficult to find a tune for the electron optics that gave linearly independent beam motion at 1 GeV for x- and y-tilts of the piezomirror. We chose to run the POS loop with a gain of 0.25 to reduce our sensitivity to poor orthogonality between the x- and y-tilts. We were free to choose the gain because we did not need 1/N scaling of the position differences.

6.4.5   Slow Reversals and Cancellations of $^{\mathrm{beam}}A_{\mathrm{LR}}$'s

It is useful to incorporate into the experiment certain "slow reversals" that change the sign of an effect with respect to its influence on the physics asymmetry. Such slow reversals serve two purposes: they generate cancellations of $^{\mathrm{beam}}A_{\mathrm{LR}}$'s and they provide a means of verifying our understanding of the measured detector asymmetry. Having multiple slow reversals allows us to study the quality of cancellation each reversal provides. If a single reversal yields the same central value for the physics asymmetry in both of its states then it provides a convincing cross check that false detector asymmetries (such as those arising from nonzero $^{\mathrm{beam}}A_{\mathrm{LR}}$'s or electronic cross talk) are well understood. However, if the two states disagree, it is difficult to quantify how to make

a correction. One can only average the results and hope that the false asymmetry contribution cancels out. Using multiple reversals provides a number of complementary cross checks, each of which is sensitive to different combinations of false asymmetries. Comparing the quality of agreement between states for each slow reversal may provide a measure of the uncertainty in the physics asymmetry.

Two types of reversal can be identified: those that are designed to reverse the sign of the physics asymmetry (A_{LR}^{ee}) without changing any false asymmetries in the experiment, and those that are designed to reverse the sign of certain $^{\text{beam}}A_{\text{LR}}$'s without changing the physics asymmetry. We have implemented one reversal of each kind in the source optics system: the insertable half-wave plate provides a slow reversal of the physics asymmetry and the Asymmetry Inverter provides a slow reversal of position differences arising from the polarization optics. These two reversals are discussed in more detail below.

Additional slow reversals can be implemented on the electron beam as well. A second means of physics reversal, running the electron beam at two energies, takes advantage of the energy dependence of the rate of g-2 precession of the beam polarization as it is brought around a bend and into End Station A. We run at two energies that each result in longitudinal polarization in End Station A but with a relative phase difference of 180°. For a given electron helicity at the source, the two energies correspond to opposite helicities on target. It would also be useful to implement a second Asymmetry Inverter in the electron beam optics, but this has not yet been done.

The slow and passive nature of these reversals is in marked contrast to the fast helicity reversal provided by the CP cell. The CP cell provides a pulse-by-pulse helicity reversal, and, by virtue of its pseudorandom sequence, one that is insensitive to noise at low frequencies and to drifts in the experimental apparatus (such as gradual changes in the detector phototube gains). The insertable half-wave plate and running at two energies both function as means of "passively" reversing the definition of helicity in the experiment in the sense that they do not involve electronic signals on a pulse-by-pulse basis, as the pulsing of the CP and PS cells do. Certain classes of false

asymmetries are not sensitive to the presence of the half-wave plate or the choice of electron beam energy. These classes of false asymmetries cancel upon averaging data for the two states of each reversal. One prime example is electronic cross talk between the CP cell high-voltage pulse and the data-acquisition electronics.

Half-Wave Plate Reversal

The half-wave plate is expected to provide a good cancellation for many classes of false asymmetries, including those arising from electronic cross talk and helicity-correlated lensing or steering differences from the CP cell. However, as is described in section 6.3.4, the behavior of $^{\text{beam}}A_{\text{LR}}$'s arising from imperfections in the circular polarization of the laser beam depends on the orientation of the half-wave plate in a complicated way, so it is not straightforward to gain a cancellation of these effects. We have two insertable half-wave plates, one on the Helicity Control Bench (which is primarily used for initially determining the operating voltages for the polarization Pockels cells) and one on the Cathode Diagnostics Bench. For physics running we use the Cathode Diagnostics Bench half-wave plate because it is downstream of all other optics except the vacuum window on the electron gun. We toggle the state of the half-wave plate once every 48 hours.

Asymmetry Inverter Reversal

Immediately downstream of the PS cell is the Asymmetry Inverter (AI), which is described in section 6.2.3. Switching between its "+" and "−" optics inverts both the position and angle of the outgoing optics rays. Averaging over all optics rays in the beam, any helicity-correlated position and angle differences resulting from the polarization optics should have opposite signs for the two AI states. We can see this by considering the helicity-correlated position and angle differences for the laser beam entering the AI, averaging over all its optics rays:

$$
D_X = \langle x \rangle_R - \langle x \rangle_L
$$
$$
D_{X'} = \langle x' \rangle_R - \langle x' \rangle_L \, .
$$

$$(6.42)$$

Then for the laser beam exiting the AI, using equation 6.15 we expect

$$D^+_{\widetilde{X}} = -D^-_{\widetilde{X}} = 2.25 D_X$$

$$D^+_{\widetilde{X}'} = -D^-_{\widetilde{X}'} = 0.44 D'_X.$$

(6.43)

Alternate running with equal amounts of physics data in the "+" and "−" modes should yield

$$D_{\widetilde{X}} = D^+_{\widetilde{X}} + D^-_{\widetilde{X}} = 0$$

$$D_{\widetilde{X}'} = D^+_{\widetilde{X}'} + D^-_{\widetilde{X}'} = 0,$$

(6.44)

cancelling any position and angle differences which arise from the polarization optics. However, the AI does not help with cancelling $^{\text{beam}}A_{\text{LR}}$'s arising from downstream optics, and it does not allow cancellation of spot size differences due to their even symmetry.

6.4.6   Measurements of $^{\text{beam}}A_{\text{LR}}$'s During T-437

Measurements of $^{\text{beam}}A_{\text{LR}}$'s were made during T-437 and are reported fully in [103]. T-437 was a one-week beam test in November 2000 which recommissioned the polarized electron source and commissioned the polarization optics, electron beam diagnostics, and SCP and E-158 DAQs that are used for controlling $^{\text{beam}}A_{\text{LR}}$'s. In particular, T-437 was an opportunity to commission the IA and POS loops, measure A_I and $D_{X(Y)}$, and study the effectiveness of the half-wave plate and Asymmetry Inverter cancellations. Here we summarize those results.

Measurements of A_I

We commissioned the IA loop and measured A_I during T-437. A pair of toroids at the 1-GeV point in the accelerator measured the beam current and A_I. The measurement from one toroid controlled the feedback while the second toroid provided an independent measurement that was used to evaluate the systematic error associated with the measurement and to determine the toroid resolution. We used miniruns of 2000 pairs in length, yielding a statistical error per minirun
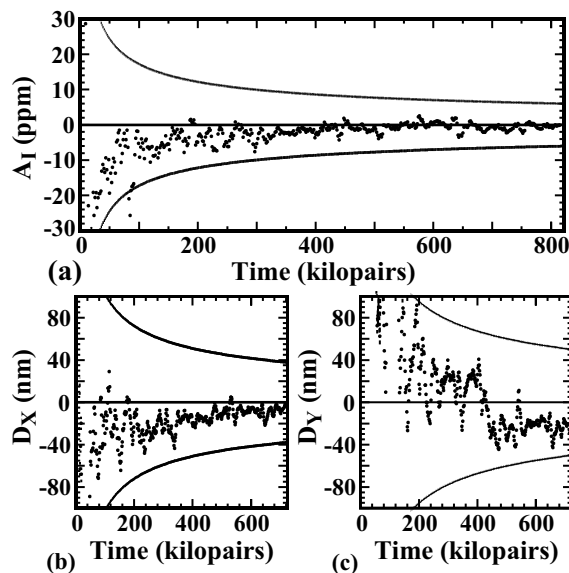
Figure 6.16: Average values of A_I, D_X, and D_Y as a function of time during T-437. Reprinted from [103].

of $\sim 5 \cdot 10^{-4}$, based upon the $\sim 0.6 - 0.8\%$ intensity jitter at that time. Figure 6.16a shows the performance of the IA loop during part of T-437. The mean value of A_I and an envelope representing the one-sigma statistical error (assuming a zero systematic offset) are plotted as a function of time in units of the number of pulse pairs included in the average. For the entire T-437 test, we measured $A_I = 0.2 \pm 5.7$ ppm, where the error bar is the statistical error (i.e., the rms width of the intensity asymmetry distribution divided by the square root of the number of pairs in the distribution). The mean value of 0.2 ppm is consistent with the expected asymmetry of ~ 0.33 ppm assuming $1/N$ scaling. Further evidence for $1/N$ scaling can be seen in Figure 6.16a, where the mean value of A_I rapidly acquires a value significantly less than the statistical error and wanders around zero. T-437 also demonstrated agreement between the two current monitors of 6 ± 12 ppb, where the error is determined by the toroid resolution.

Measurements of $D_{X(Y)}$

We also commissioned the POS loop and measured $D_{X(Y)}$ during T-437. For that test, we used three beam position monitors (BPMs) spaced at 1-m intervals and located at the 1-GeV point

in the accelerator. The middle BPM was the control device for the feedback loop. The position differences measured by the upstream and downstream BPMs were used to predict the position difference at the middle BPM and thereby provide an independent measurement that was used to evaluate the systematic error associated with the measurement and to determine the BPM resolution. We used a minirun length of $10,000$ pulses. T-437 demonstrated that the POS loop closes, as shown in Figures 6.16b and 6.16c. T-437 set a limit at the 20-nm level on the ability of the POS loop to make position differences small and was only limited by the available statistics. The corrections induced by the POS loop are tabulated in Table 6.5. The measurements at the middle (feedback) BPM were found to agree with the predicted value determined by the upstream and downstream BPMs to a level of 2 nm.

Half-Wave Plate Cancellation

We toggled the state of the half-wave plate on the Cathode Diagnostics Bench every two hours during several shifts of T-437 and found that it provided some cancellation of $D_{X(Y)}$, as shown in Table 6.4. For this running period, the IA loop was under control of the SCP DAQ and used a toroid in the injector for its feedback device; the POS loop was not used. The cancellation yields approximately a factor of three reduction in y and an order of magnitude in x. However, the degree of cancellation is extremely sensitive to the details of the source setup, so this past performance cannot be taken as a strong indication of the quality of cancellation from the half-wave plate for future running. A new cathode, realignment of the CP and PS cells, and adjustment of the imaging optics all can affect the ability of the half-wave plate toggling procedure to cancel $D_{X(Y)}$.

Asymmetry Inverter Cancellation

A test of the Asymmetry Inverter during T-437 yielded encouraging results. Table 6.5 lists the corrections applied by the POS loop for runs in each state of the Asymmetry Inverter, along with their average. For these runs, both the IA and POS loops were used under the control of the E-158 DAQ. In the case of the y position differences, for which the correction applied by the POS loop

Table 6.4: Half-wave plate cancellation results. The state of the half-wave plate was toggled every two hours over several shifts. These results are the average measured position differences for that period of time. In calculating the weighted average of the half-wave plate "IN" and "OUT" results, the sign of the "OUT" data is flipped to reflect the reversal of the sign of the physics asymmetry. Reprinted from [103].

Asymmetry	$\lambda/2$ IN	$\lambda/2$ OUT	Weighted Average
BPM 2 X	126 ± 12 nm	119 ± 11 nm	-7 ± 8 nm
BPM 2 Y	-1732 ± 57 nm	-581 ± 51 nm	-461 ± 38 nm

was large, a significant degree of cancellation is seen. It should be noted that in both states the POS loop maintained the measured values of $D_{X(Y)}$ at a level that was consistent with zero.

Table 6.5: Size of corrections applied by the POS loop for alternate states of the Asymmetry Inverter. Reprinted from [103].

Fdbk Correction Induced	-2I State	+2I State	Average
D_X Correction	262 ± 48 nm	-39 ± 71 nm	168 ± 40 nm
D_Y Correction	-862 ± 109 nm	1157 ± 130 nm	-29 ± 84 nm

6.4.7 Performance of Passive and Active Suppression Strategies

We finish this section by comparing the performance of the passive optimization and the active feedbacks. The intensity asymmetry is initially $0.1 - 0.5\%$ after setting the CP and PS cell voltages with the HF. Adjusting Δ_1 and Δ_2 manually to null it brings it to the 100-ppm level. The IA loop reduces A_I by more than 2 orders of magnitude to $\ll$ 1 ppm (for example, T-437 achieved $A_I \sim 0.3$ ppm in a short run and was statistics-limited). The Phase Feedback can reduce the average IA loop correction to the few ppm level.

Helicity-correlated position differences are typically several microns prior to the passive optimization. Optimizing the Pockels cell and laser beam setup and imaging the CP cell onto the cathode reduce $D_{X(Y)}$ to $0.5 - 1.0$ μm. The POS loop further reduces $D_{X(Y)}$ by $\sim$ 2 orders of magnitude at the 1-GeV point in the accelerator (for example, T-437 achieved $D_{X(Y)} \sim 20$ nm

and was statistics limited).

6.5 Summary of Potential Sources of $^{\mathrm{beam}}A_{\mathrm{LR}}'$s

In this section we review the mechanisms for generating $^{\mathrm{beam}}A_{\mathrm{LR}}$'s which we have identified as dominant for the SLAC source. We also mention several potential mechanisms which are not dominant but are possibly present at a smaller level. Table 6.6 provides a summary of the discussion given in the following subsections.

The mechanisms that dominate for the SLAC source may not be the same as those that dominate for other sources. Particular properties of the SLAC source that may influence which mechanisms are important include the particular model of Pockels cell in use (Cleveland Crystals QX2035), the particular cathode used (strained GaAs for T-437 and the 2001 Engineering Run; gradient-doped strained GaAsP for Physics Run I), the long physical distance between the polarization optics and the cathode (~ 25 m), and the large diameter of the laser spot on the cathode (1 cm $1/e^2$ diameter.).

6.5.1 Residual Linear Polarization Coupling to QE Anisotropy

The primary mechanism for generating A_I is residual linear polarization interacting with asymmetric transport elements, as is discussed in section 6.2.4. The key optical elements that introduce residual linear polarization are the CP and PS Pockels cells and the vacuum window, each of which possesses significant residual birefringence. Many optical components are candidates to be asymmetric transport elements, and care must be taken in setting up the optical transport system to minimize such effects. The dominant analyzing power in the system is provided by the cathode's QE anisotropy. A_I can be suppressed either by reducing the amount of residual linear polarization incident on the cathode or by reducing the cathode's QE anisotropy. Neither the half-wave plate nor the AI provide cancellations of this effect.

6.5.2 Birefringence Gradients

As is discussed in sections 6.3.3 and 6.4.1, gradients in the residual birefringence of the CP and PS cells and the vacuum window (and possibly other optics at a lower level) produce a spatial variation in A_I and are a dominant source of helicity-correlated position and spot-size differences. We suppress the contributions from the Pockels cells by carefully selecting and setting up the Pockels cells and by minimizing the beam diameter at their location. The half-wave plate provides an imperfect cancellation (see section 6.3.4) of both position and spot size differences arising from these gradients for optics upstream of it and no cancellation for effects arising from the vacuum window. The Asymmetry Inverter provides some cancellation of position differences from the Pockels cells.

6.5.3 Lensing

Helicity-correlated lensing or steering generated by the CP cell (sections 6.2.3 and 6.4.2) is present in the SLAC system at a significant level. While it is difficult to untangle the relative contributions of lensing and birefringence gradient effects, we believe that imaging has suppressed lensing sufficiently that it is comparable to or smaller than the birefringence gradient effects. When we have isolated effects that can be interpreted as lensing in laser beam measurements, we have observed that the effects cancel with the half-wave plate insertion. In addition, we expect that the Asymmetry Inverter also provides a cancellation of position differences.

6.5.4 Beam Loading

As discussed in section 6.4.3, beam loading is the primary mechanism for inducing an energy asymmetry. We compensate for beam loading by properly shaping the laser pulse (section A.2). If the dominant cause of energy jitter is intensity jitter, then we should gain additional suppression of A_E from the IA loop. Neither the half-wave plate nor the Asymmetry Inverter provides a cancellation of A_E.

6.5.5 Collimation and Spot Size at CP Pockels Cell

A converging or diverging laser beam traversing a Pockels cell acquires a gradient in its retardation that has an effect similar to a birefringence gradient as is discussed in section 6.4.1. Collimating the laser beam at the Pockels cells both minimizes the beam's angular spread and reduces the correlation between position and angle, suppressing these effects. Increasing the beam diameter also reduces this effect but increases the sensitivity to birefringence gradient effects. We compromise by placing a laser beam waist at the CP and PS cells with a size of 1 mm rms.

6.5.6 Cathode Gradients

Since we have observed that spatial variations in Δ_1 and Δ_2 lead to significant helicity-correlated position and spot size differences, it is natural to ask whether similar effects can arise from spatial variations in the other parameters of equation 6.21, the analyzing power ϵ/T and the analyzer orientation θ. We speculate that the physical mechanism underlying the observation that position differences depend on choice of Δ_1 and Δ_2 along the $A_I = 0$ line (section 6.4.1) might be a manifestation of such variations. If this is the case, then we can say that gradients in the cathode strain are a noticeable effect but clearly not the dominant effect in the SLAC system. It is likely that suppressing Δ_1 and Δ_2 also suppresses $^{\text{beam}}A_{\text{LR}}$'s arising from these variations. However, neither the half-wave plate nor the Asymmetry Inverter provides a cancellation.

6.5.7 Electronic Cross Talk

Electronic cross talk between various necessary helicity-correlated signals and the DAQ can cause a mismeasurement of $^{\text{beam}}A_{\text{LR}}$'s and the detector asymmetry. Cross talk can be caused by coupling between either the transmission of the polarization state information or the high voltage pulse applied to the CP cell (which acts as an antenna) and ground loops in the DAQ. The DAQ was carefully designed to avoid ground loops and we take the steps described in section 6.2.2 to eliminate the polarization state information as a problem. Any residual effects are sensitive to

cancellation by the half-wave plate.

6.5.8   Etalon Effects

Certain bench studies we conducted using an unwedged Pockels cell led us to consider the possibility that a Pockels cell with parallel faces can behave as a Fabry-Perot etalon. A careful analysis of such a system reveals that it is capable of producing rather large intensity asymmetries (as large as 10^{-3} for a Pockels cell without AR coatings) on the laser beam, provided that the line width of the laser beam is small compared to the free spectral range of the Pockels cell etalon (~ 3 GHz). This, however, proves not to be the case for the SLAC system, for which the Flash:Ti laser has a line width of ~ 300 GHz.

Table 6.6: Sources of $^{\mathrm{beam}}A_{\mathrm{LR}}$'s. The 2nd column indicates which $^{\mathrm{beam}}A_{\mathrm{LR}}$'s can be affected (intensity asymmetry I, position (and angle) difference P, spot size difference S, or energy asymmetry E) and the 3rd column indicates the relative importance of this effect for the SLAC source. The 4th and 5th columns indicate if some cancellation of the effect is achieved by toggling the half-wave plate or the Asymmetry Inverter optics.

Effect	$^{\mathrm{beam}}A_{\mathrm{LR}}$'s	Significance	$\lambda/2$ Cancel	AI Cancel
Residual Linear Polarization coupling to QE Anisotropy*	I	dominant	NO	NO
Birefringence Gradients	PS	dominant	Complex	position YES
Lensing	PS	large	YES	position YES
Beam Loading	E	large	NO	NO
Collimation and Spot Size	IPS	medium	Complex	position YES
Cathode Gradients	PS	medium	NO	NO
Electronic Cross Talk	IPSE	small	YES	NO
Etalon	I	negligible	NO	NO

---

*The coupling between residual linear polarization in the laser beam and the cathode QE anisotropy results in the dominant contribution to A_I. It is also a dominant source of position and spot size differences and of the energy asymmetry via spatial gradients and beam loading (listed separately).

Chapter 7

HAPPEX 99 Data Analysis

The 1999 HAPPEX run took place in two segments, April 6-May 27 and July 8-27. It was the first parity-violation experiment to use a strained GaAs cathode. The experiment ended several days earlier than scheduled when a high-voltage arc in the polarized electron gun destroyed the photocathode. The production data set includes ~ 92 C of electrons incident on the LH_2 target at typical beam currents of $25 - 50$ μA. In addition, we conducted a number of calibration runs and systematic studies. Following the run, we performed two independent analyses of the raw detector asymmetry and corrections to it due to $^{beam}A_{LR}$'s. The Syracuse group led one analysis (referred to as the "Syracuse analysis"). They had also conducted the primary analysis for the 1998 data set. I performed the second analysis (the "Princeton analysis") of the 1999 data set and report it in this chapter. The two analyses agree closely on the final results. The other facets of the analysis (average Q^2 determination, background estimation, etc.) are summarized more briefly for completeness. The 1999 HAPPEX results are published in [33] and use the Syracuse analysis for the asymmetry and the Princeton analysis for the correction due to $^{beam}A_{LR}$'s.

The analysis of a parity-violating electron-scattering experiment proceeds in several stages which form an outline for this chapter:

1. Calculate the raw physics asymmetry A_k^{raw} for each detector by studying the ratio of the integrated detector signals to the BCM signals for each pair.

2. Calculate helicity-correlated asymmetries in parameters of the electron beam, $^{beam}A_{LR}$'s.

3. Calculate the sensitivity $\frac{\partial \sigma_k}{\partial M_i}$ of the detector rates to fluctuations in measurements of the beam parameters.

4. Using the results of steps 2 and 3, calculate the contribution to the raw asymmetry from $^{beam}A_{LR}$'s, $^{beam}\widetilde{A}_{LR,k}$.

5. Perform tests on the data set to verify that it obeys counting statistics.

6. Analyze data from auxiliary runs to determine the background rates, acceptance-averaged Q^2, and electron beam polarization. Determine correction factors for the background and beam polarization.

7. Extract the physics asymmetry from the corrected raw asymmetry, beam polarization, and background flux.

7.1 Beam and Detector Asymmetries

7.1.1 Preliminaries

The standard procedure during production running was to take data runs of approximately one hour in length, corresponding to $\sim$ 50k pairs at 15 Hz. Most of the 827 production runs in the data set contain $\sim$ 50k pairs. Those that are shorter include runs that were ended because of loss of beam due to hardware failure or runs that occurred at the beginning of a maintenance period. We interrupted production running once every 24-48 hours to toggle the state of the half-wave plate used for slow helicity reversal at the source. Each time period between insertion or retraction of the half-wave plate is referred to as a "slug" of data, and there were a total of 20 such slugs over the course of the 1999 run, 10 in each half-wave plate state. We typically measured the electron beam polarization with a Møller polarimeter at least once per slug. We also took auxiliary runs to evaluate the acceptance-averaged momentum transfer and background rates periodically throughout the run.

The analysis of detector and beam asymmetries proceeds in three stages: asymmetries are computed for individual pairs, averaged over runs, and finally averaged over the entire data set. The Princeton analysis makes two passes through each run in order to generate average detector and beam asymmetries. The first pass generates an index of cuts to apply and records them in an auxiliary file for each run. The second pass reads in those cuts and calculates the beam and detector asymmetries from the data that survive the cuts. For each quantity of interest, the mean, *rms*, and error on the mean are calculated and stored in a file. The Princeton analysis code is written in C and operates on the standard ".log" files produced by the Hall A data acquisition system. It is developed from code written by Peter Mastromarino for his Senior Thesis [113]. In contrast, the Syracuse analysis code is written in Fortran. It processes the ".log" files into PAW ntuples and then performs the data analysis on the ntuples. Thus, the two analyses are conducted as independently as possible. To average the results over the entire data set, the Princeton analysis uses both PAW Fortran macros and AWK programs. The two methods give the same results.

7.1.2 Data Quality Cuts

We adopt a philosophy of making the minimal possible set of cuts of the data to avoid introducing a bias into the asymmetry. In particular, we do not cut on asymmetries in quantities, but rather only on absolute quantities. The box below, Table 7.1, summarizes the cuts we chose to apply to the data set.

The DAQ-related cuts form a redundant set which ensures that the helicity is correctly assigned to each event. The pseudorandom algorithm used to generate the sequence is predictable given the knowledge of the helicity for 25 pairs. If an event has a DAQ-related problem, we cut the 50 events (25 pairs) before and after it to ensure that the only events which are used are ones for which the helicity can be verified by its agreement with predictions from the sequence. DAQ problems are rare, however, and these cuts have a small effect on the data efficiency. For the low-current cuts, we extend the cuts backwards and forwards in time by a set number of events in order to remove

Table 7.1: Data quality cuts.

DAQ Cuts

On events: ±50 events

- Scaler increment – did a scaler that counts each *Master Trigger* increment by one count since the last event?

- *Realtime* alternation – did the *Realtime* signal toggle its state since the last event?

- Mystery triggers – cut related to running in oversampling mode.

- Sequential triggers – cut related to running in oversampling mode.

On pairs: ±50 events

- Alternating helicity – do the two members of the pair have opposite helicity?

- Pair event distance – are the two members of the pair adjacent in time?

- Helicity sequence – does the helicity information from the source match the predicted helicity sequence?

Repeated data: ±50 events

Beam and Hardware Cuts

Low current: $-10/+40$ events

- $I_1 < 1000$ ADC counts

- any BPM raw signal < 15000 ADC counts

Manual cuts: ±0 events

- Broken spectrometer

- Broken detector

- Broken BCM

---

data taken when the beam is either becoming unstable or recovering.

The manual cuts are indexed in a separate cuts file. Manual cuts are occasionally necessary to remove data during brief time periods when either a spectrometer magnet or the high voltage to one of the detectors trips off. Typically, if one spectrometer or detector trips off, the other is still working. The manual cuts provide a mechanism for making use of the data in the working spectrometer. Because the manual cuts are determined by carefully examining the data and cutting the region around which a problem occurs, it is not necessary to extend the cuts any further forward or backward in time in the analysis. During the first pass, the analysis code reads this file, looks for an entry for the run number currently being analyzed, and adds any cuts found to the list for that run. I refer to pairs which survive all data-quality cuts as "valid pairs" in the discussion

below.

7.1.3 Pair Analysis

There are a number of signals S for which we calculate helicity-correlated asymmetries and differences A(S). These signals include the detectors, BCM's, BPM's, and a number of batteries used to monitor electronic crosstalk in the DAQ (the crosstalk results are given in section 4.11.6). The raw detector asymmetry for each pair of events $A(d_k)$ is calculated according to

$$A_k = \frac{d_k^R - d_k^L}{d_k^R + d_k^L}, \tag{7.1}$$

where the superscripts R and L refer to the beam helicity, $d_k = D_k/I_1$ is detector signal k normalized to the beam current (as measured by BCM 1), and k runs over detectors 1, 2, and their sum: $D_s = D_1 + D_2$. Normalizing the detector signal to the beam current in this way automatically corrects for helicity correlations in the beam intensity (assuming the detectors and BCM are linear with respect to one another). Likewise, the intensity asymmetry A_I and the position differences ΔM at each BPM are calculated for each pair as

$$A_{Ia} = \frac{I_a^R - I_a^L}{I_a^R + I_a^L}, \qquad \Delta M_i = M_i^R - M_i^L, \tag{7.2}$$

where the subscript a runs over four BCM's (two cavity BCM's, an Unser Monitor, and a "short-gate" measurement of one of the cavity BCM's which integrates over only the first 8 ms of each 32 ms window.) and the subscript i runs over BPM's 3ax, 3ay, 3bx, 3by, and 12x.

7.1.4 Individual Run Analysis

The mean asymmetry $\langle A(S) \rangle$ for a single run is computed by taking a weighted average of the pairwise asymmetries. The pairs are weighted by the beam current incident on the target. The

average is

$$\langle A(S) \rangle = \left(\sum_n A(S)_n w_n \right) / \sum_n w_n, \quad w_n = I_1^R + I_1^L, \tag{7.3}$$

where the sum is over all valid pairs in the run. The rms is calculated as

$$\sigma(S) = \sqrt{\frac{\sum_n (A(S)_n)^2 w_n}{\sum_n w_n} - \frac{(\sum_n A(S)_n w_n)^2}{(\sum_n w_n)^2}} \tag{7.4}$$

and the error on the mean is given by $\overline{\sigma}(S) = \sigma(S)/\sqrt{N}$, where N is the number of valid pairs in the run.

7.1.5 Grand Averages

Finally, quantities from the individual runs are averaged over the entire data set. We calculate the detector asymmetries by taking a weighted average of the runs according to

$$\langle\langle A(d_k) \rangle\rangle = \left(\sum_n A(d_k)_n w_{kn} \right) / \sum_n w_{kn}, \qquad w_{kn} \equiv (1/\overline{\sigma}(d_k)_n)^2, \tag{7.5}$$

where $\overline{\sigma}(d_k)_n$ is the error on the mean for detector k for run n and the double brackets denote averaging over the entire data set. The uncertainty in the average is then

$$\delta\langle\langle A(d_k) \rangle\rangle = \left(\sum_n (1/\overline{\sigma}(d_k)_n)^2 \right)^{-1/2}. \tag{7.6}$$

For the intensity asymmetry and position differences, we choose to weight the individual runs by the error in the detector sum rather than the error in the measured quantity.* The reason is that we use these measurements to correct the raw detector asymmetry, and therefore ought to weight them by the relative statistical power of each run for determining the physics asymmetry. In this

---

*This choice of weighting is valid if the errors introduced by the beam monitors' finite resolutions are much less than the counting statistics in the detectors, as is the case for HAPPEX.

case, the formula to use to take a weighted average of the runs is

$$\langle\langle A(S)\rangle\rangle = \frac{\sum_n w_n \langle A(S)\rangle}{\sum_n w_n}, \quad w_n = (\frac{1}{\overline{\sigma}_n^s})^2, \tag{7.7}$$

where again n is an index of runs in the slug, $\langle A(S)\rangle$ is the asymmetry or difference in the parameter being calculated, and w_n is the weight for run n. Then the error on the quantity $\langle\langle A(S)\rangle\rangle$ is

$$\delta\langle\langle A(S)\rangle\rangle = \frac{1}{(\sum_n w_n)^2} \sum_n w_n^2 \delta\langle A(d_k)_n\rangle^2, \tag{7.8}$$

as can be shown by applying the standard error propagation to equation 7.7.

7.1.6 Results

Table 7.2 summarizes the results for the two independent analyses for the raw detector and beam asymmetries. For the Princeton analysis, results are given separately for the two running modes ("−" and "+") and combined. The combined Syracuse results are shown for comparison. Both analyses include $\sim$ 32.8 million pairs, while the Princeton analysis includes 24.4 thousand pairs more than the Syracuse analysis, a difference of less than 0.1%. The detector results are presented for the two detectors individually, for the sum of the detectors, and for a weighted average of the detectors. In addition, results are given for the intensity asymmetry and for the position differences. Several conclusions can be drawn from the results in Table 7.2:

1. The close agreement between the two analyses adds confidence to the results of both analyses. I discuss the quality of this agreement further below.

2. The close agreement between the detectors summed and the detectors averaged (rows 3 and 4) is consistent with the detectors making statistically independent (uncorrelated) measurements of the asymmetry. This indicates that noise due to target density fluctuations (which would show up as a correlation between the two detectors) is small compared to counting

statistics.

3. The intensity asymmetry $A_I = -1.15 \pm 0.09$ ppm, satisfying the requirement (from section 3.9.1) that $A_I \leq A_{raw}$.

4. The two cavity BCM's agree closely on the charge asymmetry. In addition, the Unser monitor, though less precise, agrees as well. This gives confidence that the intensity asymmetry is being properly measured and corrected for by normalizing the detector signals to BCM 1.

5. The Shortgate BCM, a second readout of BCM 2 which integrates over only the first 8 ms of the pulse, indicates a small but nonzero time dependence to the charge asymmetry within a pulse.

6. The position differences measured by each BPM are below 20 nm, suggesting that the corrections $^{beam}\widetilde{A}_{LR,k}$ will be small as well.

7. Comparing the "−" and "+" mode results, we see that the raw detector asymmetry is consistent in magnitude for the two half-wave plate states. Figure 7.1 shows the results for $A(d_s)$ (detector sum) for the two analyses as a function of slug number. The square wave plotted on the curve has an amplitude equal to the mean asymmetry and indicates the expected sign of the asymmetry for each half-wave plate state. The χ^2 per degree of freedom, calculated for the Princeton analysis is excellent. The sign flip with half-wave plate state is clearly evident and the agreement of the magnitude of the asymmetry for the two modes indicates that many classes of false asymmetries are under control.

The two analyses are based on the same data set, and so their results should be highly correlated. Thus, the uncertainty in the difference between them should be much less than the uncertainty in each measured quantity. The uncertainty in the difference between the results of the two analyses provides a means of evaluating the agreement between them. We estimate that uncertainty by assuming that the data set used in one analysis is a subset of the data set used in the other analysis. Since the Syracuse analysis utilizes fewer pairs, for this argument we assume that the pairs it uses

Table 7.2: Summary of the raw detector and beam asymmetry results for the two analyses. The first three columns give the results for the Princeton analysis for data taken in raw asymmetry "−" and "+" running modes and averaged (with "+" data flipped in sign when computing the average). The fourth column gives the Syracuse results, and the fifth column applies the comparison test discussed in the text below to columns 3 and 4.

	"−" Mode	"+" Mode	AVE	Syracuse	Compare
		Asymmetry Measurements (ppm)			
Det 1	-10.93 ± 1.45	11.02 ± 1.46	-10.97 ± 1.03	-10.97 ± 1.03	0.00 ± 0.05
Det 2	-11.93 ± 1.51	7.77 ± 1.52	-9.86 ± 1.07	-9.91 ± 1.07	0.06 ± 0.05
Det Sum	-11.45 ± 1.06	9.36 ± 1.06	-10.41 ± 0.75	-10.44 ± 0.75	0.03 ± 0.04
Det Ave	-11.41 ± 1.05	9.45 ± 1.05	-10.42 ± 0.74	-10.42 ± 0.74	0.00 ± 0.06
Cav BCM 1	-1.22 ± 0.11	1.03 ± 0.14	-1.15 ± 0.09	-1.14 ± 0.09	-0.01
Cav BCM 2	-1.12 ± 0.11	1.03 ± 0.14	-1.13 ± 0.09	-1.12 ± 0.09	-0.01
Unser	0.76 ± 2.42	4.76 ± 2.21	-2.25 ± 1.63	-2.17 ± 1.57	-0.09 ± 0.44
Shortgate	-1.47 ± 0.24	6.87 ± 0.26	-3.93 ± 0.18	-3.91 ± 0.18	-0.02
		Position Differences (nm)			
BPM 12x	-52.39 ± 4.28	-26.46 ± 4.51	-15.03 ± 3.11	-14.41 ± 3.08	-0.62 ± 0.43
BPM 3ax	-18.02 ± 2.69	-4.14 ± 2.72	-7.08 ± 1.91	-7.03 ± 1.92	-0.05 ± 0.20
BPM 4bx	0.03 ± 4.77	15.93 ± 5.07	-7.46 ± 3.48	-7.30 ± 3.49	-0.16 ± 0.26
BPM 3ay	-13.35 ± 1.49	5.05 ± 1.75	-9.87 ± 1.13	-9.86 ± 1.14	-0.01 ± 0.15
BPM 3by	12.00 ± 0.71	3.95 ± 0.75	4.48 ± 0.52	4.55 ± 0.52	-0.07

are a subset of those used by the Princeton analysis. If we define m_P as the mean value of a quantity from the Princeton analysis and $\overline{\sigma}_P$ to be its error, and similarly define m_S and $\overline{\sigma}_S$ for the Syracuse analysis, then we can study the difference m_D between the two analyses:

$$
m_D \equiv |m_P - m_S|, \qquad \overline{\sigma}_D^2 \equiv \left| \overline{\sigma}_P^2 \left(\frac{\partial m_D}{\partial m_P} \right)^2 + \overline{\sigma}_S^2 \left(\frac{\partial m_D}{\partial m_S} \right)^2 + 2\overline{\sigma}_{PS}^2 \left(\frac{\partial m_D}{\partial m_P} \right) \left(\frac{\partial m_D}{\partial m_S} \right) \right|, \quad (7.9)
$$

where $\overline{\sigma}_{PS}^2$ is the covariance between the Princeton and Syracuse analyses:

$$
\overline{\sigma}_{PS}^2 \simeq \frac{1}{N} \sum_{i=1}^{N} \left[A(S_i^P) - \langle\langle A(S_i^P) \rangle\rangle \right] \cdot \left[A(S_i^S) - \langle\langle A(S_i^S) \rangle\rangle \right], \quad (7.10)
$$

where i runs over all pairs used in the Princeton analysis. The derivatives $\frac{\partial m_D}{\partial m_P}$ and $\frac{\partial m_D}{\partial m_S}$ are 1 and -1, respectively. For pairs not used by the Syracuse analysis, we take $\left[A(S_i^S) - \langle\langle A(S_i^S) \rangle\rangle \right] = 0$.
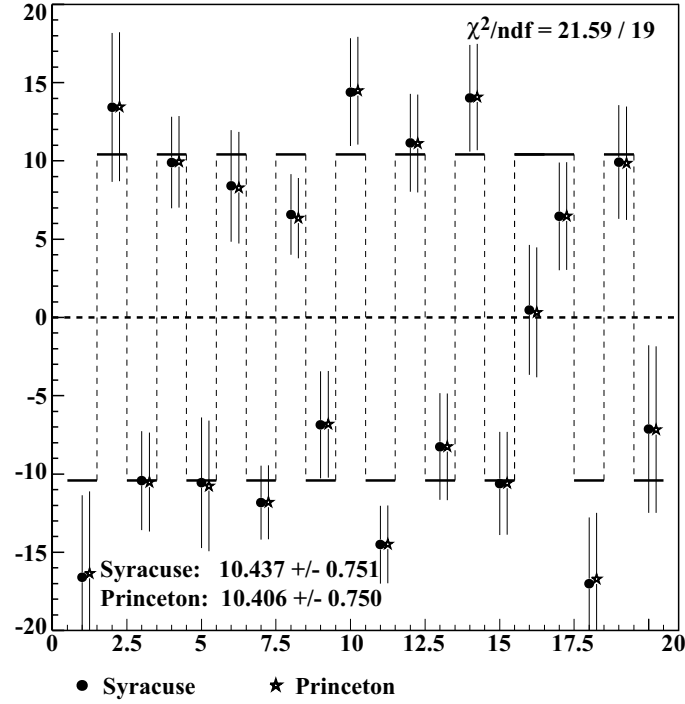
Figure 7.1: Raw detector-sum asymmetry $A(d_s)$ by slug, showing half-wave plate sign flip and the two independent analyses.

Because the difference in the data sets is small, $\overline{\sigma}^2_{PS} \simeq \overline{\sigma}^2_S$ and we have $\overline{\sigma}^2_D \simeq \left| \overline{\sigma}^2_P - \overline{\sigma}^2_S \right|$. The last column of Table 7.2 gives the results of this test and indicates that the two analyses agree well. In addition, $|m_P - m_S|$ is typically below 1% of the uncertainty for the detector measurements and below $\sim 10\%$ for the beam asymmetry measurements.

Figure 7.2 shows the detector asymmetries as a function of run number, with raw asymmetry "$-$" data shown in blue and raw asymmetry "$+$" data shown in red. In section 4.3 we defined raw asymmetry "$-$" and "$+$" slugs according to the expected sign of the physics asymmetry. The expected sign depends on the state of the insertable half-wave plate and the configuration of the source optics. For slugs 1-16 (the April/May running period), the expected sign is negative with the insertable half-wave plate out and positive with it in. This expectation is reversed for slugs 17-20 (the July running period) because of changes to the source optics (discussed in section 4.3). The typical statistical error on a one-hour production run is ~ 20 ppm, a factor of two larger than the expected raw asymmetry. Thus, we cannot see the sign of the asymmetry flip with half-
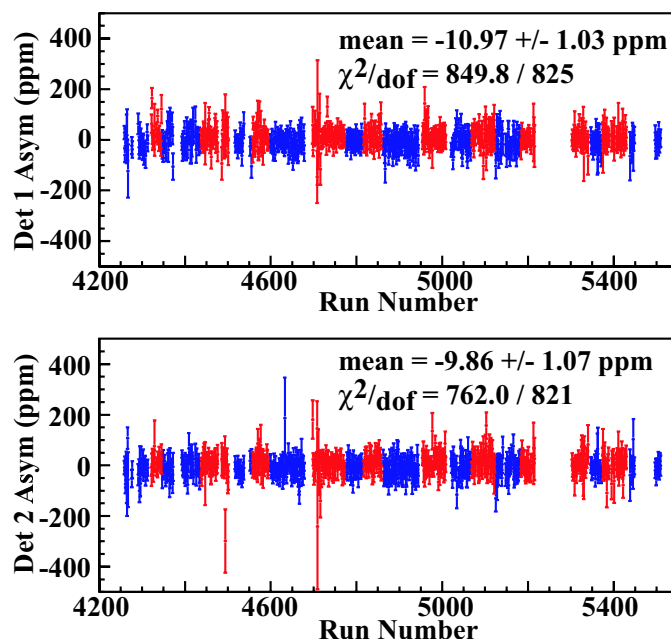
Figure 7.2: Raw detector asymmetries by run for detectors 1 (top) and 2 (bottom). Blue indicates raw asymmetry "−" mode and red indicates raw asymmetry "+" mode.

wave plate state in this plot. However, we can see that the measured detector asymmetries are stable over time and that the χ^2 per degree of freedom (taking into account the sign flip for the appropriate runs) for each detector is reasonable.

Figure 7.3 shows the intensity asymmetry measured by BCM 1 as a function of run number with the runs color-coded as above for the detector asymmetries. The vertical axis of the top plot is scaled to show all runs, while the bottom plot zooms in on the bulk of the runs which have approximately zero intensity asymmetry. The outliers in the top plot are primarily due to runs which began with the PITA DAC value reset to its nominal setting and thus had a large intensity asymmetry for the first minirun. In keeping with our philosophy of making minimal cuts, we include these miniruns in the analysis.

Figure 7.4 shows the position differences as a function of slug number. The behavior of the position differences as a function of time is presumed to be very sensitive to details of the source setup and the electron-beam tune. The average position differences are all below 20 nm. We benefit from some cancellation due to the half-wave plate as well as cancellation from (apparently)
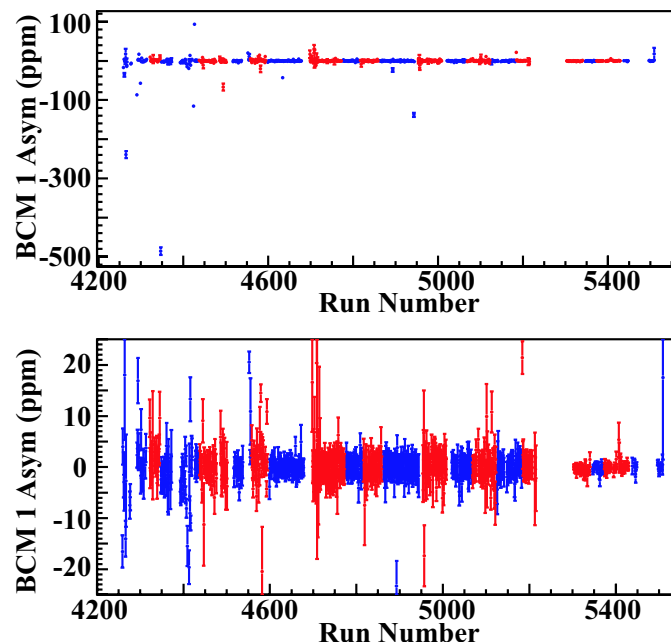
Figure 7.3: Intensity asymmetry by run. Blue indicates raw asymmetry "−" mode, and red indicates raw asymmetry "+" mode.

random slow drifts in the position differences. Thus we see, for example, that in the later slugs the energy asymmetry (as given by BPM $12x$) develops a fairly large and approximately constant value of ~ -60 nm, but that it is cancelled by the half-wave plate reversal.

7.2 Beam Modulation Analysis

As was discussed earlier in section 3.6, we use beam modulation to study the sensitivity of the detector rate to fluctuations in the beam's energy, position, and angle at the target. For HAPPEX, fluctuations in the detector rate are dominated by counting statistics in the scattering process rather than fluctuations in beam parameters (the opposite is true for E-158), and the beam modulation analysis is used solely to determine the corrections for nonzero $^{\text{beam}}A_{\text{LR}}$'s. The scattering rate into each detector (after normalizing to the beam intensity) is a function of the beam's parameters (position and angle in x and y and energy) at the target. Unfortunately, these quantities are not directly measurable. Instead, we reparameterize the scattering rate in terms of the beam

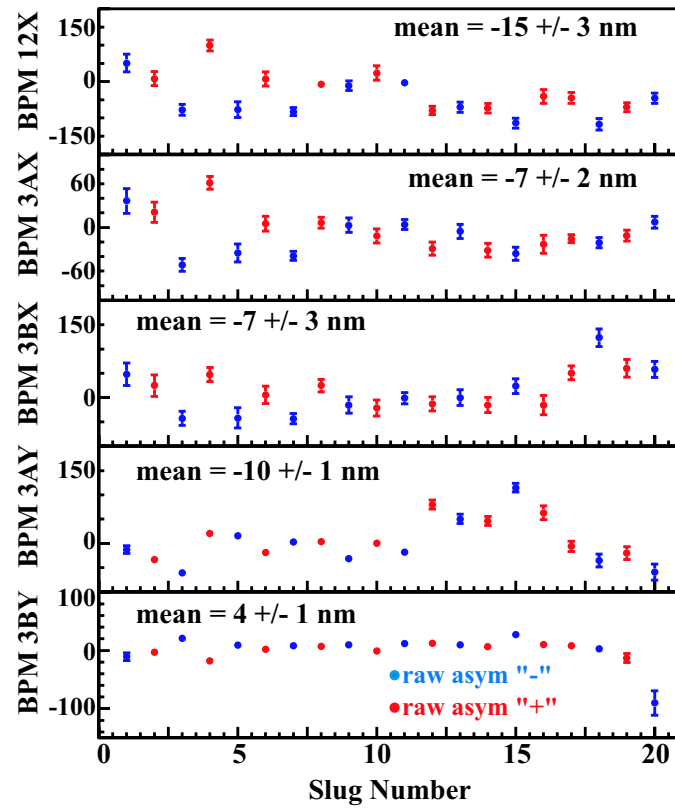Figure 7.4: Position differences at the five BPM's vs. slug number. Blue indicates raw asymmetry "−" mode, and red indicates raw asymmetry "+" mode. The mean values are averaged over the entire run and take into account the sign flip with half-wave plate state.

position at BPM's 3ax, 3ay, 3bx, 3by, and 12x because these five quantities are measurable and span the phase space available to describe the beam at the target.

7.2.1 Formalism

We modulate each coil and the energy vernier and record the response of the beam position, angle, and energy monitors and the two detectors. We encode those responses into two vectors $\mathbf{B}_{ij}$ (beam response to modulation) and $\mathbf{D}_{kj}$ (detector response to modulation):

$$\mathbf{B}_{ij} = \frac{\partial M_i}{\partial C_j} \qquad\qquad \mathbf{D}_{kj} = \frac{\partial \sigma_k}{\partial C_j}, \qquad\qquad (7.11)$$

where i runs over the five beam parameters M (x, y, x', y', E), j runs over the eight modulation coils C, and k runs over the measurements of the cross section σ by each of the two detectors. The response of the detector rate to the coils can also be expressed as

$$\frac{\partial \sigma_k}{\partial C_j} = \sum_{i=1}^{5} \frac{\partial \sigma_k}{\partial M_i} \frac{\partial M_i}{\partial C_j}, \qquad\qquad (7.12)$$

where $(\partial \sigma_k)/(\partial M_i)$, the response of the detector to changes in the beam parameters, is the quantity in which we are interested. To extract $(\partial \sigma_k)/(\partial M_i)$ from the data, we define a χ^2 (or, rather, a pair of χ^2's):

$$\chi_k^2 = \sum_{j=1}^{8} \left[\left(\frac{\partial \sigma_k}{\partial C_j} - \sum_{i=1}^{5} \frac{\partial \sigma_k}{\partial M_i} \frac{\partial M_i}{\partial C_j} \right) / \sigma_k^2 \right]^2. \qquad\qquad (7.13)$$

We minimize χ^2 with respect to $(\partial \sigma_k)/(\partial M_l)$ and find

$$\sum_j \left(\frac{\partial \sigma_k}{\partial C_j} \frac{\partial M_l}{\partial C_j} \right) / \sigma_k^2 = \frac{\partial \sigma_k}{\partial M_i} \cdot \sum_j \left(\frac{\partial M_i}{\partial C_j} \frac{\partial M_l}{\partial C_j} \right) / \sigma_k^2. \qquad\qquad (7.14)$$

We can rewrite this as

$$\mathbf{A} = \mathbf{R} \cdot \mathbf{M} \qquad\qquad (7.15)$$

by making the definitions

$$\mathbf{A} = \sum_j \frac{\partial \sigma_k}{\partial C_j} \frac{\partial M_l}{\partial C_j} / \sigma_k^2$$

$$\mathbf{R} = \frac{\partial \sigma_k}{\partial M_i} \tag{7.16}$$

$$\mathbf{M} = \sum_j \frac{\partial M_i}{\partial C_j} \frac{\partial M_l}{\partial C_j} / \sigma_k^2.$$

We solve for $\mathbf{R}$ by right-multiplying the above equation by $\mathbf{M}^{-1}$:

$$\mathbf{R} = \mathbf{A} \cdot \mathbf{M}^{-1}. \tag{7.17}$$

This gives us the response of the detector to changes in the measured beam quantities. By defining an average (unpolarized) scattering cross section $\overline{\sigma}_k = \frac{1}{2}\langle \sigma_{R,i} + \sigma_{L,i} \rangle$ for each detector, we can extract the contributions to the asymmetry from $^{\text{beam}}A_{\text{LR}}$'s as

$$^{\text{beam}}\widetilde{A}_{LR,k} = \frac{1}{2\overline{\sigma}_k} \sum_i \frac{\partial \sigma_k}{\partial M_i} \Delta M_{LR,i} \tag{7.18}$$

Finally, we can correct the raw detector asymmetry according to

$$\langle\langle A(d_k) \rangle\rangle^{cor} = \langle\langle A(d_k) \rangle\rangle - {}^{\text{beam}}\widetilde{A}_{LR,k}. \tag{7.19}$$

One strength of this procedure is that an accurate absolute calibration of neither the modulation induced by the coils and energy vernier nor the position measurements by the BPM's is necessary; the coil modulation and position measurements cancel out in calculating the effect on the scattering rate. Of course, the position monitors must be linear over the range of interest.
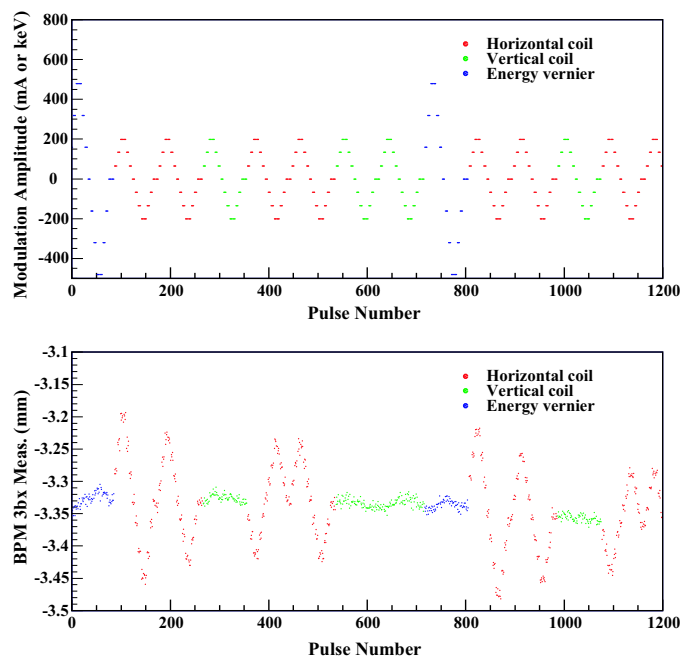
Figure 7.5: The top plot shows the sawtooth pattern of modulation induced by each coil and the energy vernier. The bottom plot shows the response of the beam at BPM 3bx. The response to horizontal coil modulation is clear.

7.2.2 Implementation

To implement the formalism described above, we vary the effects of the modulation objects (the seven coils and the energy vernier, indicated in Figure 3.1) according to a particular cycle. The cycle consists of modulating each object in a sawtooth pattern once in turn. Each object is modulated for ~ 82 events. At the end of the cycle, modulation pauses for ~ 1150 events. Thus, beam modulation is active for $\sim 36\%$ of the data taking. Figure 7.5 indicates the modulation cycle (top plot) and the response of BPM 3bx (bottom plot) from a test of the system in which the time between modulation cycles has been set to zero events.

The effects of the modulation cycle on the beam for two different beam tunes are shown in Figure 7.6. The modulation cycle is color-coded: red indicates horizontal modulation, green indicates vertical modulation, blue indicates energy modulation, and black indicates that no modulation object is active. Note that the x BPM's respond very little to vertical modulation, and the y BPM's respond very little to both horizontal modulation and energy modulation. The left-hand column

shows a modulation cycle from a "typical" production run, for which the beam tune provides a response in the x and y BPM's that spans the available phase space, whereas the right-hand column shows a modulation cycle from a run during which the beam tune did not allow the coils to span the available phase space. For example, consider the two y BPM's. In the left-hand column, both respond strongly to the first vertical coil. However, they respond very differently to the second vertical coil: BPM 3ay has a substantial response, whereas BPM 3by has a tiny response. We can say that the response of the two y BPM's to these two coils is linearly independent and hence spans the available two-dimensional phase space (vertical position and angle at the target). By contrast, the responses of the y BPM's to the same coils in the right-hand column are identical up to a scale factor. The two BPM's are measuring the same beam response. What this means in terms of the beam tune is that the phase of the beta function is not advancing signficantly between the two BPM's. For our analysis, this is a disaster: because the responses of the two BPM's are not linearly independent, they do not span the available phase space. The matrix $\mathbf{B}_{ij}$ becomes singular, and it proves impossible to invert the matrix $\mathbf{M}$ without blowing up the uncertainty in the measurement. We referred to this beam tune as a "singular tune." One responsibility of the shift-takers in performing a fast offline analysis during production running was to check the BPM response to beam modulation and verify that this singular tune was not in use.

7.2.3   Analysis and Results

The beam modulation analysis is part of the same code as the asymmetry analysis, and so it proceeds in a very similar manner. The first pass through the data develops a cuts file. The second pass analyzes the surviving data. For each individual modulation cycle, the slopes that make up the matrices $\mathbf{B}_{ij}$ and $\mathbf{D}_{kj}$ are calculated and stored as running sums. A typical hour-long production run has ~ 50 modulation cycles. At the end of the run, the average slopes and errors are computed. From these, the matrix $\mathbf{M}$ is inverted, and errors on its elements are computed exactly by brute force. Finally, the dependence of each detector's rate on each beam parameter

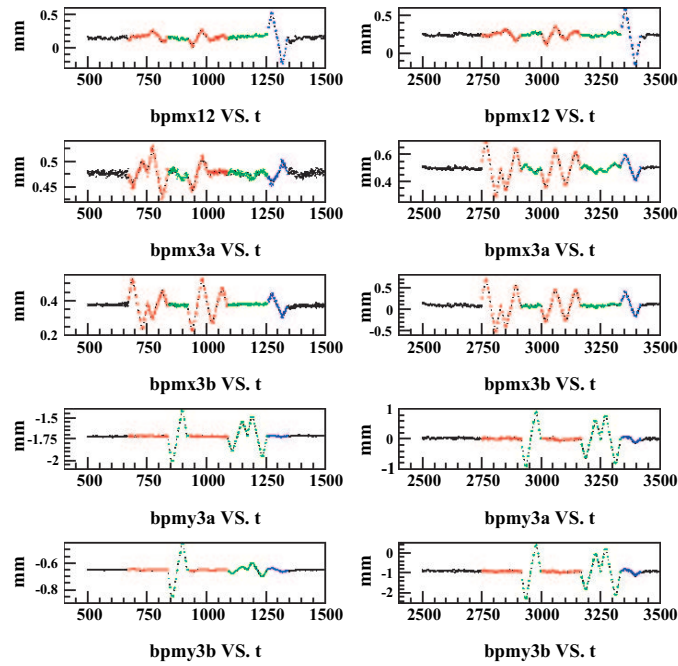Figure 7.6: Comparison of beam modulation for good and bad electron beam tunes. The left column shows the beam response to beam modulation for Run 5497, for which the beam tune was "good." The right column shows the beam response to beam modulation for Run 5443, for which the beam tune generates a singular matrix. Red: horizontal modulation. Green: vertical modulation. Blue: energy modulation. Black: modulation inactive.

(the matrice $\mathbf{R}$) is computed from equation 7.17, and these dependencies and the matrices $\mathbf{B}_{ij}$ and $\mathbf{D}_{kj}$ are stored in files.

A number of production runs were not used in the beam modulation analysis. These runs failed the analysis for a variety of reasons that were not judged to be severe enough to preclude using the data in the raw asymmetry analysis. Table 7.3 summarizes the number of runs that failed for each reason. For ~ 23 runs, beam modulation had been (usually accidentally) in an "OFF" state. Four runs had only the energy vernier turned off. For an additional 37 runs, the beam tune was singular in either x, y, or both. Six runs were taken in which for the entire run one of the detectors was inoperative. The beam modulation analysis was unable to handle the lack of valid signal from one detector, even when the other detector was taking good physics data. Finally, one run was simply too short to contain a complete modulation cycle and six runs failed for unidentifiable reasons. In total, 77 runs out of the 827 production runs were not used in the beam modulation analysis. However, because the response of the detectors to the beam parameters was remarkably constant in time, it is possible to include data in the production data set for which no modulation information is available.

Table 7.3: Inventory of runs not used in the beam modulation analysis.

Modulation Off	~ 23
Singular in Both x, y	22
Singular in y Only	11
Singular in x Only	4
Energy Modulation Off	4
Detector/Spectrometer Cuts	6
Analysis Failed	6
Too Short	1
Total	~ 77

I calculate the correction to the raw asymmetry on a slugwise basis. To compute the dependencies for each slug, I average the results for each run weighted by the statistical error in the appropriate detector asymmetry in a manner similar to the analysis of beam asymmetries. Figure 7.7 shows the dependence of the detector asymmetries on position at BPM's $12x$, 3a, and 3b as

a function of slug number. It is the stability of these dependencies over time that allows us to retain data in the raw asymmetry analysis for which the beam modulation analysis fails. Several features are worth noting in these plots. Recall that the two detectors are in nearly identical spectrometers oriented symmetrically on opposite sides of the beam line at scattering angles of 12.3°. We would naively expect from this symmetry that the dependence on horizontal position and angle for the two detectors would be roughly equal in magnitude but opposite in sign, and similarly that the dependence on vertical position and angle would be roughly equal in both magnitude and sign. The energy dependence should likewise be equal for the two detectors. We do observe that the dependence on energy (BPM $12x$) is approximately the same for the two detectors. However, we see a very strong cancellation between the two spectrometers in vertical position and angle. In the horizontal, we see a strong cancellation in the dependence on BPM $3ax$, but for BPM $3bx$ the cancellation is much weaker. Table 7.4 compiles the average dependencies for both the 1998 (from [113]) and 1999 HAPPEX runs. We would expect that for the same alignment of the spectrometers and of the detectors within the spectrometers, the dependencies should be the same. What we observe, however, is that while the general scale of the dependencies is the same, there are significant changes from 1998 to 1999. In particular, the 1998 dependencies show much less cancellation in the vertical. It is possible that the dependencies are very sensitive to the alignment of the detectors or spectrometers, and it would be interesting to do a detailed simulation of this possibility in preparation for the next round of HAPPEX experiments.

Table 7.4: Summary of the detector asymmetry dependence on BPM's for the 1998 and 1999 HAPPEX runs. The 1998 data are reprinted from [113]. All values are given in units of ppm/μm.

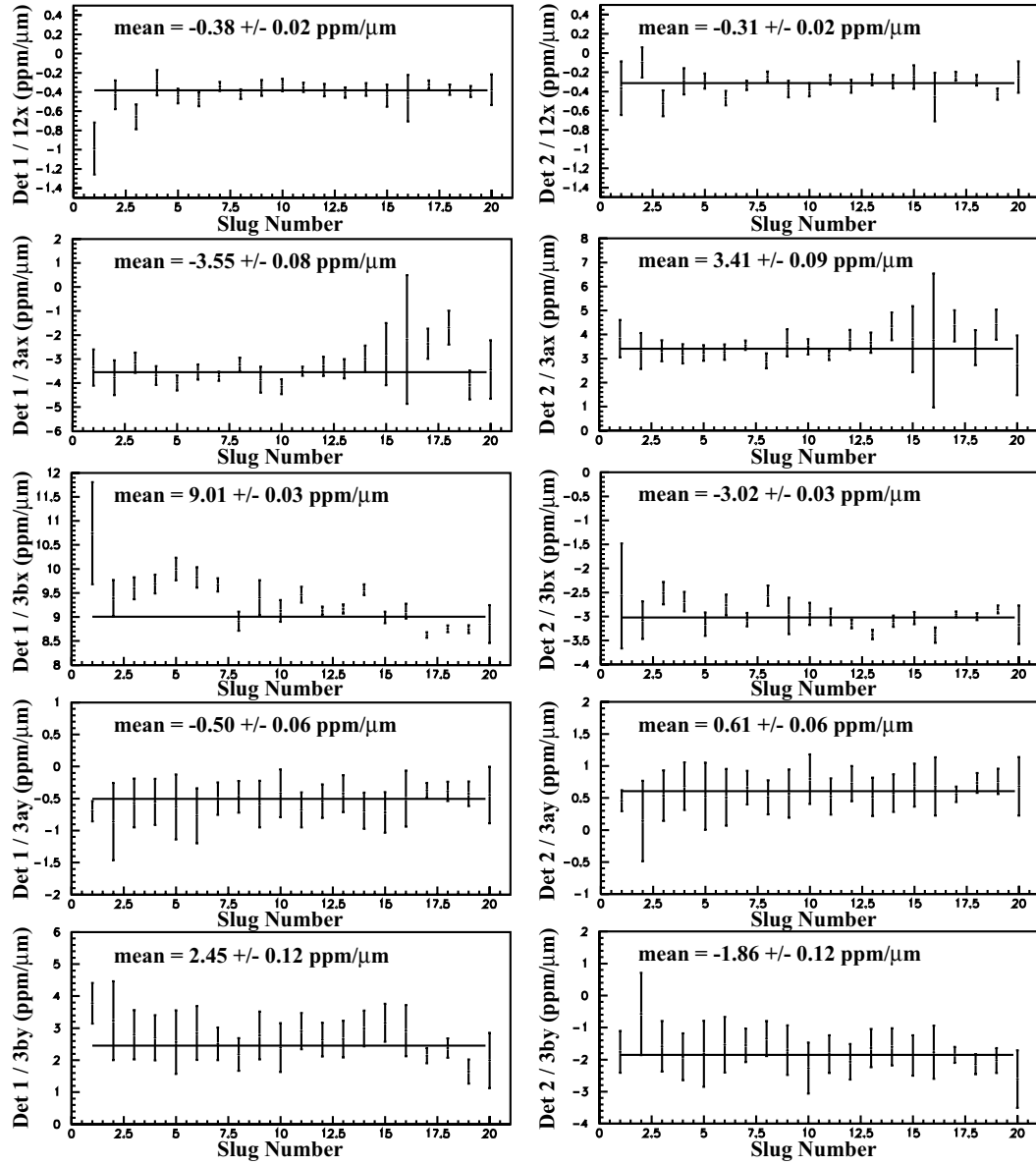| BPM	Detector 1		Detector 2	
	1998	1999	1998	1999
12x	-0.2 ± 0.05	-0.39 ± 0.02	0.5 ± 0.05	-0.32 ± 0.02
3ax	-5.0 ± 0.7	-3.59 ± 0.09	3.5 ± 0.6	3.43 ± 0.09
3bx	10.4 ± 0.9	9.07 ± 0.03	-4.8 ± 0.8	-3.04 ± 0.03
3ay	-0.5 ± 0.06	-0.51 ± 0.06	0.1 ± 0.05	0.61 ± 0.06
3by	4.7 ± 0.03	2.48 ± 0.12	0.9 ± 0.03	-1.88 ± 0.12

Figure 7.7: Detector asymmetry dependence on beam position at important BPM's as a function of slug number. The left (right) column shows the dependence of Detector 1 (2) on each BPM.

The contribution to the measured asymmetry from $^{\text{beam}}A_{\text{LR}}$'s for a given detector is then given by equation 7.18. Figure 7.8 shows $^{beam}\widetilde{A}_{LR,k}$ for each slug for both the Princeton and Syracuse analyses. The top (bottom) plot shows $^{beam}\widetilde{A}_{LR,k}$ for detector 1 (2). The largest single correction is ~ 1 ppm, but the corrections are typically a few tenths of a ppm and wander about zero. Again, the two analyses agree very well. The disagreement on the corrections for slug 20 can be explained by differences in the run sets used to calculate position differences. The Princeton analysis uses all of the runs which are in the production data set, while the Syracuse analysis eliminates a number of runs for which the beam tune was singular. Table 7.5 lists the values of the average corrections for each detector by running mode. We get a significant amount of cancellation between the two detectors and from the half-wave plate reversal. The final correction we apply to the raw physics asymmetry is $-\langle^{beam}\widetilde{A}_{LR,k}\rangle = 0.02 \pm 0.02$ ppm.

Table 7.5: Summary of $^{beam}\widetilde{A}_{LR,k}$'s from the Princeton analysis.

	$^{beam}\widetilde{A}_{LR,1}$ (ppb)	$^{beam}\widetilde{A}_{LR,2}$ (ppb)	Average (ppb)
"$-$" mode	69 ± 49	-45 ± 21	14 ± 27
"$+$" mode	151 ± 51	-39 ± 21	60 ± 28
Combined	-36 ± 35	-3 ± 15	-20 ± 20

7.3 Statistical Checks on Results

We performed several statistical tests on the data to verify that it obeys counting statistics. The first statistical test was of the counting statistics of the individual pairs. Figure 7.9 shows histograms of the asymmetry distributions for the two detectors. I created these histograms using PAW hbooks generated by the Syracuse analysis. If the scattering process is dominated by counting statistics and all events are drawn from the same parent distribution, then these histograms should be gaussian. Because the incident beam current varied between $\sim 25 - 50 \ \mu$A and the width of the distribution is proportional to $(I_R + I_L)^{-1/2}$ (where I_R (I_L) is the incident beam current for the right (left) pulse of a pair), the pairs are drawn from distributions with significantly varying
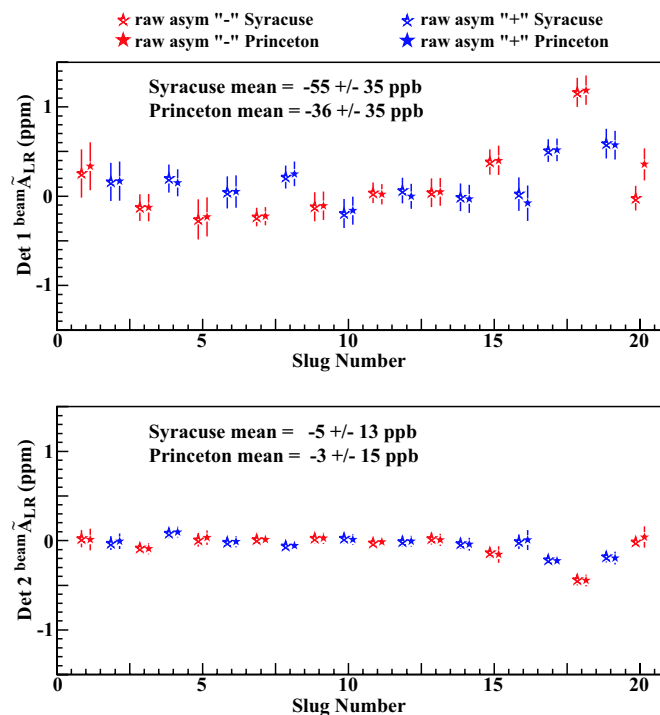
Figure 7.8: Corrections for Beam Helicity Correlations (other than the Intensity Asymmetry) by Slug for two independent analyses.

widths. To correct for this current dependence in this statistical test, each pair is normalized by a factor $(I_R + I_L)^{1/2}$. In addition, the gain of the ADC which reads out the BCM used to normalize the detector signals (see equation 7.1) was changed twice early in the run. An additional normalization factor is applied to the data to compensate for the gain change. Neither of these corrections should affect the underlying statistics of the distribution. The histograms are shown with a log scale on the vertical axis to emphasize the absence of tails. The histograms are gaussian over five orders of magnitude and have reasonable χ^2 values. They demonstrate that our data set is, indeed, dominated by counting statistics.

We also studied the run-by-run distribution of detector asymmetries. Figure 7.10 shows, for each detector and the sum of the two detectors, a histogram of the detector asymmetry for each run normalized by its statistical error. Counting statistics dictates that the distribution should be gaussian with a sigma of one. This is in fact what we observe. This test is consistent with the run-by-run asymmetries shown in Figure 7.2, which shows that the χ^2 of the distribution of

(a) Detector 1 asymmetry.

(b) Detector 2 asymmetry.
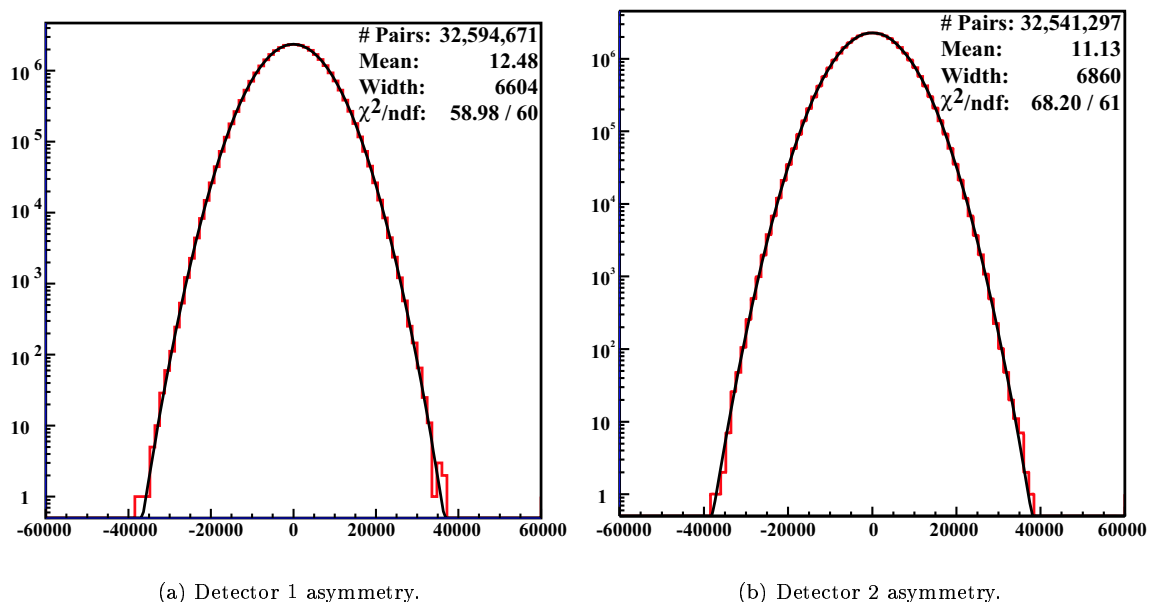
Figure 7.9: Pairwise histograms of (a) detector 1 asymmetry and (b) detector 2 asymmetry. The pairs have been normalized to account for large variations in beam current and changes in ADC board gains. The mean and width are in ppm.

asymmetries for each run is reasonable.

7.4 Polarimetry

The Møller polarimeter, described above in section 4.6, provided the polarization measurements used to normalize the raw detector asymmetry. Each data slug contained between one and three polarization measurements, and the average of those measurements was used to normalize the asymmetry for each slug. Two slugs had no Møller polarimeter measurements, and for those we used the average of the preceding and following slugs' polarizations. The average beam polarization for the entire data set was $P_b = 70.84 \pm 2.27\%$, where the error is dominated by systematics. The polarizations used to normalize each slug of data are listed in Table 7.7.

The Compton polarimeter was commissioned during HAPPEX and provided a continuous monitoring of the beam polarization during the July run period. Because the systematics of the Compton polarimeter were still being studied, we utilized this data solely to verify that the beam

(a) Detector 1 asymmetry. (b) Detector 2 asymmetry. (c) Detector sum asymmetry.
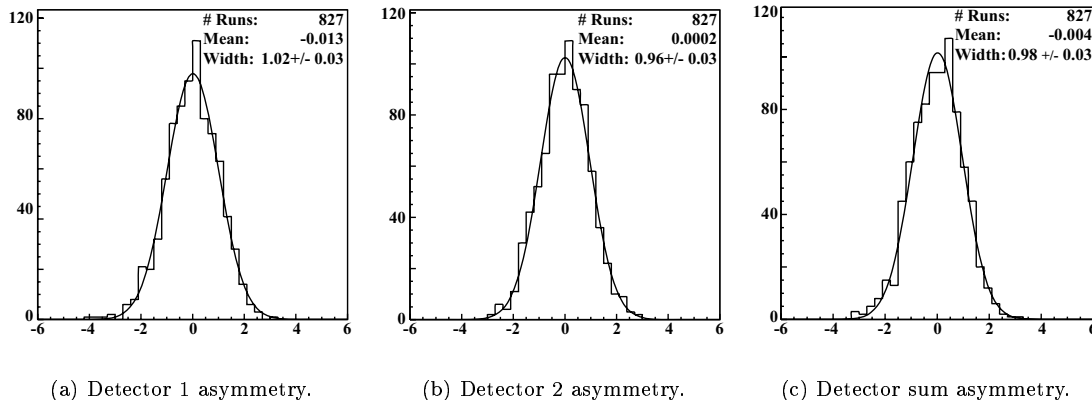
Figure 7.10: Histograms of run-by-run asymmetries for detectors 1, 2, and their sum normalized to their statistical error. For consistency with counting statistics, the distribution should be gaussian with a sigma of one.
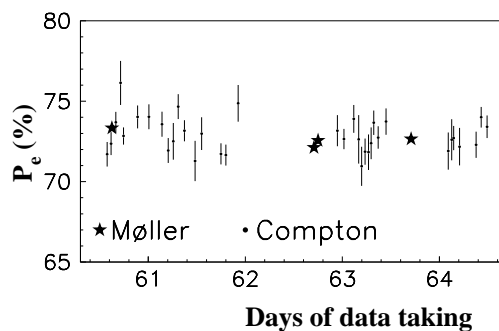
Figure 7.11: Comparison of measurements of the electron beam polarization via the Møller and Compton polarimeters for several days of data taking during the July running period.

polarization was stable between Møller polarimeter measurements. Figure 7.11 compares Møller and Compton polarimetry measurements for a several-day period. The error bars on the data points are statistical only. For the Møller data (stars), the statistical errors are smaller than the data points. Each Compton data point (dots) represents a run of approximately one hour in length. The Compton data shows that the beam polarization is not wandering significantly between Møller measurements, validating our strategy of measuring the beam polarization via the Møller polarimeter approximately once every 24-48 hours. The Compton polarimetry analysis is discussed in detail in [114].

7.5 Q^2 Analysis

An accurate determination of the average Q^2 is important for extracting the strange quark form factors from the physics asymmetry because all of the form factors are functions of Q^2 (including the electromagnetic form factors, which are necessary input for the extraction). The momentum transfer for a scattered electron can be expressed as $Q^2 = 2EE'(1 - \cos\theta)$, where E is the incident electron's energy, E' is the outgoing electron's energy, and θ is the scattering angle in the lab frame. In elastic scattering, only two of the three kinematic variables are independent, so eliminating any one of the variables in the above relation provides three additional methods of calculating Q^2 on the elastic peak with differing sensitivities to various systematic errors. For the full data set, all three kinematic variables are used to determine the average Q^2 because part of the elastic peak's radiative tail, which is not purely elastic scattering, is also detected. For events on the elastic peak, eliminating one kinematic variable can be used to provide a cross check of the analysis. The extraction of the acceptance-averaged momentum transfer squared, $\langle Q^2 \rangle$, is discussed in detail in [115, 116]. Here we summarize the analysis.

Determining $\langle Q^2 \rangle$ requires measuring the kinematic variables E, E', and θ for individual electrons. These measurements were made during auxiliary runs in a low-current mode using both the HAPPEX detectors and the standard Hall A detector packages. The beam energy was measured using both the Hall A ARC and $e - p$ energy measurement apparatuses [92]. The scattered electron energy was measured by the High Resolution Spectrometers, and the scattering angle was measured by reconstructing events and tracing the electron back to its scattering position in the target. The scattering angle determination also relies on surveys of the spectrometers' positions relative to the target. The raw asymmetry measurement is biased by the signal size each electron makes in the HAPPEX detectors. The signal size is proportional to the electron energy E' and to the efficiency of the detector at the location the electron strikes it. To correct for this bias in

calculating $\langle Q^2 \rangle$, the individual Q^2 bins are weighted according to

$$\langle Q^2 \rangle = \left(\sum Q_i^2 H_i \right) / \sum H_i, \tag{7.20}$$

where Q_i^2 is the momentum transfer squared in the ith Q^2 bin and H_i is the HAPPEX detector ADC amplitude for events in the ith bin. This weighting shifts the central value for $\langle Q^2 \rangle$ by $-0.38 \pm 0.05\%$ relative to the unweighted $\langle Q^2 \rangle$. The acceptance-averaged Q^2 for the 1999 run is $0.477 \pm 0.006\,\mathrm{GeV}^2$ for the April/May running period and $0.466 \pm 0.006\,\mathrm{GeV}^2$ for the July running period.

The total systematic error in the determination of $\langle Q^2 \rangle$ is 1.2%, or $0.006\,\mathrm{GeV}^2$. The dominant error arises from knowledge of the scattering angle, where several factors contribute to a 1% total uncertainty. Other contributions to the systematic error include the spectrometer momentum scale (0.1%), the beam energy (0.3%), the spectrometer matrix elements (0.4%), and drifts in time (0.5%).

7.6 Backgrounds

One of the challenges in an integrating experiment is to develop confidence that the background flux and asymmetry are well understood. For HAPPEX, the high resolution of the spectrometers cleanly separated the elastic stripe from the inelastic scatters (see Figure 4.6) and allowed us to position the integrating detector to avoid a large contribution from inelastic scattering. The dominant backgrounds for our experiment (summarized in Table 7.6) were inelastic scattering at the Δ resonance, quasielastic scattering off aluminum in the target endcaps, and pole-tip scattering off the spectrometer's magnets.

We evaluated the contribution of inelastic backgrounds to the energy deposited in the detectors by varying the momentum setting of the spectrometers. The count rate as measured by both the standard Hall A detector package and the HAPPEX detectors was determined as a function of

the percent change in the spectrometers' momentum setting. The results are shown in Figure 7.12 and show that the integrated detector flux drops several orders of magnitude as the elastic stripe is swept away. From this data, we conclude that only 0.2% of the energy deposited in the detector is from inelastic background.[†] The asymmetry in the inelastic background is estimated to be -47 ± 10 ppm from [118] and leads to a correction of 0.06 ± 0.02 ppm to the physics asymmetry.

Quasielastic scattering from the aluminum endcaps of the target contributed 1.4% of the energy deposited in the detector. This background was studied by reconstructing tracks of particles scattered from the LH_2 target and observing an excess of scatters originating in the target endcap regions. The amount of energy deposited in the detectors was then determined by comparing scattering rates from an empty aluminum target cell to those from the LH_2 target. The asymmetry in scattering from aluminum differs from hydrogen because of the presence of neutrons and for our kinematics is -24 ± 7 ppm [119], where a 30% uncertainty has been assumed. We apply a correction of 0.12 ± 0.04 ppm to the physics asymmetry to account for this background.

Finally, rescattering from the polarized iron in the spectrometer's magnets is a potentially serious background because of the large helicity-correlated asymmetry in polarized Møller scattering. Studies of the probability of rescattering into the HAPPEX detectors from the magnetic poletips placed an upper limit of $f = 10^{-4}$ on the fraction of energy deposited in the detector from such scattering [117]. Making conservative assumptions on the beam polarization ($P_b \leq 0.8$), the iron polarization ($P_t = 0.03$), and the analyzing power of the iron ($A = 0.11$), we can place an upper limit on the size δA of this effect:

$$\delta A = f \cdot P_b \cdot P_t \cdot A \leq 0.26 \text{ ppm}. \tag{7.21}$$

We choose to make no correction for this effect.

[†]The plot suggests a background flux of $\sim 1\%$. This is because the rescattering measured here is due to rescattering of the elastic peak, which has a much larger cross section than the Δ resonance. It is the Δ resonance that primarily produces the rescattering when the spectrometer is tuned properly. The full analysis involves an integral over energy of the ratio of the inelastic cross section to the elastic cross section and is discussed in more detail in [117].
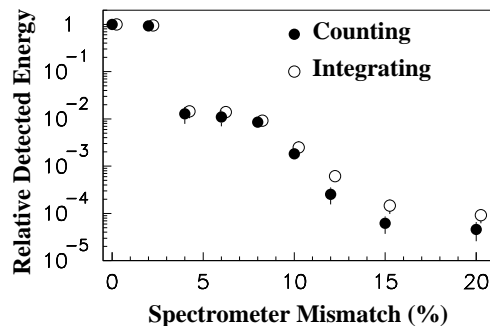
Figure 7.12: Fractional energy deposition as a function of spectrometer mismatch. "Counting" refers to data taken with the standard Hall A detector package at a sufficiently low rate to count individual electrons. "Integrating" refers to data taken with the HAPPEX detectors.

Table 7.6: Summary of background contributions to the detector signal.

Background	Fraction of Det. Sig. (%)	Asym. (ppm)	Correction (ppm)
Inelastics (Δ resonance)	0.20 ± 0.05	-47 ± 10	0.06 ± 0.02 ppm
Target endcaps (Q.E. Al)	1.4 ± 0.1	-24 ± 7	0.12 ± 0.04
Pole-tip scattering	≤ 0.01	—	0

7.7 The Physics Asymmetry

Extracting the physics asymmetry from the raw asymmetry involves several steps:

1. Normalize each slug by the electron beam polarization determined for that slug. Table 7.7 lists by slug the values of the detector raw asymmetries from the Princeton analysis and the beam polarization as measured with the Møller polarimeter. The errors are purely statistical; the polarization measurements also carry a 3.2% relative systematic error.

2. Evolve the asymmetries for slugs 17-20 from a Q^2 of 0.466 GeV^2 to 0.477 GeV^2. To do this, we assume the asymmetry depends on momentum transfer as $A \propto Q^3$.

3. Average the measurements together for the two detectors and 20 slugs. Include a correction of 0.18 ± 0.05 ppm to compensate for the contribution of backgrounds. The resulting physics

asymmetry for the 1999 data set is

$$\boxed{A^{phys} = -15.1 \pm 1.1 \text{ ppm.}} \tag{7.22}$$

4. Combine the 1999 result with the 1998 result [32] (updated to include the background correction and small changes in the beam polarization and Q^2). The final result is $A_{exp} = -15.05 \pm 0.98 \pm 0.56$ ppm, where the first error is statistical and the second systematic. The contributions to the systematic error are summarized in Table 7.8.

Table 7.7: Raw detector asymmetries and beam polarization by slug. The detector asymmetries are from the Princeton analysis. The beam polarization measurements are from the Møller polarimeter. Errors on all quantities are statistical only.

Slug	$A(d_1)^{raw}$ (ppm)	$A(d_2)^{raw}$ (ppm)	P_b (%)
1	-17.0341 ± 6.94607	-15.3116 ± 7.16933	-67.33 ± 0.11
2	18.3482 ± 6.50587	8.84523 ± 6.75283	67.38 ± 0.07
3	-8.23172 ± 4.25420	-12.6308 ± 4.42679	-69.11 ± 0.09
4	13.7466 ± 3.98085	6.52161 ± 4.09880	69.82 ± 0.10
5	-5.62093 ± 5.69333	-15.398 ± 5.89229	-70.42 ± 0.10
6	6.93857 ± 4.86916	9.51561 ± 5.02508	68.55 ± 0.10
7	-11.1223 ± 3.20928	-12.4626 ± 3.36644	-69.38 ± 0.07
8	12.4106 ± 3.54940	0.97123 ± 3.63273	70.50 ± 0.07
9	-5.10653 ± 4.69333	-8.52639 ± 4.87268	-72.95 ± 0.12
10	13.0458 ± 4.74149	15.8178 ± 4.94057	73.25 ± 0.12
11	-14.0071 ± 3.42950	-14.8719 ± 3.56185	-73.43 ± 0.09
12	12.0992 ± 4.32561	10.0242 ± 4.45385	68.43 ± 0.11
13	-8.82061 ± 4.68439	-7.61674 ± 4.90562	-69.36 ± 0.08
14	14.3738 ± 4.68990	13.8396 ± 4.89806	68.40 ± 0.08
15	-12.4106 ± 4.53140	-8.91496 ± 4.73583	-68.94 ± 0.08
16	2.95153 ± 5.71090	2.13973 ± 5.96682	70.59 ± 0.11
17	4.07992 ± 4.74055	8.25946 ± 4.95015	75.60 ± 0.20
18	-20.0714 ± 5.71119	-13.6645 ± 6.19874	-75.10 ± 0.13
19	10.2912 ± 4.99920	9.37051 ± 5.19343	76.25 ± 0.14
20	-6.33546 ± 7.32826	-7.98403 ± 7.63036	-71.20 ± 0.20

Table 7.8: Summary of corrections and contributions to the errors in % for the measured asymmetry. Reproduced from [33].

Source	Correction (%)	$\delta A/A(\%)$:1998	$\delta A/A(\%)$:1999
Statistics	—	13.3	7.2
P_e	—	7.0	3.2
Q^2	—	1.8	1.8
Backgrounds	1.2	0.6	0.6

Chapter 8

Discussion and Conclusions

In this thesis, I have discussed work on two parity-violating electron-scattering experiments, HAPPEX at Jefferson Lab and E-158 at SLAC. In this final chapter, I discuss the implications of the HAPPEX result for constraining strange form factors, the status of E-158, the prospects for continuing studies utilizing parity-violating electron scattering, and the outlook for controlling $^{\text{beam}}A_{\text{LR}}$'s at the level required by future experiments.

8.1 Extraction of Strange Form Factors

In the preceding chapter, we found that the combined result for the 1998 and 1999 HAPPEX runs was $A_{LR}^{ep} = -15.05 \pm 0.98 \pm 0.56$ ppm. The strange form factors are most easily extracted from this result using equation 2.28, which we reproduce here for convenience:

$$A_{LR}^{ep} = \left[\frac{-G_F M_p^2 \tau}{\pi \alpha \sqrt{2}} \right] \left\{ (2 - 4\sin^2 \theta_W) - \frac{\varepsilon \eta_p}{\varepsilon \eta_p^2 + \tau \mu_p^2} \frac{G_E^0 + \beta G_M^0}{(G_M^{p\gamma}/\mu_p)} \right\} - A_A, \qquad (8.1)$$

where $\eta_p = G_E^{p\gamma}/(G_M^{p\gamma}/\mu_p)$ and $\beta = (\tau \mu_p)/(\varepsilon \eta_p) = 0.392$ in our kinematics. A_A, taken from theory, is assumed to be 0.56 ± 0.23 ppm [30, 31]. The asymmetry depends on the electromagnetic form factors of the proton and neutron, and Table 8.1 collects the values we use. From these inputs, equation 8.1 yields

$$\frac{G_E^0 + 0.392 G_M^0}{G_M^{p\gamma}/\mu_p} = 1.527 \pm 0.048 \pm 0.027 \pm 0.011. \qquad (8.2)$$

The first error is statistical, the second is systematic, and the third arises from the uncertainty in A_A. We determine the contribution due to strange quark form factors using (from equation 2.27)

$$G_{E,M}^s = G_{E,M}^0 - G_{E,M}^{p\gamma} - G_{E,M}^{n\gamma} \tag{8.3}$$

and find

$$\boxed{G_E^s + 0.392 G_M^s = 0.025 \pm 0.020 \pm 0.014,} \tag{8.4}$$

where the first error is the quadrature sum of the experimental errors and the second error is due to uncertainty in the electromagnetic form factors. This result is consistent with the absence of a contribution from strange quarks.

Table 8.1: Choice of electromagnetic form factors for extracting strange form factors from A_{LR}^{ep}. The electromagnetic form factors are normalized to G_M^p/μ_p and evaluated at $Q^2 = 0.477$ GeV^2. The last column gives the fractional error in A_{th} due to the quoted error in the corresponding form factor. Note that $G_M^p = 0.9969$ in the dipole approximation at $Q^2 = 0.477$ GeV^2.

Form Factor	Value	Ref.	$\delta A_{th}/A_{th}$
$G_E^p/(G_M^p/\mu_p)$	0.99 ± 0.02	[120, 39]	3%
$G_E^n/(G_M^p/\mu_p)$	0.16 ± 0.03	[42, 41, 43, 44, 45]	4%
$(G_M^n/\mu_n)/(G_M^p/\mu_p)$	1.05 ± 0.02	[50]	2%

We chose to use the data from reference [50] for G_M^n because they are the most precise. However, there are data for G_M^n available [121] that are less precise but in disagreement with our choice from reference [50]. A possible systematic error in the data of reference [49] that could bring them into better agreement with those of reference [50] is being studied [122, 123]. Using the data from [49] would increase our result for $G_E^s + 0.392 G_M^s$ by 0.020, making it a 1.8σ deviation from the prediction for zero strange-quark contribution. New data for both G_M^n and G_E^n are currently being analyzed and additional measurements are being planned. These data will be important for validating our choices and for interpreting future measurements of strange quark form factors.

Figure 8.1a shows this result as a band in a space spanned by G_E^s and G_M^s. The solid line is the HAPPEX result, with the one-sigma errors given by the dashed lines. The experimental error and the uncertainties in the electromagnetic form factors have been added in quadrature.

Also shown are results from a number of theoretical models. Our measurement is precise enough

to rule out several models, including a dispersion-theory analysis of existing isoscalar form-factor

data [20] and a SU(3) Skyrme model [124]. However, a number of models predict either small

values for both form factors or fairly large values that conspire to cancel each other. This single

measurement cannot distinguish between these models.
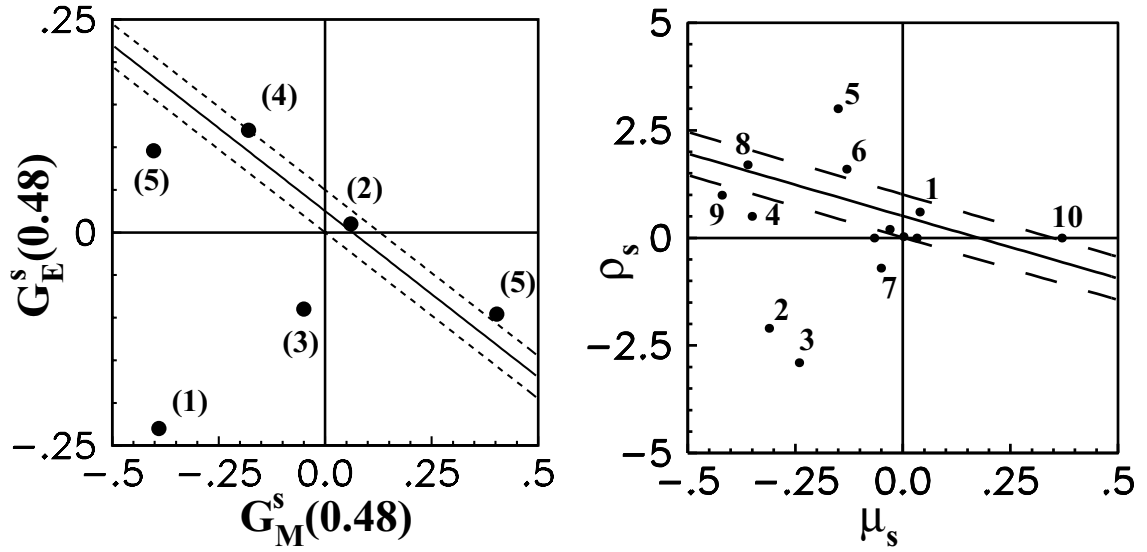
(a) Constraints imposed by this measurement on $G_E^s + 0.392 G_M^s$. The solid line is the result, and the dashed lines are the one-sigma errors. The black points are theoretical predictions arising from various models: (1) [20], (2) [22], (3) [124], (4) [25], and (5) [26].

(b) Constraint imposed by this measurement in ρ_s vs. μ_s space under the assumptions given in the text. The hashed lines represent the one-sigma error computed by adding the errors on $G_E^s + \beta G_M^s$ in quadrature. The points indicate the predictions of various models: (1) [18], (2) [19], (3) [20], (4) [21], (5) [22], (6) [23], (7) [24], (8) [25], (9) [26], and (10) [27].

Figure 8.1: Constraints imposed by HAPPEX on nucleon strangeness: (a) $G_E^s + 0.392 G_M^s$ and (b) extrapolated to $Q^2 = 0$ as discussed in the text.

We can also attempt to compare this result with theoretical predictions for $\rho_s \equiv \frac{dG_E^s}{d\tau}|_{\tau=0}$ and

$\mu_s \equiv G_M^s(Q^2 = 0)$ by assuming a parameterization of the Q^2 dependence of the strange form

factors. This is an interesting exercise because the majority of calculations are conducted solely

at $Q^2 = 0$. Like G_E^n, G_E^s is constrained to be zero at $Q^2 = 0$. This suggests that a Galster

parameterization introducing two new parameters λ_E^s and λ_M^s might be appropriate [119]:

$$G_E^s = \frac{\rho_s \tau G_E^p}{1 + \lambda_E^s \tau} \qquad\qquad G_M^s = \frac{\mu_s G_E^p}{1 + \lambda_M^s \tau}. \qquad\qquad (8.5)$$

Since λ_E^s and λ_M^s are completely unknown from theory, it might be reasonable for present purposes to assume that they are zero. Given these assumptions, Figure 8.1b plots the constraints on ρ_s and μ_s imposed by this measurement. Further progress will have to await the next HAPPEX collaboration experiments, which I discuss briefly in section 8.3.

In summary, we can draw several conclusions from the HAPPEX result:

1. HAPPEX measured $G_E^s + 0.392 G_M^s = 0.025 \pm 0.020 \pm 0.014$ at $Q^2 = 0.477\,\mathrm{GeV}^2$. This result, as shown in Figure 8.1a, is consistent with either zero contribution from strange quarks or with a conspiracy by G_E^s and G_M^s to cancel at these kinematics.

2. HAPPEX demonstrated that Jefferson Lab is an excellent facility for measuring small parity-violating asymmetries and validated the necessary experimental techniques. Jefferson Lab is capable of providing a high-current, high-polarization beam with excellent efficiency. Fluctuations in parameters of the beam are remarkably small, largely because of the accelerator's continuous-wave nature.

3. The HAPPEX and SAMPLE results provide significant constraints on strange form factors. The results are already tight enough to discriminate between models, providing important guidance to theorists.

4. Further measurements are necessary, and a multilab experimental program is now underway. This program is described in section 8.3.

8.2   Status of E-158

E-158 has completed two six-week physics runs (April/May 2002 and October/November 2002). The April/May run yielded $\sim$ 86 million good pulse pairs and was able to run at very high efficiency, $65 - 70\%$, concurrent with Babar. The October/November run took place during a scheduled down time for Babar, allowing even higher efficiency. The analysis of the April/May data set is well underway, and the collaboration expects to release first results early in the spring of 2003. The collaboration hopes to have an additional physics run during the fall of 2003, at which time it should be able to reach its proposal error bars.

8.3   Summary of Parity-Violating Electron-Scattering Experimental Program

Here I want to briefly summarize the world-wide parity-violating electron-scattering program. Most of this program is devoted to measuring the strange form factors of the proton, but other physics goals are being pursued as well. Both the HAPPEX and SAMPLE collaborations have further experiments planned, and additional experiments to measure strange form factors are currently underway at the Mainz Microtron (MAMI) and JLab Hall C. Experiments with other physics goals include two that are probing for physics beyond the Standard Model: E-158, of course, and the Q_{weak} experiment, which is going to determine $\sin^2 \theta_W$ by measuring the weak charge of the proton. Another experiment is going to measure the neutron skin* via parity-violating electron scattering off ^{208}Pb. Improved knowledge of the neutron skin is timely for several areas of physics, including atomic parity violation and determination of the equation of state for neutron stars. A number of groups are also considering possible experiments to measure various low-energy coupling constants accessible via interference of weak and strong amplitudes, but I will not discuss those

---

*For a heavy nucleus, one can define the neutron (proton) radius R_n (R_p) as the RMS radius of the neutron (proton) distribution. It is believed that heavy nuclei have a "neutron skin," i.e., that $R_n > R_p$ by several percent.

ideas further here. Table 8.2 serves as a summary of key parameters for each experiment. All of these experiments face a common set of design challenges that derive from measuring a small asymmetry with high statistical precision and small systematic errors. It is interesting to see the variety of solutions different collaborations have developed to meet these challenges.

HAPPEX II

The HAPPEX collaboration plans to run two additional experiments at $Q^2 = 0.1 \text{ GeV}^2$ and $\theta = 6°$ in 2003 [58, 59]. The first will be on hydrogen and will be sensitive to the same combination of strange form factors as the experiment reported in this thesis. The second will be on ^{4}He and so will be sensitive to G_E^s only (see section 2.1.6). The two experiments together will allow separation of G_E^s and G_M^s at a particular value of Q^2. In addition, comparison of the results on ^1H at $Q^2 = 0.477 \text{ GeV}^2$ and $Q^2 = 0.1 \text{ GeV}^2$ will allow us to begin to unfold the Q^2 dependence of G_E^s and G_M^s. The experimental design will be very similar to HAPPEX. In these kinematics, however, the scattering rates will be much higher. Fluctuations in beam parameters other than intensity will become as important source of noise. New cavity BPM's, similar to those used by E-158, are being developed with a goal of attaining 1-μm resolution. To cope with higher rates, and hence a larger radiation dose, a new detector is being built that will use quartz rather than lucite as the Cherenkov medium. HAPPEX II also has tighter constraints on $^{\text{beam}}A_{\text{LR}}$'s because of its smaller scattering angle (and hence larger sensitivity to beam fluctuations) and goal of a 50-ppb statistical error. HAPPEX II aims to control position differences, for instance, to a level of a few nanometers averaged over the course of the experiment, a limit several times more stringent than E-158's goal.

SAMPLE

The SAMPLE collaboration is making measurements of the strange form factors at backward angles and $\langle Q^2 \rangle = 0.1 \text{ GeV}^2$ [34, 35, 36]. They use a large-solid-angle air-Cherenkov detector system to compensate for (relatively) low rates at backward angles. This is feasible because the

momentum transfer does not change rapidly with angle at backward angles. Figure 8.2 gives a schematic of the SAMPLE setup. Backward-scattered electrons emit Cherenkov light that is focused and reflected by mirrors onto a set of 10 PMT's whose signals are integrated. The PMT's are heavily shielded. SAMPLE I measured the asymmetry from hydrogen and was sensitive to the combination $G_M^s + 0.44 G_A^s$. To separate the contribution of G_A^s, SAMPLE II measured the asymmetry from ^{2}D (which is sensitive primarily to G_A^s) at the same kinematics. The combined results, shown in Figure 8.3, are not consistent with a calculation of the axial form factor by Zhu *et al.* [31]. This may be because of difficulties in evaluating the radiative corrections for G_A^s, as is discussed in section 2.1.5. The SAMPLE collaboration is planning a second run (SAMPLE Lite) on ^{2}D with a lower incident electron-beam energy [125] in order to improve their measurement of G_A^s.
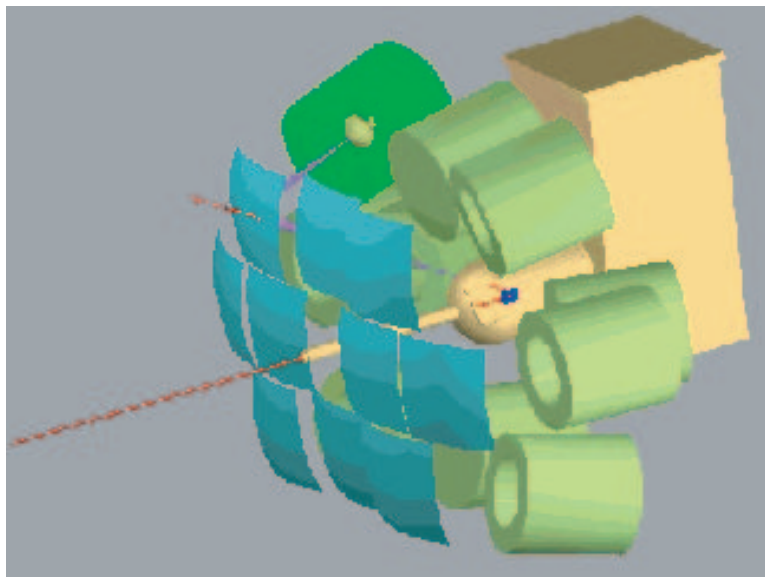

Figure 8.2: Schematic of the SAMPLE experimental setup. The electron beam, moving left to right, strikes the liquid hydrogen (or deuterium) target (blue, center). Backscattered electrons emit Cherenkov radiation in the air. An array of 10 mirrors focuses that light onto PMT's hidden inside shielding (green cylinders).
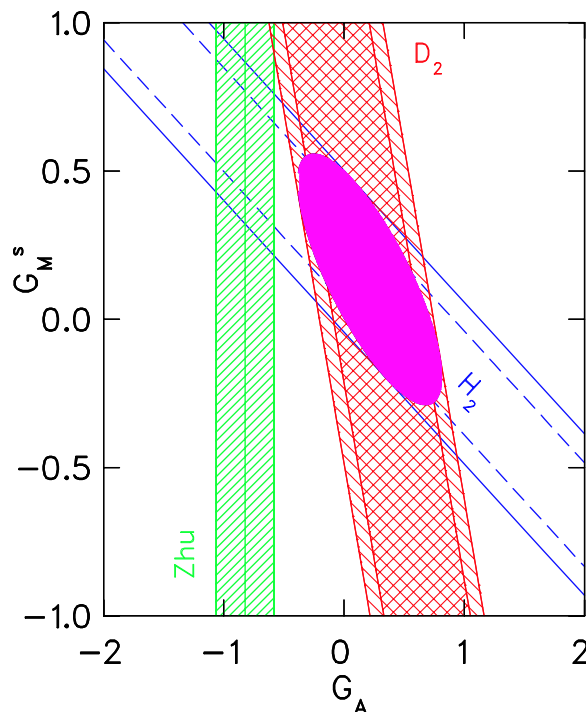
Figure 8.3: Combined analysis of the SAMPLE hydrogen [35] (blue) and deuterium (red, hash-marked) results reprinted from [36]. The error bands for the two measurements are indicated. The inner band is the statistical error alone. The outer band includes systematic uncertainties added in quadrature with the statistical error. The ellipse represents the allowed region for both form factors at the one-σ level. An estimate of the isovector axial form factor $G_A^e(T = 1)$, including both the anapole form factor and radiative corrections calculated by Zhu *et al.* [31] is also plotted (green).

Mainz A4

The A4 collaboration, working at MAMI, plans to measure both forward- and backward-angle asymmetries [80]. Unlike HAPPEX and SAMPLE, these experiments will be counting experiments and will make use of a highly segmented (1022 crystals) PbF_2 calorimeter. A schematic of the A4 experimental setup is given in Figure 8.4. Analyzing the spatial distribution of each event's energy deposition will allow separation of the elastic events from the inelastic background which is ten times larger. The detector covers a solid angle of 0.7 sr and for forward-angle measurements is centered on a scattering angle of 35˚. With a beam energy of 855 MeV ($Q^2 = 0.23$ GeV^2), the forward-angle measurement is sensitive to $G_E^s + 0.21G_M^s$ [15]. The forward-angle measurement is

currently underway, and when it is complete the detector will be reversed relative to the target to make a backward-angle measurement at 145°.
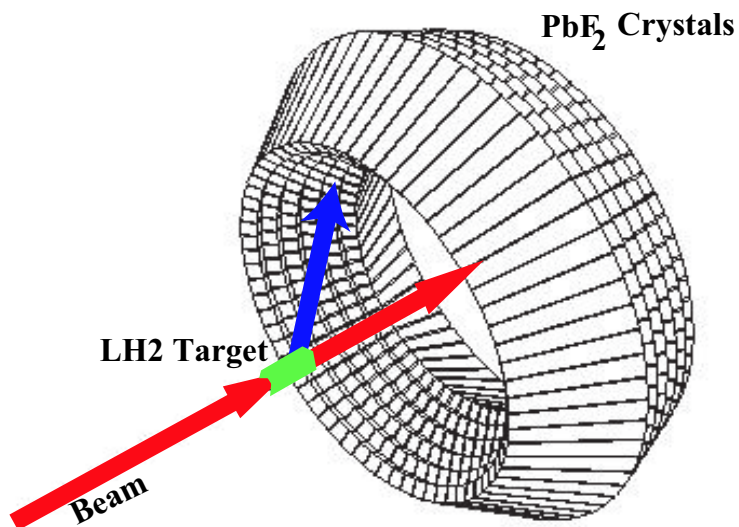

Figure 8.4: Schematic of the A4 experimental setup. The array of PbF_2 crystals is shown configured for the forward-angle measurement. The backward-angle measurement will be made by moving the array upstream of the target.

JLab $G0$

The $G0$ collaboration, working in Hall C at JLab, also plans to make both forward- and backward-angle measurements. In the initial phase, expected to begin physics data-taking in the Fall of 2003, $G0$ will measure forward-angle asymmetries from a hydrogen target simultaneously over a broad range of Q^2. This is possible because of their detector design, shown schematically in Figure 8.5: a superconducting toroidal magnet following the target will focus elastically scattered protons (rather than electrons, as in the other experiments) onto an array of plastic scintillators. The plastic scintillators are shaped to each detect protons from a particular Q^2 bin, and all together provide coverage over the range $0.12 < Q^2 < 1.0$ GeV^2. Time of flight will be used to reject

inelastic protons and fast particles (such as π^+'s), and the signal protons will be counted. Future

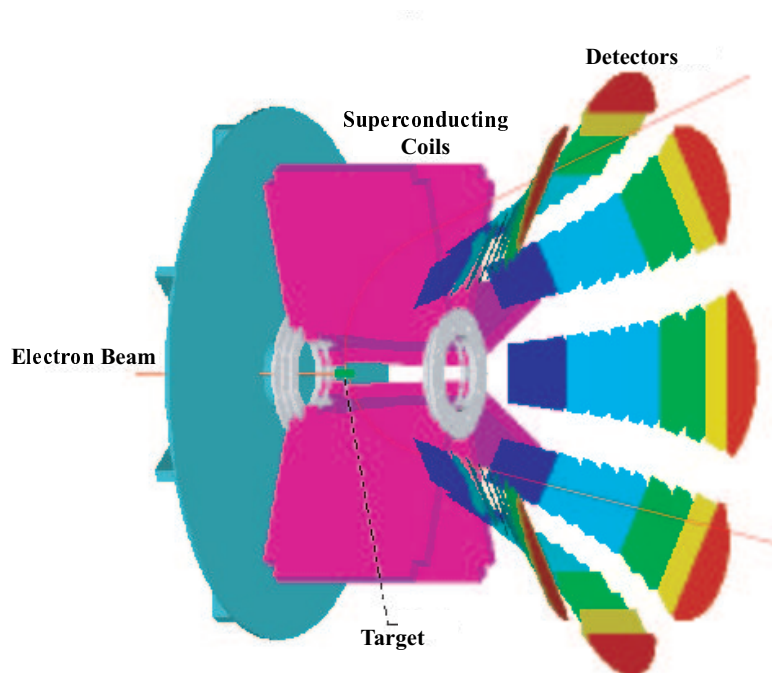backward-angle measurements are planned for both hydrogen and deuterium targets.

Figure 8.5: Schematic of the $G0$ experimental setup configured for the forward-angle measurement. The electron beam, incident from the left, strikes a liquid hydrogen target (green, center). Ejected protons are momentum-analyzed by a superconducting magnet and strike an array of scintillator paddles. Each scintillator paddle thus defines a bin in Q^2.

Q_{weak}

The Q_{weak} experiment has been approved to run in JLab Hall C [126]. Q_{weak} is a measurement of

the weak charge of the proton, and hence a measurement of $\sin^2 \theta_W$. Q_{weak} proposes to measure

$\sin^2 \theta_W$ to 0.0007, which would determine the running to 10σ within the Standard Model and give

the experiment significant sensitivity to several types of new physics, including additional gauge

bosons, supersymmetry, and leptoquarks.[†] Whereas E-158 is sensitive to purely leptonic couplings,

Q_{weak} is sensitive to hadronic couplings and thus has a complementary sensitivity to new physics.

[†]Leptoquarks are hypothetical bosons with nonzero baryon and lepton numbers.

The combination of the two experiments will provide constraints on new physics beyond what each can do individually. The experiment is designed to run at $\langle Q^2 \rangle = 0.03\,\mathrm{GeV}^2$ and a scattering-angle acceptance of $7 - 11$ degrees. A toroidal magnet will separate elastically and inelastically scattered electrons. The detector will be a quartz Cherenkov calorimeter, both for radiation hardness and to generate an adequate number of photons per detected electron. The detector will see a scattering rate of ~ 6 GHz, leading to a statistical error per asymmetry pair of 50 ppm. Q_{weak} likely will not run until after the completion of the G^0 program, and is tentatively scheduled to see first beam ~ 2006.

^{208}Pb

An experiment to measure the parity-violating asymmetry via scattering off ^{208}Pb [127] has been approved to run in JLab Hall A, and is currently expected to run in ~ 2004. This experiment is designed to measure the neutron radius of a heavy nucleus with 1% precision, thereby determining the magnitude (and sign) of the neutron skin. A number of experiments have attempted to measure the neutron radius using hadronic probes, but the results are difficult to interpret. The best estimates of the neutron radius to date come from nuclear theory and are uncertain at the $\sim 4\%$ level [128]. Several areas of physics would benefit from improved knowledge of the neutron radius, including nuclear theory [128], atomic parity violation [129], and neutron-star structure [130]. A new target, made of a 0.5-mm thick lead sheet sandwiched between two 0.15-mm thick sheets of diamond (used for its high heat conductivity), is being built for the experiment. The beam energy will be 850 MeV and the scattering angle 6°. In these kinematics, the measured asymmetry is expected to be ~ 0.5 ppm. The detected rate will be 860 MHz per detector, leading to a statistical noise of 140 ppm per pulse pair. To determine the neutron radius to 1%, the asymmetry must be measured to 3%, or 15 ppb. This leads to the toughest requirements yet envisioned for $^{\mathrm{beam}}A_{\mathrm{LR}}$'s: the charge asymmetry must be held below 100 ppb and measured to 10 ppb, and position differences must be held below 1 nm and measured to 0.1 nm. These requirements are an order of magnitude

more stringent than for E-158, even though the asymmetry is a factor of three larger, because the target is lead rather than another electron. Nuclear targets recoil much less than electrons, giving the scattered electron beam a much stronger angular dependence. The beam polarization will also need to be known to better than 1%, and several means of upgrading either or both the Møller and Compton polarimeters are under consideration.

Table 8.2: Experimental parameters and physics sensitivities of recent and planned parity-violating electron-scattering experiments. Listed for each experiment are the target, the Q^2, the lab scattering angle θ, the physics sensitivity, and the approximate physics asymmetry.

Exp't	Target	Q^2 (GeV^2)	θ	Sensitivity	Asym. (ppm)
HAPPEX [32, 33]	^{1}H	0.48	12°	$G_E^s + 0.392G_M^s$	15
HAPPEX II [58]	^{1}H	0.1	6°	$G_E^s + 0.39G_M^s$	1.7
HAPPEX II [59]	^{4}He	0.1	6°	G_E^s	8
SAMPLE I [34, 35]	^{1}H	0.1	130-170°	$G_M^s + 0.44G_A^s$	5
SAMPLE II [36]	^{2}D	0.1	130-170°	$G_M^s + 2.37G_A^s$	7
SAMPLE LITE [125]	^{2}D	0.04	130-170°		
Mainz A4 [80]	^{1}H	0.23	35°	$G_E^s + 0.21G_M^s$	6
$G^0(f)$ [81]	^{1}H	0.12-1.0	5-15°	varies	3-40
$G^0(b)$ [81]	^{1}H,^{2}D	0.3, 0.5, 0.8	$\sim 110°$	varies	3-40
Other Experiments					
E-158 [60]	^{1}H	0.025	0.25-0.45°	$\frac{1}{4} - \sin^2\theta_W$	0.18
Q_{weak} [126]	^{1}H	0.03	7-11°	$\frac{1}{4} - \sin^2\theta_W$	0.28
^{208}Pb [127]	^{208}Pb	0.008	6°	neutron skin	0.65

8.4   Outlook: Controlling $^{\text{beam}}A_{\text{LR}}$'s

Parity-violating electron scattering has matured as an experimental technique to the point where it is a valuable tool for pursuing several types of physics. As the measured asymmetries get smaller, controlling $^{\text{beam}}A_{\text{LR}}$'s becomes increasingly important. The need for high scattering rates pushes the experimenter towards small scattering angles, where the scattering rate depends very strongly on angle. HAPPEX and E-158 were the first two experiments to use strained GaAs photocathodes, and all future experiments expect to use similar cathodes in order to take advantage of the high polarization that they provide. This thesis discusses work that leads to control of the intensity

asymmetry at the sub-ppm level and position differences at the 20-nm level, where both results are statistics-limited. These results, with additional statistics, are anticipated to be sufficient for E-158. However, these results will not suffice for all future experiments. The most ambitious currently planned future experiment, a measurement of the neutron skin via scattering from ^{208}Pb, requires position differences at the 1-nm level and measured to the 0.1-nm level in order to keep the anticipated systematic error from beam helicity correlations below the statistical error. Progress can be and is being made on several fronts. Photocathodes which provide $> 80\%$ polarization with high QE, low QE anisotropy, and no charge limit are being pursued at SLAC and elsewhere. Use of feedback to control both the intensity asymmetry and position differences is becoming a standard tool. Learning to implement a position feedback which provides 1/N scaling of position differences on target would be a significant step forward. Such a feedback is under development in Hall A at JLab. Finally, there is clearly work left to be done to understand the fundamental sources of $^{\text{beam}}A_{\text{LR}}$'s and learning to eliminate them.

Appendix A

The SLAC Flash:Ti Laser System

This appendix discusses the design and operation of the Flash:Ti laser cavity, the Flash:Ti cooling flow system, the Flash:Ti modulator, the pulse shaping and intensity control optics, and the laser beam diagnostics. The Flash:Ti laser was largely designed and built at SLAC and is unique for its low jitter, long pulse length, and high repetition-rate capability. Performance results from the recent E-158 engineering and physics runs are presented. The discussion that is presented here is reproduced from the Nuclear Instrumentation and Methods A article that is otherwised included as Chapter 6 of this thesis. This material was written primarily by Axel Brachmann and edited by me for inclusion in the article.

A.1   Flash:Ti Laser Cavity

The Flash:Ti pump chamber was designed at SLAC and constructed for us by Big Sky Laser Technologies.* A schematic of the laser cavity is depicted in Figure A.1. The rod-shaped Ti:Sapphire crystal is pumped by two flashlamps, each of which is associated with an elliptically shaped reflector. The original commercial silver coatings of the reflectors and pump chamber end plates have been replaced by rhodium. This change substantially increased their mechanical and chemical surface durability and eliminated the need to purge the pump chamber with nitrogen during flashlamp changes or other maintenance work. The pump chamber parts can be exposed to air

---

*Big Sky Laser Technologies, Bozeman, MT, USA.

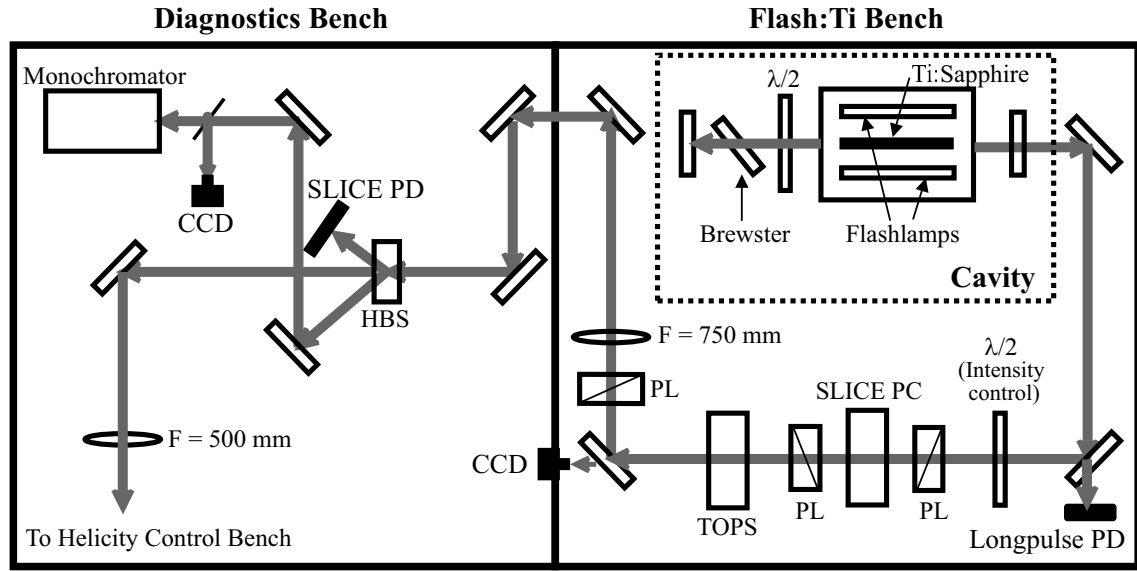**Diagnostics Bench**   **Flash:Ti Bench**

Figure A.1: Schematic of the laser cavity and the optical layout of the Flash:Ti and Diagnostics Benches ($\lambda/2$: half-wave plate, PD: photodiode, PL: polarizer, PC: Pockels cell, HBS: holographic beam sampler).

while they are handled without the risk of corrosion. Two cylindrical flashlamps[†] are used for this system. The flashlamp tubes have the following specifications: ID 4.8 mm, OD 5.98 mm, 7.6-inch arc length, Ce-doped quartz walls, and 450 Torr Xe filling. The output of the flashlamps is focused on the center of a 4-mm diameter 0.1%-doped Ti:Sapphire laser rod[‡] of 6.4-inch length. The rod, flashlamps, and pump chamber are cooled by a closed loop of ultra-pure water. The rod flow tube[§] surrounds the laser rod and its material acts as a UV filter to prevent excessive solarization of the Ti:Sapphire material.

We achieve maximum laser-cavity output power while maintaining low pulse-to-pulse jitter by using a one-meter-long cavity formed by an 85%-reflectivity planar output coupler and a 99.9%-reflectivity end mirror with a 2-m concave curvature. Both mirrors have narrow-band dielectric coatings centered at the operating wavelength (800 nm or 850 nm). A single quartz quarter-wave plate of ~ 1.3 mm thickness acts as both a Brewster plate and a birefringent tuner. It is mounted to allow for both horizontal rotation and rotation about the axis normal to its

---

[†]Model L8061E, T J Sales Associates Inc., ILC Technology Inc., Denville, NJ, USA.
[‡]Union Carbide Crystal Products, Washougal, WA, USA.
[§]KTF-2 fluorescent converter, Kigre, Inc., Hilton Head, SC, USA.

surface. In the horizontal plane the plate is set to the Brewster angle of $\sim 57°$. The effective refractive index of the quartz plate depends on the angle between the electric field vector and the optical orientation of the quartz plate. We achieve birefringent wavelength tuning by rotating the quartz plate about the axis normal to its surface. This optimizes the transmission for the desired output wavelength of 805 nm (852 nm for T-437 and the 2001 Engineering Run) with a bandwidth of ~ 0.7 nm (FWHM). A half-wave plate located between the laser head and the Brewster plate compensates for the arbitrary orientation of the Ti:Sapphire laser rod and thereby guarantees that p-polarization transmission is maximized through the Brewster plate. Recent modifications of the laser head assembly procedure allow installation of the laser rod with control of its crystallographic orientation. This eliminates the need for the half-wave plate inside the cavity and further improves the cavity's stability. Preliminary measurements in SLAC's laser development laboratory indicate a pulse-to-pulse jitter of $\sim 0.3\%$ rms. The equivalent modification of the laser head used at the polarized electron source is planned for the next E-158 physics run.

A.1.1 Thermal Lensing

Pumping the Ti:Sapphire rod with flashlamps leads to a strong thermal-lensing effect [131]. To investigate the power of the thermal lens for our system, the beam spot has been analyzed at relevant locations along the beam path under typical running conditions. A set of measurements is shown in Figure A.2. The lengths of the minor and major axes of the ellipse formed by the laser spot decrease with distance from the cavity center and increase again after the focal waist has been reached. The measurements indicate a focus at ~ 1.1 m from the center of the cavity. Compared to the curvature of the resonator mirrors, the thermal lens is the dominating optic. To optimize the laser stability, thermal lensing has been considered for end mirror selection and mirror spacing.
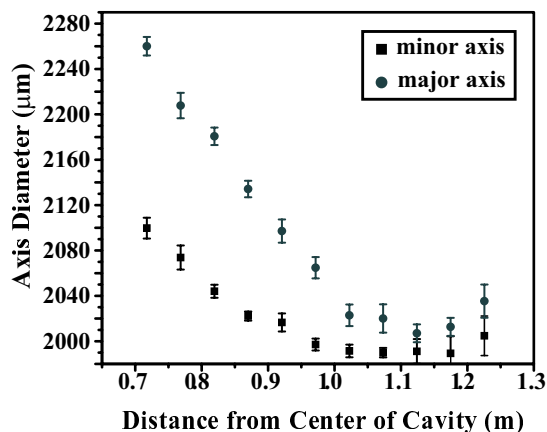
Figure A.2: Focusing of the laser beam due to thermal lensing at a laser wavelength of 805 nm and a flashlamp voltage of 8 kV. The dimensions of the laser spot ellipse are measured at the $1/e^2$ level.

A.1.2   Flash:Ti Cooling Flow System

The cooling water flow system is a closed loop and can be refilled from on-site low-conductivity water. Figure A.3 shows a schematic of the water flow system. The system is designed to ensure a constant temperature of 76° F and nearly inert water conditions. The main loop is chilled by a heat exchanger and operates at a flow rate of 2.5 GPM. Ultra-pure water quality (> 15 MΩ) is established by a 1-GPM polishing loop which contains a 0.2 μm particle filter, a deionization filter, an organic filter, and an oxygen filter. A nitrogen bubbler significantly reduces the partial pressure of oxygen in the reservoir, minimizing the amount of oxygen dissolved in the water. This was of particular importance when the silver-coated reflectors were in use. The cooling water constantly flows through a 10-μm particle filter and a heat exchanger. Either a 3-ton or a 5-ton chiller can be used to provide cooling for the heat exchanger. Interlocks are connected to water flow, resistivity, and temperature sensors mounted near the laser head. The interlocks shut off the laser power supply if the sensor values move out of tolerance. For flashlamp changes the laser head can be drained and purged by a separate N_2 supply.
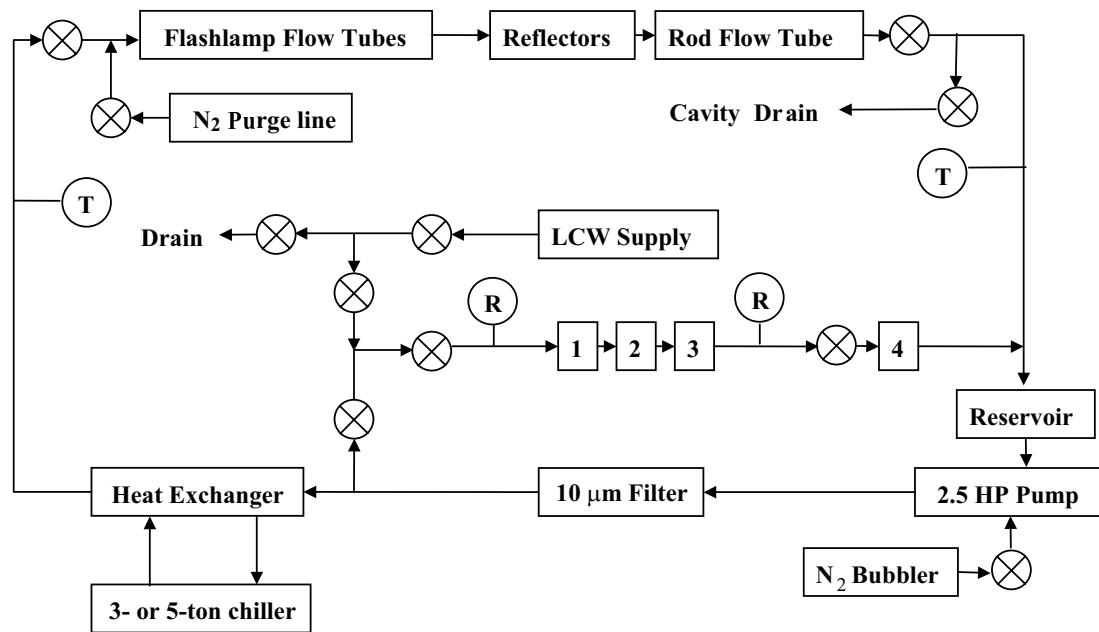
Figure A.3: Cooling water system components and water flow, including resistivity sensors (Ⓡ), temperature sensors (Ⓣ), valves (⊗), on-site low conductivity water (LCW), oxygen removal cartridge (1), activated carbon-organics filter (2), mixed bed deionizer (3), and submicron filter (4).

A.1.3 Flash:Ti Modulator

The modulator (Figure A.4) was designed and built by SLAC personnel and provides the high-voltage pulse needed to fire the flashlamps. A 1.2-μF capacitor charges from a 10-kV, 8-kJ/s power supply.[¶] Upon ignition of a thyratron, the capacitor discharges through the two flashlamps in series. This produces an over-damped electrical pulse whose characteristics are set by the capacitance of the capacitor and the stray inductance and resistance of the circuit components. The pulse has a peak current of 1 kA and a duration of 22 μs. Between pulses, a current through the flashlamps is maintained by a "simmer" power supply.[‖] The simmer current reduces the high voltage needed for conduction in the lamps and thereby extends their lifetime.

[¶]CCDS 810TI, Maxwell Technologies, San Diego, CA, USA.
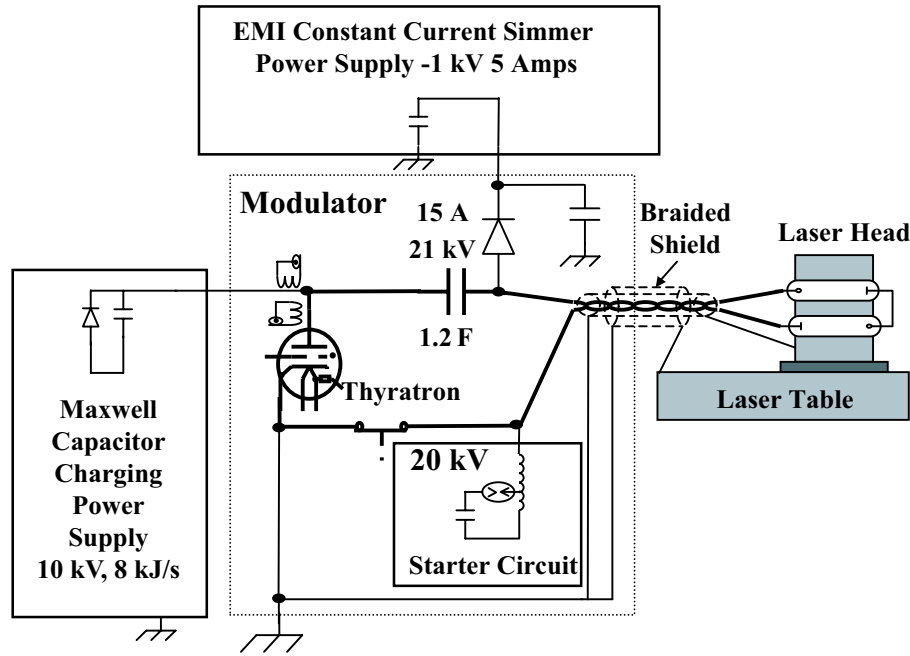[‖]Model 1000TS, EMI, Neptune, NJ, USA.

Figure A.4: Schematic circuit diagram of the Flash:Ti power supply.

A.2 Intensity Control and Pulse Shaping

Immediately following the laser cavity on the Flash:Ti bench in Figure A.1 are optics dedicated to controlling the laser pulse's energy, length, and temporal profile. Located between a pair of crossed polarizers, the "SLICE" Pockels cell is used to control the laser pulse's energy and pulse length. The "start" trigger for the SLICE Pockels cell is set at the beginning of the low-jitter section of the laser pulse (see Figure A.8b). The duration of the sliced pulse is set by its "stop" trigger. Typical sliced pulse lengths are $50 - 370$ ns. The SLICE Pockels cell is driven by a commercial high voltage pulser.** The amplitude of the high-voltage pulse controls the intensity of the laser pulse. We use the SLICE amplitude as the control device of a feedback system to stabilize the intensity of the electron beam. This feedback provides compensation for the slow decrease in cathode QE during its 3-day cesiation cycle as well as the slow degradation of the flashlamps' efficiency during their lifetime. The half-wave plate located upstream of the SLICE Pockels cell provides a means of limiting the maximum sliced laser power to a level that is safe for accelerator operation.

**Model *PVX*-3110, Directed Energy, Inc., Fort Collins, CO, USA.
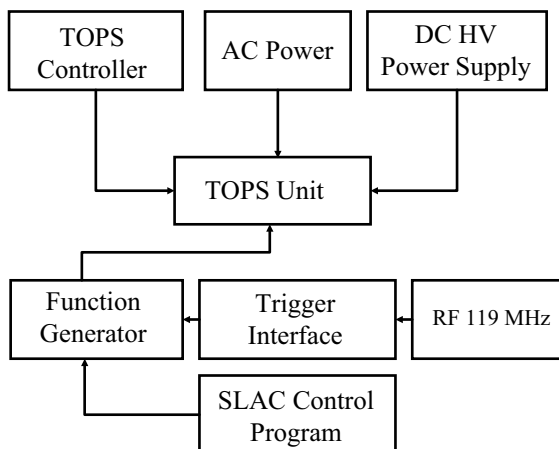
Figure A.5: Schematic of the TOp-hat Pulse Shaper electronics. The TOPS unit is installed on the Flash:Ti Bench (see Figure A.1) and contains the TOPS Pockels cell.

We shape the laser pulse's temporal profile using a Pockels cell–polarizer pair (TOPS, TOp-hat Pulse Shaper, shown schematically in Figure A.5) installed downstream of the SLICE Pockels cell. This shaping is used to compensate for beam loading and to achieve a small energy spread on the electron beam as described in section 6.4.3. TOPS is a SLAC-built pulse-shaping Pockels cell system driven by a Stanford Research Systems (SRS) DS345 30-MHz synthesized function generator. The SRS DS345 synthesized function generator has been modified internally. It uses the SLAC 119-MHz source as an oscillator. Power for the Pockels cell is supplied by a SLAC-built DC power supply. Control power for the TOPS system is supplied by the TOPS controller unit. The reference signal, which controls the Pockels cell, comes from the function generator. The function generator is integrated into the SLAC Control Program (SCP) through its GPIB interface. Remote control is achieved via an EPICS (Experimental Physics and Industrial Control System) user interface. The function generator allows one to generate an arbitrary waveform in 25-ns steps. Using TOPS to compensate for beam loading and minimize each pulse's energy spread is discussed further in section 6.4.3.

A.3 Diagnostics

The laser beam is folded at multiple locations using broadband NIR-coated (near-infrared) high-reflectivity mirrors. We use leakage light through these mirrors or a sampled beam for diagnostic purposes. We routinely monitor laser intensity, jitter, wavelength and spot size. The locations of the diagnostics are shown in Figure A.1. One photodiode installed upstream of the pulse-shaping optics monitors the Flash:Ti laser output (Longpulse PD). A holographic beam sampler[††] downstream of the pulse-shaping optics supplies two one-percent samples of the laser beam. One sample is used to monitor the intensity of the sliced pulse (SLICE PD). The second sample is focused onto a scanning monochromator for wavelength measurements or can be used to image the beam spot onto a CCD camera.

A.4 Laser Performance

We summarize below the performance of the upgraded Flash:Ti laser system during recent running. We briefly review the laser's performance during T-437 and the 2001 engineering run, and then focus on its performance during Physics Run I. The performance of the laser system for the earlier runs is more fully described in [132]. The operating parameters of the laser system for Physics Run I are summarized above in Table 6.1.

A.4.1 Flash:Ti Performance During T-437 and the E-158 Engineering Run

T-437 and the E-158 2001 Engineering Run preceded the Flash:Ti cavity optimization and thermal lensing studies. In addition, the cathode used for those runs required a wavelength of 852 nm for maximum electron polarization, causing the laser to operate fairly far from the gain maximum for Ti:Sapphire. We achieved a laser power of $\sim$ 20 mJ in a 15-μs laser pulse with the laser cavity

---

[††]Gentec Electro-Optics, Quebec, QC, Canada.

tuned to this wavelength. The SLICE Pockels cell described in section A.2 was set to slice a 130-ns pulse (370 ns for T-437) out of the area of highest stability, resulting in a pulse of 1.5% rms intensity jitter (1.0% rms for T-437). The pulse energy was ~ 175 μJ for these conditions during the Engineering Run.

A.4.2 Flash:Ti Performance During Physics Run I

A number of modifications improved the performance of the laser system for Physics Run I. First, the new photocathode requires a laser wavelength of 805 nm for peak electron polarization. At 805 nm the laser operates closer to the gain maximum of the Ti:Sapphire laser crystal, yielding a significant enhancement of laser performance. Furthermore, the consideration of thermal lensing described in section A.1.1 and appropriate end mirror selection were essential for improved performance. We also began to study the dependence of energy jitter on the laser power supply high voltage and the current of the switching thyratron. These were then optimized to minimize the laser's energy jitter. As the flashlamps and thyratron age they require small adjustments of the thyratron reservoir voltage.

Slow drifts in laser power and stability caused by humidity and temperature variations are minimized by appropriate air conditioning and humidity control. The temperature and humidity in the laser room are stable at 23.0 ± 0.1 °C and $35 \pm 1\%$, respectively. Figures A.6 and A.7 show the stability of the temperature and humidity in the Laser Room which houses the polarized source laser and optics systems.

Typical cavity output power at 805 nm is ~ 45 mJ. Pulse slicing provides a pulse of $50 - 370$ ns with a maximum energy of ~ 600 μJ per pulse (in 370 ns). During typical physics running, the laser pulse provided ~ 60 μJ in 270 ns in order to generate an electron beam pulse of $\sim 6 \cdot 10^{11}$ electrons/spill. Figures A.8a and A.8b show the temporal shape and the stability of the 15-μs laser pulse for a 100-pulse sample. Also indicated in Figure A.8b is the area of slicing, located at the point in time at which the laser energy jitter is at a minimum. The spatial profile
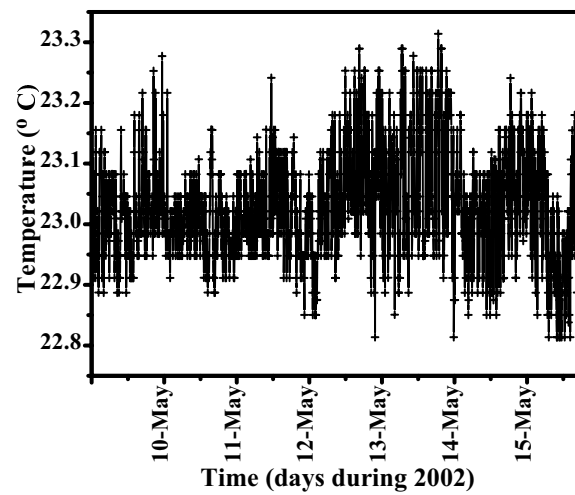
Figure A.6: Temperature stability of the Laser Room housing the polarized source laser and optics systems over a one-week time period.
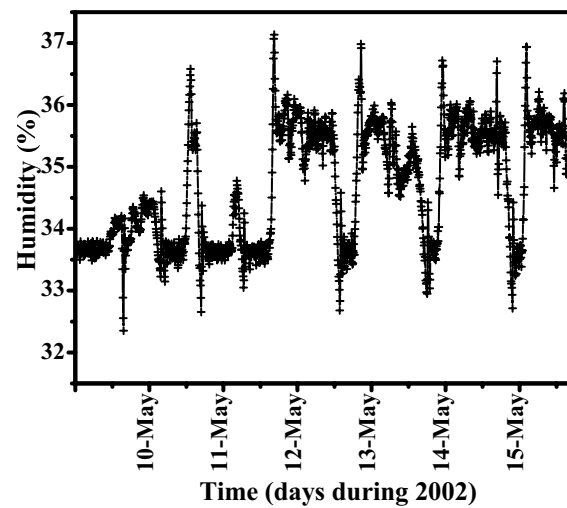

Figure A.7: Humidity stability of the Laser Room housing the polarized source laser and optics systems over a one-week time period.
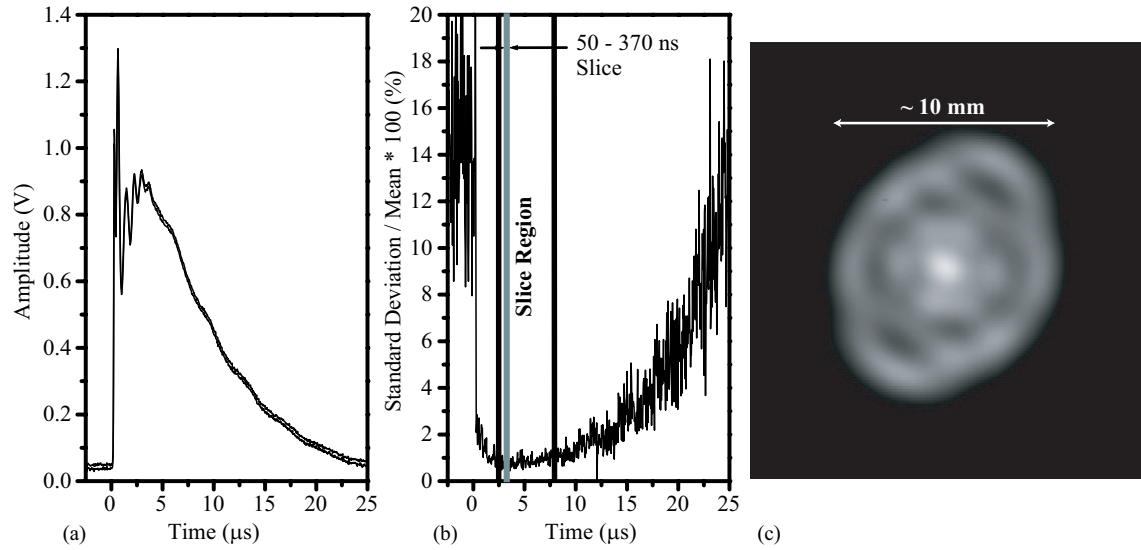
Figure A.8: (a) Photodiode signal of the Flash:Ti laser pulse. The two traces form an envelope about a sample of 100 measured pulses, indicating the pulse-to-pulse stability of the laser's temporal profile. (b) Energy jitter as a function of time within the pulse. The SLICE Pockels cell is used to select the $50 - 370$ ns region of lowest energy jitter, marked by the vertical lines. (c) The spatial profile of the sliced pulse.

of the laser beam, measured on the Diagnostics Bench and shown in Figure A.8c, indicates the multimodal structure of the laser pulse. Multimodal operation of the laser is necessary in order to generate the 15-μs pulse from which $50 - 370$ ns can be sliced with a flat-top profile. Figure A.9 shows the temporal profile of the electron beam at the first fast toroid following the cathode. Its profile reflects the profile of the sliced laser beam after it has been shaped by TOPS in order to compensate for beam-loading effects.

A pulse stability of $\sim 0.5\%$ rms was maintained throughout the run. A time history of the intensity jitter in the electron beam for a typical one-week period as measured by the first toroid downstream of the cathode (toroid 488) is shown in Figure A.10. The stability of the laser and electron beam intensities at 120 Hz as measured at the SLICE photodiode and toroid 488 are shown in Figures A.11a and A.11b, respectively. Figure A.11c shows the pulse-to-pulse jitter of the polarized electron beam at toroid AB01 60 located at the end of the accelerator near the target. The high degree of correlation between toroid 488 and toroid AB01 60, shown in Figure A.12, demonstrates the importance of a highly stable electron source. Almost no additional instabilities
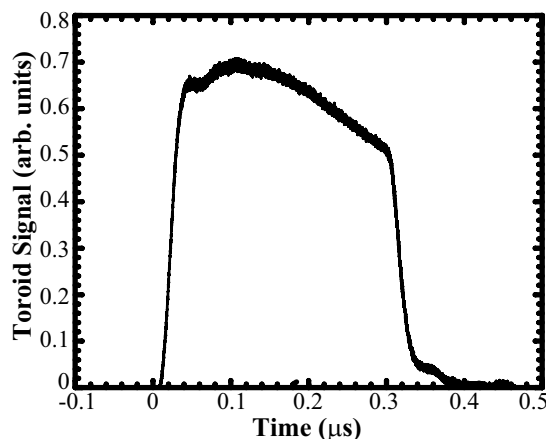
Figure A.9: Electron beam temporal profile resulting from using TOPS for beam-loading compensation.

in the intensity are introduced throughout the two-mile-long accelerator.

The maintenance of the laser system during the E-158 runs (5 months continuous operation at 60 Hz for the Engineering Run and 5 months for Physics Run I at a mix of 60 Hz and 120 Hz) consists of flashlamp changes every $\sim 1.45 \cdot 10^8$ laser pulses (28 days at 60 Hz and 14 days at 120 Hz) and cooling water system filter changes every 6 months. Changing the flashlamps requires one hour and can often be scheduled to occur during other planned interruptions to beam delivery, making the impact of laser system maintenance on E-158's running efficiency negligible. We observe no significant drop in laser performance due to the aging of flashlamps or water filters.
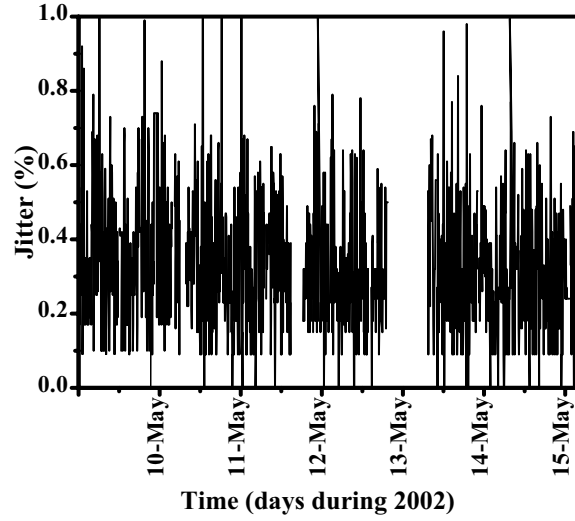
Figure A.10: Intensity jitter of the electron beam at the first toroid following the cathode over a one-week time period. Each point on the plot represents the rms of 10 sampled pulses.
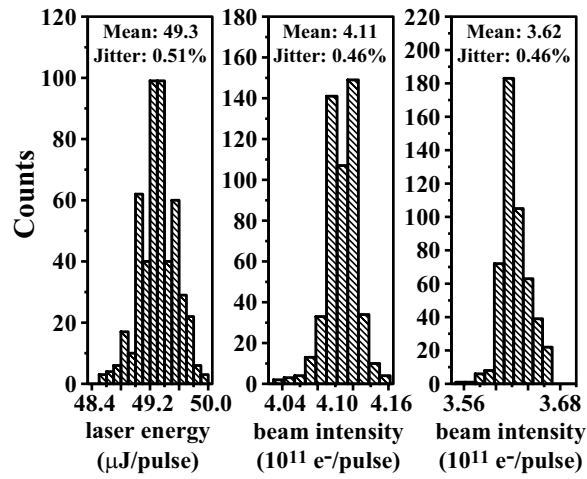
Figure A.11: (a) Histogram of the energy jitter in the sliced laser pulse. (b) Histogram of the intensity jitter in the electron beam in the injector. (c) Histogram of the intensity jitter in the electron beam at the end of the accelerator.
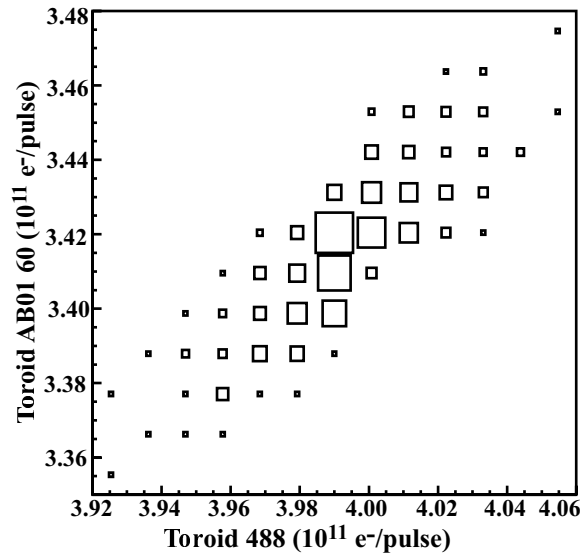
Figure A.12: Correlation plot of raw intensities as measured by toroid 488, located in the injector, and toroid AB01 60, located between the Linac and the E-158 target. The size of each square is proportional to the number of counts in its bin.

Appendix B

Derivation of the Unpolarized Electromagnetic Møller Cross Section

Here we present a derivation of the unpolarized cross section for electromagnetic Møller scattering, given in equation 2.33. The unpolarized cross section for electromagnetic Møller scattering can be derived by considering Figure B.1a, which shows the Feynman diagram for direct exchange of a photon between the two electrons, and Figure B.1b, which defines the kinematic variables in the center-of-momentum frame. The four-momentum transfer $q^2 = (p_a - p_c)^2$. In the center-of-momentum frame, the differential cross section is given by [107]

$$\frac{d\sigma}{d\Omega}\bigg|_{cm} = \frac{1}{64\pi^2 s} \frac{\mathrm{p}_b}{\mathrm{p}_a} |\mathcal{M}|^2, \tag{B.1}$$

where $s = (p_a + p_b)^2$ is the invariant total energy of the system, $|\mathcal{M}|^2$ is the invariant amplitude for this process, $\mathrm{p}_a = |\vec{p_a}|$ and $\mathrm{p}_b = |\vec{p_b}|$.

$$-i\mathcal{M} = (ie\overline{u}_c\gamma^\mu u_a)\left[\frac{-ig_{\mu\nu}}{(p_a - p_c)^2}\right](ie\overline{u}_d\gamma^\nu u_b) \tag{B.2}$$
$$- (ie\overline{u}_d\gamma^\mu u_a)\left[\frac{-ig_{\mu\nu}}{(p_a - p_d)^2}\right](ie\overline{u}_c\gamma^\nu u_b),$$

where the first term is for the direct diagram, the second is for the crossed diagram, and the relative minus sign satisfies the requirements of antisymmetrization for the interchange of iden-

219

(a) Feynman diagram for direct photon exchange.

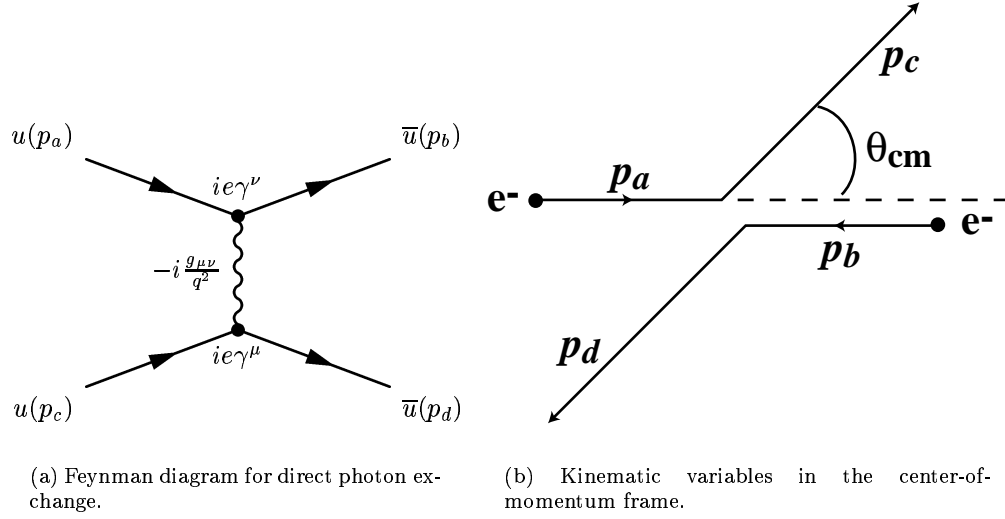(b) Kinematic variables in the center-of-momentum frame.

Figure B.1: Diagrams necessary for calculating the unpolarized Møller scattering cross section.

tical fermions. The amplitude for the crossed diagram is obtained from the direct diagram by interchanging p_c and p_d.

The spin-averaged invariant amplitude squared (averaging over the initial spin states and summing over final spin states) is given by

$$
\begin{aligned}
\overline{|\mathcal{M}|^2} &= \frac{1}{4} \sum_{s_a, r_a} |\mathcal{M}|^2 \\
&= \frac{e^4}{4} \sum_{s_a, r_a} \Bigg\{ \left[(\overline{u}_c \gamma^\mu u_a) \frac{g_{\mu\nu}}{(p_a - p_c)^2} (\overline{u}_d \gamma^\nu u_b) \right] \left[(\overline{u}_c \gamma^\mu u_a) \frac{g_{\mu\nu}}{(p_a - p_c)^2} (\overline{u}_d \gamma^\nu u_b) \right]^* \\
&\quad + \left[(\overline{u}_d \gamma^\mu u_a) \frac{g_{\mu\nu}}{(p_a - p_d)^2} (\overline{u}_c \gamma^\nu u_b) \right] \left[(\overline{u}_d \gamma^\mu u_a) \frac{g_{\mu\nu}}{(p_a - p_d)^2} (\overline{u}_c \gamma^\nu u_b) \right]^* \\
&\quad - \left[(\overline{u}_c \gamma^\mu u_a) \frac{g_{\mu\nu}}{(p_a - p_c)^2} (\overline{u}_d \gamma^\nu u_b) \right] \left[(\overline{u}_d \gamma^\mu u_a) \frac{g_{\mu\nu}}{(p_a - p_d)^2} (\overline{u}_c \gamma^\nu u_b) \right]^* \\
&\quad - \left[(\overline{u}_d \gamma^\mu u_a) \frac{g_{\mu\nu}}{(p_a - p_d)^2} (\overline{u}_c \gamma^\nu u_b) \right] \left[(\overline{u}_c \gamma^\mu u_a) \frac{g_{\mu\nu}}{(p_a - p_c)^2} (\overline{u}_d \gamma^\nu u_b) \right]^* \Bigg\},
\end{aligned}
\tag{B.3}
$$

where superscripts indicating the spin state of each spinor u_i have been suppressed for clarity.

Contracting the indices, we can simplify this to

$$\overline{|\mathcal{M}|^2} = \frac{e^4}{4} \sum_{s_a, r_a} \left\{ \frac{1}{t^2} \left[(\overline{u}_c \gamma^\mu u_a)(\overline{u}_a \gamma^\nu u_c)(\overline{u}_d \gamma_\mu u_b)(\overline{u}_b \gamma_\nu u_d) \right] \right.$$

$$+ \frac{1}{u^2} \left[(\overline{u}_d \gamma^\mu u_a)(\overline{u}_a \gamma^\nu u_d)(\overline{u}_c \gamma_\mu u_b)(\overline{u}_b \gamma_\nu u_c) \right] \qquad \text{(B.4)}$$

$$- \frac{1}{tu} \left[(\overline{u}_c \gamma^\mu u_a)(\overline{u}_a \gamma_\nu u_d)(\overline{u}_d \gamma_\mu u_b)(\overline{u}_b \gamma^\nu u_c) \right]$$

$$\left. - \frac{1}{tu} \left[(\overline{u}_d \gamma^\mu u_a)(\overline{u}_a \gamma^\nu u_c)(\overline{u}_c \gamma_\mu u_b)(\overline{u}_b \gamma_\nu u_d) \right] \right\},$$

where we have also made use of the Mandelstam variables s, t, and u:

$$s = (p_a + p_b)^2 \approx 2p_a \cdot p_b \approx 2p_c \cdot p_d$$

$$t = (p_a - p_c)^2 \approx -2p_a \cdot p_c \approx -2p_b \cdot p_d \qquad \text{(B.5)}$$

$$u = (p_a - p_d)^2 \approx -2p_a \cdot p_d \approx -2p_b \cdot p_c.$$

The approximations are valid in the ultrarelativistic limit. The completeness relation

$$\sum_{s=1,2} u^s(p)\overline{u}^s(p) = \not{p} + m_e \qquad \text{(B.6)}$$

allows us to convert equation B.4 to traces of products of matrices (where the electron mass m has been neglected in the ultrarelativistic approximation):

$$\overline{|\mathcal{M}|^2} = \frac{e^4}{4} \left\{ \frac{1}{t^2} Tr[\not{p}_c \gamma^\mu \not{p}_a \gamma^\nu] Tr[\not{p}_d \gamma_\mu \not{p}_b \gamma_\nu] \right.$$

$$+ \frac{1}{u^2} Tr[\not{p}_d \gamma^\mu \not{p}_a \gamma^\nu] Tr[\not{p}_c \gamma_\mu \not{p}_b \gamma_\nu] \qquad \text{(B.7)}$$

$$- \frac{1}{tu} Tr[\not{p}_c \gamma^\mu \not{p}_a \gamma_\nu \not{p}_d \gamma_\mu \not{p}_b \gamma^\nu]$$

$$\left. - \frac{1}{tu} Tr[\not{p}_d \gamma^\mu \not{p}_a \gamma^\nu \not{p}_c \gamma_\mu \not{p}_b \gamma_\nu] \right\}.$$

Application of the standard trace theorems (collected, for example, in [107] on pages 123 and 261)

yields

$$\overline{|\mathcal{M}|^2} = \frac{e^4}{4}\left\{ \frac{8}{t^2}[(p_c \cdot p_d)(p_a \cdot p_b) + (p_c \cdot p_b)(p_a \cdot p_d)] \right.$$

$$+\frac{8}{u^2}[(p_c \cdot p_d)(p_a \cdot p_b) + (p_d \cdot p_b)(p_a \cdot p_c)] \qquad (\text{B.8})$$

$$-\frac{8}{tu}[(p_a \cdot p_b)(p_c \cdot p_d)$$

$$\left. -\frac{8}{tu}[(p_a \cdot p_b)(p_c \cdot p_d)\right\}.$$

Making use of equations B.5, we can rewrite equation B.8 in an explicitly invariant form:

$$\overline{|\mathcal{M}|^2} = 2e^4\left\{ \frac{s^2 + u^2}{t^2} + \frac{s^2 + t^2}{u^2} + \frac{2s^2}{tu} \right\}. \qquad (\text{B.9})$$

Plugging equation B.9 into equation B.1 and observing that in the center-of-momentum frame $\mathbf{p}_a = \mathbf{p}_b$ and the Mandelstam variables are

$$s = 4(p^2 + m_e^2) \approx 4p^2$$

$$t = -2p^2(1 - \cos\theta_{cm}) \qquad (\text{B.10})$$

$$u = -2p^2(1 + \cos\theta_{cm}),$$

we find

$$\frac{d\sigma}{d\Omega}\bigg|_{cm} = \frac{e^4}{16\pi^2 s}\frac{(3 + \cos^2\theta_{cm})^2}{\sin^4\theta_{cm}} \qquad (\text{B.11})$$

$$= \frac{\alpha^2}{2m_e E_b}\frac{(3 + \cos^2\theta_{cm})^2}{\sin^4\theta_{cm}}.$$

In the last step, we used $\alpha = \frac{e^2}{4\pi}$ and $s = 2m_e E_b$ in the lab frame, where E_b is the energy of the incident electron beam. This reproduces equation 2.33.

Bibliography

[1] E. Noether. Invariante Variationsprobleme. *Nachr. v. d. Ges. d. Wiss. zu Göttingen*, pages S. 235–257, 1918.

[2] T. D. Lee and C. N. Yang. Question of Parity Conservation in Weak Interactions. *Phys. Rev.*, 104:254–258, 1956.

[3] C. S. Wu, E. Ambler, R. W. Hayward, D. D. Hoppes, and R. P. Hudson. Experimental Test of Parity Conservation in Beta Decay. *Phys. Rev.*, 105:1413–1415, 1957.

[4] C. Y. Prescott et al. Further Measurements of Parity Nonconservation in Inelastic Electron Scattering. *Phys. Lett. B*, 84:524–528, 1979.

[5] P. A. Souder et al. Measurement of Parity Violation in the Elastic Scattering of Polarized Electrons from ^{12}C. *Phys. Rev. Lett.*, 65:694–697, 1990.

[6] W. Heil et al. Improved Limits on the Weak, Neutral, Hadronic Axial Vector Coupling Constants from Quasielastic Scattering of Polarized Electrons. *Nucl. Phys.*, B327:1–31, 1989.

[7] A. O. Bazarko et al. *Z. Phys. C*, 65:189, 1995.

[8] H. L. Lai et al. *Phys. Rev. D*, 55:1280, 1997.

[9] J. Ashman et al. *Phys. Lett. B*, 206:364, 1988.

[10] The European Muon Collaboration. *Nucl. Phys. B*, 328:1, 1989.

[11] B. Lampe and E. Reya. Spin Physics and Polarized Structure Functions. *Phys. Rep.*, 332:1–163, 2000.

[12] B. Borasoy and U.-G. Meissner. Chiral Expansion of Baryon Masses and σ-Terms. *Ann. Phys.*, 254:192–232, 1997.

[13] J. Gasser, H. Leutwyler, and M. E. Sainio. Sigma-term update. *Phys. Lett. B*, 253:252–259, 1991.

[14] K. S. Kumar and P. A. Souder. Strange Quarks and Parity Violation. *Prog. Part. Nucl. Phys.*, 45:S333–S395, 2000.

[15] Douglas H. Beck and Barry R. Holstein. Nucleon Structure and Parity-Violating Electron Scattering. *Intl. J. Mod. Phys. E*, E10:1, 2001.

[16] D. H. Beck and R. D. McKeown. Parity-Violating Electron Scattering and Nucleon Structure. *Ann. Rev. Nucl. Part. Sci.*, 51:189–217, 2001.

[17] W. M. Alberico, S. M. Bilenky, and C. Maieron. Strangeness in the Nucleon: Neutrino-Nucleon and Polarized Electron-Nucleon Scattering. *Phys. Rep.*, 358:227–308, 2002.

[18] P. Geiger and N. Isgur. *Phys. Rev. D*, 55:299, 1997.

[19] R. L. Jaffe. *Phys. Lett. B*, 229:275, 1989.

[20] H.-W. Hammer, Ulf-G. Meisner, and D. Dreschel. *Phys. Lett. B*, 367:323–328, 1996.

[21] M. J. Musolf, R. Schiavilla, and T. W. Donnelly. *Phys. Rev. C*, 50:2173, 1994.

[22] H. Weigel, A. Abada, R. Alkofer, and H. Reinhardt. *Phys. Lett. B*, 353:20–26, 1995.

[23] N. W. Park, J. Schecter, and H. Weigel. *Phys. Rev. D*, 43:869, 1991.

[24] N. W. Park and H. Weigel. Orsay Report IPNO. Technical Report TH 91-57, 1991.

[25] S. J. Dong, K. F. Liu, and A. G. Williams. *Phys. Rev. D*, 58:074504, 1998. and private communication from K. F. Liu to authors of [46].

[26] M. J. Ramsey-Musolf and H. W. Hammer. *Phys. Rev. C*, 60:045204, 1999.

[27] S.-T. Hong, B.-Y. Park, and D.-P. Min. *Phys. Lett. B*, 414:229–236, 1997.

[28] M. N. Rosenbluth. *Phys. Rev.*, 79:615, 1950.

[29] Gerald A. Miller. Nucleon Charge Symmetry Breaking and Parity Violating Electron-Proton Scattering. *Phys. Rev. C*, 57:1492–1505, 1998.

[30] M. J. Musolf and B. R. Holstein. *Phys. Lett. B*, 242:461, 1990.

[31] S.-L. Zhu et al. *Phys. Rev. D*, 62:033008, 2000.

[32] K. A. Aniol et al. Measurement of the neutral weak form factors of the proton. *Phys. Rev. Lett.*, 82:1096–1100, 1999.

[33] K. A. Aniol et al. New Measurement of Parity Violation in Elastic Electron-Proton Scattering and Implications for Strange Form Factors. *Phys. Lett. B*, 509:211–216, 2001.

[34] B. A. Mueller et al. Measurement of the Proton's Neutral Weak Magnetic Form Factor. *Phys. Rev. Lett.*, 78:3824–3827, 1997.

[35] D. T. Spayde et al. Parity Violation in Elastic Electron-Proton Scattering and the Proton's Strange Magnetic Form Factor. *Phys. Rev. Lett.*, 84:1106–1109, 2000.

[36] R. Hasty et al. *Science*, 290:2117–, 2000.

[37] E. E. Chambers and R. Hofstadter. *Phys. Rev.*, 103:1454, 1956.

[38] R. C. Walker et al. *Phys. Rev. D*, 49:5671, 1994.

[39] M. K. Jones et al. *Phys. Rev. Lett.*, 84:1398, 2000.

[40] S. Galster et al. Elastic Electron-Deuteron Scattering and the Electric Neutron Form Factor at Four-Momentum Transfers $5 \text{ fm}^{-2} < q^2 < 14 \text{ fm}^{-2}$. *Nuclear Physics*, B32:221–237, 1971.

[41] C. Herberg et al. *Eur. Phys. Jour. A*, 5:131, 1999.

[42] I. Passchier et al. *Phys. Rev. Lett.*, 82:4988, 1999.

[43] M. Ostrick et al. *Phys. Rev. Lett.*, 83:276, 1999.

[44] J. Becker et al. *Eur. Phys. Jour. A*, 6:329, 1999.

[45] D. Rohe et al. *Phys. Rev. Lett.*, 83:4257, 1999.

[46] H. Zhu et al. Measurement of the Electric Form Factor of the Neutron through $\overrightarrow{d}\,(\overrightarrow{e},e'n)p$ at $Q^2 = 0.5$ (GeV/c)^2. *Phys. Rev. Lett.*, 87:081801, 2001.

[47] P. Markowitz et al. *Phys. Rev. C*, 48:R5, 1993.

[48] H. Anklin et al. *Phys. Lett. B*, 336:313, 1994.

[49] E. E. W. Bruins et al. *Phys. Rev. Lett.*, 75:21–24, 1995.

[50] H. Anklin et al. *Phys. Lett. B*, 428:248–253, 1998.

[51] H. Gao et al. *Phys. Rev. C*, 50:R546, 1994.

[52] H. Gao. *Nucl. Phys. A*, 631:170c–189c, 1998.

[53] W. Xu et al. *Phys. Rev. Lett.*, 85:2900, 2000.

[54] J. Golak et al. Extraction of Electromagnetic Neutron Form Factors through Inclusive and Exclusive Polarized Electron Scattering on a Polarized ^{3}He Target. *Phys. Rev. C*, 63:034006, 2001.

[55] C. Caso et al. *Eur. Phys. J. C*, 3:1, 1998.

[56] W. J. Marciano and A. Sirlin. *Phys. Rev. D*, 29:75, 1984.

[57] W. J. Marciano and A. Sirlin. *Phys. Rev. D*, 27:552, 1983.

[58] Jefferson Lab experiment 99-115, K. Kumar and D. Lhuillier, spokespersons.

[59] Jefferson Lab experiment 00-114, D. Armstrong, spokesperson.

[60] E. W. Hughes, K. S. Kumar, P. A. Souder, et al. A Precision Measurement of Parity Violation in Møller Scattering. *SLAC Proposal E-158*, 1997.

[61] Emanuel Derman and William J. Marciano. Parity Violating Asymmetries in Polarized Electron Scattering. *Annals of Physics*, 121:147–180, 1979.

[62] Andrzej Czarnecki and William J. Marciano. Electroweak radiative corrections to polarized Møller scattering asymmetries. *Phys. Rev. D*, 53:1066–1072, 1996.

[63] P. C. Rowson, Dong Su, and Stephane Willocq. Highlights of the SLD physics program at the SLAC Linear Collider. *Ann. Rev. Nucl. Part. Sci.*, 51:345–412, 2001. See references contained therein.

[64] A Combination of Preliminary Electroweak Measurements and Constraints on the Standard Model. Technical Report CERN-EP/2001-98, 2001. hep-ex/0112021.

[65] G. P. Zeller et al. A Precise Determination of Electroweak Parameters in Neutrino-Nucleon Scattering. *Phys. Rev. Lett.*, 88:091802, 2002.

[66] S. C. Bennett and C. E. Wieman. *Phys. Rev. Lett.*, 82:2484, 1999.

[67] M. Yu. Kuchiev and V. V. Flambaum. QED Radiative Corrections to Parity Nonconservation in Heavy Atoms. *Phys. Rev. Lett.*, 89:283002, 2002.

[68] Andrzej Czarnecki and William J. Marciano. Polarized Møller Scattering Asymmetries. *Int. J. Mod. Phys. A*, 15:2365–2375, 2000.

[69] V. A. Dzuba, V. V. Flambaum, and J. S. M. Ginges. High-Precision Calculation of Parity Nonconservation in Cesium and Test of the Standard Model. *Phys. Rev. D*, 66:076013, 2002.

[70] S. Godfrey. *Phys. Rev. D*, 51:1402–1405, 1995.

[71] J. L. Hewett and T. G. Rizzo. *Phys. Rep.*, 183:193, 1989.

[72] E. J. Eichten, K. D. Lane, and M. E. Peskin. *Phys. Rev. Lett.*, 50:811, 1983.

[73] B. W. Lynn, M. E. Peskin, and R. G. Stuart. Technical report. In *Physics at LEP*, CERN Report No. CERN-86-02 (1986).

[74] M. E. Peskin and T. Takeuchi. *Phys. Rev. D*, 46:381, 1992.

[75] M. E. Peskin and T. Takeuchi. *Phys. Rev. Lett.*, 65:964, 1990.

[76] D. C. Kennedy and B. W. Lynn. *Nucl. Phys. B*, 322:1, 1989.

[77] I. Maksymyk et al. *Phys. Rev. D*, 50:529, 1994.

[78] B. Grinstein and M. B. Wise. *Phys. Lett. B*, 265:326, 1991.

[79] J. L. Hewett et al. Indirect Probes of New Physics. 1996. SLAC-PUB-7088.

[80] Mainz experiment PVA4, D. von Harrach, spokesperson; F. Maas, contact person.

[81] Jefferson Lab experiment 00-006, D. Beck, spokesperson. 383 (1996).

[82] R. A. Mair et al. Anisotropies in Strain and Quantum Efficiency of Strained GaAs Grown on GaAsP. *Phys. Lett.*, A212:231–236, 1996.

[83] Paul Horowitz and Willard Hill. *The Art of Electronics*. Cambridge University Press, Cambridge, 1980. We implemented the pseudo-random helicity sequence according to the method described on pp. 437-442.

[84] Grady Wilson Miller IV. *Parity Violation in Forward Angle Elastic Electron-Proton Scattering*. PhD thesis, Princeton University, 2001.

[85] Richard S. Holmes. Pedestals and linearity for HAPPEX 1999. Technical report, October 1999.

[86] K. Unser. *IEEE Trans. Nucl. Sci.*, 16:934, 1969.

[87] K. Unser. *IEEE Trans. Nucl. Sci.*, 28:2344, 1981.

[88] K. Unser. Design and Preliminary Test of a Beam Intensity Monitor for LEP. In *Proc. IEEE Particle Acc. Conf., Chicago, IL*, page 71, 1989.

[89] W. Barry, J. Heefner, and J. Perry. Electronic Systems for Beam Position Monitors at CEBAF. Technical Report CEBAF-PR-90-023, Continuous Electron Beam Accelerator Facility, October 1990.

[90] W. Barry. A General Analysis of Thin Wire Pickups for High Frequency Beam Position Monitors. Technical Report CEBAF-PR-90-024, Continuous Electron Beam Accelerator Facility, October 1990.

[91] J. S. Price et al. 5 MeV mott polarimeter development at Jefferson Lab. SPIN 98 Proceedings. JLAB-ACC-97-27.

[92] B. D. Anderson et al. Basic Instrumentation for Hall A at Jefferson Lab. *Nucl. Instr. Meth. A*. Draft; to be submitted.

[93] N. Falletto et al. Compton Scattering off Polarized Electrons with a High-Finesse Fabry-Pérot Cavity at JLab. *Nucl. Instr. Meth. A*, A459:412–425, 2000.

[94] William E. Kahl. *A Measurement of the Strange Quark Content of the Proton*. PhD thesis, Syracuse University, 2000.

[95] G. D. Cates et al. The Bates Polarized Electron Source. *Nucl. Instr. Meth. A*, A278:293–317, 1989.

[96] R. Alley et al. The Stanford Linear Accelerator Polarized Electron Source. *Nucl. Instr. Meth. A*, A365:1–27, 1995.

[97] L. G. Levchuk. *Nucl. Instr. Meth. A*, 345:496–499, 1994.

[98] J. Gao et al. A Liquid Hydrogen Target for the Precision Measurement of the Weak Mixing Angle in Møller Scattering at SLAC. *Submitted to Nucl. Instr. Meth. A*, 2002.

[99] J. Gao, private communication.

[100] T. B. Humensky et al. SLAC's Polarized Electron Source Laser System and Minimization of Electron Beam Helicity Correlations for the E-158 Parity Violation Experiment. 2002. SLAC-PUB-9381. Submitted to Nucl. Instr. Meth. A.

[101] J. L. Turner et al. A High Intensity Highly Polarized Electron Beam for High-Energy Physics. Presented at EPAC'02, June 2002. SLAC-PUB-9235.

[102] M. Woods. SLAC E158: An experiment to measure parity violation in Moller scattering. In *American Institute of Physics Conference Proceedings*, volume 549, pages 910–12, 2000.

[103] P. A. Mastromarino et al. Helicity-Correlated Systematics for SLAC Experiment E158. SLAC-PUB-9071.

[104] K. H. Witte. A Reliable Low Maintenance Flashlamp Pumped TI:Sapphire Laser Operating at 120-PPS. Presented at Lasers '93, Lake Tahoe, NV, Dec 6-9, 1993. SLAC-PUB-6443.

[105] T. Maruyama et al. A Very High Charge, High Polarization Gradient-Doped Strained GaAs Photocathode. *Nucl. Instr. Meth. A*, 492:199–211, 2002.

[106] American Linear Collider Working Group (T. Abe and others). *Linear Collider Resource Book for Snowmass 2001*. 2001. SLAC-R-570, BNL-52627, CLNS-01-1729, FERMILAB-PUB-01-058-E, LBNL-47813, UCRL-ID-143810-DR, LC-REV-2001-074-US.

[107] F. Halzen and A. Martin. *Quarks and Leptons*. John Wiley and Sons, New York, New York, 1984. See pp. 105-106,126.

[108] M. Born and E. Wolf. *Principles of Optics, 6th ed.* Cambridge University Press, Cambridge, UK, 1980. See pp. 24-28.

[109] P. Saez et al. Polarization studies of strained GaAs photocathodes at the SLAC gun test laboratory. Talk given at 16th IEEE Particle Accelerator Conference (PAC 95) and International Conference on High Energy Accelerators (IUPAP), Dallas, Texas, 1-5 May 1995. SLAC-PUB-6987.

[110] F.-J. Decker et al. Interlaced Beams of Unequal Energy and Pulse Length in the SLAC Linac for PEP-II and Experiment E-158. Presented at EPAC'02, June 2002. SLAC-PUB-9361.

[111] E. Collett. *Polarized Light*. Marcel Dekker, Inc., New York, New York, 1993.

[112] K. S. Kumar. *Parity Violation in Elastic Electron Carbon Scattering*. PhD thesis, Syracuse University, 1990.

[113] Peter A. Mastromarino. Beam Fluctuations in Parity-Violating Electron Scattering Experiments. Senior Thesis, Princeton University Dept. of Physics, April 1999.

[114] Maud Baylac. *Mesure de la polarisation du faisceau d'électrons du Jefferson Laboratory par effet Compton pour l'expérience de violation de parité HAPPEX en diffusion élastique électron-proton.* PhD thesis, l'Universite Claude Bernard-Lyon I, 2001.

[115] Gary Rutledge and Robert Michaels. Systematics of Q^2 for HAPPEX. Technical report, February 2000.

[116] Gary A. Rutledge. *Measurement of the Strange Sea of the Proton.* PhD thesis, The College of William and Mary, 2001.

[117] Detailed paper on HAPPEX. In preparation.

[118] Nimai C. Mukhopadhyay, M. J. Ramsey-Musolf, Steven J. Pollock, Jùn Liu, and H.-W. Hammer. Parity-violating excitation of the $\Delta(1232)$: hadron structure and new physics. *Nucl. Phys. A*, 633:481–518, 1998.

[119] M. J. Musolf et al. *Phys. Rep.*, 239:1, 1994.

[120] R. C. Walker et al. *Phys. Rev. D*, 49:5671, 1994.

[121] E. E. W. Bruins et al. *Phys. Rev. Lett.*, 75:21, 1995. We have corrected these data down by 25% of the difference of these data and those of Ref. [50], based on a private communication from B. Schoch.

[122] J. Jourdan, I. Sick, and J. Zhao. *Phys. Rev. Lett.*, 79:5186, 1997.

[123] E. E. W. Bruins et al. *Phys. Rev. Lett.*, 79:5187, 1997.

[124] N. W. Park and H. Weigel. *Nucl. Phys. A*, 541:453–491, 1992.

[125] MIT-Bates experiment 00-04, T. Ito, spokesperson.

[126] Jefferson Lab experiment 02-020, J. Bowman, R. Carlini, J. Finn, S. Kowalski, and S. Page, spokespersons.

[127] Jefferson Lab experiment 00-003, R. Michaels, P. Souder, and R. Urciuoli, spokespersons.

[128] C. J. Horowitz, S. J. Pollock, P. A. Souder, and R. W. Michaels. *Phys. Rev. C*, 63:025501, 2001.

[129] S. J. Pollock, E. N. Fortson, and L. Wilets. *Phys. Rev. C*, 46:2587, 1992.

[130] see, e.g., C. J. Horowitz and J. Piekarweicz. *Phys. Rev. Lett.*, 86:5647, 2001.

[131] Anthony E. Siegman. *Lasers.* University Science Books, Mill Valley, California, 1986. See pp. 842-845.

[132] A. Brachmann et al. SLAC's Polarized Electron Source Laser System for the E-158 Parity Violation Experiment. In *Proc. SPIE: Laser and Beam Control Technologies*, volume 4632, page 211, 2002.